INAUGURAL - DISSERTATION

zur

Erlangung der Doktorwürde

der

Naturwissenschaftlich-Mathematischen Gesamtfakultät

der

Ruprecht-Karls-Universität Heidelberg

vorgelegt von

Jean Rehbinder

aus Paris

Heidelberg, im Mai 2013

Tag der mündlichen Prüfung: 12.07.2013

Quick and specific non-linear microscopy using shaped pulses with durations down to 10fs

Gutachter:

Herr Professor Dr. Marcus Motzkus

Herr PD Dr. Dirk-Peter Herten

Abstract

Nonlinear optical microscopy is ideally suited for *in vivo* imaging: it provides label-free contrast revealing intrinsic structural and chemical properties of the sample in a non-invasive way. Successful nonlinear microscopy relies on the use of pulsed lasers to obtain high signal levels at moderate average laser power. In particular, broadband excitation increases the nonlinear generation efficiency as well as the spectral coverage. However, lower photodamage thresholds and less straightforward signal interpretation have prevented its application to sensitive samples.

In this thesis, a pulse shaper is used to tailor ultrashort pulses for optimal imaging. This work concentrates on Coherent Anti-Stokes Raman Scattering (CARS) because it provides an access to highly specific vibrational spectra. The main concept is to encode molecule-specific information directly in the excitation. This is realized either by direct tailoring in a shaper-assisted variant of a Multiplex CARS setup or by phase shaping of a single ultrashort pulse (<10fs). The photon load reduction and the optimization of the pulse profile achieved by shaping are demonstrated with the imaging of polymer samples and sensitive biological tissue. The flexibility of the setup allows switching between spectrally resolved acquisition for precise chemical mapping and single channel detection for rapid imaging.

Further nonlinear effects can likewise be controlled by pulse shaping. In this work, the systematic modification of the relative intensities of Second Harmonic Generation (SHG), Two-Photon Excited Fluorescence (TPEF) and CARS is investigated as well as selective excitation of fluorophores and molecular vibrations. Multimodal imaging with shaped ultrashort pulses proves to be particularly efficient for biological samples as illustrated by the imaging of plant cells and skin biopsies.

Zusammenfassung

Nichtlineare optische Mikroskopie ist für die Bildgebung lebender Proben besonders geeignet: ohne den Einsatz von Kontrastmitteln offenbart sie strukturelle sowie chemische Eigenschaften der Probe. Gepulste Laser ermöglichen die Erzeugung hohes Signalintensitäten bei geringen mittleren Leistungen und bilden damit die Voraussetzung für eine erfolgreiche nichtlineare Mikroskopie. Die Verwendung breitbandiger Spektren erhöht die Effizienz nichtlinearer Effekte und ermöglicht die Anregung von Molekülschwingungen über einem weiten Spektralbereich. Ihre Anwendung auf empfindliche Proben wurde jedoch bisher aufgrund erhöhter Phototoxizität und komplizierter Signalauswertung verhindert.

In dieser Arbeit wird ein Impulsformer eingesetzt, um ein breitbandiges Spektrum für eine optimale Bildgebung anzupassen. Der Fokus liegt auf Kohärenter Anti-Stokes Raman Streuung (CARS), da dieser Effekt einen Zugang zu hochspezifischen Schwingungsspektren bietet. Das wichtigste Konzept ist dabei Molekül-spezifische Information direkt in der Anregung zu kodieren. Dies kann auf zweierlei Arten erfolgen: durch Amplitudenformung des Stokesspektrums im Rahmen eines Shaper-basierten Multiplex CARS Experiments oder ultrakurze Impulse (<10fs) werden unter Verwendung spezieller Phasenfunktionen maßgeschneidert. Die Reduzierung der Strahlungsbelastung sowie die Optimierung der Impulsform werden anhand der Bildgebung von Polymerproben und empfindlichem biologischem Gewebe demonstriert. Die Flexibilität des Aufbaus ermöglicht es zwischen spektralaufgelösten Aufnahmen für eine genaue chemische Bildgebung und Einzelkanaldetektion für eine schnelle Abbildung umzuschalten.

Andere nichtlineare Effekte können ebenfalls durch Impulsformung gesteuert werden. Die Änderungen der relativen Intensitäten von Zweiter Harmonische (SHG), Zwei-Photonen-Fluoreszenz (TPEF) und CARS werden untersucht, sowie die selektive Anregung von Fluorophoren und molekularen Schwingungen gezeigt. Multimodale Bildgebung mit geformten ultrakurzen Impulsen erweist sich als besonders effizient für biologische Proben, wie es an der Bildgebung von Pflanzenzellen und Hautbiopsien gezeigt werden konnte.

Table of Contents

1 Introduction

In vivo imaging has remained a very challenging task until today. Minimally invasive techniques are required, if possible avoiding the addition of staining agents susceptible to disturb the studied native function. Sub-cellular resolution is desirable to decipher the complex processes happening inside a tissue or a model organism. At the same time, substances of interest must be identified specifically among the numerous compounds interacting in a cell. Among the many established methods for imaging of biological systems and medical diagnosis, most fail to fulfill at least one of these requirements: the high chemical specificity of mass spectrometry comes along with sample destruction, gold standard histological procedures include fixation and staining, magnetic resonance tomography lacks cellular resolution.

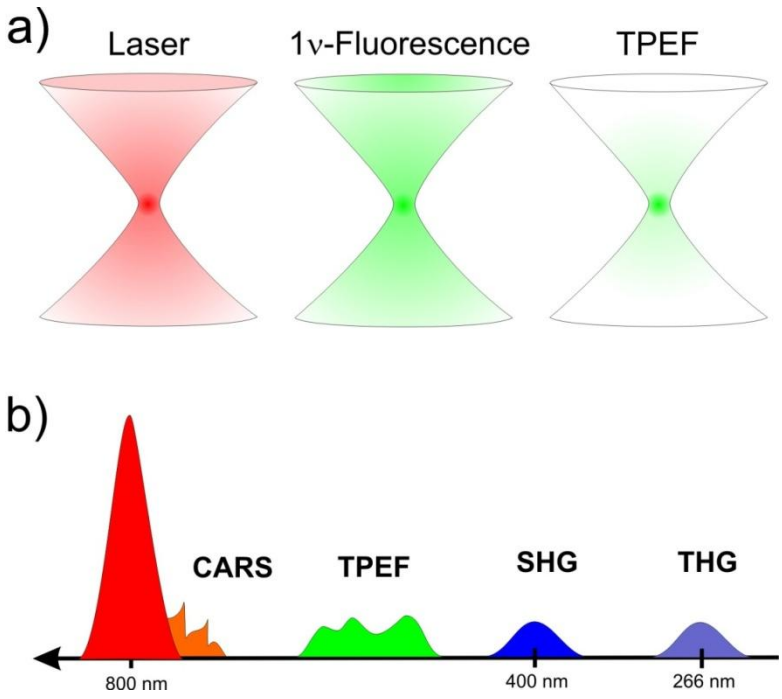

Figure 1.1 Non-linear microscopy. a) 3D sectioning through non-linear excitation. The one-photon fluorescence signal is proportional to the laser intensity, while two-photon excitation is proportional to the square of the intensity. The recorded TPEF signal is generated only at the focal point. b) Different non-linear signals appear at different wavelengths. CARS: Coherent Anti-Stokes Raman scattering, TPEF: Two-Photon Excited Fluorescence. SHG/THG: Second/Third Harmonic Generation.

Non-linear microscopy, in turn, presents a unique combination of properties making it particularly suited for in vivo studies. It inherits the sub-micrometric resolution of optical microscopy as well as its non-invasive properties. In addition, non-linear excitation restricts the effective interaction to the focal point and is responsible for intrinsic 3D sectioning as illustrated in Figure 1.1 (a). Different non-linear effects provide as many contrast mechanisms based on sample properties for label-free imaging. In this respect, Coherent Anti-Stokes Raman Scattering (CARS) presents the highest potential: it probes vibrational levels of molecules and is sensitive directly to the chemical composition of the sample. This makes CARS useful also for material science applications, where online characterization with

micrometric precision and chemical sensitivity can be of great interest. Other common non-linear effects are two-photon excited fluorescence (TPEF) and second harmonic generation (SHG). TPEF highlights the presence of endogenous and/or exogenous fluorophores. SHG is produced only by non-centrosymmetric media. In the body, collagen is the main source of SHG and a very wide spread molecule responsible for the structure of tissues.

For efficient nonlinear microscopy, ultrashort laser pulses are used. The development of non-linear microscopy has therefore been closely linked with the development of pulsed lasers. By producing short bursts of light, the peak intensities increases significantly at same mean intensity. This allows observation of non-linear signal generation even at moderate powers preventing damage of the sample. The shortest pulses are the most efficient for nonlinear generation at a given average power and ultrashort pulses of 100fs to 1ps duration are currently used in most non-linear microscopes. To bring non-linear microscopy to the next level, shorter pulses are necessary. Lasers with pulse durations under 10fs are now available but are associated with a set of additional challenges. These include non-linear photodamage due to higher peak intensities, the increased influence of an unwanted four-wave-mixing background in CARS and a less straightforward extraction of molecule specific vibrational information.

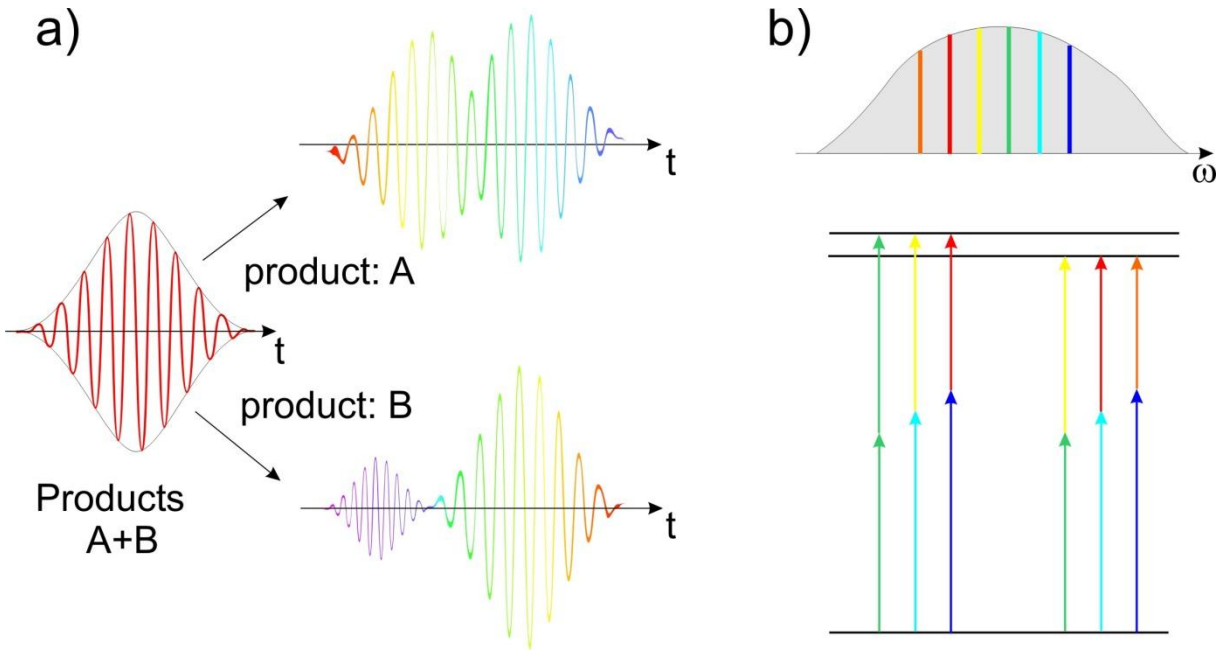

Figure 1.2 Coherent control. a) Time domain picture. By tuning the arrival time of different frequencies of the ultrashort pulse, one or the other product in a reaction can be favored. b) Spectral domain picture. Interferences between multiphoton excitation pathways can be used to excite selectively one quantum level of the system preferentially.

Pulse shaping can make the most out of sub-10fs pulses for non-linear microscopy. By manipulating precisely the temporal shape of an originally ultrashort pulse, the relative importance of different effects can be influenced, as illustrated in Figure 1.2 (a). This has been the foundation of the field of coherent control, where different reaction pathways can be favored or reduced depending on the shape of the pulse. An equivalent picture, shown in Figure 1.2 (b), considers the interference between different photon combinations reaching a quantum level of a molecule. Principles of coherent control applied to non-linear effects has

been demonstrated and allowed retrieving complete CARS spectra. In this work, pulse shaping is used to meet the requirements of quick and efficient microscopy. Proposed amplitude and phase shaping schemes are discussed theoretically and demonstrated on pure chemicals and for imaging of samples relevant to material science, biology and medical diagnosis. In more detail:

- **Chapter** 2 gives the necessary theoretical background used in the experimental demonstrations. After reviewing the main nonlinear effects used for microscopy, the CARS effect is described in detail to point out the properties that make it a powerful tool for microscopy as well as its limits using classical picoseconds sources. The generation of ultrashort pulses and the principles of pulse shaping are then described as a prerequisite for the control of non-linear processes.

- While most common CARS implementations excite only one vibrational mode, Multiplex-CARS is a method for rapid detection of whole CARS spectra. A shaper-assisted implementation of Multiplex-CARS is demonstrated in **Chapter** 3. Amplitude shaping of the Stokes pulse gives a direct and precise control over which modes are excited. The pulse combination can then be tailored to the spectrum of a particular molecule.

- In **Chapter** 4 a single shaped broadband pulse is used for CARS spectroscopy and microscopy in a scheme known as Single-Beam CARS. Previously demonstrated shaping strategies are presented and their merit for microscopy discussed. The application of this method to a medically relevant problematic was facilitated by the extension of the spectral range of the technique to the $3000cm^{-1}$ region. Spectrally resolved and single-channel implementations of Singe-Beam CARS are compared for the imaging of the border of a tumor in histological preparations from a mouse brain.

- In multimodal microscopy the complementary information obtained with different nonlinear effects is detected simultaneously. In **Chapter** 5, the CARS signal is complemented by the acquisition of TPEF and SHG signals. The effect of shaping on the different non-linear effects is compared. Imaging of moos leaves and human skin preparations as well as polarization studies on rat-tail tendon achieve to demonstrate the flexibility of the setup.

- The work is finally summarized in **Chapter 6** where an outlook for future developments is also given.

2 Fundamentals: nonlinear microscopy with shaped pulses

This chapter is devoted to the description of theoretical foundations of the work presented in this thesis. After a short introduction of the main nonlinear effects used for microscopy, particular attention will be given to Coherent Anti-Stokes Raman Scattering (CARS) as a microspectroscopy technique. Principles of broadband pulse generation and shaping will then be exposed as the working tool of the subsequent demonstrations.

2.1 Nonlinear microscopy

The non-linear interaction of light with matter is conveniently summarized as a power-series expansion generalizing the linear susceptibility of the medium to higher order interactions:

$$\boldsymbol{P}(t) = \chi^{(1)}\boldsymbol{E}(t) + \chi^{(2)}\boldsymbol{E}(t)\boldsymbol{E}(t) + \chi^{(3)}\boldsymbol{E}(t)\boldsymbol{E}(t)\boldsymbol{E}(t) + \cdots \quad (1)$$

This seemingly simple equation is in reality quite general, and presents a large number of free parameters summarized into the tensors for the first, second and third order optical susceptibilities. The linear susceptibility alone is a tensor of the second order, accounting for all effects used in the various linear microscopy methods: absorption, optical refractive index and birefringence.

$\chi^{(2)}$ and $\chi^{(3)}$ are third and fourth order tensors with 27 and 81 parameters respectively. Symmetry considerations might strongly reduce the number of free parameters; this still illustrates the variety of non-linear effects available. All of these various non-linear methods have in common properties due to the $I_{laser}^{(n)}$ dependence (n>1) on the excitation intensity. Relevant for microscopy, they share inherent 3D-sectioning properties. At the same time, the different generation mechanisms are responsible for features characteristic of each nonlinear effect.

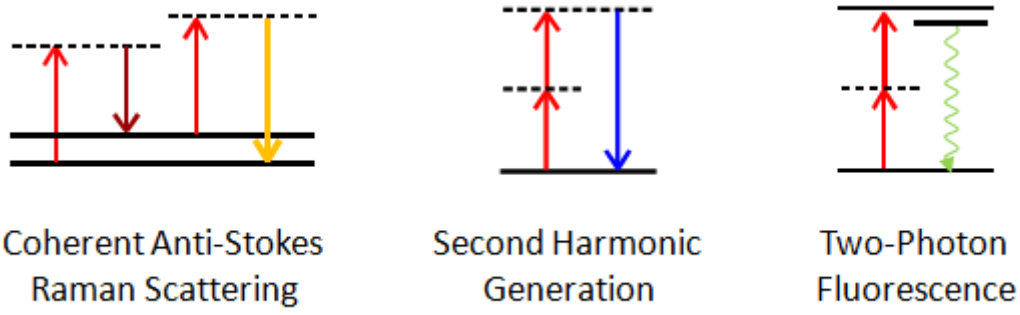

Figure 2.1 Most common nonlinear effects for microscopy. Each photon is represented by an arrow, the length of the arrow represents the energy of the photon. Horizontal lines represent energy levels of the molecule; dotted lines are virtual levels.

The photon combinations necessary for the generation of the most commonly used nonlinear effects in microscopy are summarized in Figure 2.1. The Jablonski diagrams illustrate the molecular properties probed by each effect: Coherent Anti-Stokes Raman Scattering (CARS) is mediated by vibrational levels; Second Harmonic Generation (SHG) involves only virtual levels of the molecule. In Two-Photon Excited Fluorescence (TPEF) the fluorophore is

promoted to an electronic excited state through absorption of two photons. After reaching a radiative level, the molecule returns in the electronic ground state by emitting a photon. The implications for the properties of each effect are detailed in the following.

2.1.1 Second Harmonic Generation

Second Harmonic Generation (SHG) involves the destruction of two photons from the incoming light and the production of a photon with the sum of their energies. This phenomenon is described by the second order susceptibility $\chi^{(2)}$ which gives rise to the second order polarization $P^{(2)}$. We can decompose the tensor into its components and write more explicitly:

$$\boldsymbol{P_i^{(2)}} = \sum_{jk} \chi_{ijk}^{(2)} E_j E_k \ ; \ i,j,k \in \{x,y,z\} \tag{2}$$

An important observation is that SHG contributions vanish in centrosymmetric media. This can be easily proven [1] by taking the symmetric of each term in equation (2):

$$\begin{aligned} \boldsymbol{P_i^{(2)}}(\boldsymbol{r}) &= \sum_{ijk} \chi_{jk}^{(2)} \big[E_j(\boldsymbol{r})\big][E_k(\boldsymbol{r})] \\ \xrightarrow{\textit{symmetry}} \ -\boldsymbol{P_i^{(2)}}(-\boldsymbol{r}) &= -\sum_{ijk} \chi_{jk}^{(2)} \big[-E_j(\boldsymbol{r})\big][-E_k(\boldsymbol{r})] \end{aligned} \tag{3}$$

SHG is therefore restricted to ordered and oriented structures lacking an inversion centrum on the microscopic level. Such a property can be found in certain crystals, like the BBO crystals. In biological tissues, only a few structures emit large SHG signal: microcrystalline starch granules like in potatoes, macromolecules like collagen and myosin filaments in muscle cells. Despite this strong limitation, SHG is a valuable tool for the observation of biopsies and cells, and even for *in vivo* miscroscopy because collagen is ubiquitous in the body and myosin complexes are the main building element of muscles.

SHG finds applications in muscle research, where it provides structural information label-free and reaching deep in the tissue. Further applications are related to the role played by collagen in tumor formation. Structural changes appear and the collagen matrix is also responsible for the transport of therapeutic molecules [2]. Design of SHG dyes that stain membranes extends the field of applications: for example, the sensitivity of styryl dyes to electrical fields allows to image membrane potentials with SHG [3].

Contrary to absorption or fluorescence microscopy, SHG presents the advantage of being an optically “non-invasive” method [4]: there is no need for a real state of the molecule to be in resonance with the two-photon transition and no energy is deposited in the system.

The generation of SHG signals is submitted to a phase matching condition. It is known, that for SHG generated in BBO crystals the phase matching condition imposes an acceptance spectrum. Depending on the thickness of the crystal, some wavelengths will be favored by the phase matching condition in comparison to others, leading to spectra less broad than the incoming laser. In biological systems however, the SHG-generating structures are so small that this condition relaxes. In tendon type I collagen for example, Williams et al. demonstrated that the surface layers of the fibrils are responsible for the observed signal [5] . The phase matching condition does play a role in the directionality of the signal. In the case of

imaging of membranes, the emission is peaked around two solid angles which can be observed in the far field and depend on the numerical aperture of the objective[6].

Being generated by oriented structures, SHG exhibits strong polarization dependence. This can be circumvented by varying the polarization or using a polarized laser beam for the excitation. A more precise consideration of the polarization dependence can also provide additional information about structure or conformation [7].

2.1.2 Two-Photon Excited Fluorescence:

Two-Photon Excited Fluorescence (TPEF) is the most widely used non-linear imaging modality. The combination of a femtosecond laser and a laser scanning microscope was demonstrated as early as in 1990[8]. The success of TPEF is rooted in the developments of one-photon fluorescence: the staining dyes and genetically implemented fluorescent proteins are also excitable through two-photon transitions. On this basis, the 3D sectioning due to non-linearity came as a big improvement, replacing the need for confocal systems.

The photon energies needed to access electronic states for one-photon fluorescence represent wavelengths in the visible or in the UV region. These energetic photons are more prone to cause photodamage and to scattering than the infrared photon used in TPEF. With two-photon excitation a new window of fluorophores becomes accessible with visible and infrared light. The lower scattering in the IR as well as the localized two-photon absorption increase the depth of penetration in tissues, so much so that imaging up to one millimeter deep into tissue has been demonstrated [9].

The transposition of one-photon into two-photon absorption spectra, however, is not straightforward. Differences in shape and intensity of the fluorescence are caused by a variety of phenomena [10]. In addition, two-photon absorption is also dependent on the difference in permanent dipole moments between the ground and the excited state, making it sensitive to the local electric field.

Parallel to the use of exogenous fluorophores, TPEF microscopy has also been demonstrated using native fluorescent molecules [11]. This is particularly interesting for *in vivo* imaging, where the use of external chemicals can be toxic or simply disturb the studied mechanism. The locally high concentrations of autofluorescent molecules in cells partly compensate their lower cross-sections.

Autofluorescence sources are manifold in cells and around them. Nicotinamide adenine dinucleotide (NADH) plays a central role in metabolism in every cell. It is notably involved in redox reactions. Interestingly, the emission spectra of the reduced and oxidized form are quite different, so that NADH fluorescence can be used as an indicator of metabolism [12]. Other significant fluorescent compounds of live cells are flavins, retinol, and tryptophan [11].

All of these fluorophores have rather broad excitation (typically 50 nm FWHM) and broad emission spectra (in the same range). Therefore, it is difficult to identify unambiguously the source of observed autofluorescence. An approach is to use spectrally resolved acquisition coupled with the dependence on the excitation wavelength. This allows cell type identification *in vivo*, for example [13].

Unlike SHG or CARS, TPEF is a spontaneous process. Therefore, the photons emitted by different molecules do not have a fixed phase relation and coherent artifacts (like interferences) do not affect TPEF. Phase matching is also not an issue, resulting in diffuse signals in comparison with the directed emission of SHG and CARS. TPEF is accordingly easily detected in epi-direction, and more sensitive to efficient collection (large NA collection objectives, large area detectors near back aperture). Incoherent summation of signals is also responsible for the linear dependence on the concentration (vs. quadratic in SHG and CARS).

2.1.3 Coherent Anti-Stokes Raman Scattering:

As a non-linear variation of the spontaneous Raman scattering, CARS is sensitive to vibrational and rotational levels of molecules. Therefore it is not generated by only one class of molecules like SHG or TPEF but by all molecules. The combination of universal generation and specific vibrational information makes CARS and related coherent Raman scattering effects the most promising non-linear techniques. As such, they will be treated in more detail in the next section and most of the experimental work presented in this thesis concentrated on CARS.

While SHG and TPEF are 2-photon effects, CARS as a 3-photon effect will have a much lower cross section, as far as the quantities are comparable. Indeed, if comparing the value of $\chi^{(2)} = 0{,}3.\,10^{-12} m/V$ for collagen [14] and $\chi^{(3)} = 2{,}58.\,10^{-22} m^2/V^2$ for Triglycerides [15], we observe that a field of $\chi^{(2)}/\chi^{(3)} \approx 10^{10} V/m$ is necessary to provide similar signal fields. However, concentration plays an additional role because the field produced by the molecules in the excitation volume adds up coherently. CARS can therefore reach high intensities where, like in living cells, the molecules are concentrated in vacuoles or membranes.

2.2 Coherent Anti-Stokes Raman Scattering (CARS)

If studied in detail, the theory behind the generation of the CARS signal involves a considerable number of parameters to correctly describe the interplay of three electromagnetic fields with the many-level system of the molecule. In practice, if the laser frequency used is far from electronic resonances, the theoretical description is simplified down to the few equations presented in this section.

2.2.1 Molecular vibrations and the Raman effect

The energy of vibrational eigenstates of a molecule depends precisely on the nature of the atoms, on the strength of the chemical bonds as well as on the environment, making vibrational spectroscopic techniques very sensitive even to small changes in the molecular structure.

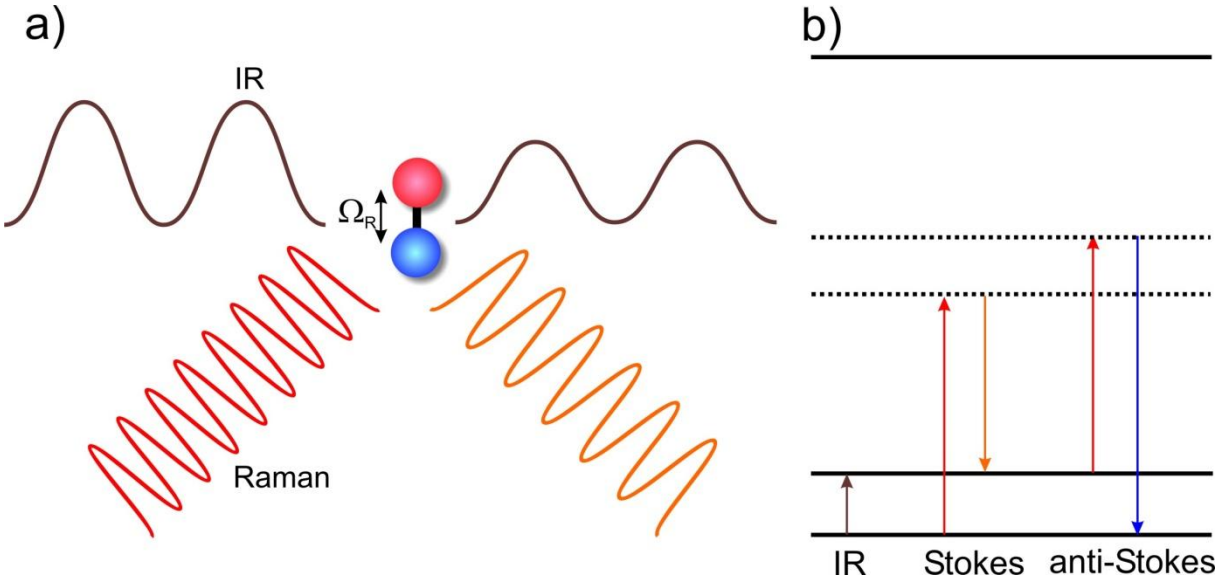

Figure 2.2 IR and Raman spectroscopies. a) Oscillations of a molecule can be excited directly through absorption of IR radiation or indirectly through inelastic scattering responsible for the Raman effect. b) Energy diagram of the molecule. The energy of IR photons matches the transition to a vibrational level. Spontaneous Raman is mediated by a virtual level (dotted line). Stokes radiation, when scattered light appears at a lower frequency than the excitation, is distinguished from the anti-Stokes signal measured at a higher frequency.

Two main mechanisms of light-matter interaction give access to the vibrational and rotational spectrum: Infrared (IR) spectroscopy and Raman scattering. In a classical model, represented in Figure 2.2 (a), a chemical bond can be seen as a spring connecting two masses. Its length is commonly noted by the generalized molecular coordinate Q(t), oscillating at an eigenfrequency ν_R [16]. As intuitively expected, ν_R usually increases with stronger bonds and with lighter atoms. For example, CH stretching modes occur around 3000cm^{-1} while deuterated compounds show peaks around 2200cm^{-1} due to the CD bonds. Many of the relevant bonds in organic materials (C-C, C=C, CO, CN, ring modes…) have energies ranging from 500cm^{-1} to 1500cm^{-1} forming the highly specific "fingerprint region". The energy of typical vibrations hence span 400cm^{-1}-4000cm^{-1}, which corresponds to photons in the IR with wavelengths of 2.5µm to 25µm. Light at these wavelengths resonantly drives the molecular oscillator resulting in strong absorption. In Raman spectroscopy, the frequency of incident electromagnetic waves is far from the resonance condition. A weak coupling to the vibration creates a transient change of the polarizability α and results in the scattering of photons with lower (Stokes case) or higher (anti-Stokes) energy. This inelastic scattering is very weak; its intensity is approximately 3 orders of magnitude weaker than elastically scattered light.

In a quantum mechanical picture, vibrations and rotations are represented by a series of discrete levels. The energy of the photons used in IR-spectroscopy matches the difference of energy between two levels. For Raman scattering, virtual levels have to be introduced. They correspond to a combination of eigenlevels of the molecules and represent the coupling between the incident photon and the transition. IR and Raman spectroscopies provide complementary information about the vibrations of the molecule, because their different mechanisms impose different selection rules. For IR spectroscopy, all relevant wavelengths have to be provided while Raman scattering gives access to the whole spectrum with a single narrowband laser. More importantly for microscopy, the spatial resolution imposed by the

Abbe limit is directly proportional to the wavelength. With an excitation wavelength at 800nm, for example, Raman scattering provides a factor 3 to 30 better spatial resolution than IR imaging, depending on the Raman shift.

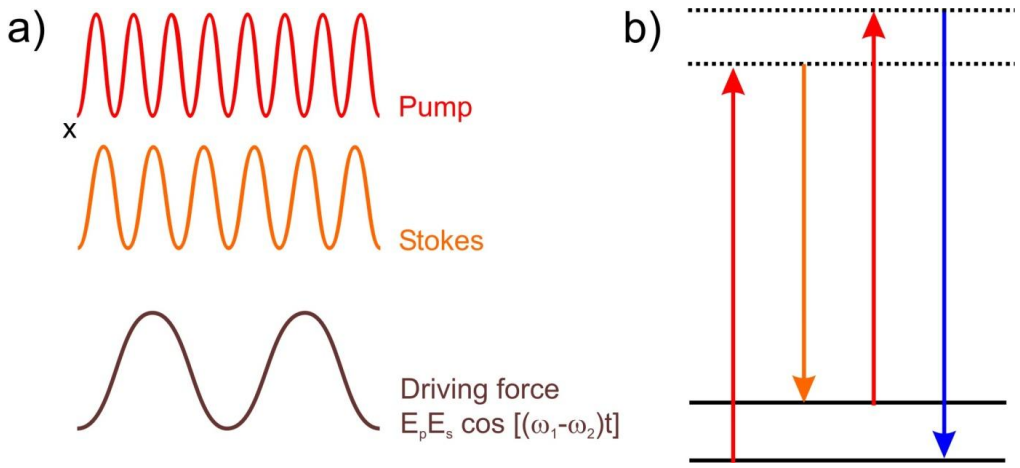

Figure 2.3 Coherent Raman scattering. a) When two lasers with different frequencies are used to excite the molecule, a beating term matching the oscillation frequency appears. The excitation is then much more efficient. b) Energy diagram for CARS. The excitation by a combination of a pump and a Stokes field is probed by a third field resulting in a signal at higher frequencies than the excitation, on the anti-Stokes side.

To take advantage of the great specificity and good resolution of Raman scattering, methods to circumvent the weakness of the signal have been developed. Notably, in recent years, enhancement through plasmons in nanostructures enabled reaching sensitivities down to the single molecule level [17]. However, because of the need for metallic nanostructures, the technique is not label-free anymore. This disadvantage does not affect coherent Raman techniques: enhancement is achieved by exciting the molecule coherently with a combination of photons, instead of relying on the weak coupling inside the molecule. In the classical picture two waves with frequencies ω_1 and ω_2 far from electronic and vibrational resonances are used as depicted in Figure 2.3 (a). They produce a force with a resonant component given by [16]:

$$F_Q = \frac{1}{4}\frac{\partial \alpha}{\partial Q} E_1 E_2^* \cos[(\omega_1 - \omega_2)t], \tag{4}$$

where α is the electric polarizability, E_1 and E_2 the electric fields of pump and Stokes beam respectively and ω_1 and ω_2 their frequencies. The generalized molecular coordinates function Q(t) is then solution of the classical equation for a driven oscillator:

$$\ddot{Q} + \Gamma_Q \dot{Q} + \Omega_Q Q = F_Q \tag{5}$$

where Ω_Q is the resonance frequency of the molecular oscillation and Γ_Q its damping factor. When the difference in frequencies ω_1-ω_2 matches Ω_Q the oscillation is resonantly driven resulting in efficient excitation of this level. This rather simple model captures a lot of the physics of coherent Raman scattering. More accurate calculations based on the evolution of the density matrix in a two-level system deliver similar equations for the evolution of the system. The Raman coordinate is then identified with $Q = \rho_{rg} + \rho_{gr}$, where the subscripts g and r designate the ground state and excited Raman state respectively, and ρ_{rg} and ρ_{gr} are the off-diagonal elements of the density matrix.

Various ways to detect the coherently driven oscillation are available, differing in the detection wavelength and in whether an additional wavelength is used or not. In the following, only CARS will be considered. The corresponding photon scheme is shown in Figure 2.3 (b): the coherent excitation is realized by a pump and a Stokes field and is then probed by a probe field.

2.2.2 Coherent buildup and phase matching

Through the coherent driving of molecular resonances, the signal is increased by several orders of magnitude with respect to spontaneous Raman, following two mechanisms. First, the excitation of a vibrational level is stimulated through the introduction of the Stokes light. In comparison, spontaneous scattering relies on the vacuum fluctuations in the electromagnetic field. Second, the use of two lasers imposes a phase relationship between the photons scattered by different molecules inside the sample, which add coherently.

This coherent buildup is responsible for the phase-matching condition. It states that not only the frequencies should be matched as:

$$\omega_{AS} = \omega_p - \omega_S + \omega_{p'} , \tag{6}$$

with $\omega_{AS,p,S,p'}$ the frequencies of the anti-Stokes signal, pump, Stokes and probe excitation waves, respectively, but their wavevectors should also correspond. This is achieved by minimizing the wavevector mismatch Δk defined as:

$$\Delta k = k_{AS} - k_p + k_S - k_{p'} . \tag{7}$$

Different configurations fulfill this constraint: among others the folded BOXCARS geometry is represented in Figure 2.4 (a) and the collinear arrangement is represented in Figure 2.4 (b). The folded BOXCARS geometry optimizes separation of the signal beam from the incident beams[18]. It is therefore well suited for weak signals and low lying Raman modes, where the angle between the beams in a planar configuration is rather small. The collinear configuration is more robust against misalignment. It maximizes the overlap between the beams, in particular in media where the dispersion is low and the angle between the Stokes and the pump/probe beams is very small [19].

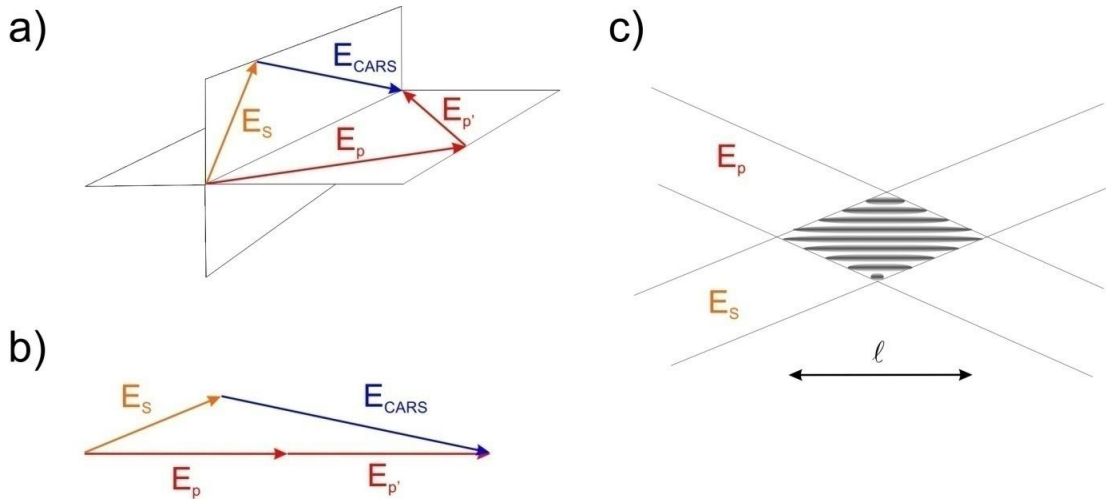

Figure 2.4 Phase matching condition. a) Folded BOXCARS configuration for easy separation of the signal from the excitation. b) Collinear configuration maximizing the interaction length. c) Representation of the transient grating created in the excitation volume by the pump and Stokes lasers. When $k_{p'}$ is properly chosen, the CARS signal builds up coherently thoughout the propagation length ℓ.

In both cases, the phase matching condition can be understood best by considering the polarization created by the combination of the pump and the Stokes beams. The dipoles inside the excitation volume have a precise phase relationship determined by the propagation of the exciting beams. A grating of dipoles with constant phases is then formed as shown in Figure 2.4 (c). The probe pulse is then scattered on this grating. In order for the CARS signal to reach a maximal intensity at the end of the length ℓ of the excitation volume, the CARS signal produced in the first layers and propagating with the probe pulse has to reach the same phase as the CARS signal from later layers. This results in the condition in equation (7). If the phase mismatch becomes too important, CARS signals originating from different position in the sample can even interfere destructively and can lead to a lower signal as the interaction length increases. Finally, the signal depends on Δk through [20-21]:

$$I_{AS} \propto \ell^2 \cdot \mathrm{sinc}^2\left(\frac{\Delta k \ell}{2}\right) \tag{8}$$

where sinc is the cardinal sine function.

2.2.3 The nonlinear susceptibility

The third order susceptibility $\chi^{(3)}$ summarizes the relationship between the excitation fields and the resulting density of dipoles. It accounts for all effects described by the simultaneous interaction with three fields:

$$\mathrm{P}_\mathrm{i}^{(3)} = \sum_{jkl} \chi_{ijkl}^{(3)} E_j E_k E_l \; ; \; i,j,k,l \in \{x,y,z\} \tag{9}$$

The nonlinear polarization density $\mathbf{P}^{(3)}$ then acts as a source term in Maxwell's wave equations. $\mathbf{P}^{(3)}$ is directly linked with the mean dipole density: $\mathrm{P}_\mathrm{i}^{(3)} = N\langle\mu\rangle$.

The 81 parameters of $\chi_{ijkl}^{(3)}$ also have a spectral dependence summarized in the Maker-Terhune notation accounting for every combination of three photons [22]: $\chi_{ijkl}^{(3)}(-\omega_3, \omega_2, \omega_1, \omega_0)$, where $\omega_{0,1,2}$ are the frequencies of the incident fields and ω_3 the frequency of the generated field. The four arguments of the susceptibility must sum to zero and can be freely permutated.

In this work, only the spectral dependence of the CARS signal is of interest. We therefore write $\chi^{(3)}(\Omega)$, with Ω the Raman shift corresponding to the frequency difference between the pump and the Stokes pulses. We therefore neglect the polarization dependence of $\chi^{(3)}$ as well as all nonlinear effects other than CARS which are described by $\chi^{(3)}$.

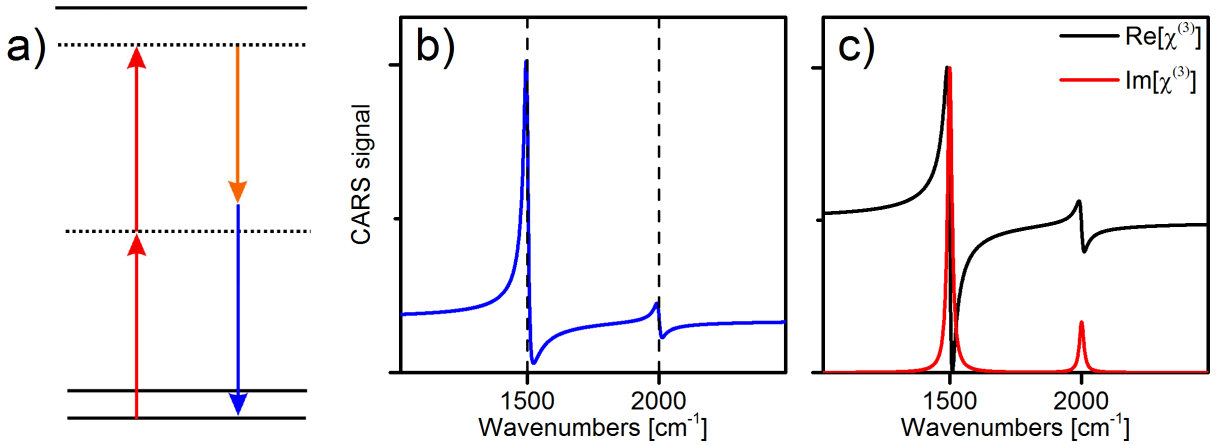

Figure 2.5 Spectral dependence of $\chi^{(3)}$. a) One mechanism for the generation of nonresonant background. This contribution appears as a purely real term in $\chi^{(3)}$. b) The CARS signal is proportional to $|\chi^{(3)}|^2$. The lineshape is distorted by the interference between the resonant and nonresonant terms. The dotted lines indicate the resonance frequency of each Raman level. c) Decomposition of $\chi^{(3)}$ into its real and imaginary part. The imaginary part is only due to the resonant part and is detected in spontaneous Raman spectroscopy. The real part shows a dispersive shape.

In this approximation, the third order nonlinear susceptibility contains two terms: a vibrationally resonant contribution and a nonresonant background. The nonresonant background is only due to four-wave mixing mediated by the electronic cloud. In the energy diagram, it is represented by a combination of photons leading to the creation of a photon with the same energy as in the CARS process, without mediation of the vibrational level. An example of such a combination is given in Figure 2.5 (a). In the Born-Oppenheimer approximation (far from electronic resonances), the nonresonant background is a constant. At the wavelengths considered in the following (NIR), electronic response is considered instantaneous: the phase of the nonresonant background is therefore zero. The vibrational contribution, in turn, has the typical spectral dependence of a driven oscillator. The phase of the response depends on the excitation frequency with respect to the resonance frequency. A quantitative expression of this phenomenon is derived from perturbation theory quantum calculations[20, 23]. For a single resonance:

$$\chi_{R,i}^{(3)} = \frac{A_i}{\Omega_i - (\omega_p - \omega_S) - i\Gamma_i} \qquad (10)$$

where A_i is a constant summarizing the strength of the dipole interactions with the light fields, Ω_i the resonance frequency, ω_p and ω_S denote the frequencies of the pump and Stokes fields and Γ_i is a damping factor. Γ_i is related to the dephasing time of the vibration and indicates the spectral width of the resonance, typically 10-20cm^{-1} in liquids. A molecule combines a nonresonant contribution and several Raman bands resulting in the total expression:

$$\chi_{CARS}^{(3)}(\Omega) = \chi_{NR}^{(3)} + \sum_i \chi_{R,i}^{(3)}(\Omega) \qquad (11)$$

where $\Omega = \omega_p - \omega_S$ in equation (10). In a mixture, the susceptibilities of the components add linearly in proportion of their respective concentrations.

An important property of the CARS signal is its quadratic dependence on the concentration. The generated CARS field E_{CARS} is proportional to the polarization density $P^{(3)}$, and hence proportional to the number of scatterers. The detected signal is the CARS intensity:

$$I_{CARS}(\omega_{CARS}) \propto \left|\mathbf{P}^{(3)}\right|^2 \propto \left|E_{p'}\right|^2 |E_S|^2 \left|E_p\right|^2 \left|\chi^{(3)}_{CARS}(\omega_p - \omega_S)\right|^2 \quad (12)$$

An example of the evolution of the detected CARS signal with the Raman shift is simulated in Figure 2.5 (b). Here two bands were chosen at 1500cm^{-1} and 2000cm^{-1}, with respectively A=300 and 50, Γ=10cm^{-1} for both bands and χ_{NR}=15. Due to interferences between the resonant and non-resonant parts, the peaks appear shifted. The dispersive lineshape is more evident in the case of weaker signals. This case is common in biological applications where the molecules of interest are surrounded by water. The solvent produces a strong nonresonant background on top of which the resonant signal appears in a form close to its real part (see Figure 2.5 c).

A lot of CARS schemes have been developed to get rid of the nonresonant background and the associated distorted lineshapes. Among others, polarization resolved [24-25] and time resolved techniques [21] suppress the background at the cost of signal intensity. As an alternative to mere suppression, the heterodyne technique [26] makes use of the coherent nature of the signal. By providing an additional field (the local oscillator) at the CARS emission frequency and controlling either the phase of this additional field or the phase of the CARS signal itself, E_{CARS} is extracted from the interference pattern between them. This results in a signal enhancement through the usually stronger local oscillator but requires comparing several measurements with varying phases.

2.2.4 CARS and spontaneous Raman signals

To take advantage of the rich Raman literature, an important question is how the spectral dependence of the CARS signal relates to spontaneous Raman spectra. At first glance, the relationship between the spontaneous mechanism and the four-wave mixing observation of vibrational levels does not seem straightforward. Careful theoretical considerations [27] show that only some of the terms included in the general expression of $\chi^{(3)}$ contribute to spontaneous emission. The Kramers-Heisenberg expression for Raman scattering gives[28]:

$$I_{Raman}(\omega) \propto \sum_j \left|\chi_j(\omega)\right|^2 = \sum_j \frac{A_j \Gamma_j}{(\Omega_j - \omega)^2 + \Gamma_j^2} \quad (13)$$

where the subscript j runs through the Raman resonances of the molecule. Equation (13) is mathematically equivalent, after multiplication by a constant, to the imaginary part of the expression of $\chi^{(3)}$ from equations (10) and (11). To obtain Raman equivalent spectra it is therefore sufficient to extract the imaginary part of the susceptibility. As seen in Figure 2.5 (c), the imaginary part is free from electronic contribution and presents no dispersive lineshape.

2.2.5 CARS microscopy with picosecond pulses

The application of CARS to microscopic imaging [29] has experienced a tremendous development since 1999 [30], where a collinear arrangement was first demonstrated. Systems based on picosecond lasers can be considered as state of the art and are available commercially. Most advantages of this implementation translate to the broadband approach.

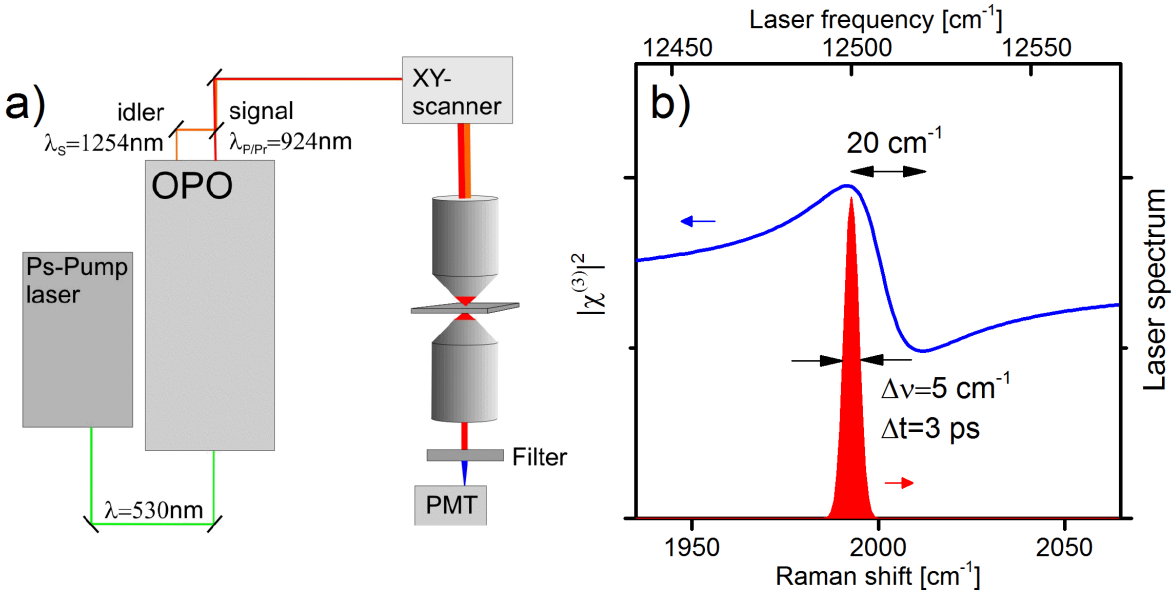

Figure 2.6 CARS microscopy with picosecond pulses. a) Typical ps-CARS microscopy setup. The pump/probe and Stokes pulses are obtained by nonlinear generation in an optical parametric oscillator. Values for Stokes and pump/probe wavelength given as an example excite the polystyrene band at 2850cm^{-1}. Rapid XY-scanning is realized by a galvanometer. The filter signal is integrated on a single-channel detector. b) Comparison of the bandwidth of the laser and of a typical Raman band.

A typical picosecond-CARS (ps-CARS) setup is sketched in Figure 2.6 (a). To produce the two laser beams necessary to coherently drive a vibration in the sample, nonlinear frequency conversion is used. This is realized in an Optical Parametric Oscillator (OPO), which converts a higher-energy pump light (typically around 530nm) into two less energetic beams called "signal" and "idler". The difference in frequency depends on a phase matching condition and is continuously tunable by turning or by heating the nonlinear crystal inside the OPO [31]. The acquisition of CARS spectra is therefore possible yet slow. The system is optimized for imaging at a single Raman shift.

Due to the nonlinear nature of CARS signal generation, a shorter pulse will provide greater CARS signal at constant mean power. However, taking into account the typical bandwidth of Raman transitions and the presence of a broadband nonresonant background, pulse durations of the order of 1ps have been claimed to be ideal for CARS microscopy [20, 32]. In Figure 2.6 (b), the spectral width of a picosecond pulse (typically 3-5cm^{-1}) is compared with the typical width of a resonance (10-20cm^{-1}). The picosecond pulse minimizes the amount of nonresonant background excited simultaneously with the desired signal. The red shift of the peak can be taken into account by tuning the frequency difference slightly lower than the expected position of the resonance.

Ps-CARS is particularly successful for rapid imaging of biological tissues with sub-cellular resolution. The frequency difference is usually chosen to select a band specific of an important structural or functional class of molecules inside the cell. The most common example is lipid imaging based on the strong resonances around 3000cm^{-1} attributed to different vibrations of the CH bonds [33]. Other examples are the phosphate stretch vibration specific of nucleic acids, the amide I vibration at 1666cm^{-1} [34] or the OH stretching mode of water. The phase matching condition is relaxed by the large number of k-vectors at the focal point and is less critical because of the small interaction length (compared to the coherence

length). In addition to the chemical specificity of the signal, CARS is not overlapped by one-photon fluorescence which afflicts spontaneous Raman microscopy of biological samples. The strong CARS signal coupled with rapid scanning using galvanometer-based mirrors and sensitive photon-counting detection allowed the demonstration of video-rate *in vivo* imaging [35].

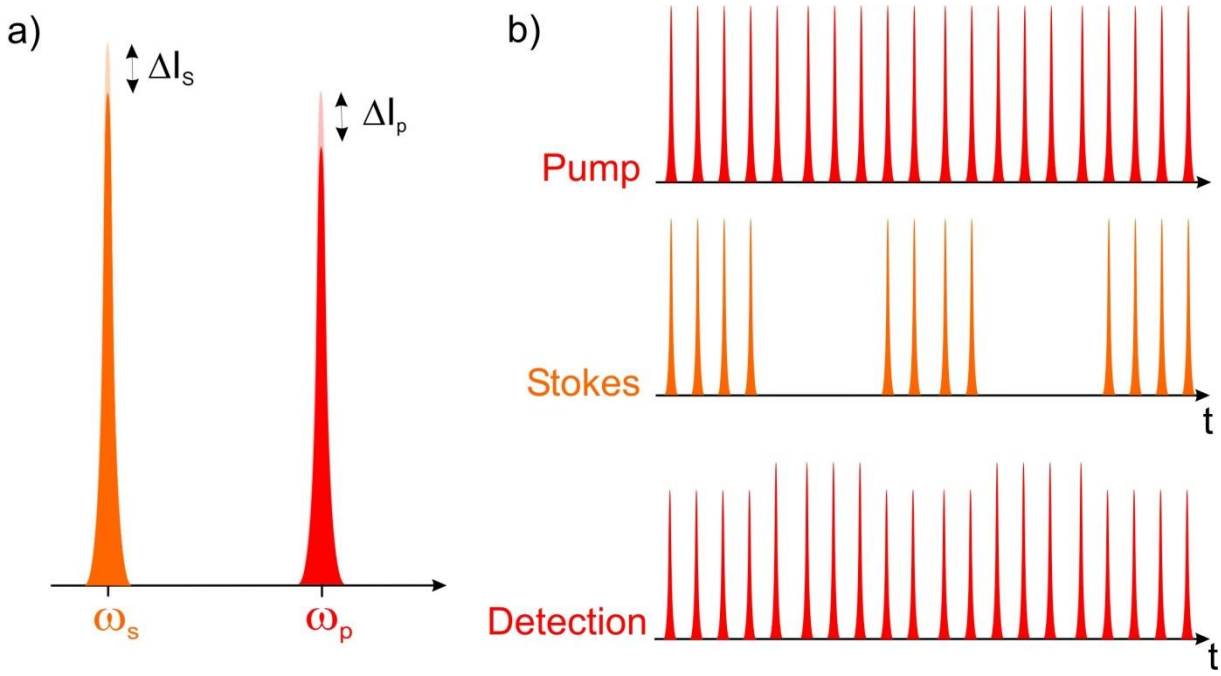

Figure 2.7 Principle of Stimulated Raman Scattering. a) Change in intensity of the Stokes and of the pump pulses when ω_p-ω_S matches the energy of a Raman level in the sample. b) Detection method for SRS. One of the pulses is modulated with high frequency (here the Stokes pulse). The resulting variation in intensity of the other pulse (here the pump) is detected. Lock-in detection greatly increases the sensitivity.

The main limitations of the ps-CARS approach are linked with the presence of the nonresonant background and with the nonlinear concentration dependence. To circumvent these obstacles for quantitative chemical imaging, a new coherent Raman microscopy modality has been the subject of increased interest in the last few years: Stimulated Raman Scattering (SRS) [36-38]. In SRS the presence of a resonance is detected by measuring directly the intensity variations of the pump and Stokes pulses. When ω_p-ω_S matches a vibration of the molecule, energy is transferred to the molecule while a pump photon is annihilated (Stimulated Raman Loss, SRL) and a Stokes photon created (Stimulated Raman Gain, SRG). This is represented in Figure 2.7 (a), where SRG is indicated by the variation ΔI_S and SRL by ΔI_p. This process does not occur without the resonance so that the method is free from the CARS nonresonant background. However, the very small variation ΔI_p or ΔI_S has to be detected on top of the excitation pulse. Adequate sensitivity requires modulation and lock-in detection at very high frequencies (MHz). The principle of this implementation is explained in Figure 2.7 (b): the rapid modulation of the Stokes beam results in a variation at the pump wavelength with the same frequency, allowing for suppression of slower experimental sources of noise. Such a high frequency implementation is not yet available with spectrally resolved detection [36] and SRS, as well as ps-CARS are still limited to the observation of a single Raman mode.

2.2.6 Broadband CARS

The simultaneous observation of several Raman levels with CARS requires providing all needed frequency differences at once and relies on the use of broadband, ultrashort lasers. Before describing the generation and managing of such pulses in the microscope focus, the necessary formalism [39] to accurately describe broadband CARS generation is exposed in this section.

In a broadband CARS experiment, a particular vibration can be driven by a lot of different photon pairs. For each Raman shift Ω, a probability of excitation A(Ω) can be calculated taking into account all matching photon combinations:

$$A(\Omega) = \int E^*_{Stokes}(\omega' - \Omega) E_{pump}(\omega') d\omega'. \qquad (14)$$

Note that A(Ω) is a complex quantity that describes both the amplitude and phase relationship between the different excited modes. The molecular response $\chi^{(3)}(\Omega)$ is then modulated by A(Ω) to describe the excited system. If the probe pulse is also broadband, interferences between photons appearing at the same wavelength but originating from different pathways occur. This is expressed through the generalized equation for broadband CARS:

$$E_{CARS}(\omega) \propto \int E_{probe}(\omega - \Omega) \chi^{(3)}(\Omega) \int E^*_{Stokes}(\omega' - \Omega) E_{pump}(\omega') d\omega' \; d\Omega \qquad (15)$$

This equation will be used extensively in the next chapters.

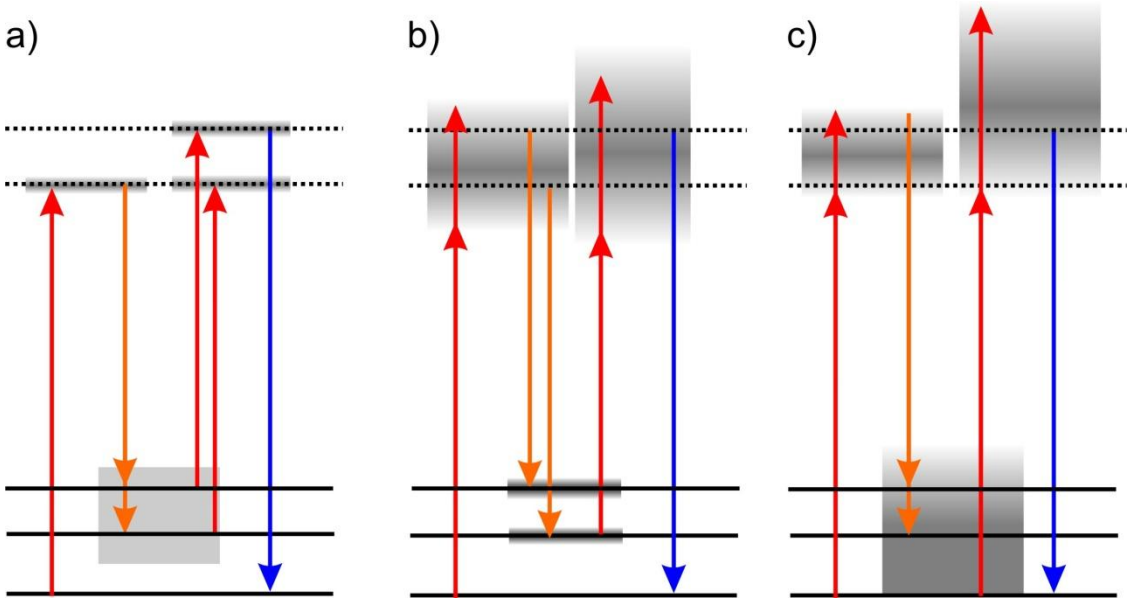

Figure 2.8 Broadband CARS schemes. a) Multiplex CARS, only the Stokes beam is broadband. A narrowband pulse acts as pump and probe simultaneously. b) Pump and probe are broad, Stokes is narrowband. c) Single-Beam CARS: all three fields are spectrally broad. Pump, Stokes and probe are a single pulse.

Main challenges faced by broadband CARS setups are:

- the extraction of spectral information in presence of a strong nonresonant background
- nonlinear photodamage due to multiphoton mechanisms.

These mechanisms include plasma formation, optical breakdown, two- and three-photon absorption and Raman induced vibrational absorption [40-42]. Any combination of broadband and narrowband pulses can be studied: the main schemes demonstrated to date are

summarized in Figure 2.8 [43-45]. In this work, the Multiplex and the Single-Beam schemes will be examined in more detail (see chapter 3 and 4).

2.2.7 Time-resolved CARS

One way to get rid of the nonresonant background is to delay the probe pulse with respect to the excitation. First applications of femtosecond pulses to coherent Raman spectroscopy were time-resolved measurements[46], because they provide enough temporal resolution to follow precisely the molecular dynamic. They provided a direct way to probe decoherence times T_2 of Raman modes, which are of the order of a picosecond. When two modes are excited simultaneously a beating feature is observed, lasting in some cases much longer than the individual decoherence times. In a collinear geometry, where the vibrationally resonant CARS signal interferes with a nonresonant background, the beating is also present for a single Raman mode. The general expression of the third order polarization $P^{(3)}(t)$ obtained by time-dependent perturbation theory is given by[45, 47]:

$$\begin{aligned} P^{(3)}(\mathrm{t}) = -\frac{i}{\hbar^3}\sum_{nfm}\mu_{fm}\mu_{mg}\mu_{gn}\mu_{nf}\exp\left(-\left(i\omega_{gm}+\Gamma_{\mathrm{gm}}\right)t\right) \\ \cdot\int_{-\infty}^{t}dt_1\int_{-\infty}^{t_1}dt_2\int_{-\infty}^{t_2}dt_3\,E(t_3)E^*(t_2)E(t_1) \\ \cdot\exp\left(\left(i\omega_{fm}+\Gamma_{\mathrm{fm}}\right)t_1\right)\exp\left(\left(i\omega_{nf}+\Gamma_{\mathrm{nf}}\right)t_2\right)\exp\left(\left(i\omega_{gn}+\Gamma_{\mathrm{gn}}\right)t_3\right) \end{aligned} \tag{16}$$

Where $|g\rangle$, $|n\rangle$, $|f\rangle$ and $|m\rangle$ are the ground, first virtual, vibrational, second virtual levels involved in the CARS process respectively, μ_{ij} the corresponding transition dipole moments, ω_{ij} the related frequencies and $\Gamma_{ij}$the linewidths. This expression in the time domain is equivalent to equation (15) in the spectral domain. The detected signal is directly linked to the polarization by [27, 48-49]:

$$S_{CARS}(\tau)\propto\int_{-\infty}^{+\infty}dt\left|P^{(3)}(t,\tau)\right|^2 \tag{17}$$

Here, τ expresses the time delay between the excitation by the pump and Stokes pulses and the probe pulse and summarizes the dependence on t_1,t_2 and t_3. Then, in an equation where the excitation of the Raman coherences is expressed in the spectral domain and the probing by the delayed pulse in the time-domain [27, 50]:

$$S_{CARS}(\tau)\propto\int_{-\infty}^{+\infty}dt|E(t)|^2\left|\int_{-\infty}^{+\infty}d\Omega\exp\left(-\mathrm{i}\Omega(\mathrm{t}+\tau)\right)\mathrm{A}(\Omega)\cdot\chi^{(3)}_{\mathrm{CARS}}(\Omega)\right|^2 \tag{18}$$

The integral in the spectral domain contains the whole dynamics of the excited system, $A(\Omega)$ accounting for the impulsive excitation since:

$$A(\Omega)=\int_{-\infty}^{+\infty}dt\,\exp(i\Omega t)|E(t)|^2 \tag{19}$$

If we now assume infinitely short pulses, the integrals simplify to:

$$S_{CARS}(\tau)\propto\left|\int_{-\infty}^{+\infty}d\Omega\exp(-\mathrm{i}\Omega\tau)\cdot\chi^{(3)}_{\mathrm{CARS}}(\Omega)\right|^2 \tag{20}$$

And it becomes clear that the signal measured in time-resolved CARS experiments contains the whole information about the third-order nonlinear susceptibility and the Raman resonances are retrievable by means of simple Fourier transformation.

Time-resolved CARS schemes have therefore been reported as Fourier-Transform CARS (FT-CARS) [51]. Generally a single laser is used; however the beam is divided in an interferometer in a similar fashion to autocorrelation based on SHG. This scheme was applied to microscopy of polymer beads [51-52] and to spectroscopy with ultra-broadband pulses (down to 5fs)[49].

2.3 Ultrashort laser pulses

Nonlinear microscopy is but one of the many applications of ultrafast lasers[53]. Laser pulses with durations of picoseconds down to femtoseconds have enabled the observation of atom motion on molecular scales. The unprecedented time resolution enabled by ultrashort laser pulses continues to be reduced with the advent of attosecond physics and the unraveling of electron dynamics [54]. Applications to biology require reliable and easy-to-operate lasers and nonlinear microscopy benefits of the continuous development of ultrafast lasers. Commercially available sub-10-fs oscillators on the one hand and efficient broadening in highly nonlinear materials on the other hand are therefore the enabling technologies at the core of this work. While the high peak intensities of picosecond lasers are the only relevant criterion in ps-CARS, broadband CARS makes use of the coherent interplay between several of the laser frequencies.

2.3.1 Pulse duration and spectral width

The pulsed sources used in nonlinear microscopy produce ultrashort bursts of light separated by comparatively large dark periods of time. The pulse length will typically span between 10fs and a few picoseconds while two consecutive pulses are separated by an interval of the order of 10ns. Hence, a pulse can be mathematically described through a single transient electrical field E(t), arbitrarily centered at t=0.

E(t) is decomposed into its spectral components through Fourier transformation (noted $\mathcal{F}$):

$$E(\omega) = \mathcal{F}(E(t)) = \frac{1}{2\pi}\int_{-\infty}^{+\infty} E(t)e^{-i\omega t}\,dt \qquad (21)$$

Although E(t) is a real quantity, E(ω) is complex and we note its phase $\phi(\omega)$. To avoid taking into account the Fourier components with negative frequencies, a complex valued time dependent field is introduced, defined as:

$$\tilde{E}(\mathrm{t}) = \frac{1}{2\pi}\int_{0}^{+\infty} E(\omega)e^{-i\omega t}\,d\omega \qquad (22)$$

The real field is E(t) simply the real part of $\tilde{E}(\mathrm{t})$.

The spectal and the temporal width of the pulse are linked through a Fourier transform and hence cannot be arbitrarily narrow at the same time. If we assume a pulse with a Gaussian temporal shape, the spectrum is also a Gaussian. The spectral full-width at half maximum (FWHM), Δω, and the FWHM of E(t), Δt, verify the inequality:

$$\Delta\omega\Delta\mathrm{t} \geq 2\pi\mathrm{K}\,, \qquad (23)$$

with K=0.441. Similar relationships are valid for other temporal profiles with other values for K (Hyperbolic secant: K=0.315, Lorentz: K=0.142). Usually, the spectrum is much easier to measure than the temporal profile for ultrashort pulses. When the limit imposed by equation (23) is reached, one speaks of a Fourier-transform limited (FTL) pulse. As an illustration of

the bandwidth difference among ultrafast lasers, Figure 2.9 (a) compares the normalized spectra of the two Titanium-Sapphire (Ti:Sa) lasers used in the following chapters: the MIRA900 laser producing pulses of about 160fs and a sub-10fs laser, the FusionPRO. The electric field of the FTL pulse corresponding to the measured spectrum of the Fusion is shown in Figure 2.9 (b) (note that the wavenumber unit in Figure 2.9 (a) is linked to the frequency ω of the preceding equations through $\tilde{\nu} = \frac{\omega}{2\pi \cdot c}$).

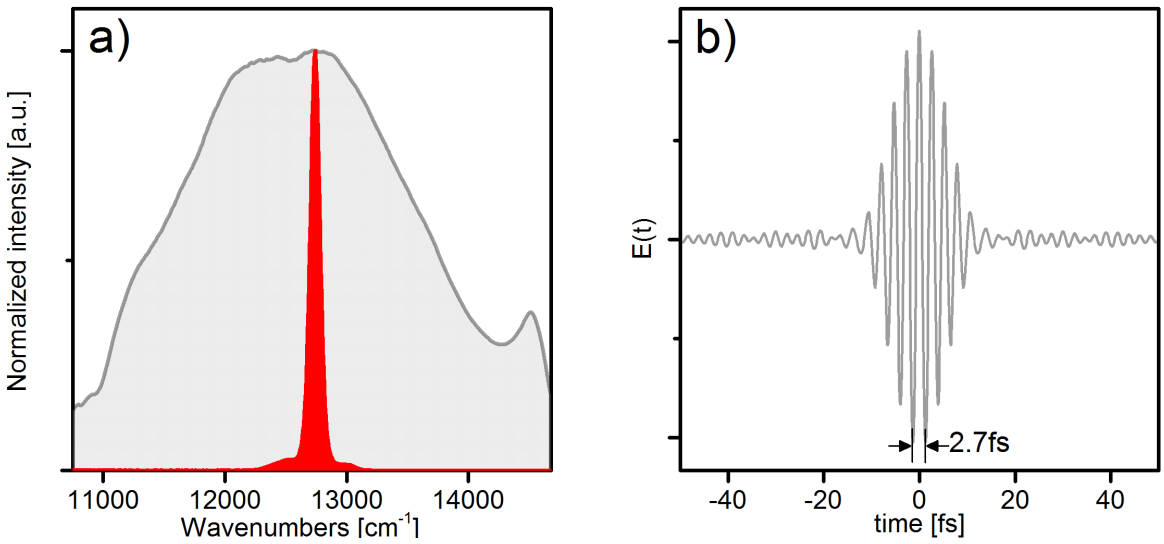

Figure 2.9 Time-frequency relationship. a) Spectra of the lasers used in the experimental demonstrations. Red: laser Mira900 with pulse duration ~160fs. Grey: Fusion PRO, <10fs pulses. b) Temporal evolution of the electrical field for the Fusion PRO, calculated using the spectrum shown in (a) and equation (14)

Since the bandwidth of the pulse (Δω~400THz for the short pulse) is usually much smaller than the central frequency (ω_0~2.35PHz), the temporal evolution can be decomposed in a slow varying envelope modulated by the central frequency. We note the envelope $\mathcal{E}(t)$ and obtain the expression:

$$\tilde{E}(\mathrm{t}) = \mathcal{E}(t)e^{-i(\omega_0 t+\phi)} \qquad (24)$$

In the near infrared, sub-10fs pulses come close to the few-cycle limit, the period of a light wave with λ=800nm being about 2.7fs.

2.3.2 Generation of ultrashort pulses

The challenge of ultrashort pulses generation consists in providing a large and coherent spectrum (spanning up to several 1000cm^{-1}), which means that the phase relation between the spectral components has to be well defined and constant from pulse to pulse. In lasers, the first requirement for a broadband spectrum can only be met if the gain medium possesses a large number of modes with a greater amplification by stimulated emission than losses. This, however, does not guarantee pulsed operation. Firstly, the laser cavity selects discreet frequencies in the same way a Fabry-Perot interferometer does, separated by $\Delta\nu = \frac{c}{2nL}$ with c the speed of light in vacuum, n the refractive index inside the cavity and L its length. The lasers used in this work have L~2m and the modes lie very close to each other. Secondly, in a gain medium with homogeneous gain saturation, only one or a few of the strongest modes make use of most of the gain in a "winner takes it all" mechanism contributing to monochromatic operation. Thirdly, the modes originate from the amplification of randomly

generated fluorescence photons and may not have a well defined phase relationship to one another.

Mode-locking is a set of methods to counterbalance these effects and favor the pulsed operation regime. Active mode-locking methods introduce a controlled modulation of the losses inside the cavity and are limited to pulse lengths achievable with electronic switching times. Passive mode-locking is therefore preferred for the generation of ultrashort pulses. An element with increased transmission for higher peak intensities is inserted in the cavity. The most common mechanism for passive mode-locking relies on the Kerr effect. It makes use both of the temporal and spatial profile in the laser. At higher intensities, the refractive index varies linearly with the intensity. Illumination with a Gaussian spatial profile then produces a retardation profile corresponding to a lens (Kerr lens effect). The strength of this self-focusing depends on the intensity and the cavity can be designed to minimize losses for the focal length obtained for a short pulse.

Lasers with Titanium-Sapphire as a gain medium are best suited to cover the NIR spectral region favorable for imaging in biological conditions: far from electronic resonances on the blue side and from water absorption on the red side [55-56]. Its fluorescence spectrum spans from slightly above 600nm to almost 1µm. An important limitation to pulse duration is the dispersion inside the cavity. The shorter the pulses at the output of the crystal, the stronger it is affected by the difference in cavity length experienced by its components. Systems with intra-cavity dispersion compensation using pairs of prisms have been limited to pulse durations slightly above 10fs due to third order dispersion (TOD) [57]. Lasers with more precise dispersion compensation are obtained by using chirped mirrors. The broad spectral bandwidth of Ti:Sapphire can then be fully exploited and pulses in the two-cycle regime have been generated directly from an oscillator [58]. Ti:Sa oscillators integrating this technology have become available commercially recently. They require more careful operation than lasers producing pulses in the 100fs to 1ps range.

2.3.3 Spectral broadening

The challenging production of sub-10fs pulses directly from an oscillator can be avoided by nonlinear spectral broadening of longer pulses [59]. The most common mechanism for broadening is Self Phase Modulation (SPM). SPM occurs due to the Kerr effect: the change of refractive index with the intensity creates, for an already short pulse, a rapidly varying temporal phase:

$$\phi(\mathrm{t}) = \frac{\omega}{c} n_2 I(t) L \qquad (25)$$

Where ω is the central frequency of the laser, c the speed of light in vacuum, n_2 the nonlinear index of the medium used for broadening, I the temporal pulse intensity and L the interaction length. This varying phase causes the appearance of new frequencies. A more efficient broadening is obtained when the interaction length is increased for example through guided wave propagation in a hollow fiber.

In this respect, the development of photonic crystal fibers (PCF) is an example of particularly efficient spectral broadening and enabled the generation of very broad pulses with much lower input powers than usually necessary. PCFs represent a paradigm shift in the way light is

guided inside an optical fiber: instead of total internal reflection based on the difference in refractive index between the core and the cladding of the fiber, the confinement of light in a PCF is realized by a photonic crystal surrounding the core. It is created by a periodic arrangement of microscopic structures (size of the order of the wavelength) [60]. The periodic alternation of regions with higher and lower refractive indices creates photonic band gaps extending guided modes to new wavevector- and frequency-regions. Advantages of PCFs include e.g. low losses and high birefringence for well chosen symmetric structures. In addition, PCFs have ultrahigh nonlinearity and tunable dispersion properties. The tight confinement of laser energy in the small core creates various nonlinear effects leading to the transformation of a moderately energetic, narrow fs-pulse (few 100fs) into a very broad supercontinuum. Supercontinuum generation is a complex mechanism because the dominant nonlinear effects depend on various parameters like the duration of the pump pulse, its intensity, the presence of chirp, the length of the PCF and the characteristics of the photonic crystal. Therefore the experimental demonstration of supercontinua spanning over one or two octaves [61] were achieved a few years ahead of the simulation tools allowing insight in the interplay of the various parameters [62]. The main nonlinear broadening mechanisms to take into account in the PCF are SPM, four-wave mixing (FWM), modulation instability, soliton fission, dispersive wave generation and Raman scattering. Some of these effects are deleterious for the coherence of the output of the PCF. This comes in addition to dispersion inside the fiber and pulses obtained by spectral broadening are usually not as well characterized as the output of ultrashort oscillators.

2.3.4 Spectral phase and temporal profile

The duration of a broadband pulse is very sensitive to the phase relationship between its spectral components. In practice, every material transmitting the pulse has a wavelength-dependent refractive index and adds dispersion between the wavelengths of the pulse. If we consider the wavenumber $k=2\pi n/\lambda$, we can decompose its dependence on the angular frequency ω into a Taylor series:

$$k(\omega) = k_0 + \frac{\partial k}{\partial \omega}(\omega - \omega_0) + \frac{1}{2}\frac{\partial^2 k}{\partial \omega^2}(\omega - \omega_0)^2 + \frac{1}{6}\frac{\partial^3 k}{\partial \omega^3}(\omega - \omega_0)^3 + \cdots$$

The total phase accumulated by a spectral component of the pulse is given by $\varphi(\omega) = l.k(\omega)$ where l is the propagation length through the material and we put aside any nonlinear effect on the phase for now. The FTL pulse corresponds to the case when all spectral components have the same phase φ_0. When this is not the case, the pulse duration increases and the temporal profile of the pulse can assume a variety of shapes.

The first term k_0 represents the phase velocity of the central frequency and is just a phase offset that does not affect the form of the pulse. The first derivative of k determines the group velocity in the material:

$$\frac{\partial k}{\partial \omega} = \frac{1}{v_g}$$

v_g determines the speed of propagation of the envelope of the pulse and can substantially differ from the phase velocity. It adds up to a group delay $T_g = \frac{\partial \varphi}{\partial \omega}$ at the end of the material:

the pulse is shifted in time in comparison to the value predicted on the basis of the phase velocity. T_g has to be taken into account in interferometric applications but plays no role for nonlinear signal generation, because the shape of the pulse is not affected.

Conversely, the term $\frac{\partial^2 k}{\partial \omega^2}$, called group velocity dispersion (GVD), is responsible for an increase of the pulse length. It quantifies the rate of variation of the group delay across the frequencies: if the pulse was cut in a blue and a red part, the corresponding sub-pulses are separated by an offset in time. Usually the group delay is smaller for longer wavelengths than for shorter ones (normal dispersion). The result for the pulse is a stretched envelope at the exit with a change in time of the instantaneous frequency $\omega_I(t)$. At a time t, the introduction of a varying phase function in equation (24) can modify the apparent frequency of the light wave under the envelope $\mathcal{E}(t)$:

$$\tilde{E}(\mathrm{t}) = \mathcal{E}(t)e^{-i(\omega_0 t+\phi(t))} = \mathcal{E}(t)e^{-i(\omega_I(t)\cdot t+\phi_0)}$$
$$\omega_I(t) = \omega_0 + \frac{d\phi(t)}{dt} \qquad (26)$$

This time dependence of the instantaneous frequency is called chirp. When the instantaneous frequency rises with time the term “up-chirp” or “positive chirp” is used. GVD is sometimes used indifferently with the term “group delay dispersion” (GDD), although the GVD is the GDD accumulated per unit length and the pulse form is directly related to the final GDD.

With broad spectra or with long propagation lengths through highly dispersive optics higher-order dispersion occurs and in first place Third Order Dispersion (TOD). The term $\frac{\partial^3 k}{\partial \omega^3}$ in the development of k expresses this variation of the GVD. It is sometimes also referred to as “second order chirp”.

An initially shorter pulse will be more affected by the same amount of GVD than a pulse with less spectral bandwidth. If we assume a given GDD, this can be easily understood: the delay difference between the red and the blue wing of the spectrum is bigger when they are further apart. In practice, significant temporal broadening of the pulse is observed when the GDD is bigger than the square of the FTL pulse duration. For example, microscope objectives are responsible of GDD in the order of few $1000fs^2$ [63-64]: picosecond pulses remain mainly unaffected while 10fs pulses are stretched by 10 to 100 times. In Figure 2.10, the effect of GDD=$200fs^2$ is compared for a pulse with an FTL duration of 100fs and a 10fs pulse. The 100fs pulse will remain almost unchanged after applying the phase function (Figure 2.10 a,b) while the 10fs pulse will be significantly stretched to about 10 times the FTL value (Figure

2.10 c,d). This stresses the importance of phase management for broadband pulses.

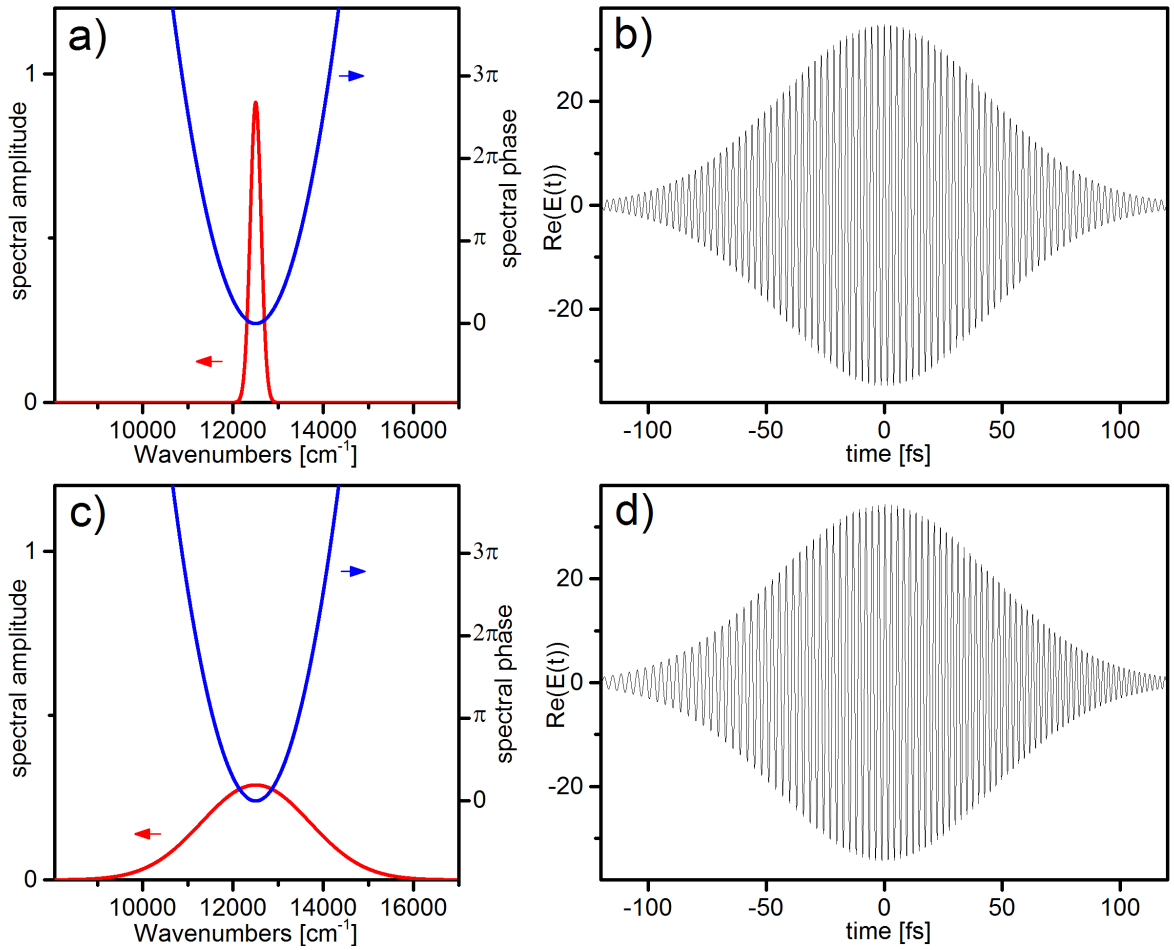

Figure 2.10 Effect of a quadratic phase function. A 200fs^2 phase function is applied in the spectral domain to a 100fs (upper part) and a 10fs pulse (lower part). a) $|E(\omega)|$ (red) and $\phi(\omega)$ for the 100fs pulse. b) The time profile of the pulse remains almost unchanged. c) $|E(\omega)|$ (red) and $\phi(\omega)$ for the 10fs pulse. d) This time the pulse envelope is stretched to a duration comparable to the spectrally narrow pulse in b). The instantaneous frequency varies linearly with time.

2.4 Pulse shaping

The precise control of the temporal form of an ultrashort pulse, or equivalently the precise control of its spectral phase, is attractive in many regards and has been applied to a variety of fields [65]. In the field of coherent control, for example, a precisely timed succession of laser impulses of different frequencies can lead a molecule to favor a relaxation pathway over another one and determine the outcome of a reaction [66-68]. Since energy flow processes on the molecular scale can happen as rapidly as in a few tens of femtoseconds, pulse durations and timing must be in the same range. In a frequency domain picture, the coherent addition necessary for multiphoton excitation strongly depends on the phase among the spectral components of the pulse [69]. This way an electronic level can be addressed selectively even with broadband pulses [70-72]. The same principles apply to nonlinear microscopy and in particular to CARS, although no electronic resonances are involved. In this section, most common pulse shaping strategies are shortly presented to lead to the introduction of the pulse shaper used throughout this work.

2.4.1 Strategies for pulse shaping

The complexity of a pulse shaping setup depends on the level of control needed in the experiment. The issues related to dispersion and temporal broadening can be corrected using passive optics with only a few parameters. Some engineered materials have anomalous dispersion compensating the chirp introduced by other elements. These include some optical fibers and chirped mirrors. The amount of dispersion compensation can be regulated by choosing the appropriate fiber length or by adjusting the number of bounces on the chirped mirror. Continuously adjustable chirp compensation is provided by pairs of dispersive elements. Such a system is depicted in Figure 2.11 (a): the longer wavelengths travel a longer optical path than the shorter ones, contrary to what is the case in most materials. By adjusting the position of the second prism, the amount of glass and therefore of normal dispersion acquired by the pulse changes, adjusting the chirp compensation.

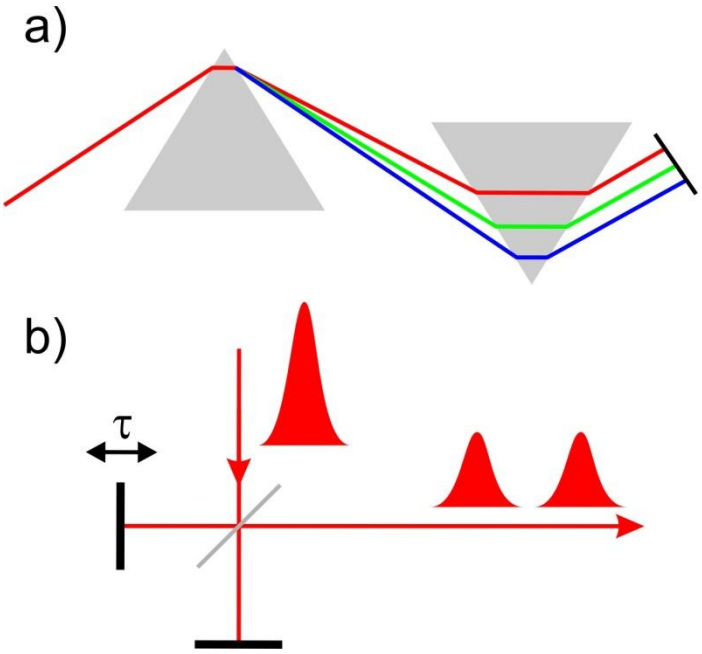

Figure 2.11 Examples of pulse shaping methods based on passive elements. a) Prism compressor. The red frequencies experience a longer pathway through the prism-pair than the blue ones, compensating normal dispersion. b) Michelson interferometer for the production of a pair of identical pulses with variable delay. Alternatively, the beam-spliter can be replaced by a dichroic mirror for two-color excitation.

Higher order dispersion is more difficult to compensate than GVD. The highly dispersive material of prisms used for GVD correction introduces also TOD, which cannot be easily uncoupled from the chosen GVD. The combination of a prism pair with chirped mirrors can be used to tackle this problem; however the compensation of higher-order dispersion usually requires adapting the compensation optics specifically to the particular setup.[73]

Simple shaping of the temporal profile is also possible based only on passive elements, by dividing the pulse into different pathways with variable lengths. The simplest example is illustrated in Figure 2.11 (b) with a Michelson interferometer. Such a simple scheme can suffice to retrieve a CARS spectrum [51, 74]. Alternatively, the beam-splitter can be replaced by a dichroic mirror. In spectral focusing, additional dispersion is then applied in one of the arms for precise excitation of a Raman level (see chapter 4, in particular 4.3.4). Arbitrary

shaping of the pulse envelope directly in the time domain, however, is impossible at the time scales of ultrashort pulses. Therefore, control strategies based on a precise tailoring of the pulse have almost always to be realized in the frequency domain.

Notable exceptions are the Acousto-Optical Dispersive Filters (AOPDFs), also known as Dazzler [75]. In this implementation, unique properties of acousto-optical dispersive filters are used: light is transferred from propagation along the ordinary axis (fast) to the extraordinary axis (slow) if a phase matching condition is met. The phase matching depends on the wavelength of the light and on the frequency of the acoustic wave sent through the device. The choice of an appropriate acoustic waveform determines the distance traveled by each frequency component on the fast and the slow axis, which translates into the control of the temporal shape.

2.4.2 Shaping in the frequency domain: the 4f-line

Shaping in the frequency domain relies on modulation of the pulse in the Fourier plane of a 4f-line [76]. This setup is represented schematically in Figure 2.12 and operates the transfer of the pulse from the time domain into the spectral domain and back. It consists of the combination of dispersive and focusing elements separated exactly by the focal length of the focusing parts. The dispersive element (in our experiments, gratings were used) transforms the spectral distribution into an angular distribution. The lens (or focusing mirror) then performs a transformation from the k-space into a position in the Fourier plane.

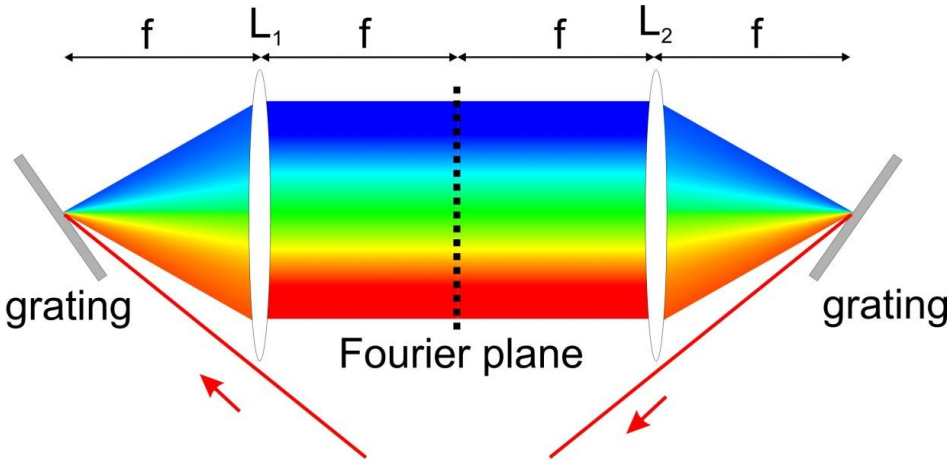

Figure 2.12 Schematic representation of a 4f-line. The pulse is dispersed into its components using a grating or a prism. A focusing element (here lens L_1) situated at a focal length of the grating, ensures the propagation of the spatially distributed components into the Fourier plane. At this position, phase and amplitude modulations can be realized directly in the spectral domain. The symmetric arrangement returns the pulse in the time domain. In the absence of modulation in the Fourier plane, the pulse has the same form at the output as at the input of the 4f-line.

A spatial light modulator (SLM) placed in the Fourier plane controls directly the spectral phase and/or amplitude of the pulse. This can be written as a modulation by the complex mask function M(ω):

$$E_{out}(\omega) = E_{in}(\omega) \cdot M(\omega) \tag{27}$$

The temporal shape of the pulse at the output of the shaper can be calculated using the Fourier transform M(t) of the spectral mask:

$$E_{out}(t) = \int_{-\infty}^{+\infty} E_{in}(\tau) \cdot M(t-\tau) d\tau \tag{28}$$

2.4.3 The liquid crystal mask

Various types of spatial light modulators have been proposed. High resolution shaping masks can be obtained by microlithographic patterning [77], with the great disadvantage that the mask is static. Acousto-optic Modulators (AOMs) are able to control the phase and amplitude of femtosecond pulses [78]. Their rapid switching times (μs range) make them attractive in combination with kHz-repetition rate lasers. They are not suitable, however, for lasers operating with repetition rates in the MHz range. Deformable mirrors have been demonstrated [79] and are particularly suited for shaping at wavelengths were no transmittive SLMs are available. In this work, the most common liquid crystal masks has been used.

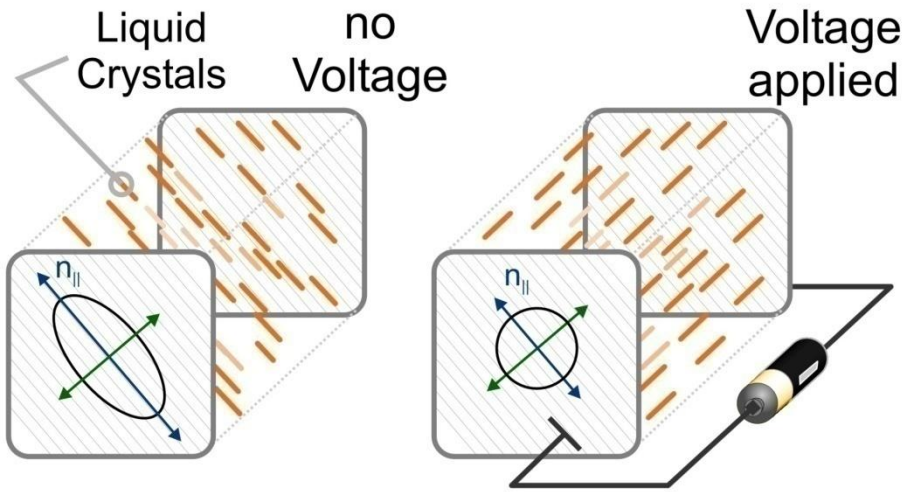

Figure 2.13 Representation of one pixel of the LC-mask. When no voltage is applied (left), the long axis of the liquid crystals is in the plane perpendicular to light propagation, forming an angle of 45° with the polarization. The created polarization is corrected by an additional mask, where the LCs long axis forms an angle -45° with the polarization. When a voltage is applied, the LCs tend to align with the electric field. When they reach a position where they are aligned with the propagation direction, the material loses its birefringence and the polarization remains unchanged.

A liquid-crystal (LC) SLM is a 1D array of pixels. Each pixel contains LCs that are simultaneously birefringent and orientable through the application of an electric field. Such a pixel is represented in Figure 2.13. Rod like liquid crystals can be rotated from a position where their long axis is perpendicular to the light propagation (no voltage) to a position where it is parallel to the propagation (when maximum voltage is applied). Depending on the orientation of the long axis LC-SLMs designed to modulate only the phase or the phase and the amplitude of the pulse are available. In our case, both parameters can be varied and two masks are necessary. In the first mask, the long axis is oriented at +45° to the polarization direction of the pulse and in the second at -45°. Each mask can change the polarization state and the retardation at each wavelength. At the output of the mask (or of the shaper), a polarizer transforms the polarization modulation in an amplitude modulation.

2.4.4 Polarization shaping

In absence of the polarizer, polarization shaping [80-81] is possible. The polarization direction for each pixel can be turned from 0° to 90°. Due to the limited number of free parameters, the control over the amplitude is lost and the ellipticity of the polarization cannot be chosen.

Other methods to gain control over the polarization of a broadband pulse using a pulse shaper have been demonstrated. At least five solutions with increasing levels of control and complexity can be distinguished [82]. Until recently, polarization shaping was done exclusively based on liquid crystal displays (LCDs), but some of the strategies are transferable to shaper relying on acousto-optical modulators (AOMs) [83].

Full control of the electric field requires no less than 4 LCD masks. Indeed, 4 parameters have to be controlled independently for each wavelength: phase, amplitude, polarization orientation and polarization ellipticity. In the most advanced setups, these four masks are physically present in the Fourier plane of the 4f-line [82]. When only one double mask is available, the pulse can be sent twice through the device [84]. Alternatively, it is first decomposed in two perpendicular polarizations that are independently shaped and interferometrically recombined [85]. If the control over amplitude is given up, an 8f-line with a double and a simple mask was demonstrated to allow full control of the polarization [86].

2.4.5 Limitations

In the process of pulse shaping, the theoretical phase applied by the experimenter is not perfectly reproduced at the output of the device. Several factors, of intrinsic or of practical nature, limit the accuracy accessible experimentally. We will keep in mind these limitations in the following chapters.

Even an ideal 4f-shaper introduces some artifacts in form of spatio-temporal coupling [87-88]. The phase applied by the mask diffracts the pulse resulting in a shift of the beam coming out of the 4f-line. The LCM can be seen as an optical element of varying thickness, depending on the applied phase. For example, a quadratic phase function acts like a lens and a linear phase function will slightly shift the beam like a very thin prism. In our case the short distances between the shaper and the microscope as well as the strong focusing smooths the potential variations.

A practical limitation is imposed by the pixilation of the LC-mask. Commercially available masks are divided into 128 to 640 pixels [89]. The size of a pixel is usually of 100µm, including a 97 µm wide active region and a gap of 3 µm. The gap regions are not precisely controlled. They have a smoothing effect on the phase but also created unwanted effects, like unshaped pulse replicas. For the active region, the Nyquist limit imposes a boundary to the phase difference between two adjacent pixels: it must not exceed π, otherwise the applied phase function is not correctly reproduced. This limits the maximal slope of a linear phase function and hence the maximal delay accessible with the shaper. The precision of the delay in turn depends on the precision of the phase for each pixel. In practice, the 12-bit coding available provides a precision going way beyond the experimental requirements, down to zeptoseconds [90].

2.4.6 Pulse shaper design

The shaper design used in this work is shown in Figure 2.14. The lenses schematically represented in Figure 2.12 introduce chromatic aberrations affecting the temporal shape of the pulse as well as the focusing in the Fourier plane. To avoid these effects for the 10fs pulses used in this work, only reflective optics are used. A simple collinear alignment is then

impossible. Several configurations have been proposed to minimize aberrations due to reflection on tilted mirrors and gratings [91]. In the adopted configuration, the 3rd dimension is used. The grating is slightly tilted to increase the height of the beam. After reflection on the folding mirror, the dispersed pulse is reflected by the cylindrical mirror parallel to the horizontal direction. It travels slightly higher (about one beam diameter) above the folding mirror before reaching the liquid crystal mask.

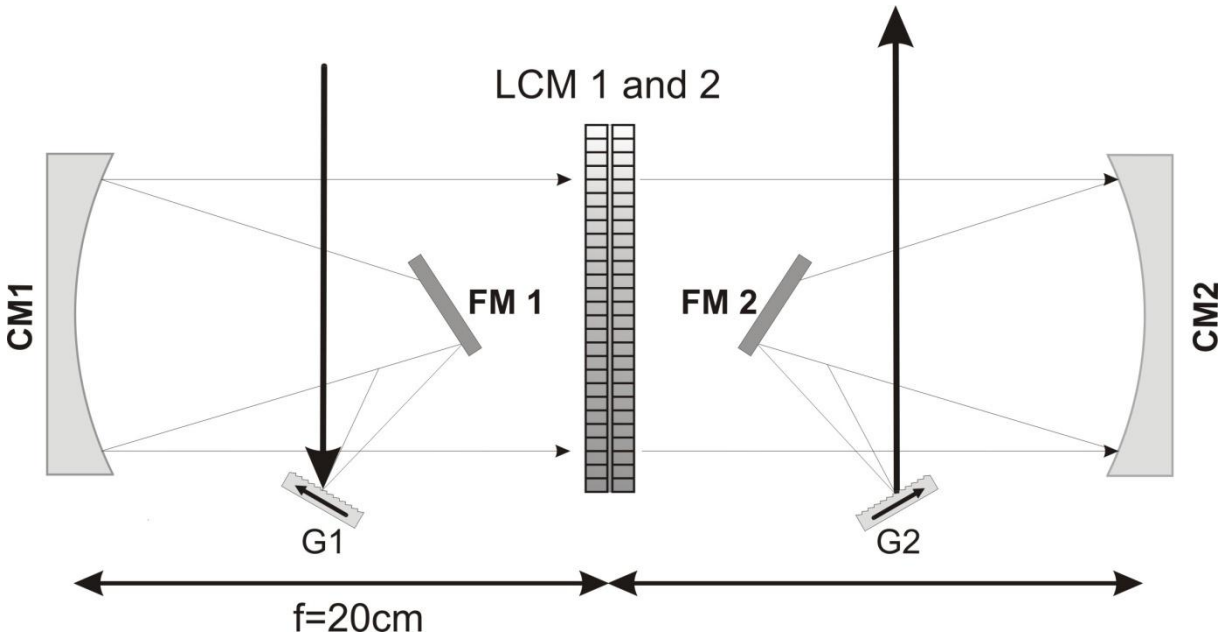

Figure 2.14 Shaper design used in this work. G1/2: gratings. The arrow indicates the blaze direction. FM1/2: folding mirrors. CM1/2: Cylindrical mirrors with focal length f=20cm. LCM1/2: Liquid crystal masks (640 pixel).

In the following chapters, the shaper parameters are described in detail for each experiment. Given the focal length (f=20cm in our case), the gratings determine the dispersion and hence the resolution as well as the width of the shaped spectral window and the spectral resolution. Pairs of gratings with 600 gr/mm guarantee a broad spectral range while 1200 gr/mm gratings favor the resolution. A smaller dispersion also reduces the effects due to reflections on tilted optics, so that the 1200gr/mm solution requires a more careful adjustment of the shaper.

2.4.7 Pulse shaping strategies for CARS

Pulse shaping is the cornerstone of the broadband CARS implementations presented in the following chapters. Unlike in classical coherent control experiments, no excited electronic state or branching between different energy pathways in the molecule are involved. The system is completely described by $\chi^{(3)}(\Omega)$ and the outcome of each shaping strategy will be simulated on this basis.

The goal of shaping strategies for CARS has been the acquisition of precise spectra over large spectral ranges [92], or the specific excitation of a particular molecule in a mixture [93]. Here the stress is put on properties relevant to microscopy: maximizing the spectral information acquired on a single-channel detector and minimizing the photodamage of sensitive samples are the key challenges.

3 Shaper Assisted Multiplex CARS

In this chapter, precise amplitude shaping is used to improve imaging with a multiplex CARS (MCARS) setup. On the one hand, the ability of MCARS to record whole spectra make it a powerful technique for chemical mapping. The wealth of information accessible with MCARS provides a critical advantage over ps-CARS when subtle changes in the sample have to be identified. On the other hand, video-rate imaging demonstrated with setups addressing a single Raman shift is not compatible with the pixel dwell times required for spectrally resolved detection.

Shaper-assisted multiplex CARS (SAM-CARS) gives a way out of this dilemma and combines the advantages of both techniques: rapid imaging with maximal spectral information.

3.1 Multiplex CARS

Here a short introduction to Multiplex CARS is provided as a basis in order to later on discuss the benefits of the shaper-assisted Multiplex CARS setup. A more detailed description of the Multiplex CARS setup used in this work and its use for imaging can be found in earlier works from our group (see [94-95]).

3.1.1 Principles

A major advantage of spontaneous Raman microscopy lies in the ability to record whole spectra at each point in the sample. Spectral analysis allows identification of unknown compounds and chemical imaging, at the basis of the numerous studies based on the Raman effect in material science [96] and biology [97]. In the identification of diseased tissues, small differences in spectra have to be analyzed to differentiate cancerous and healthy parts [98-99]. In this respect, the rapid imaging using CARS in a picoseconds-laser based setup fails to achieve the level of specificity of a thorough analysis of spontaneous Raman data[100].

Among the broadband CARS methods (see 2.2.6), MCARS is the most straightforward way to acquire spectra. A scheme of the principle is illustrated in Figure 3.1 : the pump and probe beams remain narrowband while the Stokes beam covers a broader spectral range. This way several Raman bands can be excited simultaneously. The narrowband probing transfers the spectral information directly into the CARS spectrum (Figure 3.1 b).

In the early demonstrations of MCARS for applications to spectroscopy in the gaseous phase, the use of an infrared dye laser with 5-7nm bandwidth for the Stokes pulse allowed recording a whole Q-branch rotational spectrum [101]. A first demonstration of MCARS spectroscopy at the focal point of a microscope objective, still using dye lasers [102], was shortly followed by microspectroscopy of lipid vesicles based on synchronized picosecond- and femtosecond-lasers for a better stability [43, 103].

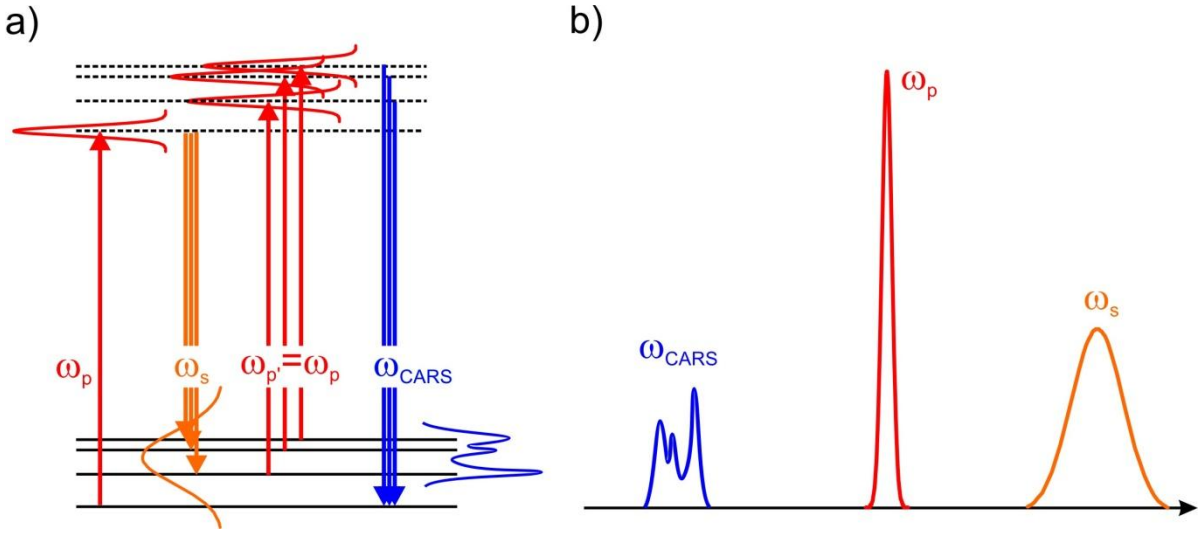

Figure 3.1 Principle of Multiplex-CARS. a) Photon diagram representing the Multiplex CARS excitation: the combination of a narrowband pump (ω_p) and a broadband Stokes (ω_s) pulse excites several Raman levels. Narrowband probing ($\omega_{p'}$) results in a spectrally resolved CARS signal. b) Representation of the excitation and of the CARS signal in the spectral domain.

The generation of CARS spectra is simplified in the context of microscopy because the relaxed phase matching condition can be met for a great number of Raman shifts under strong focusing conditions. Recording a CARS spectrum rather than relying on the contrast provided at a single Raman shift presents several advantages. Specifically for CARS, the presence of a non-resonant background and its variation across the imaged sample is of much concern. In the spectral domain, the non-resonant background varies slowly and can be identified and quantified on the basis of neighboring spectral regions without resonances. Identifying components in the sample on the basis of spectral profiles also provides a self-validation of the method and makes it less sensitive to laser power fluctuations or time jittering as well as to the presence of contaminants. A wealth of information often used in spectroscopy is the evolution of the linewidth, of the position and of the relative strength of Raman lines. If the spectral profile of the Stokes laser is known, this information can be determined precisely [43] and give access to an analysis of the thermodynamic state of lipid vesicles. Quantitative chemical mapping is possible when the spectra of the components in the sample are known like in polymer blends. The fitting of a calculated MCARS spectrum to the measured data allows retrieving the local concentration of each constituent [104]. MCARS is also ideally suited for imaging without or with minimal *a priori* knowledge of sample composition. In this case however, a maximal spectral coverage is desirable. Indeed, in the imaging of cells for example, the most relevant spectral position for imaging might not be known in advance.

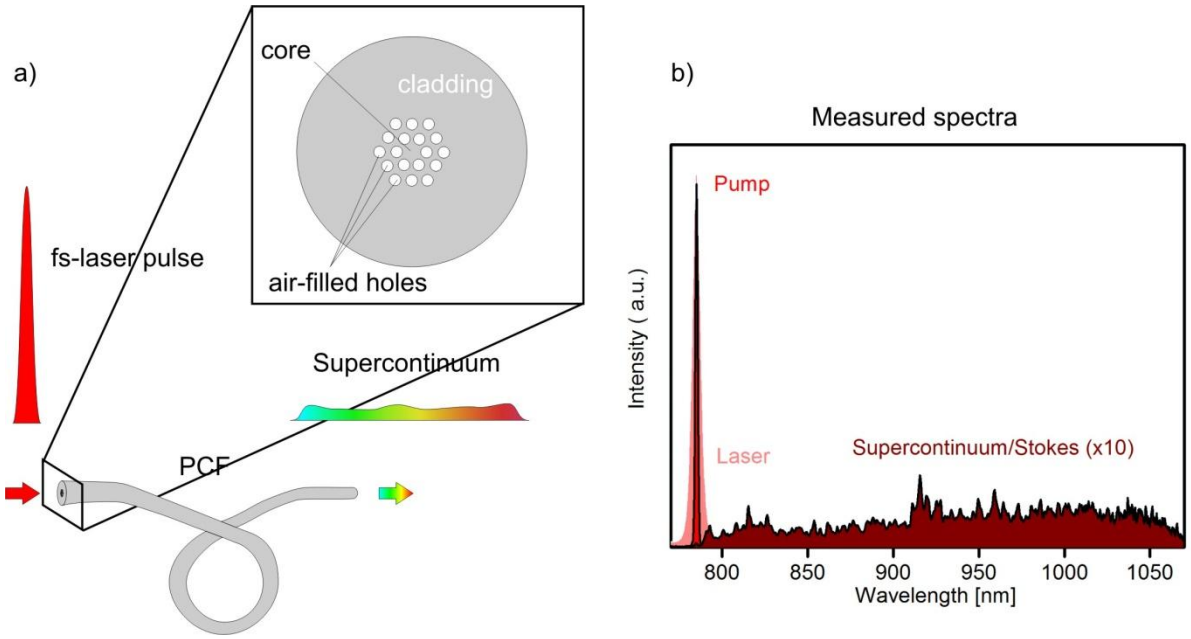

Figure 3.2 Generation of ultrabroadband Stokes pulses using a photonic crystal fiber. a) Structure of a PCF (inset): the core of the fiber is surrounded by a lattice of microscopic holes creating photonic band gaps. Non-linear effects are favored by the confinement and a supercontinuum is efficiently generated from a narrowband fs-pulse. b) Spectra of the pulses used in this work. The Pump beam is obtained by filtering the laser with a narrowband notch filter. Only the red part of the supercontinuum is used as a Stokes pulse (here enhanced 10x for visibility).

In order to cover the whole spectral range of relevant Raman shifts, the Stokes spectrum has to reach above 3000cm^{-1}. This represents pulse duration shorter than 10fs which are challenging to produce and synchronize using an additional femtosecond oscillator. The development of photonic crystal fibers (PCF) (introduced in section 2.3.3) paved the way to a much simpler way to achieve this spectral coverage, enabling a dramatic widening of the spectral range of MCARS setups by one order of magnitude from few hundreds to few thousands of wavenumbers [105-106].

A few features of spectral broadening in PCFs (Figure 3.2 a) that may prove important for MCARS deserve consideration at this point. A first characteristic already finds application in our setup: with a supercontinuum covering a large spectral area, dispersion inside the imaging optics becomes important. The design of PCFs with anomalous dispersion allows pre-compensation of the dispersion directly in the fiber by choosing an appropriate fiber length [107-108]. No further dispersion compensation device is then necessary to record the whole available CARS spectrum simultaneously. A second important parameter is the output spectral energy of the supercontinuum. It cannot be simply adjusted by increasing the laser power coupled into the PCF: a higher pump power may increase the width of the supercontinuum rather than its spectral intensity. The excess incident energy can also be transferred in solitons at wavelengths outside the useful spectral window. The choice of a fiber type (with a given dispersion curve), length and input energy for sufficient broadening are therefore interrelated. Finally, a last property of the supercontinuum of interest in our context is its spectral coherence [109-110]. Decoherence usually originates from shot noise fluctuations and spontaneous emission phenomena later amplified in further nonlinear interactions inside the fiber. The influence of these sources of decoherence depends strongly

on the pump pulse duration and wavelength, with coherent supercontinuua being generated by shorter pulses and wavelengths in the normal dispersion regime [62].

Alternatives to PCFs are tapered and highly-nonlinear fibers [111], however they do not offer the same anomalous dispersion properties. The spectra generated in the MCARS setup used in the following are shown in Figure 3.2 (b). The laser pulse produces a supercontinuum covering more than 250nm on the red side of the pump/probe pulse, which corresponds to over 3000cm^{-1}. This results in a simple setup based on a single laser, without the need for synchronization.

3.1.2 Theory

The MCARS signal generated by the combination of a broadband Stokes and narrowband pump and probe pulses is described using the integral formula for broadband CARS introduced in section 2.2.6 (equation (12)):

$$E_{CARS}(\omega) \propto \int E_{probe}(\omega-\Omega)\chi^{(3)}(\Omega)\int E^{*}_{Stokes}(\omega'-\Omega)E_{pump}(\omega')d\omega'\ d\Omega \qquad (29)$$

If we approximate the narrowband pulses with Dirac distributions, the generated CARS field simplifies to:

$$E_{CARS}(\omega+\Omega) \propto \chi^{(3)}(\Omega)E^{*}_{Stokes}(\omega_p-\Omega), \qquad (30)$$

where the linear dependence on the pump and on the probe field was left out. The CARS field gives hence direct access to the molecular response $\chi^{(3)}$, weighted by the Stokes spectrum. From these formulas the main properties of MCARS spectra can be derived. Equation (22) makes evident that the spectral extent of the Stokes pulse directly determines the spectral coverage of the method. While in spontaneous Raman the measured intensity is proportional to Im($\chi^{(3)}$), the measured intensity in CARS corresponds to $|E_{CARS}|^2$. Retrieval of Raman equivalent spectral information is not straightforward as illustrated by the comparison of spectra obtained with the two methods shown in Figure 3.3. The sample chosen here was Polyethylene Teraphtalate (PET), a polymer displaying a number of strong Raman levels in the fingerprint region as well as in the CH region at 3000cm^{-1}. MCARS spectra display distorted lineshapes charecteristic of the interferences between vibrationally resonant and nonresonant parts of the third-order susceptibility:

$$S_{CARS}(\omega+\Omega) \propto \left|\chi^{(3)}_{res}(\Omega)+\chi^{(3)}_{NR}\right|^2 = \left|\chi^{(3)}_{res}(\Omega)\right|^2 + 2\chi^{(3)}_{NR}Re\left[\chi^{(3)}_{res}(\Omega)\right] + \left|\chi^{(3)}_{NR}\right|^2 \qquad (31)$$

In mixtures, the contributions of the different components interfere with each other resulting in a complex interpretation of the data [43]. Therefore a linearization of the detected spectra is desirable. Heterodyne techniques retrieve the generated CARS field, but rely on interferences with a local oscillator. This usually comes along with complex experimental setups because an additional laser has to be provided at the CARS wavelength [26, 112]. Even when this technical requirement can be circumvented, the phase relationship between CARS and local oscillator also has to be controlled precisely [113]. Alternatively, algorithmic phase-retrieval methods have been developed and will be discussed in more detail in the next section.

Experimentally, the pump and probe pulses have finite bandwidths. The probe pulse determines the spectral resolution of the setup. Since the same pulse is usually used as a pump and probe pulse, the signal intensity depends quadratically on the narrow band pulse. A

resolution of the order of the typical width of Raman lines (10-20cm^{-1}) can be regarded as ideal, because it maximizes the signal while conserving good spectral resolution. A wider probe pulse would deteriorate the ratio between resonant and nonresonant signals.

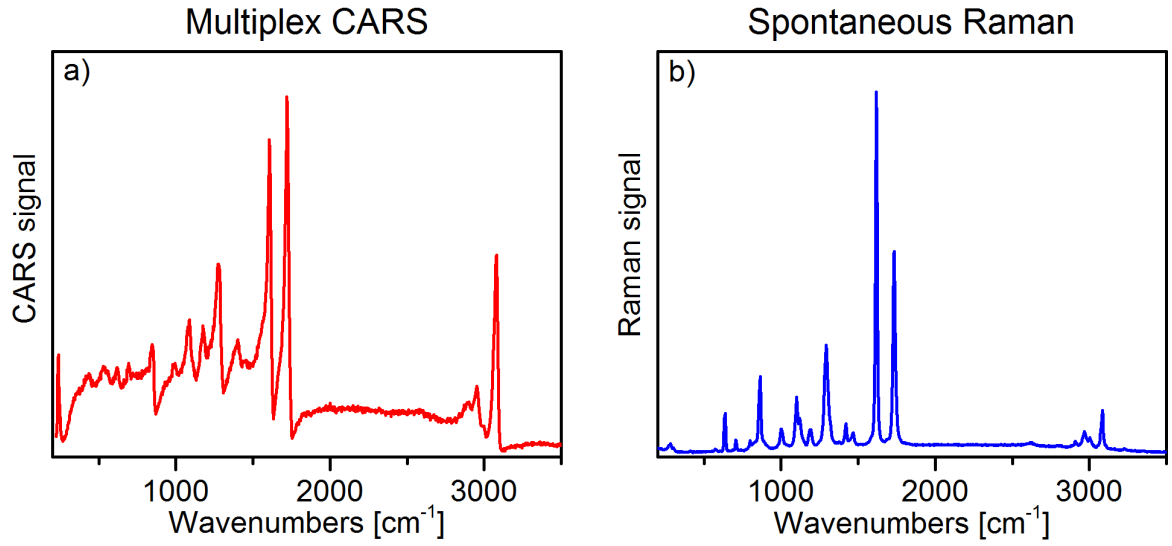

Figure 3.3 Comparison of Multiplex CARS and spontaneous Raman spectra. (a) Multiplex CARS and (b) spontaneous Raman spectra of PET. Note the presence of a nonresonant background throughout the whole spectrum in MCARS, as well as the dispersive lineshape creating a dip feature on the blue side of each line.

In the preceding theoretical description of MCARS signal generation, we arbitrarily assigned the role of the Stokes pulse to the supercontinuum and of pump/probe to the narrowband part. However, another contribution can be produced when the broadband pulse alone impulsively excites the sample and the narrowband pulse only probes the system. Equation (29) then transforms into:

$$E_{CARS}(\omega_p + \Omega) \propto E_n \chi^{(3)}(\Omega) \int E_b^*(\omega' - \Omega) E_b(\omega') d\omega' \qquad (32)$$

where $E_{b,n}$ denote the broadband and the narrowband pulse, respectively. This process is sometimes referred to as a 3-color CARS process in the literature, as opposed to the 2-color CARS process of MCARS [114]. The excitation process by the broadband supercontinuum is similar to the single-beam CARS excitation scheme described in detail in the next chapter: all available photon pairs inside the supercontinuum interfere to generate coherences over a large set of Raman shifts. Impulsive excitation of Raman levels can be used to produce time-resolved spectra by delaying the probe pulse [111, 115]. This reveals the coherence time of individual Raman bands and allows minimization of the nonresonant background at well chosen probe delays. However, the impulsive excitation is usually spectrally less broad than the achievable MCARS range, because it relies on the autocorrelation of the broadband spectrum. It also requires a powerful and highly coherent PCF output, which is challenging and can produce photodamage [116]. Finally, this contribution can have a detrimental effect by interfering with the expected MCARS signal. In our setup, the spectral intensity in the Stokes supercontinuum is two orders of magnitude lower than in the pump/probe pulse, so that the pure MCARS contribution dominates largely. Therefore spectral analysis on the basis of the theoretical background of equations (29) and (30) can be used to analyze the data.

3.1.3 Analysis of MCARS data

Depending on the level of *a priori* knowledge about the sample and the excitation, different approaches are available to extract Raman like spectra from the distorted MCARS lines. These methods are summarized in Figure 3.4 and can be divided into methods applicable to mixtures of known components and methods for unknown samples.

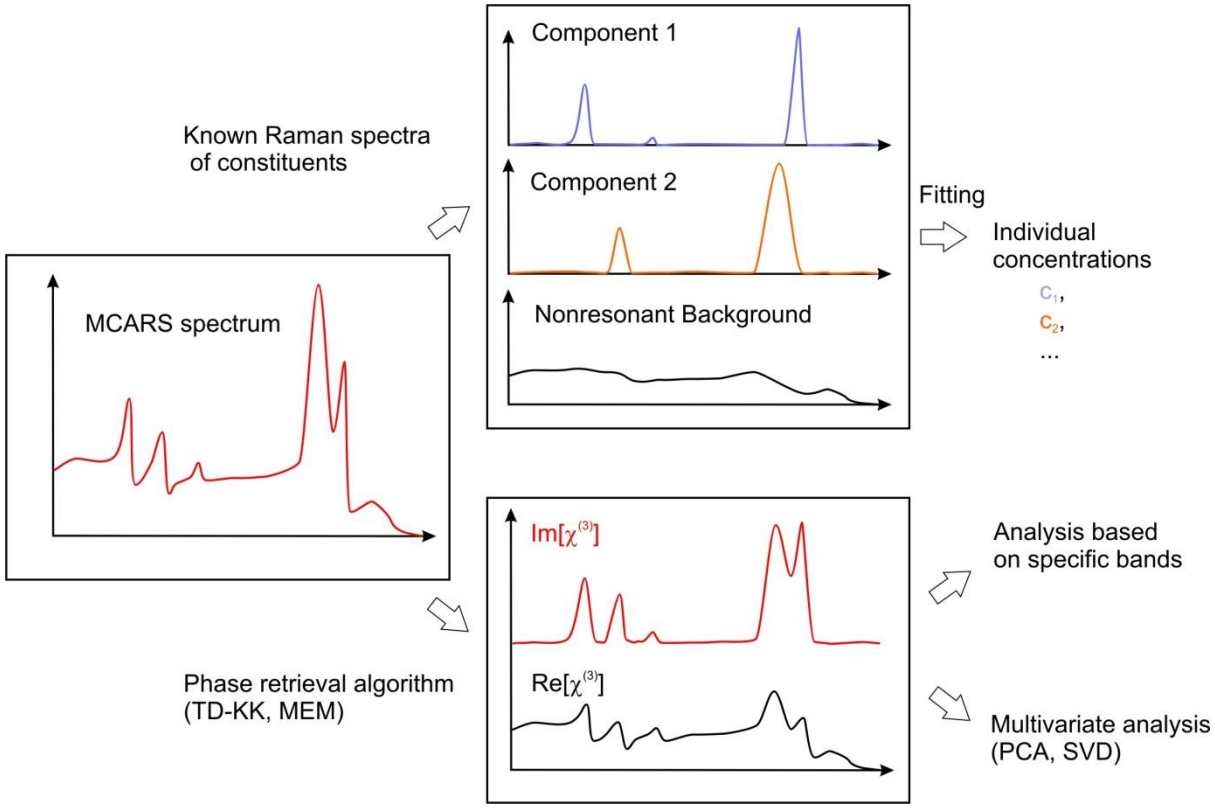

Figure 3.4 Analyis methods for MCARS data. If the components are known in advance and their nonlinear susceptibilities can be estimated, a fitting of the data with the respective concentrations as parameters provides quantitative data (upper path). In the case of unknown samples, phase retrieval algorithms extract Raman information from the CARS spectra before further analysis.

The first case is found mainly in material science applications, where the microscopic arrangement of chemical building blocks must be imaged or the evolution of the concentration of a reagent has to be monitored. It has been applied to the imaging of polymer blends [104], but also to model systems for biology [117-118]. The analysis of a mixture of known components relies on the simulation of measured data according to previous equations. Thus the signal can be written as:

$$S_{mix}(\omega + \Omega) \propto \left| \sum_i c_i \cdot \chi_i^{(3)}(\Omega) \right|^2 \qquad (33)$$

Where c_i are the concentrations of the species and the subscript i runs through the components in the mixture. The complex susceptibilities of each component is obtained either from spontaneous Raman spectra or by fitting of MCARS data acquired from pure components. Other methods are now available for a direct measurement of the phase of $\chi^{(3)}$ [119] and could be used in this context. The mathematical problem is then overdetermined with a few concentrations as parameters to fit a whole spectrum. The adjustment is calculated for example by minimizing the sum of the squared difference with specific algorithms. Despite its

conceptual simplicity, this method have found only few applications because the requirement of a completely known composition is rarely met and the need for characterization of $\chi^{(3)}$ is a strong constraint.

A much more widespread strategy applies to systems of unknown composition. The large information carried by MCARS spectra allows retrieving quantitative data mathematically using only a few assumptions. Many phase functions can in principle lead to the same observed signal; however only a few have a physical meaning. Starting directly from an expression of $\chi^{(3)}$ as a combination of a constant, real nonresonant background and a limited number of Lorentz lines proves to be impractical. Mathematical approaches have been imported from other research fields where the same phase retrieval problem emerges. Two are commonly used in the MCARS literature: the Time-Domain Kramers Kronig relations (TD-KK)[120] and the Maximum Entropy Method (MEM)[121]. Both use more general constraints to obtain a simpler and deterministic way to compute the phase. The Kramers-Kronig relation gives the following analytical solution to the phase problem [122]:

$$\varphi(\omega) = -\frac{P}{\pi}\int_{-\infty}^{+\infty} \frac{\ln|\chi(\omega')|}{\omega' - \omega} d\omega' , \tag{34}$$

simply assuming that the function is analytic and respects the causality principle. This approach is equivalent to a transformation into the time domain where only a signal at positive time delays is kept. TD-KK also takes into account the non-instantaneous character of the excitation which results in a slowly varying nonresonant background. This method therefore requires to estimate the background variation either by measuring it in a medium without resonances (like glass) or by polynomial fitting.

In MEM, the starting principle is to state that the most random time profile having a spectrum in accordance with the measurement corresponds to the physical reality. It has been proven [123] that in the case of CARS the phase can then be calculated by rewriting the measured signal as the inverse of a **finite** sum of M Fourier components:

$$\left|\chi^{(3)}(\nu)\right|^2 = \frac{|\beta|^2}{\left|1 + \sum_{k=1}^{M} a_k \exp(-i2\pi k\nu)\right|^2} \tag{35}$$

And the coefficients verify:

$$\sum_{k=0}^{M} a_k C(n-k) = \begin{cases} |\beta|^2, & n = 0 \\ 0, & n = 1, \dots, M \end{cases} \tag{36}$$

where $C(k) = \mathcal{F}_k\left\{\left|\chi^{(3)}(\nu)\right|^2\right\}$, $\mathcal{F}$ being the Fourier transform operator. By solving these equations, the phase is obtained with a constant offset which can be determined using a point where only nonresonant background is recorded. In the case of a varying background, a slowly varying phase distortion is observed experimentally and can be corrected using a polynomial fit. The choice of the number of Fourier components M in equation (27) determines the accuracy of the retrieval but also the computational cost.

With the right choice of M, both TD-KK and MEM provide comparable results [95, 124-125]. Further data analysis based on the linearized spectrum is similar to the techniques used in spontaneous Raman spectroscopy. If specific bands are known, quantitative chemical imaging is achieved by simply comparing their intensities [126]. In more complex samples, where the

composition cannot be deduced directly from few identifiable bands, small variations across the spectrum are highlighted by multivariate analysis. By comparing the spectra acquired at each pixel, Principal Component Analysis (PCA) computes spectral patterns responsible for the largest variations. Each spectrum is then described as a linear combination of these patterns. Imaging of healthy and tumorous brain tissues was demonstrated using PCA after phase extraction of MCARS spectra [95].

3.2 Shaper-Assisted Multiplex CARS

As briefly shown in the precedent section, MCARS is ideally suited for rapid recording of spectra. Raman equivalent information is obtained at a much higher rate than is possible with spontaneous Raman setups. However, the impressive video-rate imaging capabilities of setups addressing a single Raman shift have not been demonstrated to date with MCARS. This is due to a technical limitation imposed by spectrally resolved detection. Although the signal-to-noise ratio would allow imaging with shorter integration times, the charge-coupled devices used for MCARS are limited to dwell times in the ms range. At the same time, photomultipliers (PMTs) used in ps-CARS or fluorescence measurements can be operated in the µs range.

The question is therefore how to bridge the gap between narrowband and broadband setups and suppress the dilemma between high spectral coverage and high speed imaging. Shaper-Assisted Multiplex CARS provides a solution with a setup able to adapt to the amount of information and to the rapidity needed in a given application.

3.2.1 Tailoring the excitation

In MCARS, the range of Raman shifts acquired simultaneously in the spectrum is directly given by the extent of the Stokes pulse. If the spectral intensity of the Stokes pulse can be precisely controlled, this gives access to a direct control of the excitation. This can be easily seen using the equations describing the CARS process. If we designate by the function M(ω) a spectral amplitude mask, then the Raman excitation probability A(Ω) can be written as:

$$A(\Omega) = \int [M(\omega' - \Omega) E_S^*(\omega' - \Omega)] E_p(\omega') d\omega' \propto M(\omega_p - \Omega) E_S^*(\omega' - \Omega) \qquad (37)$$

The simplification is carried out assuming the Pump is a Dirac delta function. With this scheme, the control over A(Ω) is straightforward as compared to other shaper assisted implementations using phase shaping [44-45].

The possibilities offered by the control of the Stokes amplitude are summarized in Figure 3.5. The whole CARS spectrum can still be recorded when the Stokes spectrum is completely transmitted. Hence, the advantages of spectrally resolved detection are still available. For rapid imaging, a narrowband section can be cut out of the Stokes pulse resulting in an excitation equivalent to ps-CARS setups. Finally, more complex M(ω) could address the main Raman lines of a molecule specifically in a way that is not accessible in traditional schemes.

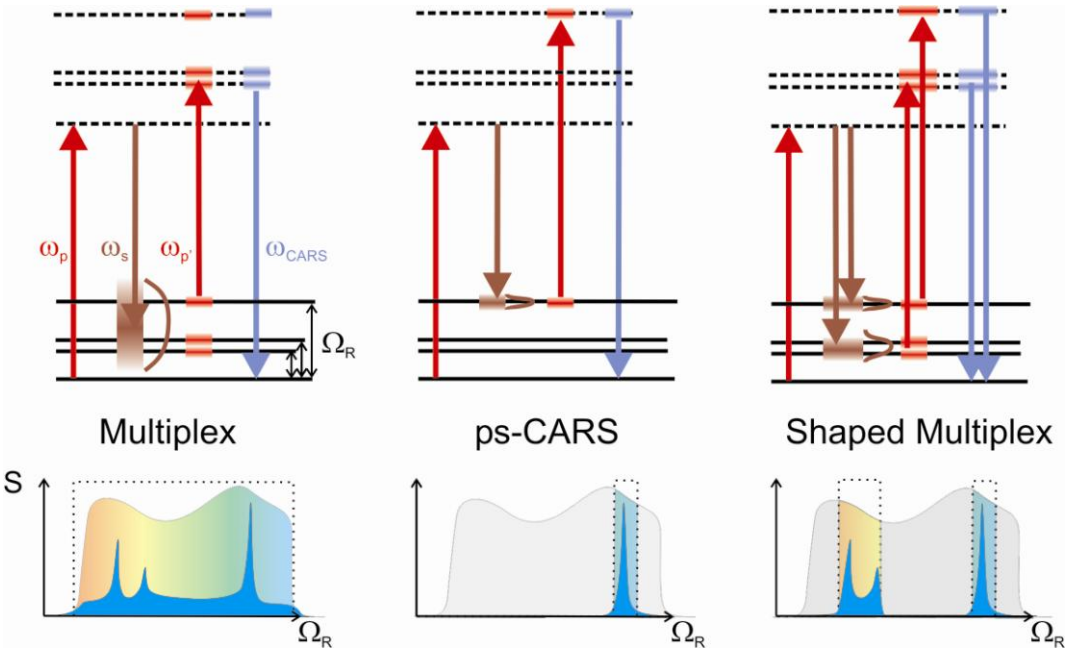

Figure 3.5 Tailored excitation using an amplitude mask for the Stokes pulse. Photon schemes (upper row) and spectra (lower row) for different masks M(ω). A complete MCARS spectrum can be measured using a constant M(ω)=1 (left). By selecting a narrow spectral region, a single Raman band is excited emulating ps-CARS schemes (center). Complex excitation schemes tailor the excitation to the molecular spectrum (right).

On the detection side, a combination of a CCD and one or several PMTs with an adequate set of filters can take advantage of the flexibility of the excitation. For imaging, one channel detectors allow for example rapid scanning for identification of regions of interest in larger areas where time consuming quantitative imaging is later applied. Controlling the Stokes spectrum has several advantages over a simple filtering of the MCARS signal after the sample. In first place the reduction of the photon load is of importance with regard to photodamage. The broadband Stokes pulses, if they are transform limited, can trigger nonlinear photodamage. Concentrating the excitation energy in the most relevant Raman shifts then optimizes the obtainable signal. Following the same logic, tailoring the Stokes pulse avoids the effects due to impulsive excitation.

3.2.2 Experimental setup

Shaper Assisted Multiplex CARS is an experimental realization of this concept, where the Stokes pulse is tailored using a pulse shaper. The setup used here for its demonstration is shown in Figure 3.6. It relies on a single laser (Mira 900F, Coherent) producing pulses of 160fs length with 12nJ energy at a repetition rate of 76MHz. The spectrum of the laser is centered at 785nm and is 5nm wide (FWHM). The laser beam is divided into a pump/probe and a Stokes arm using a beam-splitter. In the Stokes pathway, 250mW of the laser output are used to efficiently pump an end-sealed PCF (NL-PM-750, Crystal Fiber A/S) and produce a supercontinuum. The remaining laser power is filtered down to a spectral width of 1nm at 785nm, corresponding to $16cm^{-1}$, for best resolution and signal level. A delay stage in the pump/probe pathway ensures the simultaneous arrival of both pulses. After recombination using an interference filter, the excitation corresponds to the spectra in Figure 3.2 (b).

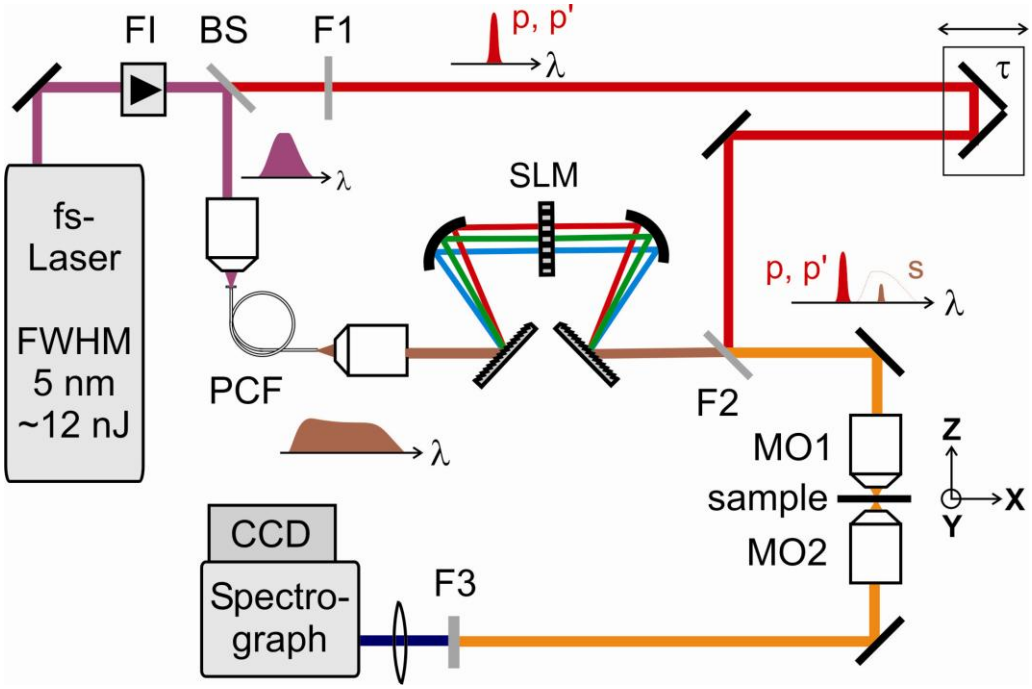

Figure 3.6 Shaper-Assisted Multiplex CARS setup. FI: Farraday Isolator, BS: Beam Splitter, F1: Bandpass filter, SLM: Spatial Light Modulator, F2: Longpass filter, MO1,2: Microscope objectives, F3: Shortpass filter.

A 4f-shaper (see section 2.4.6) is introduced in the Stokes arm. In the symmetric 4f-line, spherical mirrors with f=20cm are used while dispersion is realized using gratings with 600 grooves/mm. At the Fourier plane, a computer controlled 640-pixel double liquid crystal mask (CRI Inc.) equipped with two broadband polarizers is used to control the amplitude at each spectral position in the supercontinuum. In the microscope (Olympus BX51), the sample is raster scanned for imaging using a piezo stage (Physikinstrumente). After a short-pass interference filter, the signal is dispersed by a monochromator (SP2300, Acton Research) on an electron-multiplying CCD camera (Newton, Andor).

3.2.3 Spectral coverage and background suppression

Characterization of the setup begins with the determination of two key factors: the spectral coverage after the shaper and the extinction power of the device. Both properties are measured using spectra acquired in diiodomethane (CH_2I_2). This compound presents a very intense nonresonant signal: it allows determining the extent of accessible Raman shifts and efficient use of the dynamic range of the camera to quantify the extinction.

Figure 3.7 (a) compares the signal obtained in CH_2I_2 for two masks: first with all pixel set to full transmission (red curve), then with only 3 pixels set to full transmission and the others to full extinction (black curve). The recorded signal spans about 3000cm^{-1} starting at about 700cm^{-1} to 3700cm^{-1}. Hence, even with a MCARS setup covering a very broadband spectral range, the shaper can support most of it. Both the central spectral position and the spectral coverage are adjustable using the parameters of the 4f-line: the spectral window depends on the angle of the first grating and the width of the transmitted spectrum depends on the groove density of the gratings. In turn, the spectral range affects the achievable resolution (see next section).

Although Figure 3.7 (a) shows nicely the extinction obtained with the shaper, a more reliable account is given by the logarithmic plot in Figure 3.7 (b). In single channel implementations of SAM-CARS, the nonresonant background of much broader suppressed regions may add up to a significant signal competing with the strong but narrow resonant CARS. In our setup, the extinction exceeds 2 orders of magnitude over the whole spectral range. The mean extinction even reaches over 400 times. This corresponds to extinction ratios typically achievable with liquid crystals [76]. To optimize the On/Off-ratio two polarizers are used, one just before and one just after the LCM, which slightly reduces the overall transmission.

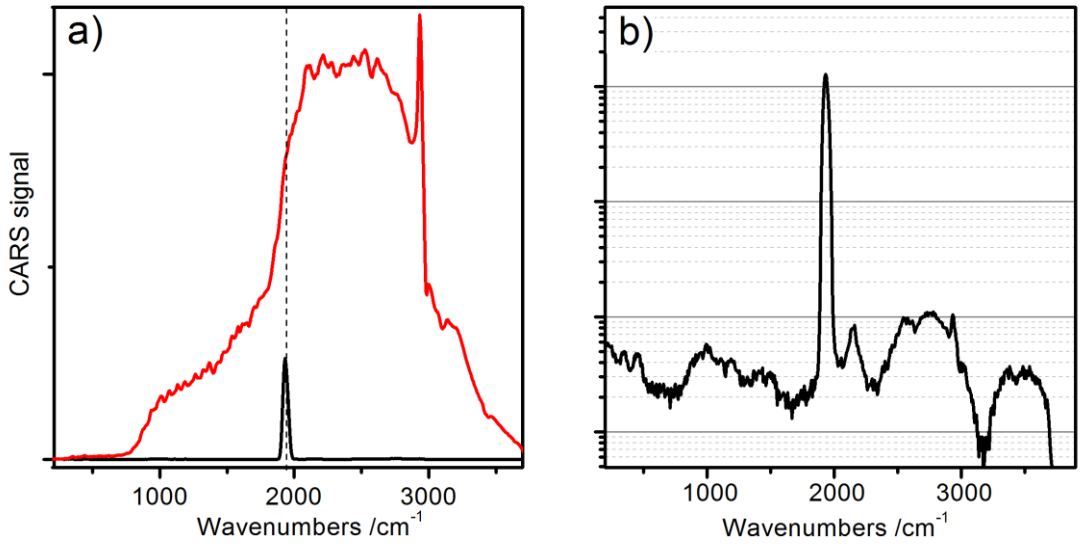

Figure 3.7 Shaper: transmitted spectral range and extinction. a) Comparison of spectra obtained in CH_2I2 with full transmission (red) and with a spectrum narrowed down to 3 pixel at the position of the dotted line (black). This measurement is reproduced in b) with a logarithmic scale to show that the extinction exceeds 2 orders of magnitude in the whole spectral range.

3.2.4 Spectral resolution of the shaper

The precision of Raman band selection in SAM CARS depends on the resolution of the shaper. The spectral width per pixel is measured by scanning a 3-pixel transmitted window across the shaper, resulting in the plot shown in Figure 3.8 (a). The relationship between pixel number and peak position is not linear because the grating dispersion is proportional to the wavelength. The accessible spectral range spans over about 370 pixel resulting in a mean resolution of 7cm^{-1}/pixel. Locally, the resolution varies from more than 13cm^{-1}/pixel at low wavenumbers down to less than 5cm^{-1}/pixel at the high end of the spectrum. This has to be put in relation with the usual width of Raman lines as well as with the width of the pump/probe pulse. Indeed, the resolution of the excitation results from the convolution with the 16cm^{-1}–wide pump pulse. Therefore the excitation with narrower features in the Stokes pulse does not improve substantially the resolution of the excitation while reducing strongly the recorded signal. With a narrower pump pulse, the shaping precision can however be refined by increasing the dispersion of the gratings: a reduced spectral range is then spread onto a constant number of pixels.

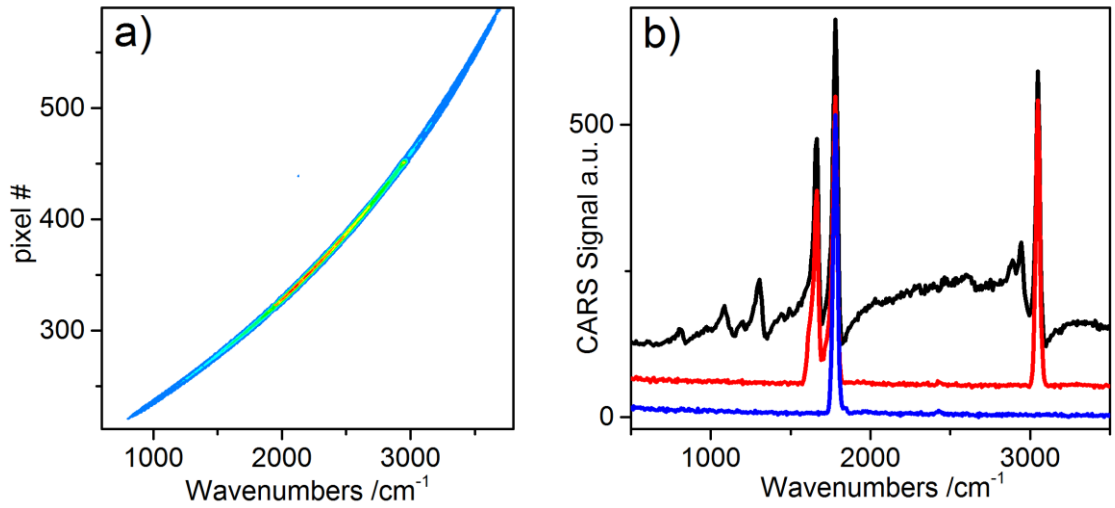

Figure 3.8 Resolution and shaping capabilities. a) Intensity plot obtained by recording a CARS spectrum in CH_2I_2 for each position of a narrow-band excitation of 3 pixel. The central pixel of the window is displayed on the y-axis. b) SAM-CARS spectra of PET obtained: with full transmission (black line), with the selection of a part of the fingerprint region simultaneously with a single band in the CH stretch region (red line) and by selecting a single band at 1780cm^{-1}(blue line).

The precision of shaping for practical applications is illustrated on the example of PET. The three excitation schemes proposed in Figure 3.5 are here realized experimentally. In black, a MCARS spectrum covering a large spectral range is recorded similar to the PET spectrum shown previously (Figure 3.3). The blue curve demonstrates the ability of the shaper to select a single Raman band (here at 1780cm^{-1}) and to isolate it from adjacent bands. Finally, a specifically designed excitation profile for PET selects the three most prominent bands (red line). Detection with a single channel detector will then provide increased contrast with respect to single band excitation. The bands in the fingerprint region are well separated from the CH-stretch region: a dichroic filter could separate the signal in the two regions for simultaneous recording, either with two single channel detectors or combining a CCD and a PMT, could increase specificity.

3.2.5 Considerations on phase shaping

After the demonstration of precise amplitude control, a tempting thought and a natural step is to consider phase shaping since it is already accessible with the shaper. The idea would be to correct the phase profile of $\chi^{(3)}$ in order to suppress the dispersive lineshape seen in MCARS spectra and facilitate data interpretation. In experiments using a shaped broadband pump and probe pulse, an improvement of the resolution was even achieved using the phase profile of resonances [44].

In a first approach to evaluate the effect of phase shaping, we consider again the pump/probe pulse as infinitely narrow. In this approximation, we have seen that the recorded signal can be written as:

$$\begin{aligned} S_{CARS}(\omega+\Omega) &\propto \left|\chi^{(3)}(\Omega)M(\omega_p-\Omega)E^*_{Stokes}(\omega_p-\Omega)\right|^2 \\ &= \left|\chi^{(3)}(\Omega)\right|^2\left|M(\omega_p-\Omega)\right|^2\left|E^*_{Stokes}(\omega_p-\Omega)\right|^2 \end{aligned} \tag{38}$$

Only the amplitude of the mask plays a role and the effects of phase shaping disappear in the recorded signal. This can also be understood by considering that the phase mask acts equally on the resonant and on the nonresonant parts of $\chi^{(3)}$. The interference responsible for the dispersive lineshape, however, depends on their relative phase. With other words, $M(\omega_p\text{-}\Omega)$ turns the susceptibility in the complex plane while the measurement gives access to its modulus.

This approach does not hold when the phase function varies over intervals of the order of the pump width. Yet the shaper resolution allows phases with features down to 5cm^{-1} while the pump pulse is 16cm^{-1} wide. In a second approximation, we consider an infinitely steep π-phase step in the Stokes pulse. The result is a suppression of the signal at the position corresponding to the phase step, as can be seen if we write $A(\Omega_0)$ for this position:

$$A(\Omega_0) = \int_0^{\Omega_0} E_S^*(\omega'-\Omega_0)\,E_p(\omega')d\omega' - \int_{\Omega_0}^{+\infty} E_S^*(\omega"-\Omega_0)\,E_p(\omega")d\omega" \tag{39}$$

Both integrals annihilate if E_p is a symmetric pulse (a Gaussian for example) and if $|E_S|$ is constant. This behavior has been observed experimentally (data not shown). It proves that phase shaping can have an effect but that no straightforward correction of distortions due to the phase of $\chi^{(3)}$ is accessible in a setup where the intensity of the CARS signal is detected.

3.3 SAM-CARS imaging

In the following, the presented SAM-CARS setup will be applied to imaging of model systems for applications in material science and biology. Each example intents to demonstrate the improvement achievable with SAM-CARS as compared to MCARS and to ps-CARS experiments. On one hand, by adapting the excitation profile to the spectra of molecules of interest, the specificity of SAM-CARS measurements is increased with respect to single-band implementations. On the other hand, limitations arise from the integration of the signal in single-channel SAM-CARS data when compared to the acquisition of full spectra and their analysis with the state of the art algorithmic arsenal.

3.3.1 Ternary polymer blend

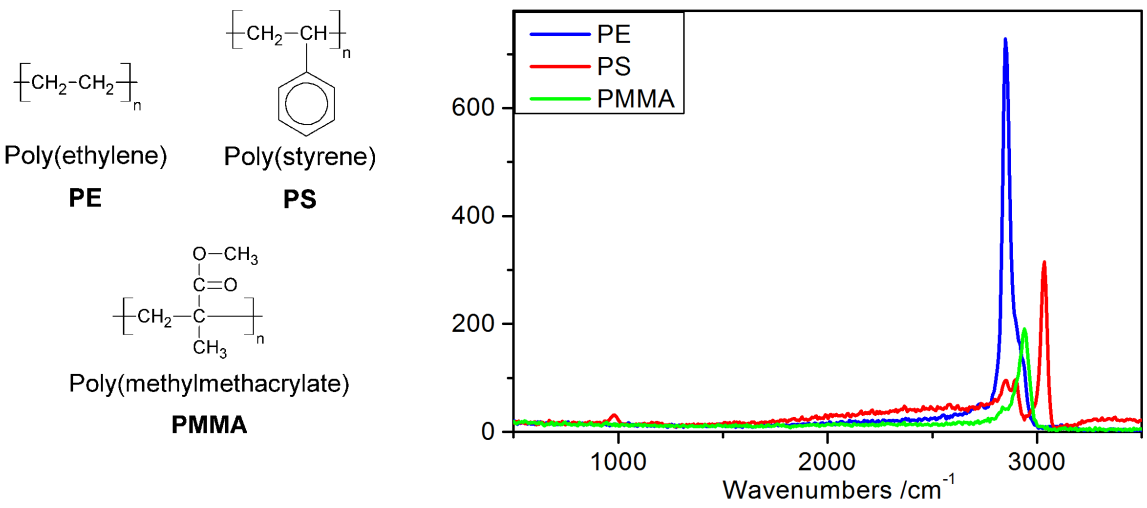

Figure 3.9 MCARS spectra of PE, PS and PMMA. Chemical structure (left) and MCARS spectra measured in the SAM-CARS setup (right) for PE (blue), PS (red) and PMMA (green). The spectral information is concentrated around 3000cm^{-1}, where the polymers have closely lying bands with partial overlap.

Polymers are very often used to demonstrate the capabilities of a CARS setup. They present well characterized Raman bands in the CH stretch region. A typical set of polymers consists of Polyethylene (PE), Polystyrene (PS) and Polymethylmethacrylate (PMMA). The polymers and their MCARS spectra are shown in Figure 3.9: they have close lying, partly overlapping bands around 3000cm^{-1} and are used to test the resolution of the setup. Compared to polymer spheres suspensions, polymer blends are a more complex and relevant sample. Mixtures of polymers provide a set of new materials whose properties depend on the original polymers and on their arrangement inside the blend. Immiscible polymers interpenetrate with structures in the microscopic level. MCARS offers the opportunity to image rapidly and in a label-free manner this arrangement and could be used to characterize routinely the material or clarify the emergence of new properties. It avoids resorting to staining agents which can interfere with the formation of the blend. Since all the components are known in advance, rapid quantitative imaging of a polymer blend was demonstrated using MCARS [104] by fitting the recorded spectra with a combination of reconstructed spectra of the components. The same polymer blend is imaged here with SAM-CARS.

The sample was provided by *BASF SE*: a mixture of PE, PS and PMMA was annealed for two minutes then melt pressed at the same temperature. The blend is transparent and the different regions cannot be recognized using bright field imaging. In addition to the sample, sheets of the polymer used to form the blend were available and were used to choose the mask functions for imaging. In Figure 3.10 (a), (b) and (c), MCARS spectra obtained with full transmission are shown for each polymer (dotted lines) as well as the signal after the dedicated mask has been applied. Here the masks simply consist of a narrowband window selecting the most intense band of each polymer. The position and width of the individual masks was chosen as a compromise between maximal signal and minimal overlap resulting in the different ratios between the signal intensity in the MCARS spectrum and the signal intensity with the SAM-CARS in Figure 3.10.

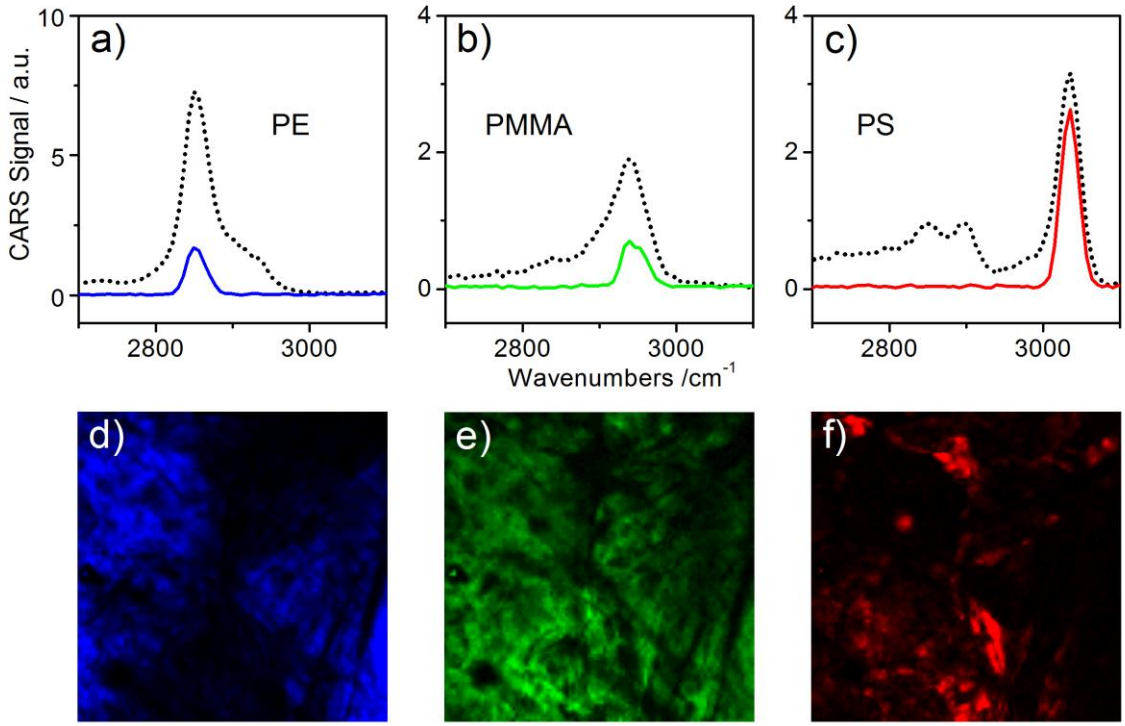

Figure 3.10 SAM-CARS images of polymers in a blend. a) (resp.b,c) MCARS spectrum of PE (resp. PMMA, PS) (dotted) and with application of the PE-mask (resp. PMMA-, PS-mask) (blue, resp. green, red) d)e)f) 100µmx100µm region of the polymer blend imaged with the PE-, PMMA- and PS-masks respectively.

To simulate single-channel detection, the spectra recorded with the CCD camera are integrated over a large spectral region spanning from 2800cm^{-1} to 3500cm^{-1}. For each mask, the same 100µmx100µm region of the polymer blend is scanned with a 1µm step. The images are shown in Figure 3.10 (d), (e) and (f) revealing the distribution of PE, PMMA and PS respectively. PMMA can seem ubiquitous on the basis of Figure 3.10 (e), but this is due to overlap by the much stronger PE signal. However, a RGB plot combining the distributions shown in Figure 3.10 allows a clear identification of each polymer domain (see Figure 3.11). Hence, the combined information obtained with each mask improves the specificity of the imaging. Intensity variation inside each region gives qualitative concentration information.

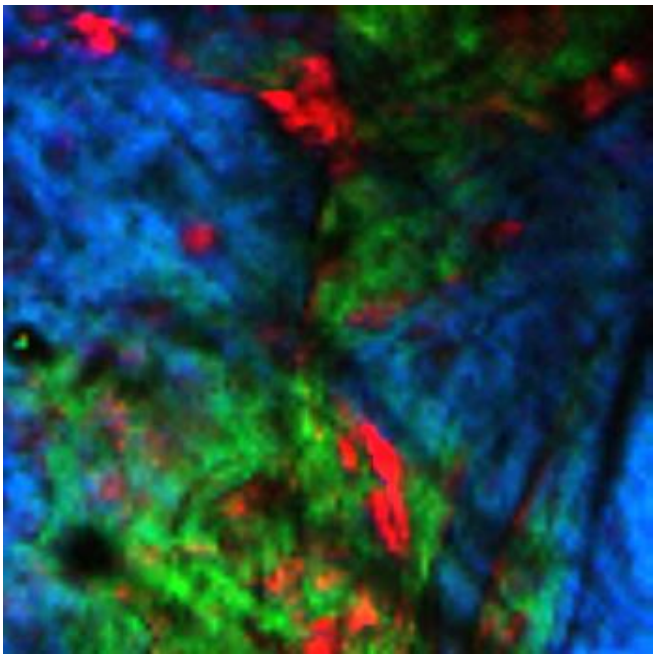

Figure 3.11 Chemical mapping with SAM-CARS. RGB plot of the selected 100µmx100µm region in the blend obtained by combining the measurements shown in Figure 3.10 (PE: blue, PMMA: green, PS: red).

Finally, the rapid analysis of SAM-CARS data with only three points integrated at the most relevant spectral position allows efficient identification of the arrangement of the polymers inside the blend, using the spectral resolution of the setup. Quantitative information is not available in this single-channel implementation but can be carried out with MCARS spectra acquired with full shaper transmission.

3.3.2 Worm C. elegans

To illustrate a possible application of the SAM-CARS scheme to biological samples, the *Caeonorhabditis elegans* worm has been imaged. This model organism has been very extensively investigated in biology, where it allows studying complex genomic, metabolic and developmental behaviors on the scale of a whole organism. *C. elegans* has a rod-like form with a length of about 1mm. Its genome and whole cellular organization were readily characterized. Despite its simplicity and ease of use, many genes identified in *C.elegans* have human homologues and it allows studying disease development on a cellular level. Being transparent, it is convenient for imaging with optical techniques. Although most studies are based on fluorescent staining, CARS has been recently demonstrated as an interesting alternative for the study of lipid storage in the worm based on the band at 2840cm^{-1} [127].

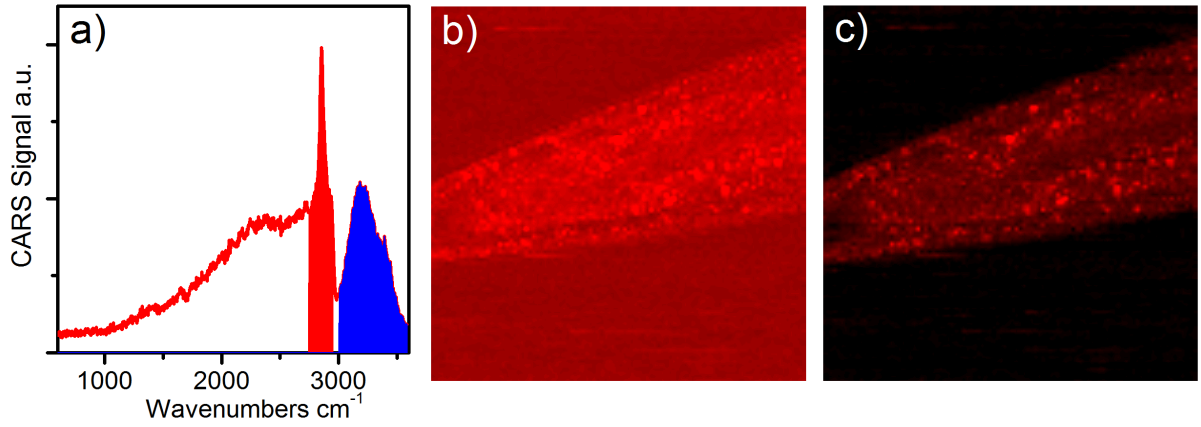

Figure 3.12 SAM-CARS imaging of C. elegans. a) MCARS spectrum acquired inside the worm, showing the typical lipid band at 2840cm^{-1} and a strong water-specific signal above 3000cm^{-1}. The regions selected by shaping for imaging are shown in red for mask1, specific of lipids, and in blue for mask2, for water. b) Image obtained with single channel detection using mask1. c) Image obtained by subtracting an image obtained with mask2 from b). The intensity has been scaled in order to suppress signal outside of the worm, were only water is present.

Here, SAM-CARS is used to eliminate the nonresonant background from a *C.elegans* image. We use the fact, that the worm is kept in aqueous environment and that water contribute strongly to the nonresonant background outside and inside the worm. A region specific of the water contribution is available at high wavenumbers, which is due to OH vibrations. The measurement is realized with a single channel detector integrating a signal with previously selected excitation. The masks are shown in Figure 3.12 (a): mask1 in red selects a narrow region around 2840cm^{-1} and is assigned to lipids; mask2 covers the water-specific wide band around 3200cm^{-1}. The image obtained only with mask1 shows a strong background from the water surrounding the worm, as can be seen in Figure 3.12 (b). Taking into account the signal obtained with mask2, this background can be greatly reduced and an image with much better contrast is obtained (Figure 3.12 c). The intensity of the image obtained with mask2 is multiplied by a constant before subtraction. This constant is obtained from a region in pure water. High concentrations of lipids are found in droplets disseminated across the worm body, as expected from previous studies.

This example demonstrates a typical way SAM-CARS can be applied to biological samples. On the detection side, each region of interest (fingerprint, CH-stretch and OH regions for example) can be roughly selected using a set of filters integrated on a dedicated PMT. Combined with the precise spectral selection provided by SAM-CARS on the excitation side, a more specific imaging than with simple ps-CARS is obtained, keeping the advantages of single-channel detection.

3.3.3 Contrast enhancement

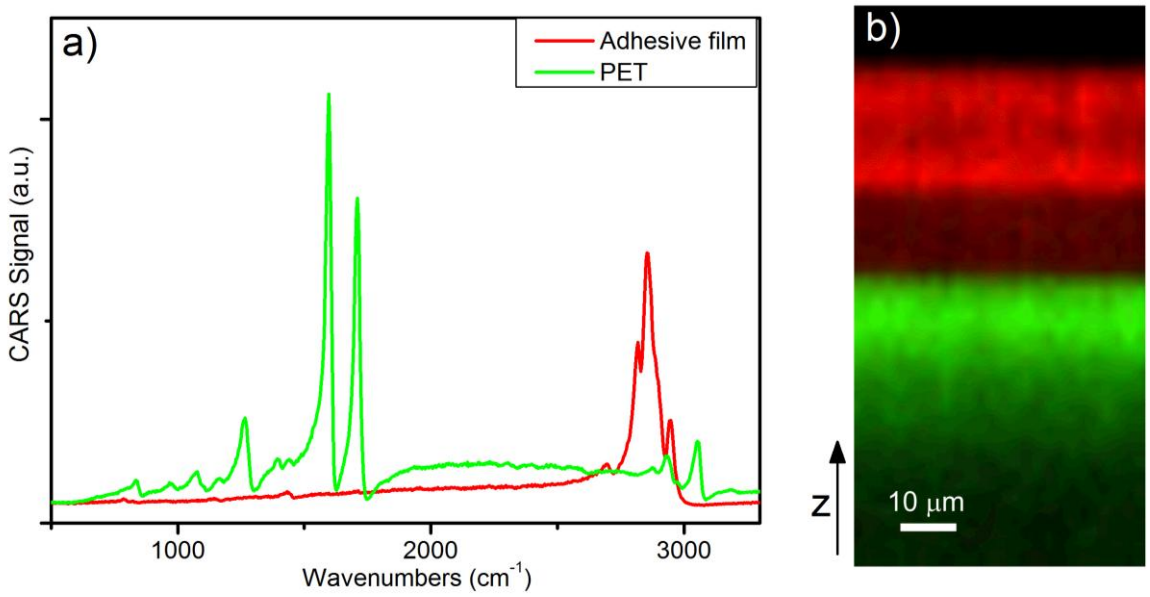

Figure 3.13 Sample for multiple-band SAM-CARS imaging. The sample consists of an adhesive film placed on top of a PET sample. a) MCARS spectra of the constituents (adhesive film: red, PET: green). b) XZ plot of the sample. The red channel of the RGB plot represents the spectral intensity at 2860cm^{-1} (adhesive film) and the green at 1595cm^{-1} (PET) from MCARS hyperspectral data.

When a compound is known in advance, it is advantageous to excite several of its Raman bands to image it specifically. It is evident when considering the acquisition of the intensity at each band position on separated channels but it is also true when the signal is integrated regardless of the emission wavelength. In a sample with multiple constituents, the spectral background added to the spectrum of interest may vary across the sample. Considering several specific bands will then balance the spatial variations and increase contrast. In the following example, the benefits of multiple-band excitation for contrast are shown in an homogenous sample.

A well characterized sample is obtained by sticking an adhesive film on top of a PET sample. The adhesive film consists of two polymers, both having a very different signature from PET (Figure 3.13 a). Adhesive film has a stronger signal in the CH-stretching region and PET dominates in the fingerprint region, with a complex set of bands. A XZ-plot (Figure 3.13 b) easily shows the obtained layer structure: two polymers from the adhesive film in red and then PET in green. The color plot is obtained by taking the signal evolution at a chosen spectral position from a first dataset obtained using complete transmission through the shaper combined with spectrally resolved detection. Based on spectrally resolved data, four masks were designed for specific single-channel imaging of PET and are shown in Figure 3.14. M1 and M2 correspond to single band excitations centered at the most intense bands of PET at 1710cm^{-1} and 1595cm^{-1}, respectively. Multiband imaging is realized with M3, combining M1 and M2, and with M4, where a large part of the fingerprint region is excited from 1200cm^{-1} to 1800cm^{-1}.

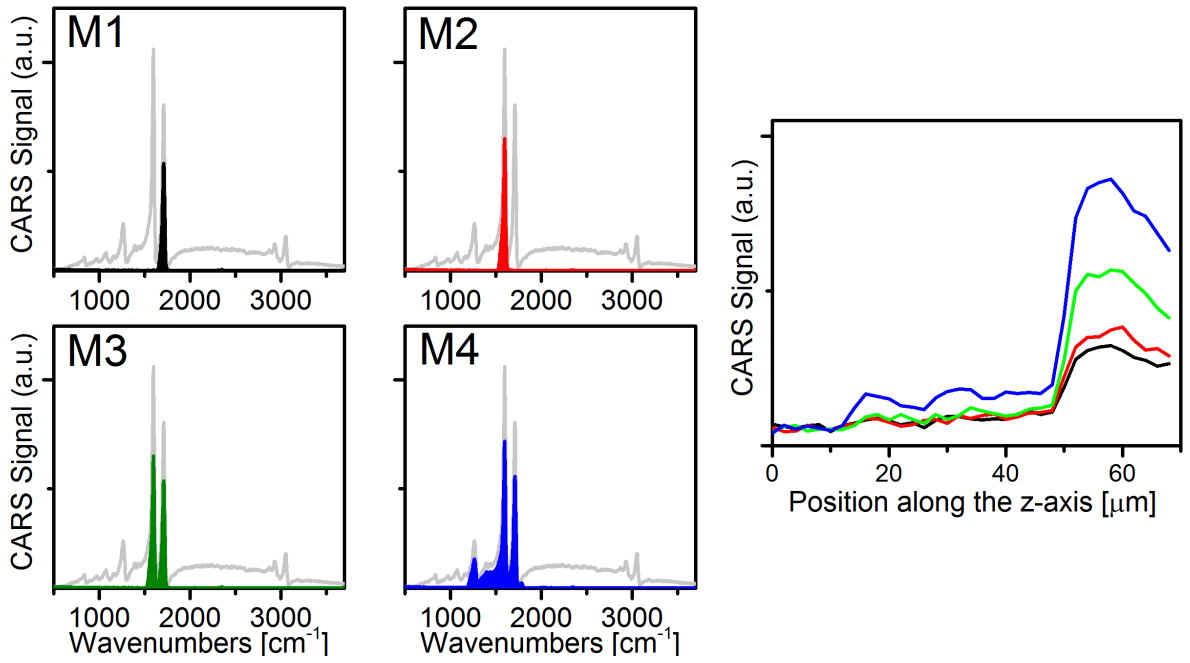

Figure 3.14 Contrast improvement with multiple-band excitation. A profile along the z direction is acquired by integrating the SAM-CARS signal obtained with four masks. M1: narrowband excitation at 1710cm^{-1}, M2: narrowband excitation at 1595cm^{-1}, M3: M1+M2, M4: broadband excitation from 1200cm^{-1} to 1800cm^{-1}. Right: profiles obtained with M1 (black), M2 (red), M3 (green) and M4 (blue).

Profiles along the z-direction obtained by integrating the signal generated with each mask with a PMT are shown in Figure 3.14 (right). Both single-band approaches give similar contrast. A slight improvement is seen with the somewhat stronger band in M2. The signal obtained with M3 shows a clear increase as compared to the single-band masks inside PET and no visible increase of the baseline inside the adhesive film region. This is not the case with the broadband excitation of M4: the signal continues to rise inside PET but this time signal is also visible in the rest of the sample and the contrast is diminished.

This example shows that only a precise control of the excitation allows contrast improvement through multiple-band excitation. Hereby, SAM-CARS greatly simplifies the access to dual-pump CARS that previously necessitated the introducing of an additional conversion stage to produce the additional pulse[128]. This scheme is now transposable to any combination of relevant Raman levels without changes in the setup.

3.4 Current limitations and perspectives of further development

The demonstrated advantages of SAM-CARS can be implemented in any MCARS setup in combination with any shaper. In comparison to the presented experimental setup, the following parameters can be optimized:

- the speed of scanning and
- the relative intensity of the pump/probe and of the Stokes pulses.

The first limitation can be easily overcome with the use of commercially available rapid laser-scanning systems. The second improvement is however necessary to increase the signal intensity to a level compatible with high speed imaging. The two orders of magnitude difference in spectral density used in MCARS is far from ideal for a ps-CARS

implementation. Indeed, when only one Raman level is excited and the impulsive contribution is not relevant, a similar energy level in both the pump and the Stokes are desirable. More precisely, if the limiting parameter fixed by the photodamage threshold is proportional to the total energy ($I_{p/pr}+I_S$), theory predicts an ideal ratio of 2:1 (based on the fact that ICARS is proportional to $I_{p/pr}^2$ and to I_S). In our implementation, the transmission of the shaper lies below 40%, further decreasing the available power and, if a narrow band of the same width as the pump is selected with the SAM-CARS setup, the ratio between the energy of the Stokes and the energy of the pump/probe pulse will be above 100.

The limiting photodamage threshold depends on many parameters including the central laser wavelength, the effective pulse duration, the numerical aperture of the objective, the repetition rate of the laser and the scanning speed. In terms of intensities, values found in the literature for safe imaging of living cells are of the order of 10mW at the sample with picoseconds pulses [42] and around 3mW with 100-300fs pulse durations [41] (to our knowledge, no data has been published for pulses in the 10fs range). In practice, *in vivo* video-rate imaging has been demonstrated with as much as 50mW for each beam [35, 129]. Thresholds for material science applications or imaging of fixed tissue can be much higher. In our setup, the pump intensity at the sample is about 9mW and Stokes intensity 26mW (without shaper).

To optimize the SAM-CARS setup, an increase of the Stokes intensity of about one order of magnitude is necessary. Then, when a ps-CARS scheme is reproduced by shaping, a 10 fold improvement in CARS signal can be achieved for an increase of total energy of only 10%. In turn, when MCARS spectra are acquired, the shaper will have to be used to reduce the power. Experimentally, such an improvement of the Stokes energy is challenging. It cannot be achieved simply by increasing the pumping of the PCF because of the highly nonlinear processes involved in supercontinuum generation. A single laser implementation also limits the total energy of the excitation. In this work, the total energy of the narrowband pump/probe pulse and of the supercontinuum are comparable. To achieve the proposed ideal configuration, a dramatic increase of the original laser power is needed and could also be an obstacle. Alternatively, an additional sub-10fs oscillator, like the Fusion Pro used in the next chapter, could be synchronized with the narrowband laser. This is feasible, but comes at a high experimental-complexity cost.

Such an approach was for example realized in the demonstration of an approach similar to SAM-CARS but using Stimulated Raman Scattering (SRS) [130] that was published shortly after the work presented here [131]. For SRS, the possibility of single-channel detection is decisive because of the high frequency lock-in detection required to detect the signal. Encoding the molecular information on the excitation side is therefore the only way to simultaneously detect several Raman lines. (Recently, Multiplex SRS schemes have been proposed [132-134]. However, they rely on a rapid sequential measurement of signals for different Raman shifts.).

Further development of SAM-CARS can solve the difficulties linked to low Stokes energy by enhancing the signal level using heterodyning. As in other heterodyne setups, the interference with a local oscillator is expected to deliver stronger signals, with better sensitivity using lock-in detection and with linear dependence on the concentration. These features are

particularly suitable for the SAM-CARS setup: a local oscillator is easily derived from the supercontinuum generated in the PCF and covers a sufficient spectral range; the problem of the weakness of the signals after the shaper is then elegantly solved. In addition the phase correction of the line shape presented in 3.2.5 becomes possible, and the knowledge of the relative phase between signal and LO gives additional information about the position of the resonances.

In addition, single channel integration of the signal coupled with modulation of the narrowband pump/probe pulse at high rates would greatly increase the sensitivity of the method in the same way as in SRS setups. Compared to SRS, heterodyne SAM-CARS would have a few additional advantages by uncoupling the energy of the excitation and the heterodyne amplification. When detecting stimulated Raman loss, for example, the signal is proportional to the pump intensity but, at the same time, it has to be detected on top of it. It would be advantageous to be able to choose the intensity of the local oscillator without affecting the signal intensity: this can be realized in heterodyne SAM-CARS. Also, the relative phase of the signal and of the local oscillator can be controlled independently of signal generation.

4 Single-beam CARS

While amplitude shaping has been successfully demonstrated for SAM-CARS in the previous chapter, Single-Beam CARS is mainly based on phase shaping. To this end, a well-defined and intense broadband pulse obtained directly from a Ti:Sa oscillator is ideally suited for phase shaping. Experimentally, a single beam of shaped pulses (Figure 4.1) suffices by taking advantage of coherent control schemes for selective excitation of molecules and acquisition of spectra. This strategy advantageously avoids common sources of instability due to the recombination of beams with interferometric stability, the synchronization of lasers or nonlinear generation of additional wavelengths.

Although single-beam CARS (SB-CARS) has been demonstrated to be a flexible way to address many Raman transitions, important limitations prevented its application to efficient imaging of biological samples at the beginning of this thesis: the accessible spectral range was limited to the fingerprint region and the need for intense ultrashort pulses caused photodamage. For application in microscopy, the technique still lags behind setups with more straightforward interpretation of the acquired signals. The scope of this chapter is to present advantages and drawbacks of three possible approaches to single-beam CARS microscopy: time resolved, spectrally resolved and finally mode selective strategies.

4.1 Concept of Single-Beam CARS

The single-beam approach, also called single-pulse CARS, was pioneered by the Silberberg group (seminal works [45, 70, 135-139], then [92, 140-144]) and further developed in our [50, 113, 119, 145-151] and other groups [152-163]. Single-beam CARS has found application mainly in standoff detection of chemicals, spectroscopy of gases and in microscopy.

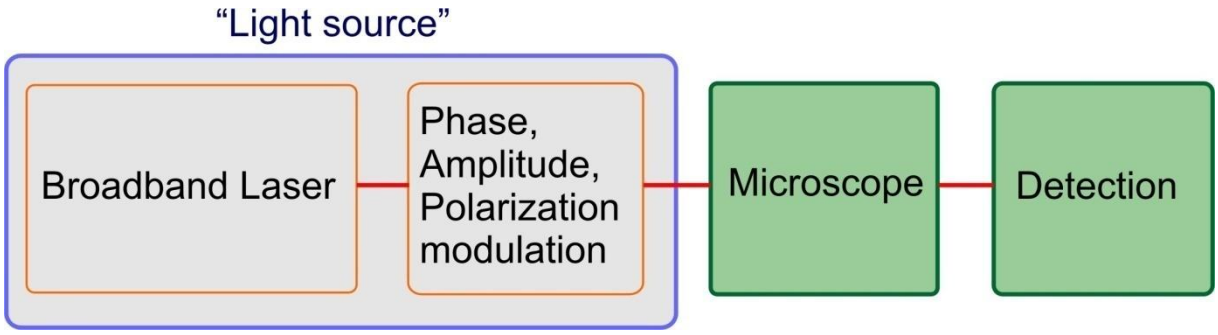

Figure 4.1 Generalized scheme of a single-beam CARS setup. A single broadband laser is combined with a pulse shaping method creating a flexible light source for nonlinear optical microscopy.

Before analyzing the specificities of each approach, the framework of single-beam CARS generation and the problem of analysis and extraction of vibrational data shall be presented. Like in ps-CARS and MCARS-setups, the single-beam CARS signal can be calculated with the general expression (see equations (14) and (15), section 2.2.6) reproduced here:

$$E_{CARS}(\omega) \propto \int E_{probe}(\omega-\Omega)\chi^{(3)}(\Omega)\int E^{*}_{Stokes}(\omega'-\Omega)E_{pump}(\omega')d\omega'\ d\Omega \qquad (40)$$

However, in single-beam CARS setups none of the pulses can be replaced by a dirac distribution to simplify the equation. Indeed, the single laser pulse is simultaneously pump,

Stokes and probe and has to have enough bandwidth to access different Raman shifts. Two challenging aspects result from this configuration (illustrated in Figure 4.2): a part of the generated signal overlaps with the exciting laser and the featureless signal contains a large non-resonant contribution.

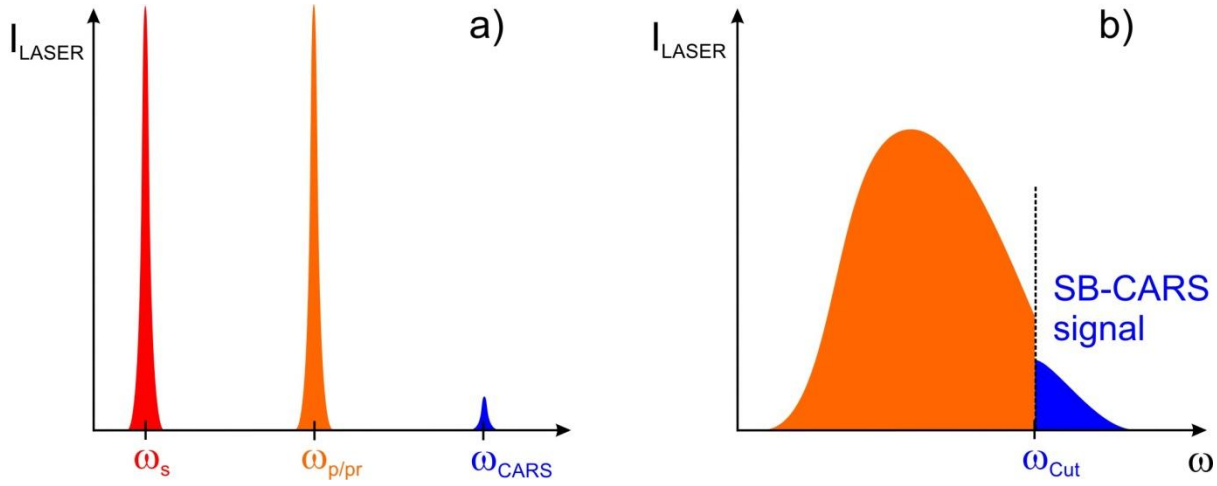

Figure 4.2 Schematic comparison between ps-CARS and the single-beam CARS scheme. a) In ps-CARS, the pump/probe and the Stokes pulses are narrowband. The CARS signal appears at a well defined spectral position: symmetrical to the Stokes frequency with respect to the pump frequency. b) Single-beam CARS uses a single, broadband pulse. The many photon combinations inside the pulse result in a broadband excitation. The CARS signal is strong and broad, but does not directly provide spectral information.

Figure 4.3 details the calculation of $A(\Omega)$. The Raman excitation probability is given by the coherent sum of all pump-Stokes pairs inside the broadband pulse as expressed by:

$$A(\Omega) = \int E^*(\omega' - \Omega)E(\omega')d\omega'. \tag{41}$$

The relative amplitude of the available contributions to the Raman level Ω_0 is given by $|E^*(\omega' - \Omega_0)E(\omega')|$ and is represented in the figure. For an FTL pulse, the integral of this function directly gives A(Ω) resulting in the characteristic shape of the autocorrelation of a Gaussian pulse. $A(\Omega)$ is maximized for $\Omega = 0$ and then decays until the edges of the pulse are reached: the maximal accessible Raman energy in a single-beam CARS setup is determined by the bandwidth of the laser. The picture in Figure 4.3 does not show the phase of the photon pairs participating to the excitation of Ω_0. It is given by $E^*(\omega' - \Omega_0)E(\omega')$ and its phase $\varphi^R_{\Omega_0}(\omega') = \varphi(\omega') - \varphi(\omega' - \Omega)$, φ being the spectral phase of the laser. In a similar way to the Brumer-Shapiro [67] coherent control mechanism, the outcome of integration over all photon pairs involved depends on the phase relationship between them. When the phase varies among photon pairs, they can add in the complex plane to a much smaller or even zero resultant than in the FTL case. This property is central to single-beam approaches and will be extensively used in the presented experiments.

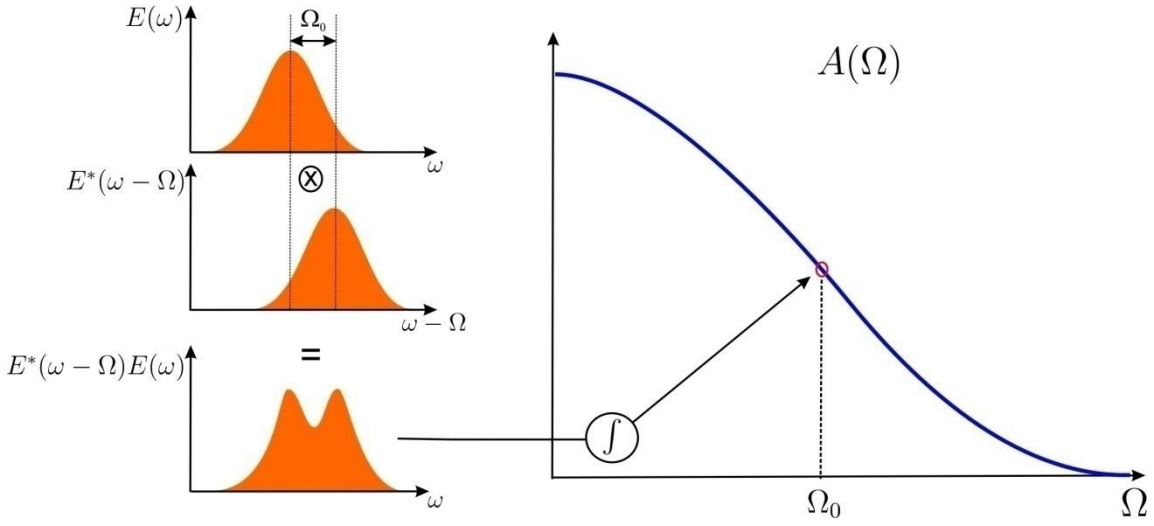

Figure 4.3 Raman excitation probability of single-beam CARS. The Raman excitation probability A(Ω) is given by the autocorrelation of the single pulse. For a given Raman shift Ω_0, A(Ω_0) is obtained as a sum over the photon pairs having the corresponding energy difference. (left) The relative contribution of all pump/Stokes pairs to the excitation of the level at Ω_0 is obtained multiplying E(ω) by E*(ω- Ω_0). (right) A(Ω) for a FTL pulse.

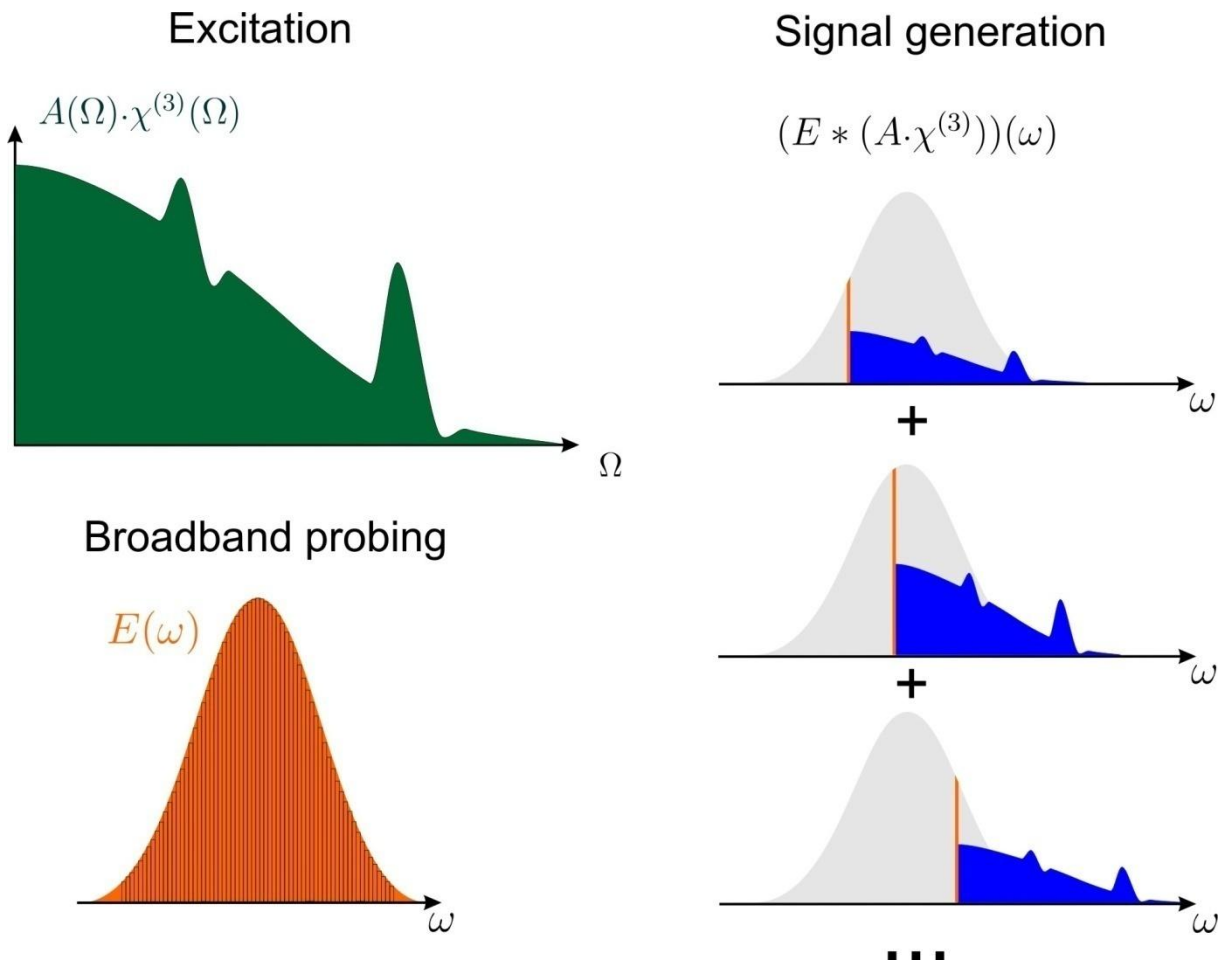

Figure 4.4 Signal generation in single-beam CARS The excited system consists of the molecular response $\chi^{(3)}(\Omega)$ weighted with the excitation probability A(Ω). The broadband probe can be seen as a sum of narrowband spectral components. Each narrowband probe creates a MCARS signal proportional to the excitation. The generated signal is the sum of all those MCARS contributions.

The Raman excitation probability is then multiplied with the actual response function of the molecule represented by $\chi^{(3)}$ (Figure 4.4). Once the molecule is excited, probing is a further control opportunity for the CARS signal. From equation (32) we see that the signal is the result of a convolution between the weighted molecular response and the probing pulse. In a more intuitive way, this is equivalent to dividing the pulse into spectral components and using each of them as a narrowband probe pulse, then adding the obtained CARS spectra as shown in the figure. Equivalent to MCARS (see previous chapter), probing with a narrowband pulse at ω_{pr} simply projects the function $A(\Omega) \cdot \chi^{(3)}(\Omega)$ on the blue side of ω_{pr}. As a result, the features of $\chi^{(3)}$ are washed out by summation of the spectra over the probe energies i.e. by the convolution between the broadband pulse and the molecular response. The broadband CARS signal largely overlaps with the exciting pulse. Detection of the SB-CARS signal therefore relies on the choice of a filter edge ω_{cut} as a compromise between lost laser energy and increased detectable CARS signal (see Figure 4.2).

4.2 Experimental Setup

After these theoretical considerations, our experimental implementation of the single-beam CARS scheme is briefly presented in the following. A more general description of pulse shaping has been done in chapter 2.4, a modified version of the setup with single-channel detection is described in the next chapter (section 5.3.1) about multimodal nonlinear optical microscopy.

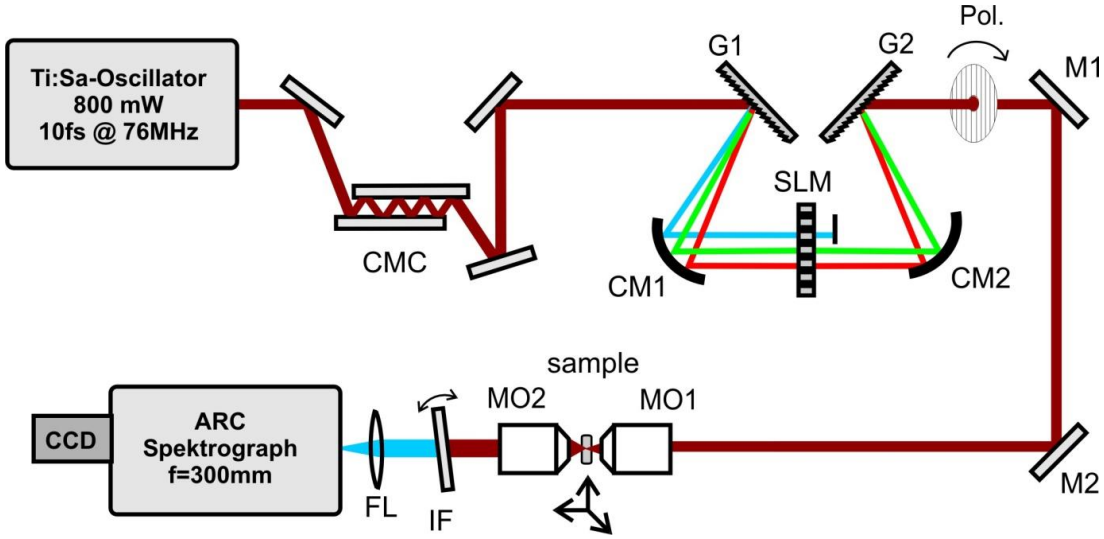

Figure 4.5 Single-Beam CARS setup. A commercial broadband Ti:Sa oscillator produces 10fs pulses. A chirped mirrors compressor (CMC) applies a negative chirp to compensate the dispersion of the microscope. The pulse shaper consists of a 4f-line (gratings G1,G2 and cylindrical mirrors CM1,2) with a spatial light modulator (SLM) in the Fourier plane. Shaped pulses are sent into a home built microscope, the samples being scanned by moving it with a piezo stage. The signal is detected with spectral resolution using a monochromator and an ICCD camera, after filtering out the laser light with an interference filter (IF).

4.2.1 Laser source and setup

The setup is shown in Figure 4.5. Shortly, it consists of a commercial high-power broadband Ti:Sa oscillator (Fusion Pro 800, Femtolasers) producing 10fs pulses in the NIR (center wavelength λ_0 =800nm). Before reaching the microscope, the pulses are pre-compressed using

a chirped-mirrors compressor (Layertec). The pulse shaper is designed according to section 2.4.6 with cylindrical mirrors (f=20cm, custom product, Hellma Optik). In the Fourier plane, a computer controlled 640-pixel double liquid crystal mask (Jenoptik, SLM 640d) controls spectral phase and polarization. The polarization is transformed in amplitude modulation by a broadband polarizer (Femtolasers) at the output of the shaper. The shaped pulse is then sent into a home built microscope with two Olympus microscope objectives: MO1 (60x, NA=0.7) focusing the light onto the sample and MO2 (40x, NA=0.6) collimating the CARS signal. Imaging is realized by moving the sample using a piezo stage (PI 611.3 Physikinstrumente, scanning range 100µmx100µmx100µm, precision <1nm). Before reaching the intensified charge coupled detector (ICCD, Andor Technology), the CARS signal is separated from laser light using a short-pass interference filter (Semrock, λ<670nm). A f=300mm lens focuses the signal into a monochromator (Acton Research, 300i) for spectrally resolved detection.

The use of pulses directly from a short-pulse oscillator is advantageous in comparison to schemes using nonlinear spectral broadening because it provides smoother and more stable spectra. As laser technology improves, more robust and powerful laser sources with comparable bandwidths are expected to be available in the future..

4.2.2 Pulse characterization

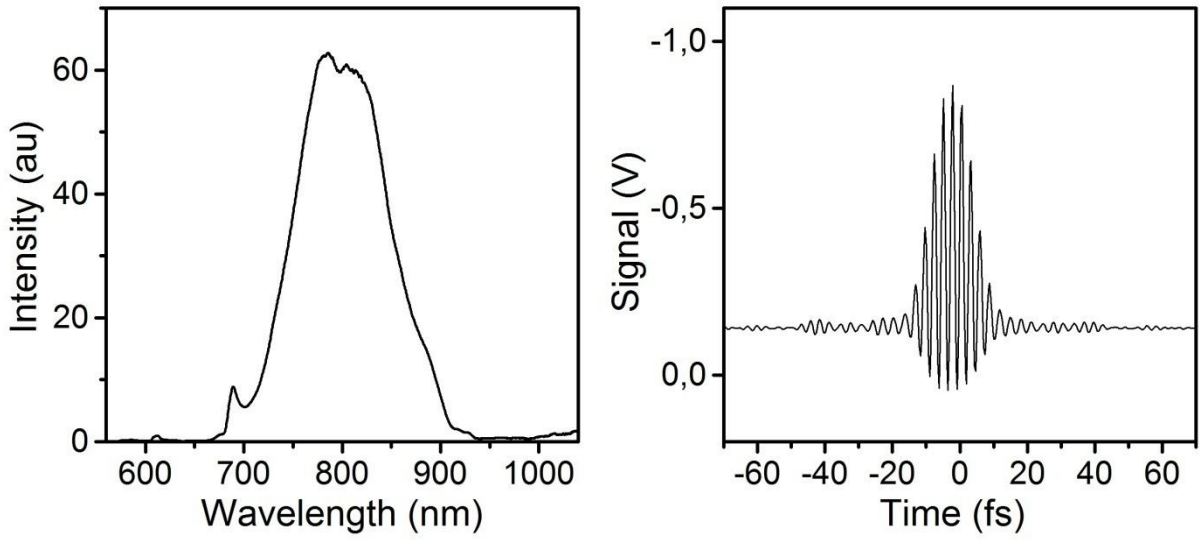

Figure 4.6 Laser spectrum and autocorrelation. Left panel: spectrum of the laser. Right panel: Interferometric autocorrelation measured at the output of the laser.

The laser provides 800 mW power at 76 MHz, which represents a pulse energy of 10.5 nJ. The spectrum is shown in Figure 4.6; it has a FWHM of 100 nm and covers a region from 685 nm (14600 cm^{-1}) to 905 nm (11050 cm^{-1}). The pulse is characterized at the output of the laser using a commercial autocorrelator (Femtometer, Femtolasers).

Interferometric autocorrelation (IAC) is a simple and efficient way to measure ultrashort pulses [164]. It is a more accurate method than intensity autocorrelation, because the self calibrating counting of fringes (knowing the center frequency) provides a better assessment of the pulse length. Due to phase matching considerations, very thin crystals have to be used for signal generation. For 10 fs pulses the maximum length of the BBO crystal is 60 µm well

above the crystal thickness in the commercial autocorrelator (<25 µm). Deleterious effects due to beam splitter coating have been taken into account in the device[165].

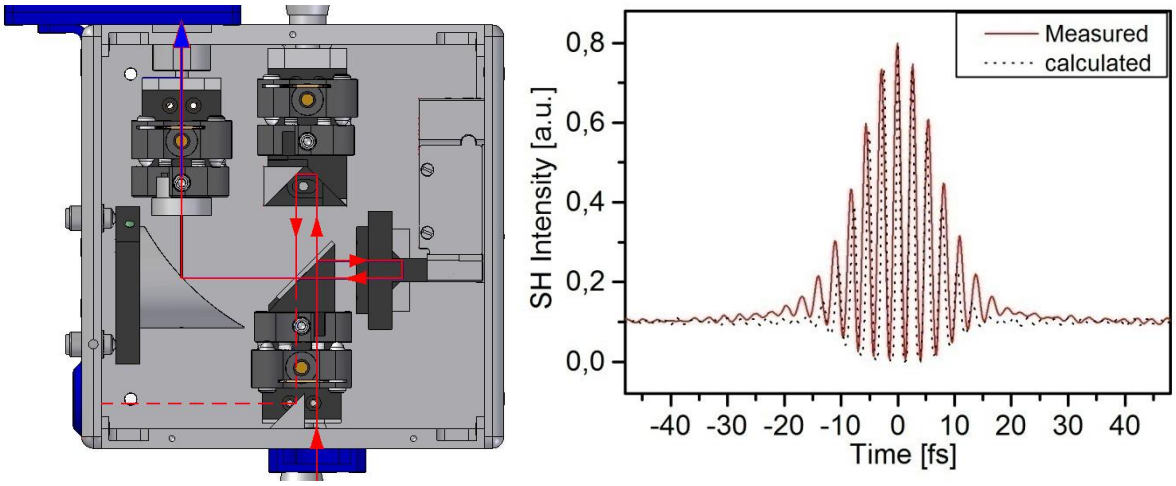

Figure 4.7 Interferometric autocorrelation. Left: Setup of the autocorrelator (Femtometer, Femtolasers). Right: Comparison of a measured autocorrelation trace (red) and a simulation based on the laser spectrum (dotted black).

The SHG signal is generated by interfering pulses and, for a delay τ, the SHG field in the time domain is given by:

$$E_{SHG,\tau}(\mathrm{t}) \propto (E(t) + E(t-\tau))^2 \tag{42}$$

The SHG intensity is integrated by the detector and we obtain:

$$S(\tau) \propto \int_{-\infty}^{+\infty} \left|E_{SHG,\tau}(\mathrm{t})\right|^2 dt \tag{43}$$

Based on this equation, it can be shown that a peak to baseline ratio of 8:1 is expected. It means that if the difference between the interference minima and the incoherent addition of SHG signals is set to 1, the difference between interference maxima and minima should be 8. Assuming this ratio, the fringes are automatically counted and the pulse duration is assessed assuming a fixed deconvolution factor (1,55 for a sech^2 shape). Typically, 9 to 10fs are obtained with this method. Since the spectrum is not a perfect sech^2 function, a more accurate method to determine whether the pulse is transform limited is to calculate the theoretical IAC trace based directly on the measured spectrum. After the simplifications described in [166], the calculated IAC trace shown in Figure 4.7 is in good agreement with the measured trace.

The correction of phase distortions introduced by high-NA microscope objectives to obtain short pulses at the focal point is an important challenge for broadband CARS microscopy. In this respect, the compression of 10fs pulses down to their FTL duration lies close to the limit of what is achievable experimentally [167]. One the one hand, GDD correction is not sufficient for broadband pulses, where TOD and higher-order dispersion play an increasing role. On the other hand, the chromaticity of the objectives can prevent the perfect overlap of all spectral components necessary to obtain FTL duration.

A common approach to correct the phase distortion introduced by the objectives is the use of variants [168-169] of usual phase characterizations methods like Frequency Resolved Optical Gating (FROG) [170] and Spectral Phase Interferometry for Direct Electric-field Reconstruction (SPIDER)[171]. The flexibility offered by a single-beam setup equipped with

a shaper allows a notable simplification of the characterization scheme [172-173]. A widely used example is the Multiphoton Intrapulse Interference Phase Scan (MIIPS) [174] where a spectrally resolved trace is recorded upon scanning of a known phase function over the spectrum of the laser (for example a sinusoidal function or a parabolic one).

To avoid the complexity of these methods and the use of SHG signals, a simpler strategy was adopted in our setup. Instead of characterizing the phase of the pulse in focus, the CARS signal was optimized. An evolutionary algorithm [175-176] was used to compress the pulse[177]. Since the output of an oscillator was directly used without nonlinear broadening, only pulse distortions induced by the optics have to be compensated. Hence the phase function assumes a smooth shape and can be described mainly with a GDD and a TOD part. However, to account for higher order dispersion also, a b-spline parameterization with 24 points was chosen [94], limiting the search space. This method has two advantages for our application. First, the signal is optimized directly in the same configuration as for the subsequent imaging: in the sample when neat liquids where studied and in the microscope slide for imaging. This way, no additional spectrometer or thin BBO crystal were needed. A second advantage of this approach is the sensitivity of CARS to phase distortions. As a three-photon effect, CARS is more affected by small variations with respect to the FTL case than SHG ([178], see also simulations in section 5.2.1). Usual *in situ* pulse characterization strategies based on SHG present higher uncertainties in the wings of the spectrum, due to the spectral narrowing related to the two-photon mechanism. Although CARS presents a higher nonlinearity, the narrowing does not affect the single-beam CARS signal. On the contrary, it is particularly sensitive to the phase of the blue wing, which plays an important role in the probing mechanism (see Figure 4.4).

With the broad bandwidth of the pulse, the compensation of the GDD introduced by the microscope objectives becomes more difficult. On the wings of the spectrum, a very high slope has to be applied to obtain an FTL pulse in focus. A high slope requires many phase wrappings in the shaper which produces unwanted effects and affects the intensity. Also, the dynamic range used to compensate phase distortions is not available for further shaping schemes needed for spectroscopy or microscopy. To avoid these effects, passive optical elements can be used to pre-correct the GDD. In our setup, a set of broadband chirped mirrors introduces $-40fs^2$ per bounce. 24 bounces result in a total compensation of $-960fs^2$, keeping the remaining phase corrections in an acceptable range. An additional correction is possible by detuning the position of the second grating in the shaper. This option however can produce unwanted distortion in the spatial profile of the pulse.

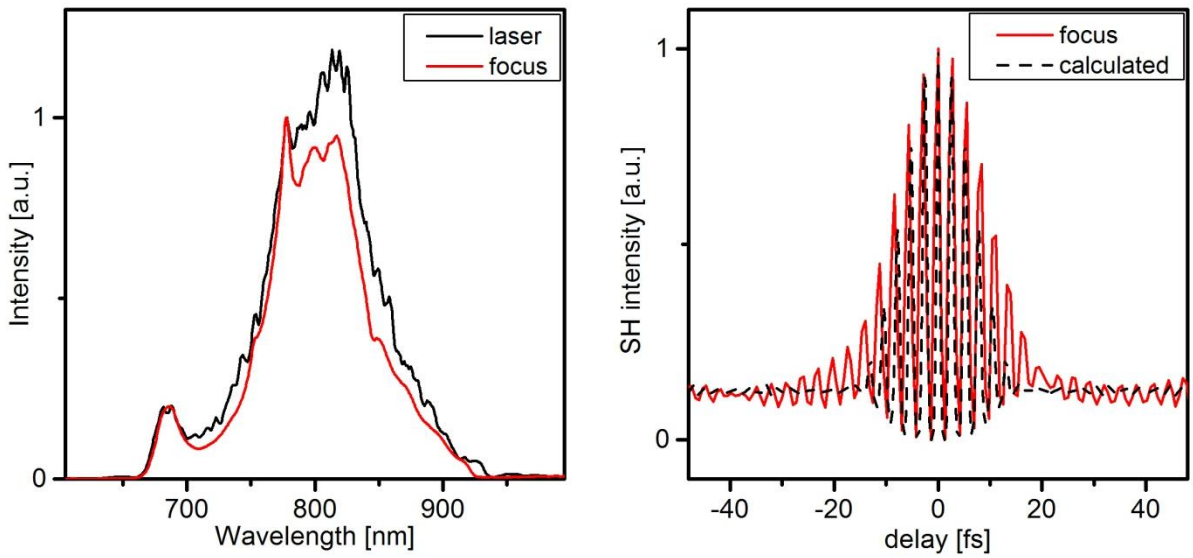

Figure 4.8 Pulse compression in focus. Left: spectrum measured at the laser output (black) and in the microscope focus (red). Right: FRIAC measured in focus (red) and calculated using the spectrum in focus (black, dotted).

The result of pulse compression in the focus is shown in Figure 4.8. The spectrum measured in the microscope seems slightly narrower than the spectrum at the output of the laser but only a very small region is lost around 920nm, mainly because of the transmission in the shaper. The autocorrelation *in situ* was measured with a detector head composed of a thin BBO crystal, an SHG filter and a PMT. Even after correction with the shaper, the measured autocrorrelation does not match perfectly the simulated IAC (duration calculated by counting the fringes: 11,0fs). Along with slight misalignment of the shaper causing distortion of the beam profile and imperfect phase correction, this can also be an inherent effect of the measurement technique. With high peak powers, depletion of the pulse due to $\chi^{(3)}$ effects reduces the measured intensity at the maxima of the IAC therefore producing a seemingly longer trace[179]. Eventually, significant phase distortions can be ruled out considering the results obtained for spectroscopy.

4.3 Single-Beam CARS spectroscopy

A single-beam CARS signal obtained with an FTL pulse is intense yet featureless; it contains contributions from all excited Raman transitions but also a very strong nonresonant contribution. The challenge of SB-CARS spectroscopy is to extract spectral information from the signal using shaping. In the following, time-resolved and spectrally resolved methods are applied to acquire broadband spectra using 10fs pulses. The bandwidth available in our setup allows reaching the important 3000cm^{-1} region. Spectral resolution and suitability for imaging are discussed for each method.

4.3.1 Reaching the 3000cm^{-1} range

In the case of chemical mapping, the C-H vibrational region (around 3000 cm^{-1}) is of particular interest. Most demonstrations of CARS imaging relied on this large band to identify polymers or to image cells [180], so that CARS is sometimes referred to as a technique for specific imaging of fat. Fatty acids indeed provide an ideal basis for CARS imaging. The huge concentration of C-H bonds in fatty acids is favourable for CARS because the signal is proportional to the concentration squared. The level of specificity of the band (signal

identified as “fat” in general) is adapted to the amount of information available from picoseconds CARS measurements (a single Raman region).

By carefully analyzing bands in the region around 3000cm^{-1} much more precise chemical assessment is possible. Differences between the CH_2 and CH_3 modes allow distinction between lipids and proteins [181] while saturated or unsaturated lipids can be selectively imaged by the resolution of –C-H and =C-H levels [182]. However, single-beam setups have been unable to reach this region until recently because of the broad bandwidth needed. Figure 4.9 illustrates the regions of the Raman spectrum reachable in a single-beam setup depending on the FTL-length of the pulse. 100fs pulses give access to low wavenumber modes, which are difficult to access with usual CARS methods[147]. To cover the whole fingerprint region, pulses as short as 22fs are needed. This region contains the most specific information and is extensively used in spontaneous Raman and the focus of most of SB-CARS experiments. Nonetheless, it is often a congested region: excellent spectral resolution is necessary and interpretation of spectra is not straightforward. The Raman excitation probability calculated for the spectrum at the output of our laser is overlaid with the Raman spectrum and shows that Raman shifts greater than 3000cm^{-1} are accessible.

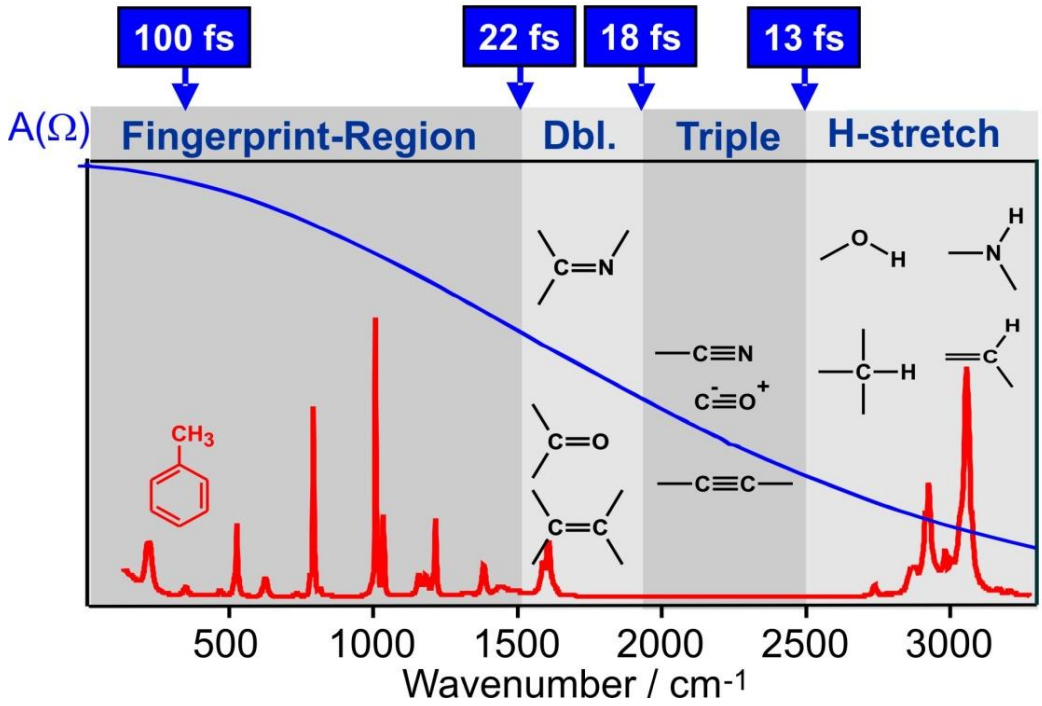

Figure 4.9 Assignment of spectral regions in Raman spectra. A(Ω) calculated on the basis of the spectrum of the 10fs pulses used in the setup is overlaid with the Raman spectrum of toluene (from: Sigma Aldrich database). On the top, the vibration period corresponding to the Raman shift is shown.

4.3.2 Time-resolved techniques

The full control of the temporal profile allowed by the shaper has enabled reproducing and going beyond time-resolved CARS schemes based on interferometers (presented in section 2.2.7). The single-beam, shaper-assisted approach has been implemented in several variants, using multipulse trains[137, 183], double pulses [146] as well as polarization resolved [50] and heterodyne[149-151] schemes. In the following, the use of multipulses to obtain spectral

information is discussed in more detail as obtained in our setup. Its experimental realization is easier than for the conceptually simple double-pulse concept.

To produce a sequence of pulses, a sinusoidal phase $\varphi(\omega)$ is applied with the shaper [176]:

$$\varphi(\omega) = a \cdot \sin(b\omega + c) \tag{44}$$

This results in a sequence of pulses with a constant spacing in time, as illustrated in Figure 4.10. This spacing is directly related to b. For example, if ω is given in THz, b is the delay between two subpulses expressed in ps. The parameter a determines the depth of the phase modulation and influences the energy distribution across the subpulses as well as their number. In the example in Figure 4.10, an ideal value of a=1,22 has been used. When a smaller value of a is used, the central peak at 0-delay is increased and the side pulses reduced. Lastly, the constant c does not change the envelope of the multipulse but the phase relation between the subpulses.

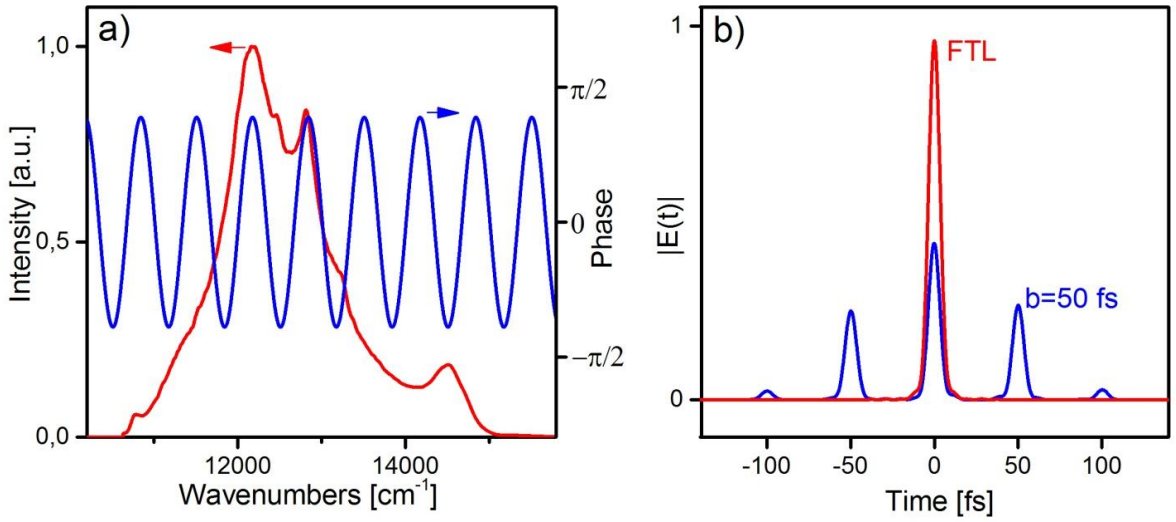

Figure 4.10 Multipulse excitation scheme. a) A sinusoidal spectral phase (blue) is applied to the broadband laser spectrum (red). b) In the time domain, this corresponds to a splitting of the original pulse (red) into a series of subpulses, each as short as the FTL pulse and separated by a constant time delay.

To retrieve the spectral information, the time delay b between the subpulses is scanned. When the interpulse delay matches the period of a vibrational resonance of the molecule, the signal is maximized giving rise to an oscillatory pattern consisting of all the Raman levels accessible within the bandwidth of the laser. The period T of an oscillation due to a Raman level is linked to its energy by:

$$T = \frac{1}{c \cdot \tilde{\nu}}, \tag{45}$$

where c is the velocity of light in vacuum and $\tilde{\nu}$ the Raman shift (in cm^{-1}). For example, a band at 3000cm^{-1} oscillates with a period of T=11,1fs.

In the spectral domain, the multipulse method can be seen as a shaping strategy based on the control of A(Ω) (stage 1 in Figure 4.3). This is illustrated by the results of a simulation shown in Figure 4.11. For a particular Raman shift Ω_0, the contributions of all photon pairs with the right energy differences are summed as complex numbers to calculate A(Ω) (see equation (41)). The result is maximized when $\varphi(\omega + \Omega_0) - \varphi(\omega) = const$, i.e. when the phase of all

pairs is constant. With the sinusoidal phase, this is the case every time $b = \frac{2\pi}{\Omega_0}$. For all other Raman shifts, A(Ω) is reduced with respect to the FTL pulse. For an appropriate choice of a, A(Ω) reaches zero exactly one time between two maximas (a =1.22, as in Figure 4.11 a). The resulting fringe structure of A(Ω) moves as the parameter b is scanned. In the simulation, we chose $\chi^{(3)}$ on the basis of acetonitrile. $\chi^{(3)}$ was calculated as a sum of a contant nonresonant background and of three lorentzian functions:

$$\chi^{(3)}(\Omega) = \chi_{NR}^{(3)} + \sum_i \frac{A_i}{\omega_i - \Omega + i\Gamma_i}, \qquad (46)$$

For acetonitrile, we take $\chi_{NR}^{(3)} = 15$, a first band at ω_1=918cm^{-1} with A_1=500 and Γ_1=10, second band at ω_2=2249cm^{-1} with A_2=1000 and Γ_2=7 and a third band at ω_3=2942cm^{-1} with A_3=2000 and Γ_3=15. As can be seen from Figure 4.11 (a), the calculation of A(Ω) also explains the oscillations of the signal. For b=90fs (blue) the excitation overlaps with the 2249cm^{-1} and with the 2942cm^{-1} vibrational modes almost to the level of FTL pulses whereas the resonant signal coincides with the minima of A(Ω) for b=96fs (gray). The sinusoidal phase has also an influence on the generated CARS spectrum, but not on its integral. Figure 4.11 (b) shows the interference features present in the signal for nonresonant (gray) as well as for resonant (blue) excitation. Spacing between the peaks in the pattern depends on b and the parameter c causes a shift (compare the black and blue curves). This shift has to be compensated when the spectral integration window is narrow but cancels out when a lot of fringes are integrated as it is the case here.

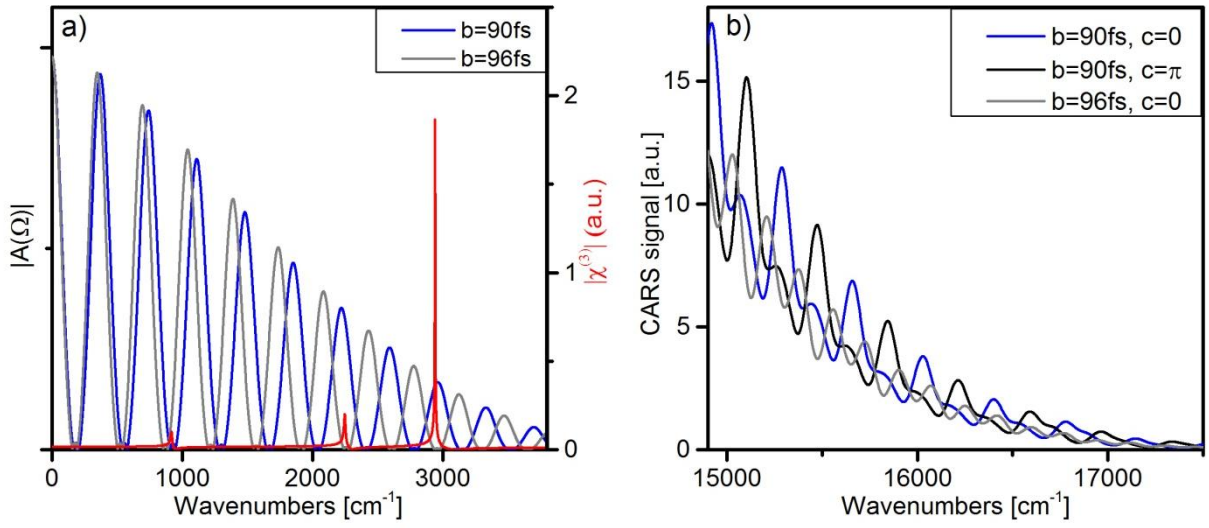

Figure 4.11 Effect of a sinusoidal phase on A(Ω) and on the recorded CARS spectrum. a) |A(Ω)| obtained for b=90fs (blue) and b=96fs (gray) overlayed with the simulated molecular response of acetonitrile $|\chi^{(3)}|$ (red). The Raman modes at 2249cm^{-1} and 2942cm^{-1} are excited when b=90fs and extinguished for b=96fs. b) generated CARS signal recorded on the blue side of the excitation spectrum. An interference pattern is produced in the CARS spectrum by the interplay of the phase of A(Ω) and of the pulse (acting as a probe). Contrary to |A(Ω)|, this feature is sensitive to the parameter c.

The evolution of the integrated CARS signal with increasing b parameter is shown in Figure 4.12, in the left panel. A transient calculated using equation (40) and the parameters previously described for $\chi^{(3)}$ shows excellent agreement with the measurement realized in acetonitrile. Both transients are normalized by their maximum value and no other fitting has been done. At early times (<10fs), a "coherent spike" corresponds to the much larger signal

produced by an FTL pulse. Until about b=50fs, the measured data show a slower decay than the simulated one probably due to remaining phase distortions after pulse compression. Starting from b=50fs, the expected oscillations are clearly visible with a good recognizable beating pattern between two main modes of acetonitrile at 2249cm^{-1} and at 2942cm^{-1}, with oscillation periods of 14,8fs and 11,3fs respectively. A closer look at the data (insert in Figure 4.12, highlighting the region from 215fs to 320fs) shows that the beating has a period of about 48fs, which corresponds to the difference frequency between the two main lines. The oscillations occur over a background of 12% of the initial maximum. It corresponds to the nonresonant signal obtained from the individual sub-pulses of the multipulse and is also present in the spectrally resolved signal (Figure 4.11 b). The dephasing of the vibrations is not expected to affect this offset, but rather to damp the oscillation. Surprisingly, the simulated data seem to present a quicker damping than in the measured transient. This can be due to an overestimation of Γ_i in the expression used for the nonlinear susceptibility. However, limited length of transients acquirable with the shaper does not allow a precise measurement of dephasing: in molecular liquids T_2 is of the order of several picoseconds. Additionally, phase wrappings for high frequency sinusoidal phases can decrease the intensity of the oscillations artificially.

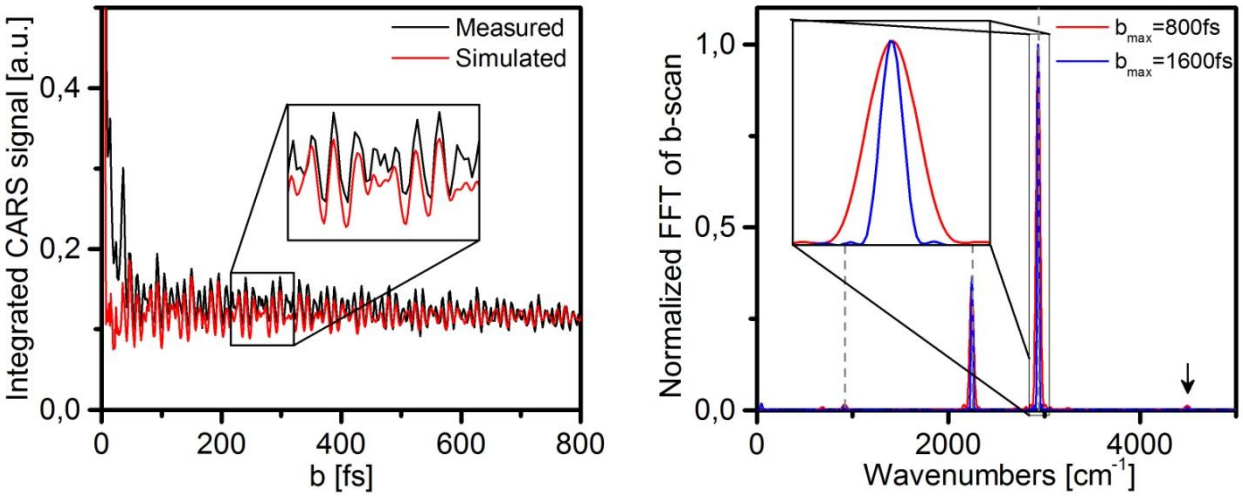

Figure 4.12 Obtaining spectra from b-scans. Left: Normalized integrated CARS signal as a function of b. A transient measured in acetonitrile (black) is compared with data simulated using $\chi^{(3)}$ as described above (red). Right: spectra obtained by Fourier transform of the transient from b=50fs to b=800fs (red) and from b=50fs to b=1600fs(blue). The dotted lines mark the position of Raman modes of acetonitrile known from literature.

The position of the Raman lines, in turn, can be determined with exactitude. The advantage of the time-resolved approach is that the nonresonant background responsible for the distortion of spectral lines can be completely and easily removed. Indeed, the separation of the FTL pulse in subpulses of smaller intensity strongly reduces the nonresonant contribution. The remaining background is almost constant when varying b and can be subtracted prior to Fourier transformation. The obtained spectra are shown in the right panel of Figure 4.12 and match perfectly the literature values. The small peak observed at the position of the arrow, almost as intense as the real band at 918cm^{-1} is due to an artifact characteristic of a multipulse experiment. For a given time delay, the subpulses also probe the double (threefold, etc.) time delay resulting in bands appearing at the double (triple, etc.) Raman shift. Knowing the

bandwidth of the pulse, the marked artifact can be excluded. Like in other Fourier transform methods, the spectral resolution is limited by the length of the transient (as seen from Figure 4.12). A spectrum obtained from a 1600fs long transient (blue) has a resolution about two times better than for an 800fs long transient (red). The maximal b attainable with the shaper is limited due to the finite number of pixels. In our setup, a little less than 4000cm^{-1} bandwidth are distributed over 640 pixels. The Nyquist sampling theorem states that a sinusoidal phase will be correctly reproduced with more than 2 pixels per period. This corresponds to

$$b_{max} < \frac{\pi}{2\pi c \cdot \Delta\tilde{\nu}_{pix}} \tag{47}$$

With c the velocitiy of light and $\Delta\tilde{\nu}_{pix}$ the wavenumber difference between two adjacent pixels. If we take simply the mean over all pixels, the result is $b_{max} = 2{,}9$ ps. Experimentally, artifacts due to undersampling are already observed starting at 1860fs, closer to 3 pixels per period. However, $\Delta\tilde{\nu}_{pix}$ is not constant across the shaper (while $\Delta\lambda_{pix}$ is). The maximal wavenumber difference is found on the blue side of the spectrum to be about 9cm^{-1}, which matches the observed maximal b obtained experimentally.

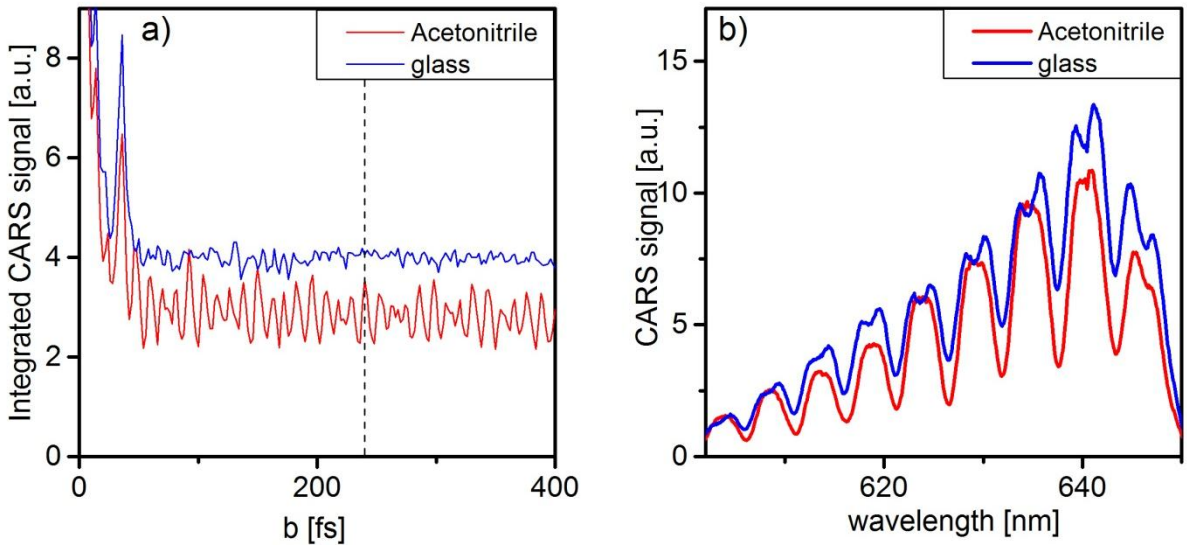

Figure 4.13 Applicability of the multipulse scheme to imaging. a) Transient for acetonitrile (red) and glass (blue). b) CARS spectra acquired with a sinusoidal phase of parameter b=240fs (position marked by a dotted line in a)) for acetonitrile (red) and glass (blue).

Although the multipulse method provides very good spectra and solves the problem of distortions caused by the nonresonant background it is poorly adapted for imaging, in particular for biological samples. The acquisition of whole transients [51] is much too slow. In turn, limiting the observation to a single b parameter is not satisfactory, as illustrated in Figure 4.13. It shows a comparison between a transient acquired in acetonitrile and in glass (coverslip). The transients show a clear difference with regular and large oscillations in acetonitrile and small and noisy features in glass. However, even for a pulse sequence resonant with the molecular vibrations (b=240fs), the spectra do not show much differences as seen in Figure 4.13 (b). Even more critical for a single-channel implementation, the signal is bigger in glass than in the sample due to high nonresonant contribution. Finally, the method is

either slow or needs prior knowledge of the chemicals in the sample. Therefore, microscopy based on multipulses has been applied only on polymer beads or neat liquids.

4.3.3 Spectrally resolved techniques

Most of more recent applications of single-beam CARS have used spectrally resolved techniques [113, 119, 140, 160-162, 184]. They are all based on a common general principle: introducing a sharp feature in the excitation, that causes a modulation of the broad signal in presence of resonances. This includes schemes based on the use of phase, amplitude and polarization gates or a combination of them. The resonant features are then retrieved from the modulation pattern. In the following, strategies relying on phase and amplitude shaping only will be discussed. In our case the sharp feature is a phase- or amplitude-gate, i.e. the choice of a group of pixel with a constant phase or amplitude offset, the rest of the pulse remaining Fourier-transform limited. As shown in Figure 4.14, the CARS spectrum is fairly similar when a small portion of the spectrum is shifted by a phase of π or simply extinguished. Here the gate is 45cm^{-1} wide and centered at 740nm, which represents a little less than 1% of the pulse energy. The large and mainly nonresonant CARS signal from the rest of the pulse remains almost constant, but two peak-dip features appear due to the resonances of acetonitrile. The position of the peak-dip features is determined by the energy of the Raman levels and the position of the gate. For example, with a gate centered at 13513cm^{-1}, the 2249cm^{-1} -band appears at 15762cm^{-1} and the 2942cm^{-1}-band at 16455cm^{-1}. Conceptually, spectrally resolved CARS schemes can be seen as schemes based on the control of the probing (Figure 4.4). The advantage compared to the control of A(Ω) is that the ability of broadband pulses to excite simultaneously many Raman modes can be exploited to provide chemical information in single-shot experiments. Spectrally resolved schemes are therefore advantageous for the rapid identification of chemicals.

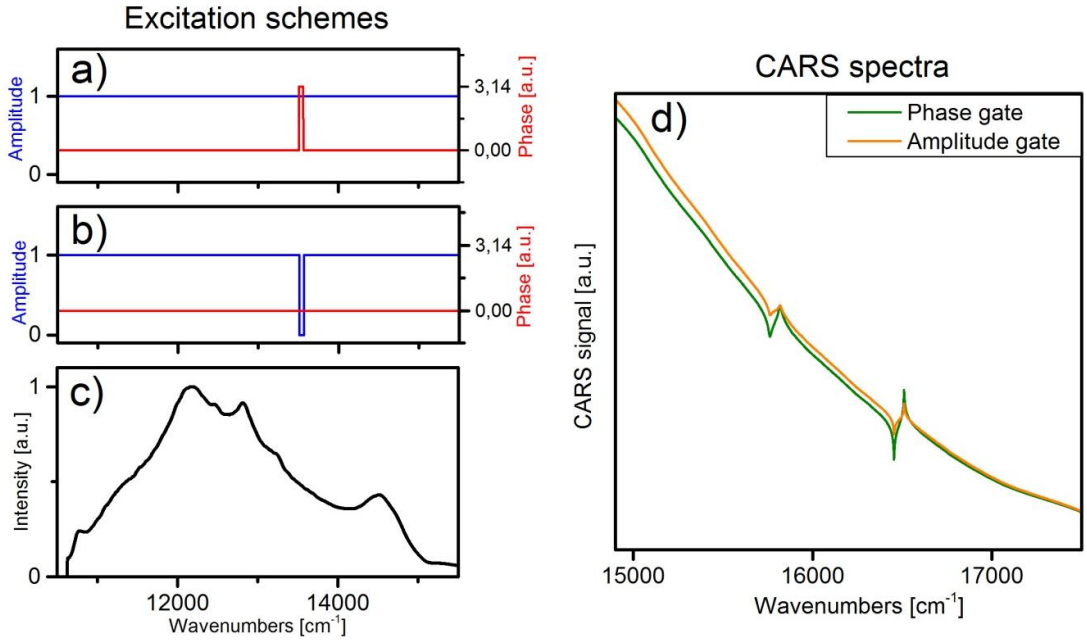

Figure 4.14 Excitation schemes for spectrally resolved single-beam CARS. The amplitude (red) and phase (blue) masks used to introduce a) a π-phase gate and b) an amplitude gate in the excitation spectrum (bottom row). Both gates are 45cm^{-1} wide centered at 740 nm (13513,5 cm^{-1}). c) Laser spectrum. d) Simulated CARS spectra for acetonitrile obtained for the scheme shown in a) (green) and in b) (orange).

We consider the approximation that A(Ω), as a convolution, is left almost unchanged by the introduction of a narrowband structure. To account for the effect of the narrowband phase gate, we can separate the probing in a broad part and a narrow part: $E_{probe} = E_B + E_n$. We obtain from equation (40):

$$E_{CARS}(\omega) \propto \int (E_n(\omega - \Omega) + E_B(\omega - \Omega))\chi^{(3)}(\Omega)A(\Omega)\ d\Omega \tag{48}$$

The CARS signal resulting from broadband probing will not differ significantly from the FTL case. The signal obtained with the narrowband probe in turn resembles the MCARS case (see chapter 3.1): if we note ω_n the probe energy and neglect the width of E_n, we have

$$E^n_{CARS}(\omega) \propto E_n(\omega_n)\chi^{(3)}(\omega - \omega_n)A(\omega - \omega_n) \tag{49}$$

Both contributions interfere and the detected signal is given by:

$$\begin{aligned} S(\omega) &\propto \left|E^B_{CARS}(\omega) + E^n_{CARS}(\omega)\right|^2 \\ &= \left|E^B_{CARS}(\omega)\right|^2 + |E^n_{CARS}(\omega)|^2 + 2|E^n_{CARS}(\omega)|\left|E^B_{CARS}(\omega)\right|\cos\varphi \end{aligned} \tag{50}$$

$|E^n_{CARS}(\omega)|^2$ can be neglected so that there remains a large slowly varying background and the interference term. Keeping in mind equation (49), the interference term gives access to the molecular response:

$$\begin{aligned} |S(\omega) - S_{FTL}(\omega)| &\propto \left|E^B_{CARS}(\omega)\right||E_p||A(\omega - \omega_p)||\chi^{(3)}(\omega - \omega_p)|\cos\varphi \\ \varphi &= \varphi_p + \varphi_\chi \end{aligned} \tag{51}$$

With $\phi_{p,\chi}$ being the phase chosen for the narrowband probe and the molecular phase, respectively. In this expression, two approximations are made: first, that the phase of A(Ω) is 0 (which is exact for $\phi_p=\pi$) and second, that $E^B_{CARS}(\omega)$ is a real quantity. This is usually valid for the liquids and biological samples used in this work, where $\chi^{(3)}_{NR}$ is not too small.

The extraction of molecular information from the interference pattern can be done in various ways depending on the level of control chosen in the experiment. Three possible schemes are shown in Figure 4.15 and detailed in the following.

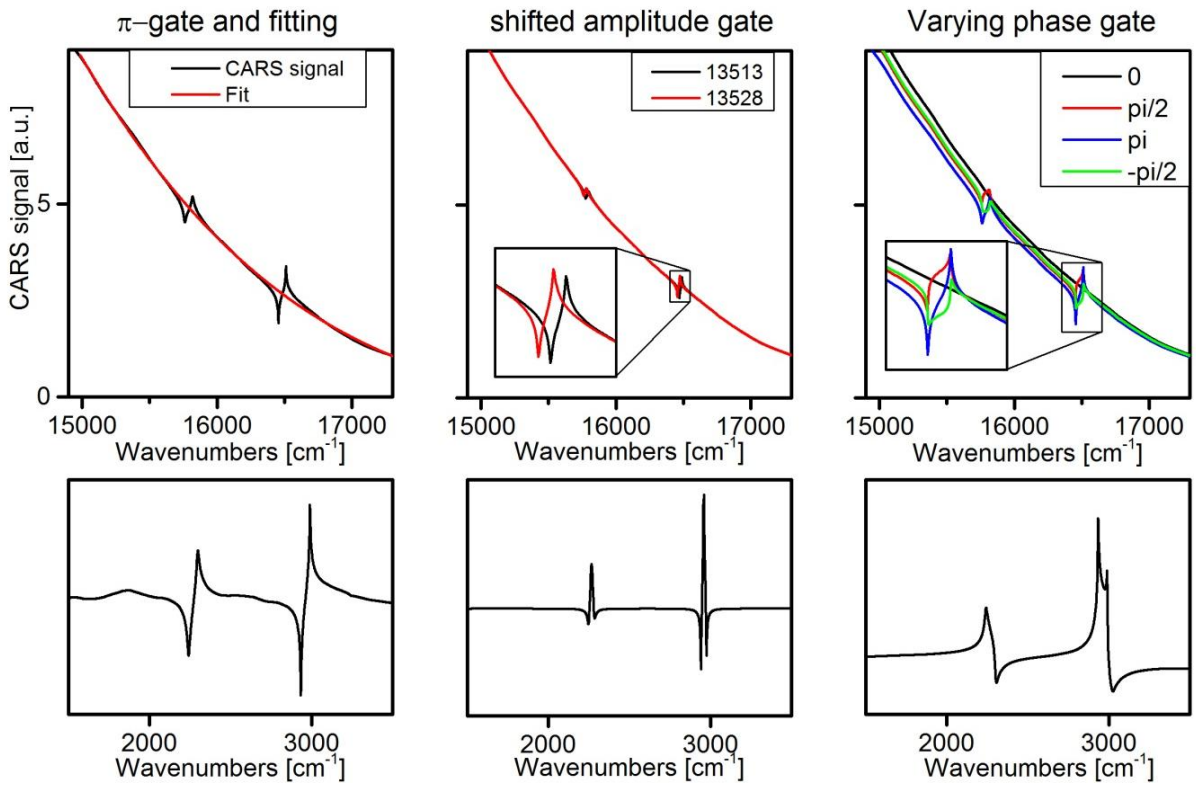

Figure 4.15 Extraction of molecular information from single-beam spectra. Simulated raw SB-CARS spectra (upper row) and extracted spectral lines after processing (lower row) for different spectrally resolved SB-CARS schemes. (left) Single measurement with a π-gate. The nonresonant background is fitted with a smooth function and removed. The retrieved spectral lines have the dispersive shape of the real part of the resonant Lorentz line. (center) Two measurements with slightly shifted π-gate position. Subtraction of the two measurements allows to locate the band positions precisely but also has negative values. (right) Four measurements with cycling of the phase of the gate. DQSI retrieves the MCARS spectrum as well as its phase.

π-gate

A first example, in the left panel of the figure, is the acquisition of a single spectrum with a π-phase-gate and fitting of the signal with a smooth function. Here, the simulated data are fitted with a 3rd-order polynomial. After subtraction, dispersive line shapes of the resonances appear clearly. This is not surprising, because the interference pattern created by a π-gate corresponds to the real part of the susceptibility. Indeed, if we use equations (50) and (51) the retrieved difference is proportional to:

$$\left|\chi^{(3)}(\omega-\omega_p)\right|\cos(\pi+\varphi_\chi) = -Re(\chi^{(3)}(\omega-\omega_p)) \qquad (52)$$

Further correction of the dependence on the background signal and on A(Ω) is required to obtain the intensity ratio of Raman lines. The advantage of such a simple method is that it requires only one measurement. Robustness against laser fluctuations and rapidity of acquisition are valuable for imaging applications. However, the spectroscopic accuracy can be limited to strong Raman lines in practice, because experimentally the background presents some features and noise which cannot be distinguished from resonant signal in this implementation. The conversion from the real part of $\chi^{(3)}$ to the imaginary part (which is measured in spontaneous Raman experiments) can be done, like for MCARS data, using Kramers-Kronig relations[120] or the maximum entropy method[121] (see section 3.1.3). Rapid analysis based on fast Fourier transforms has also been used for rapid single-beam CARS imaging[156].

Shifted amplitude gate

To get rid of unwanted influence of the system response, the shifting of an amplitude gate has been proposed (shown in the middle panel of Figure 4.15). To produce an amplitude gate, the shaper can be replaced by a notch filter. A resonant photonic crystal slab (RPCS) even allows a fast tuning of the gate position by rotation of the filter [140]. Mathematically, the introduction of an amplitude gate is very similar to a π-phase-gate. Indeed, if we consider for simplicity a punctual amplitude gate at ω_0, the shaped pulse E^0_{shaped} is related to the original pulse through $E^0_{shaped}(\omega) = E(\omega) - E(\omega_0)$. When a π-phase-gate is used, we have $E^\pi_{shaped}(\omega_0) = E(\omega_0)e^{i\pi} = -E(\omega_0)$ and the expression for the shaped pulse is given by $E^\pi_{shaped}(\omega) = E(\omega) - 2E(\omega_0)$. This explains the similarity of the spectra shown in Figure 4.14 as well as the two time bigger features observed in the case of a phase gate. By moving the gate, only the interference features created by resonances of the molecule are changed and parasitic peaks are removed when the weighted difference is calculated:

$$\Delta S(\omega) = \frac{S_1(\omega) - S_2(\omega)}{|E^B_{CARS}(\omega)|} \tag{53}$$

The background can be either fitted as previously on the raw data or measured in a sample without resonances, but has little influence on the recorded spectrum. The lineshape resulting from the difference presents also typical negative values, but the position of the bands is determined precisely. The relative intensity of Raman modes depends on their width and on the difference between the two probe positions.

Varying phase gate

A third option presented in the right panel of Figure 4.14 relies on the control of the phase of the probe pulse and can achieve full characterization of $\chi^{(3)}$ [119]. Based on equation (50), four measurements are enough to extract the amplitude and the phase of the $\cos(\phi)$ term. This method is known as Double Quadrature Spectral Interferometry (DQSI) [185] and relies on simple trigonometry. For example, by calculating the intensity of the interferometric modulation we obtain:

$$\left|\chi^{(3)}(\omega - \omega_p)\right| \propto \frac{\sqrt{\left[S_{\varphi_p=0}(\omega) - S_{\varphi_p=\pi}(\omega)\right]^2 + \left[S_{\varphi_p=\pi/2}(\omega) - S_{\varphi_p=-\pi/2}(\omega)\right]^2}}{\left|A(\omega - \omega_p)\right||E^B_{CARS}(\omega)|} \tag{54}$$

This corresponds to the information available in multiplex experiments (see chapter 3.1 and [113]). The multiplex spectrum for acetonitrile obtained using DQSI is shown in Figure 4.16. Along with the calculated MCARS-like spectrum (red), a spontaneous Raman measurement (blue) is displayed for comparison (Confocal Raman microscope: "alpha 300 R", Witec, λ_0=532nm). The lines in the retrieved spectrum are distorted with a shift towards smaller Raman shift, showing that the method provides both resonant and nonresonant contributions to $\chi^{(3)}$. With DQSI, the direct measurement of the phase and amplitude of the nonlinear susceptibility possible, which is valuable for simulations of CARS experiments and cannot be extracted from spontaneous Raman data[119]. Experimentally, the spectral range obtainable in a single measurement with DQSI is limited to a little more than 1000cm^{-1}. However, the position of this spectral window is tunable with the choice of the spectral position of the probe pulse, which allows covering the whole spectrum from 200cm^{-1} to over 3000cm^{-1}. The

spectral resolution of the method depends on the width of the probe. The shaper configuration used in Figure 4.16 contained gratings with 600grooves/mm. The gate at 730nm was two pixels wide corresponding to a 32cm^{-1} resolution and 1 pixel at 760nm for 15cm^{-1} resolution.

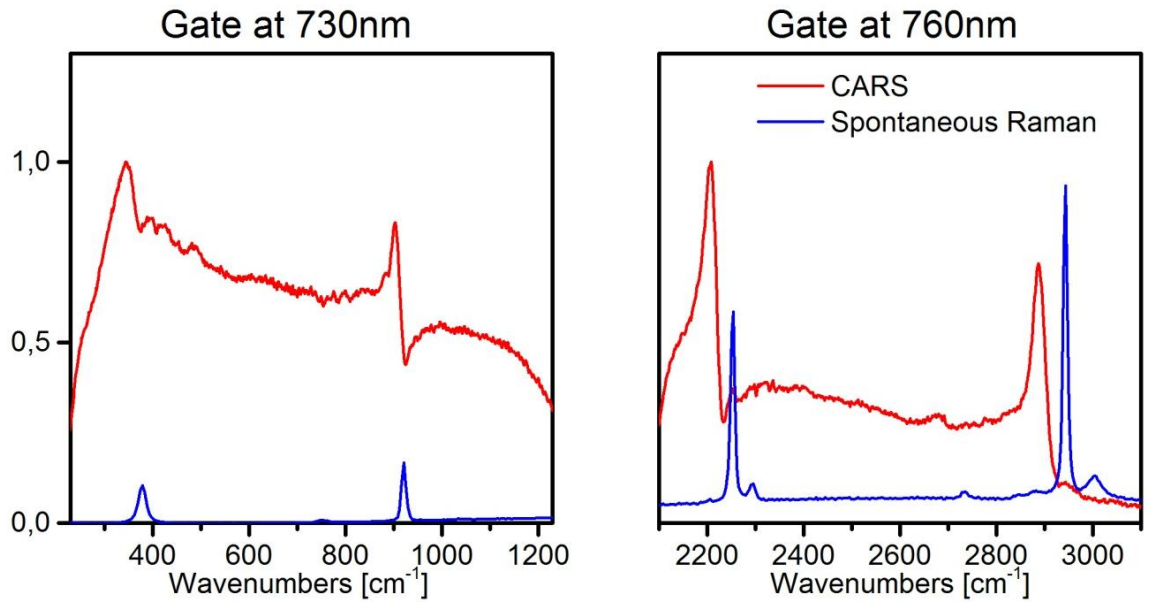

Figure 4.16 Measured acetonitrile spectra with DQSI. The position of the gate selects the probed spectral region. The width of the spectrum is limited by the spectral extension of the nonresonant background. The raw CARS spectrum (red) is compared to a spontaneous Raman spectrum (blue) of acetonitrile measured in a commercial spontaneous Raman microscope.

Considerations for imaging

For imaging, the dwell time per pixel should be kept low. In this case the ratio between the background and the signal produced by the narrow probe should be taken into account. A compromise has to be found between the intensity of the modulation and the spectral resolution. This trade-off is illustrated in Figure 4.17, by comparing the spectrum simulated with a 20fs as compared with a 10fs pulse. Gaussian pulses have been assumed, the cut-off frequency was chosen at 1/10 of the maximal intensity. Simulated $\chi^{(3)}$ had a single band at 1000cm^{-1} and the π-gate was chosen to have alternatively 15cm^{-1} and 30cm^{-1}. Because we try to extract a small variation over a large local oscillator, the ratio between resonant signal and the intensity of the local oscillator is important. Indeed, although the heterodyne enhancement factor is proportional to $|E^B_{CARS}(\omega)|$ (equation (50)) so is the shot-noise of the background. The relative intensity of the signal of interest and the background, in turn, is affected only by the probe width and position. With the approximations described earlier, both rely on the same A(Ω) and the ratio between the narrowband CARS signal and the broadband LO is proportional to the intensity ratio between the narrowband probe and the rest of the pulse. From the simulation, a similar signal to background (S/B) ratio is obtained for a 15cm^{-1} gate in a 20fs pulse and a 30cm^{-1} gate in a 10fs pulse. Another factor is the relative intensity of resonant and nonresonant contributions, which is given by the sample. In biological samples this ratio can be less advantageous than in neat liquids.

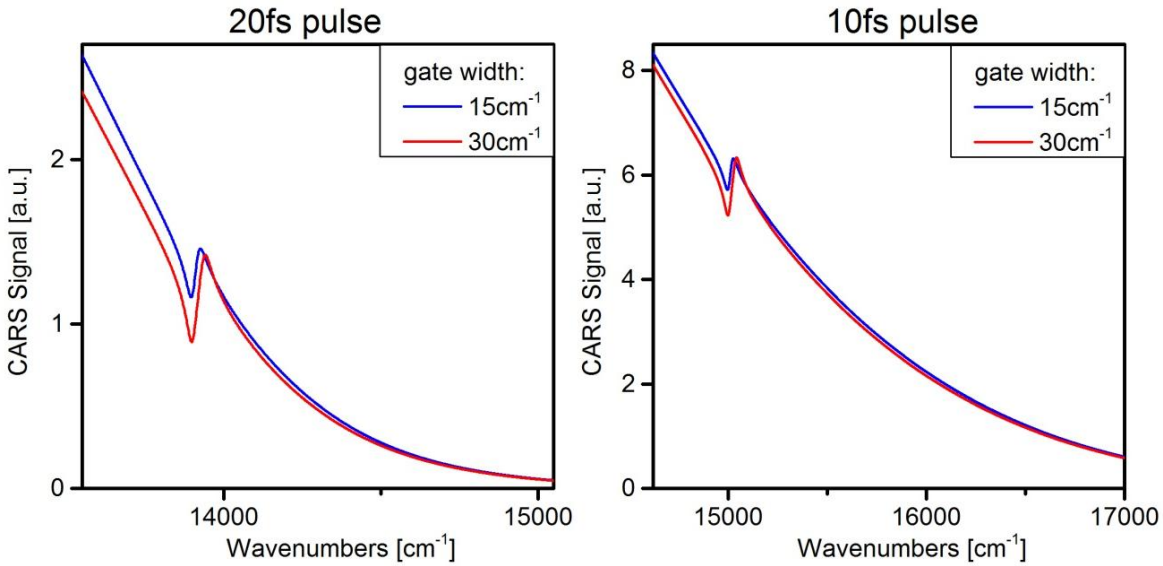

Figure 4.17 Comparison of signal to background ratio depending on pulse length and gate width. The depth of the interference signal is compared for two gate widths ($15cm^{-1}$ in blue and $30cm^{-1}$ in red) for two pulse durations (left: 20fs, right: 10fs). For the same spectral precision, the depth of the interference pattern is divided by two as the pulse gets twice shorter.

When the signal of interest is too small compared to the background, its extraction can be problematic. The dynamic range and bit depth of the detector along with noise artifact features in the nonresonant background limit the detectability of the multiplexed signal. Also, laser fluctuations can affect the acquisition of chemical maps. A way to improve the S/B ratio is to increase the relative energy of the probe. The probe being drawn from the single pulse, this requires reducing the intensity of the broadband part as will be shown in the imaging section.

4.3.4 Spectral focusing

Another way to improve the ratio between nonresonant and resonant signal is to use spectral focusing. The idea relies on the introduction of linear chirp in broadband excitation of CARS or other nonlinear processes to obtain a narrowband and easily tunable excitation. This concept was introduced by Hellerer et al. [186] for CARS microscopy but was already present in earlier works using a noncollinear geometry[187]. In the following, a theoretical description of the scheme is presented in the time domain and in the spectral domain before exploring its single-beam implementation with the shaper.

The common experimental realization of a spectral focusing scheme is illustrated in Figure 4.18 (a). A broadband pump and a broadband Stokes pulse are recombined after the introduction of a given amount of GDD and sent into the microscope. The scheme is compatible with a single-source implementation, if a single ultrashort pulse is split by a dichroic mirror into higher- and lower-frequency components [157, 188]. The chirp of both pulses has to be carefully matched: the difference between the instantaneous frequency of the pump and of the Stokes pulse then remains constant and the resulting excitation is narrowband. In the literature, the application of a rigorously equal chirp to the pump and the Stokes pulse has been realized using two grating compressors [186] or a combination of dispersive elements (highly-dispersive glass SF51, [188-190]). Figure 4.18 (b,c) depicts the

pulse configuration in a time-frequency plot (Wigner representation). In the diagrams shown in (b), the instantaneous frequencies of the pump and of the Stokes pulses are shown to evolve linearly with time according to the applied chirp. In (c), the corresponding pump-Stokes photon pairs are represented. To access another Raman level inside the range provided by the broadband excitation pulses, a simple change in the delay between the chirped pulses is sufficient.

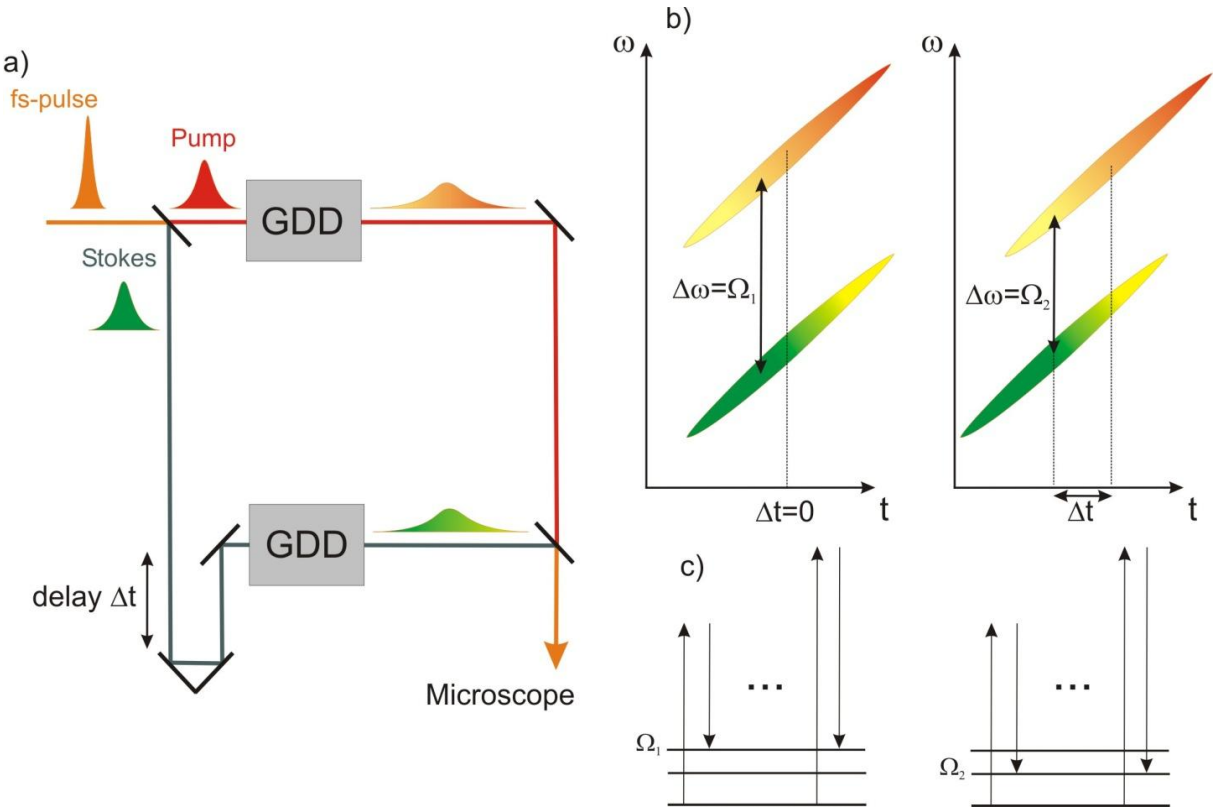

Figure 4.18 Principles of spectral focusing for CARS microscopy. a) Experimental realization: broadband pump and Stokes pulses (obtained from a single fs-pulse or by nonlinear conversion) are stretched in time by dispersive elements. The amount of GDD is the same for both pulses. The delay can be varied to excite different Raman modes of the molecules. b) By stretching the pulses with the same GDD, the difference between the instantaneous frequencies of pump and Stokes pulses remains constant over time. The delay Δt tunes the difference Δω (right diagram). c) Selective excitation of Raman modes within the bandwidth of the broadband pulses is achieved.

Time-domain picture

This can be understood by describing the pulse sequence in the time domain. The introduction of a linear chirp in a Gaussian pulse corresponds to adding a quadratic temporal phase [39]:

$$\tilde{\mathcal{E}} = \mathcal{E}_0 \exp\left[-\left(\frac{t}{\tau}\right)^2 + i(\omega_0 t + \varphi(t)\right], \qquad \varphi(t) = \beta t^2 = a\left(\frac{t}{\tau}\right)^2 \tag{55}$$

With ω_0 the central frequency and β the linear chirp parameter. τ is the length of the chirped pulse, which depends on the FTL pulse duration τ_0: $\tau = \tau_0\sqrt{1+a^2}$. The instantaneous frequency is defined as $\omega(t) = \omega_0 + \dot{\varphi}(t)$.

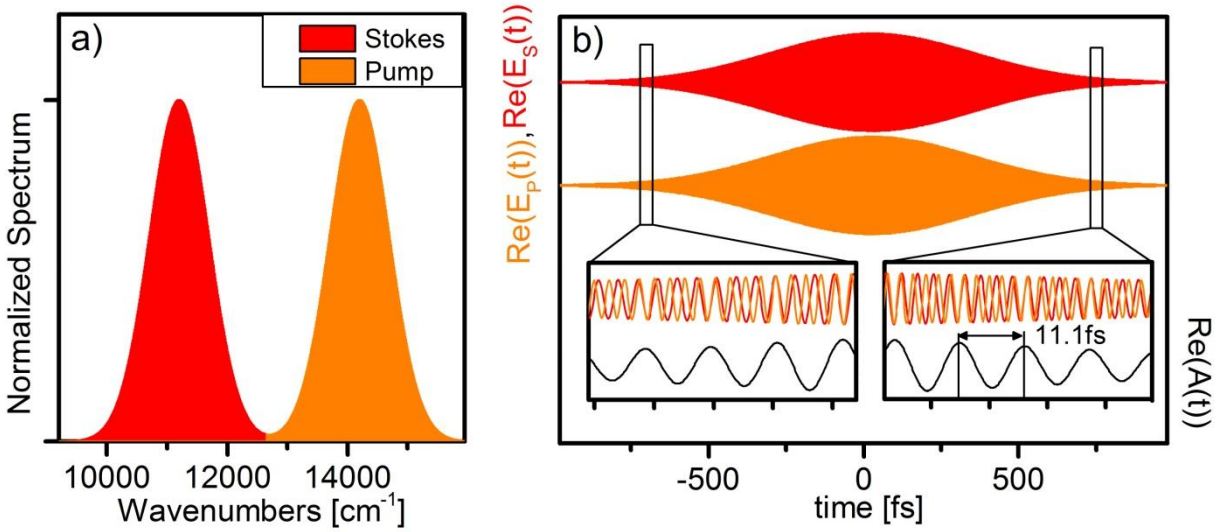

Figure 4.19 Spectral focusing: time domain picture. a) The simulated excitation consists of two broadband (700cm^{-1}) pulses centered at 11200cm^{-1} and 14200cm^{-1}. b) Each pulse is affected by a total GDD of 3500fs^2 and Δt=0. The pulses are stretched to a duration in the range of 1 ps. In the insets, both fields are shown as well as A(t). The higher frequency of both pulses for positive times results in a constant beating frequency. The observed 11.1fs period of A(t)corresponds to the selected 3000cm^{-1} mode.

In presence of the chirped pump and Stokes pulses, the driving force seen by the molecules is given by $A(t) = \mathcal{E}_P(t)\mathcal{E}_S^*(t)$. If we suppose equal chirp parameters β applied to both pulses and get rid of constant phase offsets, we obtain [157, 191]:

$$A(t) \propto \exp\left[-\frac{\Delta t^2}{2\tau^2} - \frac{2\left(t - {}^{\Delta t}/_{2}\right)^2}{\tau^2} + i(\omega_P - \omega_S + 2\beta\Delta t)t\right] \qquad (56)$$

For a delay Δt between the centers of the pulses. The imaginary part in equation (56) shows that the instantaneous frequency of A(t) remains constant and is tunable around ω_p-ω_s using the delay between the chirped pulses. The real part indicates the time interval during which the driving force is effective. It is of the same order of magnitude as the duration of the chirped pulses: the FWHM is calculated to be only $\sqrt{2}\tau$. The interplay of these parameters is illustrated by Figure 4.19. 3

For this simulation, the Pump pulse is chosen with a center at 14200cm^{-1} and the Stokes pulse at 11200cm^{-1}, both have a bandwidth of 700cm^{-1} (FTL pulse duration ~15fs). Both pulses are chirped to a duration of the order of 1ps. In Figure 4.19 b), the oscillations of the pump and Stokes light fields are not resolved: the insets show the beating between them as well as the resulting A(t) (black) on a time scale of 40fs. Over the whole duration of the chirped pulse, the period of A(t) remains constant (11.1fs)

The duration of the envelope of A(t) determines how efficiently the instantaneous and the vibrational parts of χ(t) are driven by the pulse combination. Broadband pulses lengthened by chirp are less efficient for the generation of the instantaneous nonlinear signal, but this is compensated by the longer interaction for the resonant part. The presented example is then equivalent to a ps-CARS scheme: the same A(t) with the same modulation frequency would have been achieved with narrowband ps-pulses centered at 11200cm^{-1} and 14200cm^{-1}. The

spectral resolution of the scheme is hence directly linked to the duration of the chirped pulses and is given by the Fourier transform of the envelope of A(t).

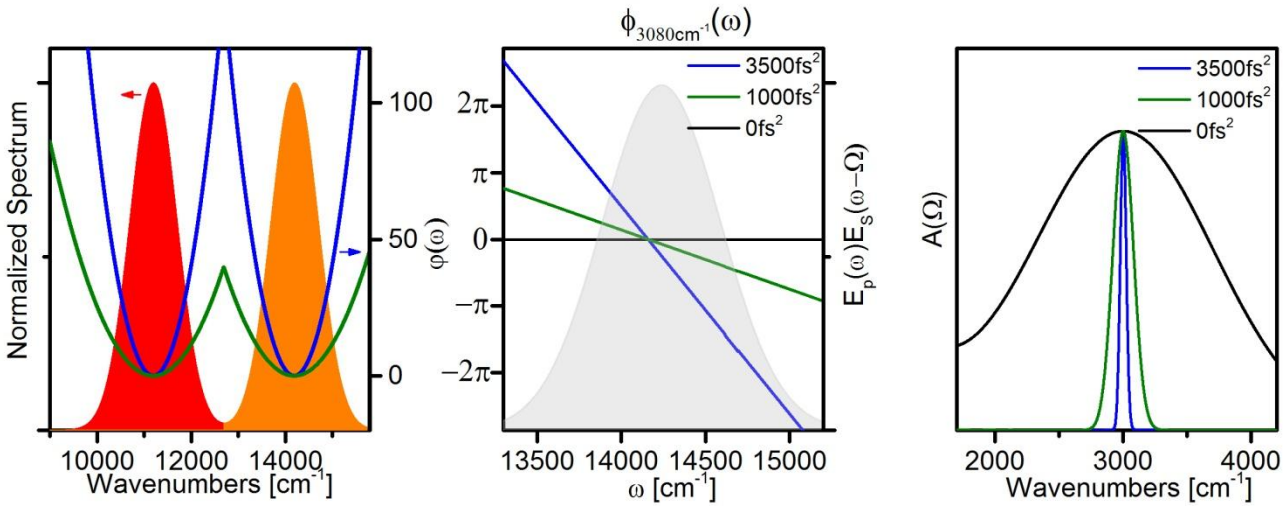

Figure 4.20 **Spectral focusing: spectral domain picture.** (left) GDD = 3500fs^2 (blue) and 1000fs^2 (green) with ω_p-ω_S =3000cm^{-1} is applied to the same spectrum as in **Figure 4.19**. (middle) In gray, the available photon pairs for Ω = 3080cm^{-1}. The spectral focusing phases are centered at Δω = 3000cm^{-1}. The relative phase of the photon pairs is shown for the FTL pulses (black) and the two spectral focusing phases (green and blue). (right) A(Ω) for FTL pulses (black) and for spectral focusing phases (green, GDD=1000fs^2, blue, GDD=3500fs^2). Note that for a spectrum with two modes like here, A(Ω) is not centered around 0 a single broadband Gaussian spectrum.

Spectral domain picture

How to achieve a similar excitation scheme with the pulse shaper? In the spectral domain, chirp corresponds to a parabolic phase function and delay to a linear phase function. Thus, to apply a delay to the pump pulse is equivalent to move the center of the parabola from ω_{p0} to ω_p:

$$\varphi_p(\omega) = \alpha\left(\omega - \omega_{p0}\right)^2 + \Delta t\omega = \alpha\left(\omega - \omega_p\right)^2 + c$$
$$\omega_p = \omega_{p0} - \frac{\Delta t}{2\alpha} \tag{57}$$

Where c is a constant and does not affect the shape of the temporal envelope of the pulse. The addressed Raman mode is given by the difference between the central frequencies of pump (ω_p) and Stokes (ω_S) parabolas. This can be seen if we calculate A(Ω):

$$A(\Omega) = \int E_p(\omega + \Omega)E_S(\omega)\exp[i\phi_\Omega(\omega))]\,d\omega$$
$$\phi_\Omega(\omega) = \alpha\left(\left(\omega + \Omega - \omega_p\right)^2 - (\omega - \omega_S)^2\right) = 2\alpha\left[\left(\Omega - (\omega_p - \omega_S)\right)\omega\right] + const. \tag{58}$$

Where ϕ_Ω is the phase of photon pairs contributing to A(Ω) (modulo a constant phase shift). For Ω matching the difference between the centers of the GDD functions, all available phase pairs add up constructively, like in the FTL case. For other Raman shifts, ϕ_Ω is linear. Its slope is proportional to the mismatch Ω-(ω_p-ω_S) and to the GDD. The photon pairs then add up less efficiently and even interfere destructively when a phase difference of more than π is introduced within the bandwidth of the pulse. An estimate of the spectral resolution $\delta\omega$ is then given by:

$$\delta\omega = \frac{\pi}{2D_\omega \cdot \alpha}, \tag{59}$$

with D_ω the bandwidth of the pulse.

If we consider the precedent example of Figure 4.19 now in the spectral domain (see Figure 4.20), the applied phase is a GDD=3500fs^2 parabola for pump and for Stokes (blue line), separated by 3000cm^{-1}. To see the effect of GDD on spectral resolution, we compare this case to GDD=1000fs^2 and to FTL pulses. If no phase distorts the broadband pulses, A(Ω) has a bandwidth of about 1600cm^{-1}. It is reduced to about 190cm^{-1} for GDD=1000fs^2 and to 54cm^{-1} with the steeper parabolas of 3500fs^2, in accordance with equation (59). At a Raman shift of Ω=3080cm^{-1}, slightly away from the Raman resonance selected by spectral focusing, for FTL pulses A(Ω) is almost as big as A(3000 cm^{-1}), for GDD=1000fs^2 it is still substantial and when GDD=3500fs^2 A(Ω) is already vanishing. The middle panel of Figure 4.20 shows how the phase of the photon pairs for this mode depends on the pump frequency, which is given by $E_p(\omega)E_S^*(\omega - 3800\text{cm}^{-1})$. At GDD=0fs^2, all available photon pairs (shown in gray) interfere constructively, with GDD=1000fs^2 the phase difference does not exceed π in the bandwidth of the pulse and reaches more than 2π when GDD=3500fs^2 explaining the evolution of A(3080cm^{-1}) with increasing chirp.

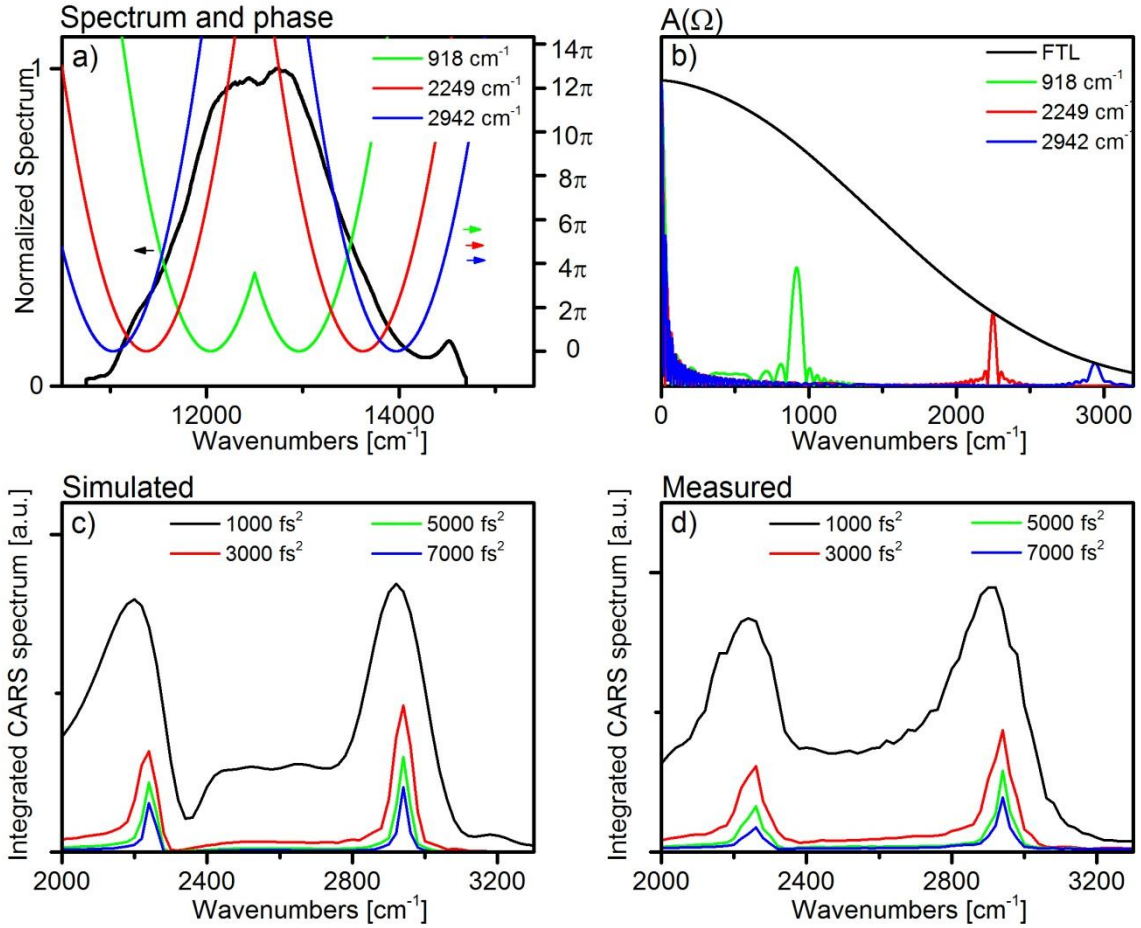

Figure 4.21 Simulated and measured spectral focusing spectra of acetonitrile. a) The phase applied by the shaper on the single broadband pulse consists of two parabolas, one for ω<12500cm^{-1} and one for ω>12500cm^{-1}. Represented are phase functions with GDD=3000fs^2 and with increasing distance between the centers of the two parabolas: 918cm^{-1}, 2249cm^{-1} and 2942cm^{-1} (green, red and blue lines). b) A(Ω) for each phase (same color code) compared to the FTL pulse (black line). c) Simulated CARS spectra: for each distance Δω between the parabolas the signal integrated. GDD increases from 1000fs^2 (black line) to 3000fs^2 (red), 5000fs^2 (green) and 7000fs^2 (blue).d) same as c) with measured data.

Spectral focusing in the SB-CARS setup

Spectral focusing can be considered as a method based on the control of A(Ω) like the time resolved single-beam CARS techniques presented earlier. Unlike multipulses, however, it reduces the excitation to a single Raman shift and therefore limits the amount of nonresonant background. It also allows acquisition of spectra by scanning the parameter $\Delta\omega = \omega_p - \omega_S$. This is shown experimentally on the previously used example of acetonitrile in Figure 4.21. In the single-beam experimental realization of spectral focusing, the broadband spectrum is arbitrarily divided in a pump and a Stokes spectral region by choosing a separation wavelength ω_c (here at the center of the pulse, ω_c =12500cm^{-1}). Using the shaper, the careful matching of glass thickness is replaced by the simple writing of a phase on the SLM [157]. The amount of GDD is also easily controlled, allowing a tuning of the spectral width of the excitation. The delay between pump and Stokes to select the Raman shift is replaced by the choice of central frequencies of the phase functions. This is illustrated in Figure 4.21 a) and b). $\Delta\omega$ is tuned to the main resonances of acetonitrile at 918cm^{-1}, 2249cm^{-1} and 2942cm^{-1}, producing narrowband A(Ω) around the chosen bands.

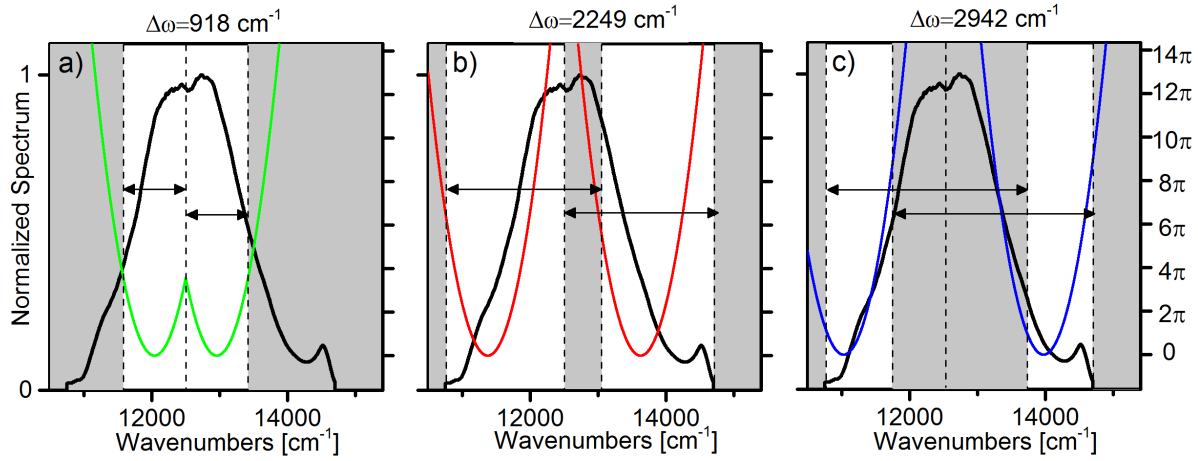

Figure 4.22 Available bandwidth depending on Δω. Spectral components either further away than Δω from the central frequency ω_{cut} or from the borders of the spectrum do not contribute to the excitation. Efficient regions are shown in white and regions that do not contribute to the excitation in gray.

The excitation probability at the selected Raman shift reaches the same level as for the FTL pulse for $\Delta\omega$=2249cm^{-1} and $\Delta\omega$=2942cm^{-1} but remains well below for $\Delta\omega$=918cm^{-1}. This phenomenon is due to the limitations of the available bandwidth for the Stokes and the pump pulses. The limitations can be summarized as follows:

- Stokes photons must be lower in energy than ω_c,
- pump photons must be higher in energy than ω_c,
- all photons must be included in the bandwidth of the pulse, between ω_{min} and ω_{max} (for the lowest and the highest frequency in the pulse respectively).

The effect of these limits for different selected Raman shifts is illustrated in Figure 4.22. For example, for photon energies higher than $\omega_c+\Delta\omega$ there are no Stokes photons available. The available bandwidth for $\Delta\omega$=918cm^{-1} is therefore limited to the white region in Figure 4.22. For $\Delta\omega$ larger than the bandwidth of the pulse, the last limitation comes into play. At pump energies lower than $\omega_{min}+\Delta\omega$, there are no Stokes photons available discarding the gray

regions in the center of the spectrum in Figure 4.22 for $\Delta\omega$=2249cm^{-1} and $\Delta\omega$=2942cm^{-1}. However, this effect is also present for the FTL pulse, and the excitation probability is conserved. Note finally that a small region around 0cm^{-1} is always excited (Figure 4.21 b). The width of this region depends on the GDD parameter. After probing, the CARS signal of this contribution remains mainly overlapped by the exciting pulse and a slight shift of the detection window suffices to eliminate it.

Spectra of acetonitrile obtained with different steepness of the parabolas are shown in Figure 4.21 c) (simulated) and d) (measured data). The CARS signal is integrated from slightly above 15000cm^{-1} to 18000cm^{-1} and $\Delta\omega$ is scanned from 2000cm^{-1} to 3300cm^{-1}. Measured spectra are in very good agreement with the simulation showing the increase in resolution with increasing GDD. Simultaneously the signal decreases, which is due to the narrower excitation spectrum. The bandwidth of the peaks is also limited by the natural bandwidth of the molecular bands. The typical 10-20cm^{-1} are obtained for A(Ω) with GDD=7000-8000fs^2. However for later imaging applications values in the 3000-5000fs^2 are preferred as a compromise between resolution and signal level and because the C-H stretching region contains usually broader bands.

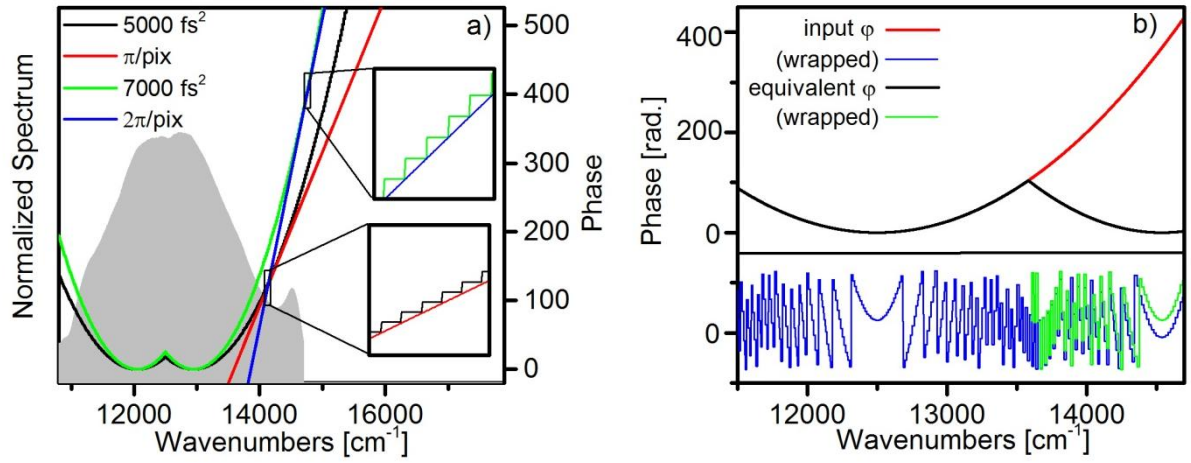

Figure 4.23 Resolution limitation in single-beam spectral focusing. a) When addressing a Raman mode at 900cm^{-1} the slope of the spectral focusing phase reaches π per pixel (red line) within the pulse for GDD=5000 fs^2 (black line) and 2π per pixel (blue line) with 7000fs^2 (green line). In the insets, the pixelated phase functions are shown when reaching these limits. b) An input phase of GDD=5000fs^2 centered at 12500cm^{-1} (red line) on a pixelated shaper (blue line) is similar to applying two a new parabola starting above 13500cm^{-1}(black and green curves). The new parabola represents GDD=6400fs^2 and is centered at 17380 cm^{-1}, 4080 cm^{-1} away from the center of the pulse.

Like in the other SB-CARS schemes, the spectral resolution is limited by the number of pixels of the shaper. The maximal GDD parameter is given by the limitation of its slope to π per pixel. This limit affects mainly the wings of the applied phases, making spectral focusing a robust technique. According to equation (59), the resolution is inversely proportional to the chirp parameter and to the bandwidth of the pump and Stokes pulses. To calculate the resolution, two interdependent limits must therefore be taken into account: the maximal chirp parameter and the available bandwidth. If we note ω_{pix} the spectral width covered by a pixel, the condition for the maximal slope provides the following limit for the chirp parameter α:

$$\alpha_{max} = \frac{\pi}{2D_\omega \cdot \omega_{pix}}. \qquad (60)$$

Combing this expression with equation (59), we obtain $\delta\omega \sim \omega_{pix}$. In practice, the conditions for equation (59) (Gaussian pump and Stokes) are not fulfilled and the bandwidth accessible for one particular level is not constant (see Figure 4.22), but the achievable resolution of the excitation is of the order of the spectral resolution in the shaper, in our case 14cm^{-1} when using 600gr/mm gratings and 7cm^{-1} for 1200gr/mm gratings. The π-per-pixel limit is reached within the pulse already for GDDs matching ideally the usual bandwidth of Raman levels. In Figure 4.23, a 5000fs^2 and a 7000fs^2 phase with Δω=900cm^{-1} are chosen. A linear function representing the π-per-pixel limit is represented in red. With GDD=5000fs^2, the phase function is correctly reproduced by the shaper over 75% of the bandwidth. This does not affect A(Ω) because the effective bandwidth is limited to a 1800 cm^{-1} region at the center of the pulse for this mode. However, unwanted artifacts can occur due to the incorrect reproduction of the applied phase function outside of the effective bandwidth.

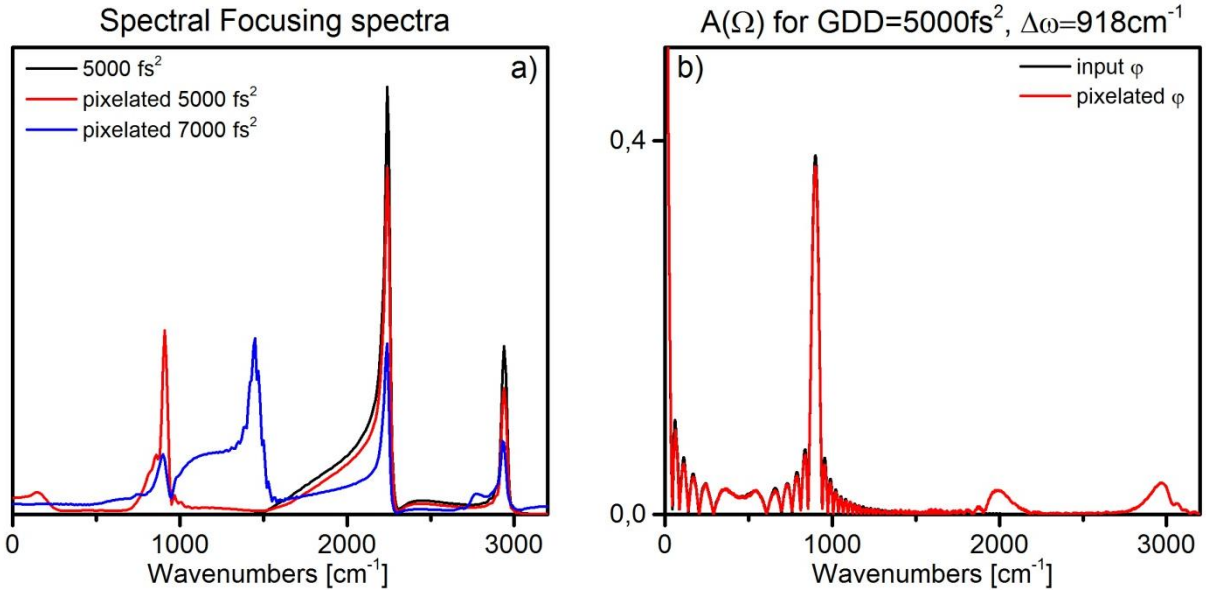

Figure 4.24 Spectral artifact due to pixelisation. a) Simulated spectra with smooth 5000fs^2 (black) and pixelated 5000fs^2 (red) and 7000fs^2 (blue) Spectral Focusing phases. b) A(Ω) for Δω tuned to the 918cm^{-1} transition of acetonitrile with smooth (black) and pixelated (red) phases.

Pixelation artifact

To understand these pixilation artifacts, the phase function seen by the pulse when too high slopes are applied should be understood. Once the limit fixed by the pixel width is reached, phase wrappings occur very rapidly. This is shown in Figure 4.23 b) on the example of a simple 5000fs^2 chirp function centered at 12500cm^{-1}. From 13500cm^{-1} to 13750cm^{-1} adjacent pixels will have phase differences of about π. Not visible in the simulation, this produces a grating function in the Fourier plane of the shaper and depletes the spectral intensity in this region. Further away from the center, the wrapped phase is undistinguishable of a function obtained by subtracting a 2π-per-pixel linear function (blue line in Figure 4.23 a). The GDD=5000fs^2 function taken as an example is equivalent, after substraction, to a phase function with GDD=6400fs^2 and centered at 14540cm^{-1} [1]. Finally, instead of the initial phase

[1] Note that the difference between the GDD of the original function and the equivalent function is due to the nonlinear wavenumber distribution across the shaper (see chapter 2.4.2 for details)

function (red line) the pulse is shaped according to a double parabola (black line): a simple chirp is transformed in a Spectral Focusing function by pixel effects.

Pixilation artifacts appear clearly in spectral focusing spectra, as becomes evident from the simulation shown in Figure 4.24 (a). A spectral focusing spectrum is calculated for acetonitrile from 0cm^{-1} to 3200cm^{-1}. In the simulation, the applied functions are either smooth (GDD=5000fs^2, black curve) or pixilated (GDD=5000fs^2, red curve, GDD=7000fs^2, blue curve). The spectrum obtained with a well resolved phase function is almost zero below 1500cm^{-1} whereas a peak appears in the pixilated case. The artifact position depends on the GDD parameter, moving towards higher wavenumbers with increasing parabola steepness. The cause of the artifact is identified in Figure 4.24 (b). The additional parabolas created at the positions where the slope of the applied function exceeds 2π-per-pixel create, in addition to the selected Raman shift, an excitation at further positions. For example, when GDD=5000fs^2 and Δω=918cm^{-1}, A(Ω) becomes non-zero around 2000 cm^{-1} and 3000 cm^{-1} with our shaper configuration. The pixilation artifact occurs even if the parabolas are reproduced correctly over the available bandwidth for this GDD and this Δω.

Another effect of the new parabola created by pixelation effects is due to its role in the probing mechanism of spectral focusing, which will be now exposed in more detail.

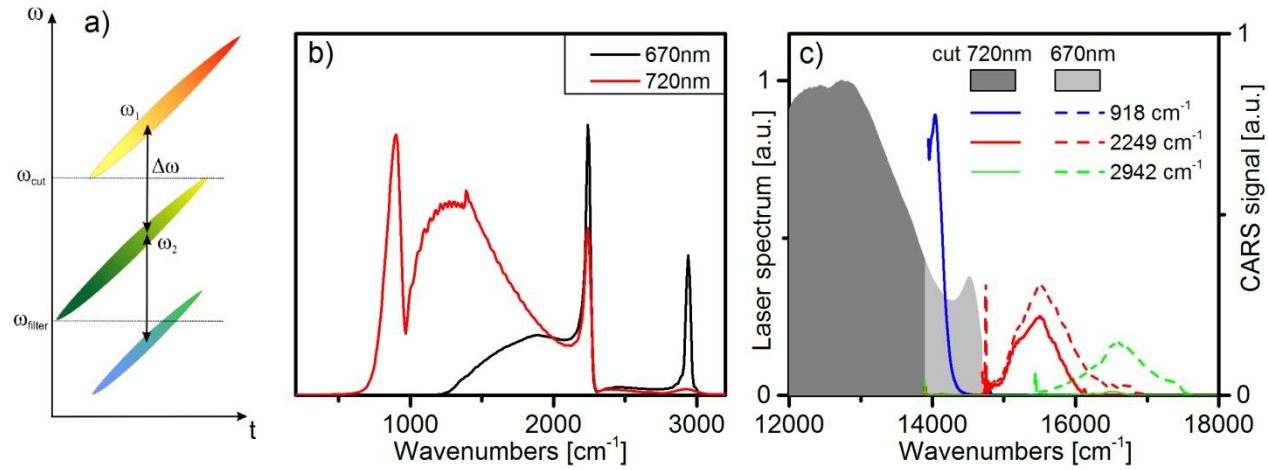

Figure 4.25 Probing process in Spectral Focusing. a) time-frequency plot representing CARS signal generation for Δω smaller than the bandwidth of the pump and Stokes pulses. b) Simulated single-beam CARS Spectral Focusing spectra obtained with a filter edge at 670nm (black) and at 720nm (red). Other parameters are: GDD=5000fs^2 and ω_{cut}=12500cm^{-1}. c) Normalized available laser spectrum when filter edge is 720nm (dark gray) and 670nm (light gray). Spectrally resolved CARS spectra for spectral focusing phases with Δω=918cm^{-1}, 2249cm^{-1}, 2942cm^{-1} (blue, red and green respectively. Plain lines for the 720nm filter and dotted line for 670nm).

Probe pulse in spectral focusing and accessible spectral range

The probing process in spectral focusing is assumed by the chirped pump. In a time-frequency picture the CARS signal simply appears at the spectral position $\omega_p+\Omega$, similar to the picoseconds case. In Spectral Focusing, Δω remains constant over time but ω_p is swept across the broadband pump spectrum. As seen in Figure 4.25 a), the resulting CARS signal is broadband and chirped as the pump and Stokes pulses. The bandwidth of CARS is limited by the duration of the interaction, maximized when Δω matches the differences between center frequencies of pump and Stokes. The diagram also reveals that for Δω smaller than the

bandwidth of the pulses, a part of the CARS signal overlaps with the blue wing of the pump pulse. Simultaneously, this part does not contribute to the probing process: a shift in the filter wavelength λ_{cut} then reveals the CARS signal without attenuating it. In the single-beam CARS setup, spectra acquired with the same parameters (ω_c=12500cm^{-1}, GDD=5000fs^2) give access to different spectral ranges depending on the filter wavelength. The simulation shown in Figure 4.25 (b) compares spectra obtained with ω_{cut}=14925cm^{-1} (λ_{cut}=670nm, black line) as used in the experiment and ω_{cut}=13889cm^{-1} (λ_{cut}=720nm, red line). The shift of the filter edge reveals a region starting at about 750cm^{-1} which is not visible in the original spectrum and contains a resonance of acetonitrile (at 918cm^{-1}). The upper limit of the spectrum is given by the bandwidth of the laser, which is reduced by the new filter and the band at 2942cm^{-1} disappears. Figure 4.25 c) sums up the compromise between lower and higher lying Raman modes in the spectrum: available laser spectra for each filter are shown in gray, spectrally resolved CARS signals are plotted for GDD=5000fs^2 spectral focusing phase functions selecting the main modes of acetonitrile (blue: 918cm^{-1}, red: 2249cm^{-1}, green: 2942cm^{-1}). The mode at 2249cm^{-1} is well visible with both filters and the spectrally resolved CARS signals are similar. The lower lying mode is excited by both pulses but is undetectable with the 670nm because of spectral overlap. Finally the higher lying mode is well away from the excitation but the spectrum cut at 720nm lacks bandwidth to excite it. The choice of the separation frequency ω_c can be used to optimize the spectrum but does not significantly change the visible spectral range. As this technique is mainly suited for imaging, the limitation of the accessible spectral range does not play a deleterious role and ω_{filter} should simply be chosen in advance to optimize the signal from the chosen band.

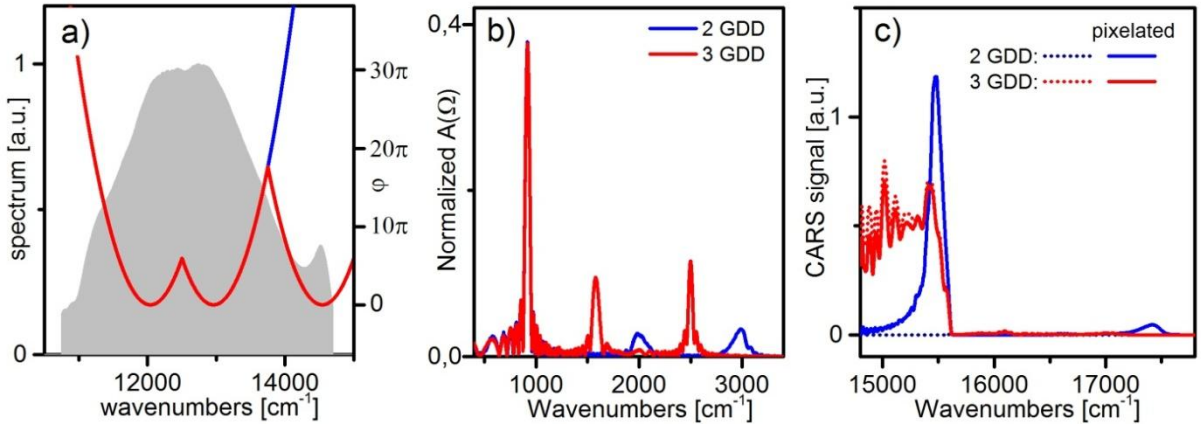

Figure 4.26 Additional probe and multiple-band excitation. a)Spectral focusing phase with 2 GDD functions (blue) is compared to a scheme with 3 GDD functions (red) b)Corresponding A(Ω) calculated taking into account pixelisation effects c) CARS signals obtained with the phases in a). Signal generated with a smooth phase function (dotted lines) is compared to the case of a pixelated function (plain lines).

An alternative way to increase the spectral range without changing the excitation efficiency or the filter wavelength is to introduce an additional probe pulse near to the blue wing of the excitation. In figure Figure 4.26 a), the same example as in Figure 4.24 is taken: $\Delta\omega$ is set to 918cm^{-1} and GDD=5000fs^2. The artifact appearing with the pixelated shaper can be replaced by a well defined parabola also centered at 14540cm^{-1}. Interestingly, the side bands in A(Ω) become more intense and are simultaneously shifted to smaller values (Figure 4.26 b). This is due to the better correspondence of GDD parameters with the two original spectral focusing parabolas. The CARS signal is then better defined and corresponds to the signal expected if

the phase where smoothly reproduced by the shaper (Figure 4.26 c, red curves). On the contrary the CARS signal obtained with the pixelisation artifact contains contribution of other bands and differs largely from the expected values (Figure 4.26 c), blue curves). Nevertheless, these observations open the way to multiple excitation based on spectral focusing. However, the distance between bands excited with a strategy based on three parabolas with same GDD cannot be chosen arbitrary: for example, the distance between the first and the second parabola can be chosen and between the first and the third but the distance between the second and the third parabola is then fixed. More complex phase shaping like pseudorandom binary phases [163] and the use of polarization to separate the probing process from the excitation may lift ambiguities.

4.4 Single-Beam CARS imaging

With the successful demonstration of the ability of various SB-CARS methods to reach the 3000cm^{-1} region and beyond, the application of the setup to imaging of sensitive biological samples remains to be shown. This part will consider separately the spectrally resolved and the spectral focusing (single-channel) techniques, as corresponding to applications where precise spectral information or speed of imaging have a predominant role.

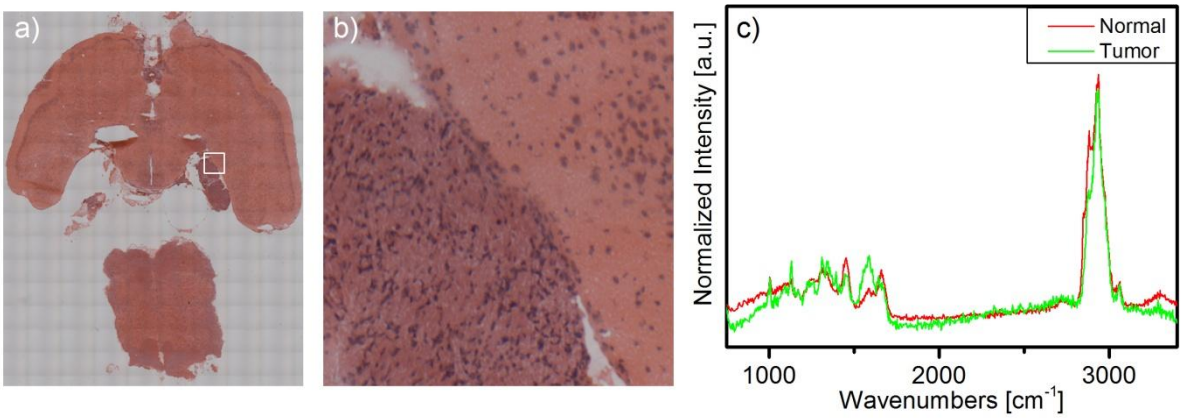

Figure 4.27 Mouse brain sample. a) Whole mouse brain section (HE-stained) displaying a solid tumor (region colored in a deeper purple than the rest of the brain, on the right side) b) detail of the tumor boundary with normal tissue (region marked with a white square in a). The cell nuclei appear in deep purple and cytoplasm in lighter colors. The tumor presents a higher density of nucleic acids and the nuclei are less well defined. c) Spontaneous Raman spectra taken from tumorous (green) and normal (red line) tissue. While having many similarities, distinct features are notable in the fingerprint and in the CH-stretching regions.

4.4.1 Brain tissue sample

The sample used to demonstrate the capabilities of single-beam CARS for imaging is brain tissue. CARS has a high potential for imaging of the brain and of the whole nervous system because of the lipidic myelin layer protecting the axons and because it provides a resolution on the cellular level. In the following, brain slices from a murine model were provided by PD Dr. Kirsch from the Neurochirurgie group of Prof. Dr. Schackert at the Universitätsklinikum Carl Gustav Carus in Dresden. The samples were obtained within the MEDICARS project dedicated to explore the application of CARS techniques to brain imaging. Fresh mouse brain sections were alternatively prepared by a standard staining method (Hematoxylin-Eosin, HE) or air dried. The sample presented in Figure 4.27 was obtained after intracerebral stereotactic implantation of murine melanoma cells. The formation of a solid tumor is easily observed in

the HE-stained preparation (Figure 4.27 a). The tumor appears as a clump with a darker shade of pink on the edge of the lobe seen on the right of the image. A closer view of the limit of the tumor is shown in Figure 4.27 b). The darker color of the tumor is due to a denser distribution of nuclei and to darker cytoplasm. A study of the sample with a spontaneous Raman microscope (Witec, alpha 300) has been performed [95] and shows that, although the spectra inside the tumor and the healthy tissue are quite similar, a few bands show significant differences (notably at 1660cm^{-1} and 2890cm^{-1}) as seen from Figure 4.27 c).

4.4.2 Spectrally resolved imaging

We first consider spectrally resolved techniques to evaluate the capacity of SB-CARS to extract spectral information from the sample. On one hand, the results obtained in acetonitrile show that precise location of the Raman bands over a large spectral range is possible with the acquisition of one or only a few SB-CARS spectra. On the other hand, the limitations imposed by the sensitive sample play an important role for the spectrally resolved schemes notably because of the need for short pulses.

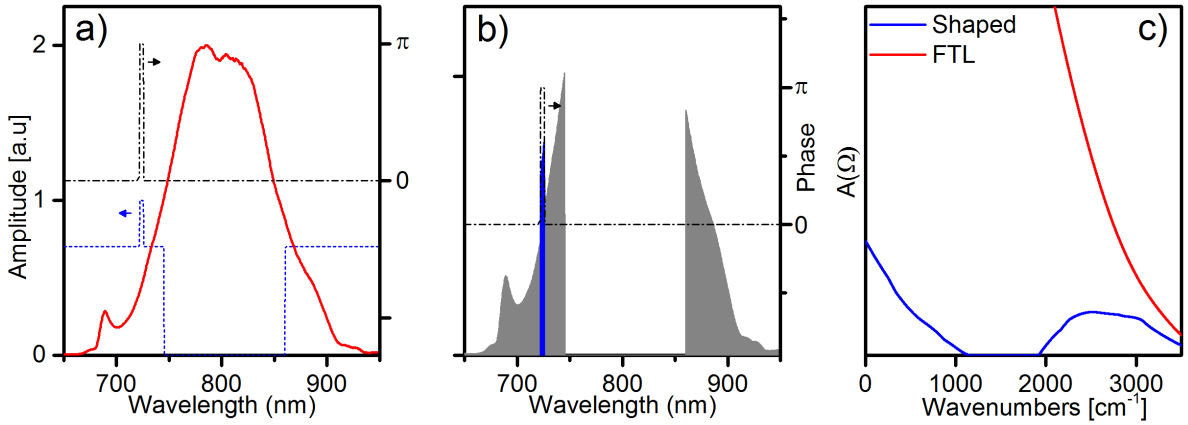

Figure 4.28 Shaping scheme for the spectrally resolved imaging of sensitive samples. a) Original laser pulse (red line), phase (black, dotted) and amplitude (blue, dotted) masks applied by the shaper. b) Resulting excitation amplitude(gray) and phase (black, dotted). The narrowband probe is highlighted in blue. c) Comparison of the Raman excitation probability between the FTL pulse (red) and the shaped excitation (blue).

The need for pulses near the transform limit in spectrally resolved SB-CARS techniques is due to the necessity of a broad signal to create the detected interference pattern (see section 4.3.3). This strongly limits the maximal incident power to avoid photodamage of the brain tissue. At the same time, the depth of the interference pattern created by the phase gate should be increased: imaging conditions limit the time available per pixel and hence the possibility to increase the signal-to-noise ratio through averaging.

Both limitations are addressed by amplitude shaping. Knowing that the brain tissue is mainly constituted of lipids, and based on the spontaneous Raman and MCARS spectra shown in Figure 4.27, we narrow the excitation to the strong bands around 3000cm^{-1}. Since a large part in the centrum of the spectrum does not contribute to A(Ω) in this region (see Figure 4.22), its elimination by amplitude shaping does not affect the excitation efficiency of the pulse. This also presents the advantage of increasing the relative power in the probe pulse at same spectral resolution and decrease the nonresonant background. The interference pattern created by the phase-shifted multiplexed CARS signal is then more prominent and easier to detect in

presence of noise at small integration times. To further increase the relative intensity of the features, the amplitude of the pulse is reduced by a factor 0,8 except the narrowband probe. The resulting phase and amplitude masks are shown in Figure 4.28 (a) and the final excitation pulse in Figure 4.28 (b). The probe pulse consists of a 5-pixel region (≈70cm^{-1}) centered at 725nm and has a phase of π with respect to the rest of the pulse. Compared to the pulses used in neat liquids, the total intensity of the shaped pulse is only about 15% of the original pulse intensity while the probe pulse energy increases from 1 or 2 pixel to 5. For bands around 3000cm^{-1}, A(Ω) is less than 2 times smaller than for the FTL pulse, as shown in Figure 4.28 (c).

π-gate

Spectra obtained with the shaped pulse are shown in Figure 4.29 (a). A first observation is the clear change in the form of the broadband signal: instead of a monotonous decrease towards blue wavelengths, a minimum is observed at about 630nm. The red part of the background is mainly due to the single-beam signal generated by the transform limited part of the laser spectrum situated next to the filter edge. The broad peak centered at 610nm is generated by both wings selected by amplitude shaping. At some points of the tumor with intense resonances the dip feature reaches about half the size of the local oscillator (see the red line in Figure 4.29 (a). In a single-shot approach, the spectral information is extracted by fitting (see section 4.3.3). Here, a cubic function is used and the fitting is limited to the blue part of the spectrum (blue lines). After subtraction, the treated spectra have a peak-dip structure, shown in Figure 4.29 (b). Unlike in the simulation in Figure 4.15, the structure is not sharp due to the width of the resonances and to the width of the probe pulse and a direct interpretation of the spectra in terms of band position is not possible. Nevertheless, the tumor boundary is nicely imaged using the treated spectra: the integrated region of the peak is used as the red channel and of the dip as the green channel in Figure 4.28 c). Consistent with MCARS studies of this sample, higher signals and a rougher structure is observed in the normal tissue.

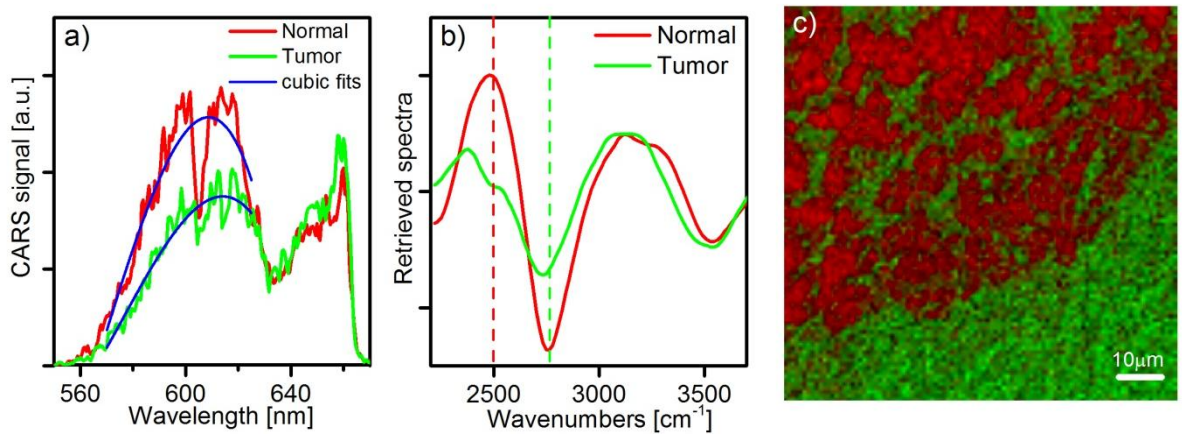

Figure 4.29 Spectrally resolved imaging of the boundary between tumor and healthy tissue. a) Recorded raw CARS spectra in the tumor (green) and in normal tissue (red). In blue, the cubic fits of the raw spectra. b) Spectra obtained after the subtraction of the cubic fit. The Raman shift scale is calculated with a probe position of 725nm. c) Image of a 100x100µm region at the tumor boundary. The green (resp. red) channel corresponds to an intensity map of the peak (resp. dip) positions in the treated spectra marked by dotted lines in b).

DQSI

An alternative to obtain more reliable spectral information is given by the DQSI method. Even if the need for four measurements can induce increased noise due to laser fluctuations, the influence of fitting errors is avoided. Laser fluctuations can additionally be corrected by normalizing raw spectra over a region free of resonances. Spectra obtained at one point inside the region identified as tumorous are shown in Figure 4.30 (a). At this position, laser fluctuation did not have a major influence and the spectra are shown as measured. The phase of the probe region is cycled, taking values 0, π/2, - π/2 and π. The sequence of spectra has two remarkable features: first, the interference pattern created by the resonant signal follows a similar evolution to the calculations shown in the theoretical description of DQSI. Second, the broadband signal does not remain constant when the phase of the narrowband probe changes, thereby preventing an extraction of Raman-equivalent spectra and retrieval of the phase of $\chi^{(3)}$ using the simple DQSI-equations. More importantly, the phase shift affects the broadband signal in a wavelength-dependent manner: the dependence on the probe phase is most pronounced near the filter edge while the blue wing of the CARS signal remains constant. This is due to the much larger ratio between the energy in the narrowband probe and the energy in the broadband part of the pulse than what was the case for SB-CARS spectroscopy.

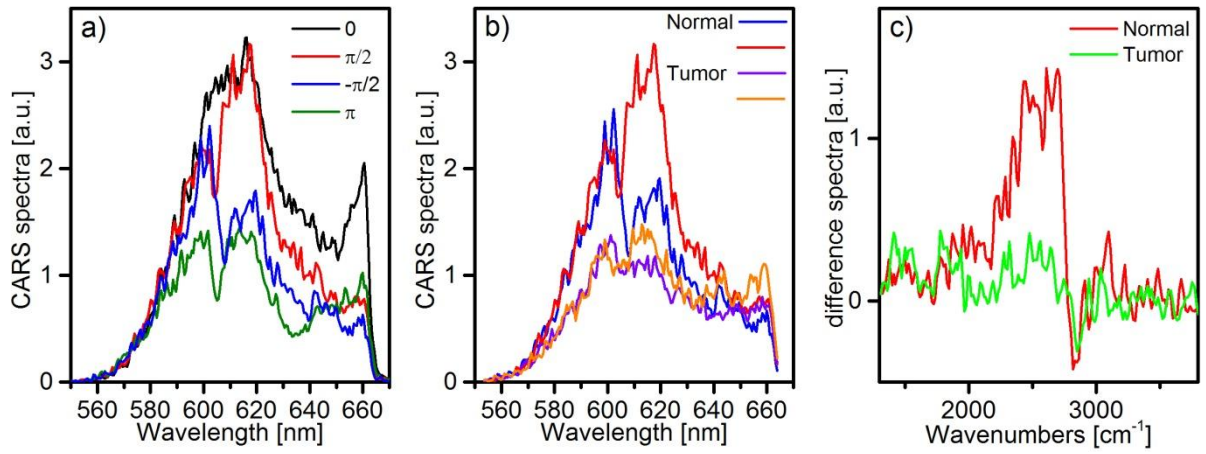

Figure 4.30 Acquisition of DQSI spectra in brain and tumorous tissues. a) Raw CARS spectra obtained inside the normal tissue with a probe phase of 0 (black curve), π/2 (red), - π/2 (blue) and π (green). b) Comparison of (π/2)- and (-π/2)-phase spectra in the normal tissue (red and blue, same as in a) and in the tumor (orange and violet). c) Spectra obtained by subtraction of the signals shown in b) in the tumor (green) and in the normal region (red). The Raman shift is calculated with respect to the center of the probe pulse.

From equation (54), we learn that the spectrum calculated by DQSI depends on the quantity:

$$\sqrt{\left[S_{\varphi_p=0}(\omega)-S_{\varphi_p=\pi}(\omega)\right]^2+\left[S_{\varphi_p=\pi/2}(\omega)-S_{\varphi_p=-\pi/2}(\omega)\right]^2} \qquad (61)$$

where $S_{\varphi_p=\alpha}(\omega)$ denotes the raw CARS signal when the phase of the probe pulse is assigned to α. This analysis method is sensitive to the strong variations of the background. The spectra in Figure 4.30 (a) make apparent that the background is maximized when $\varphi_p = 0$ and minimized for $\varphi_p = \pi$. In turn, π/2 and –π/2 phases have the same effect on the nonresonnant contribution but affect differently the resonant signal. This is confirmed by the observation of spectra inside the tumor and in the healthy tissue (Figure 4.30 b) for these phases. Additionally, if we suppose the background has a constant phase equal to 0, a Raman-

equivalent signal can be obtained from two measurements only. Starting from equation (50), we calculate:

$$S_{\varphi_p=\pi/2}(\omega) - S_{\varphi_p=-\pi/2}(\omega) \propto -4\left|E^p_{CARS}(\omega)\right|\left|E^B_{CARS}(\omega)\right|\sin\varphi_\chi \propto -Im(\chi^{(3)}_{CARS}) \qquad (62)$$

Spectra obtained by this subtraction method are shown in Figure 4.30 (c). The much stronger signal in the healthy tissue allows imaging its margin with a similar contrast to Figure 4.29 (c). However, the retrieved spectra do not correspond to the Raman data measured with the spontaneous Raman system. A comparison with Figure 4.27 (c) shows that the bands are expected around 2900cm^{-1}, a region where negative signals appear in Figure 4.30 (c). We therefore must conclude that the broadband signal is also sensitive to the phase and hence not purely nonresonant. This is easily understood by considering the change in A(Ω) obtained by amplitude shaping (Figure 4.28 c): the portion of the broadband signal due to vibrationally resonant contributions is not negligible anymore. The broad peak covering the region from approximately 2200cm^{-1} to 2800cm^{-1} in Figure 4.30 (c) is due to this resonant portion of the broadband signal.

The presented method is efficient to extract a resonant signal from the raw data but does not provide Raman equivalent spectra. For the studied melanoma tumor in the brain, a simple comparison of integrated signals allows contrasted imaging. The spectral differences could be also useful in more complex samples. The use of principal component analysis (PCA) in unknown samples[95] is for example applicable to SB-CARS spectrally resolved data. Although precautions are necessary in the interpretation of single-beam spectra, imaging of unknown samples is then possible.

4.4.3 Imaging with spectral focusing

In turn, spectral focusing is ideally suited when a single resonance is known to provide the maximal contrast. It allows rapid imaging in a single-beam CARS setup without the need of spectrally resolved detection. Based on the spontaneous Raman and MCARS spectra of healthy and tumorous tissue, the band at 2890 cm^{-1} specific of lipids is chosen.

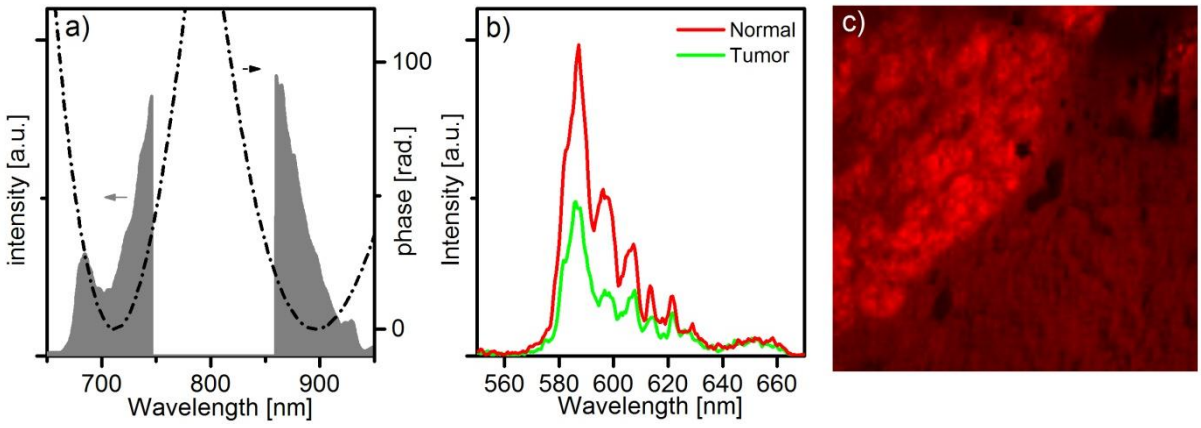

Figure 4.31 Spectral focusing imaging of the tumor boundary. a) Shaping scheme: amplitude shaping eliminates the part of the pulse not contributing to the excitation of the 3000cm^{-1} region (gray curve). The spectral focusing phase selects Δω=2890cm^{-1} and GDD=5000fs^2 (dotted line). b) Raw CARS spectra obtained in the tumor and in normal tissue. c) Image of a 100µmx100µm region at the tumor boundary obtained by integrating the signal.

Amplitude shaping is again used to reduce the incident intensity and a spectral focusing phase (GDD=5000fs^2) is added (Figure 4.31 a). The central part of the pulse does not contribute to

the excitation of the higher lying Raman shifts; it does neither contribute to the probing in spectral focusing. Amplitude shaping also avoids potential artifacts due to phase wrappings in the central region. In comparison to spectrally resolved techniques, the signal obtained by spectral focusing does not compete with a strong background. If we consider the spectrally resolved spectra obtained in the tumor and in the normal region shown in Figure 4.31 (b), it becomes evident that the form of the signal is now independent of the position in the sample. A contrast similar to what has been obtained with spectrally resolved methods is obtained here by integrating the signal to image the tumor boundary (image in Figure 4.31 c).

4.5 Discussion and outlook

Three important experimental challenges have been mastered in the work presented in this chapter: first, precise shaping of a broadband sub-10fs pulse in a compact folded 4f-line has been realized. Second, the translation of this precise shaping in the focus of a microscope objective was achieved. Third, the acquisition of whole CARS spectra up to the CH stretch region based on a SB-CARS were demonstrated with time resolved, spectrally resolved and spectral focusing techniques.

These experimental realizations stand at the foundation of the successful imaging of a sensitive biological sample for the first time with SB-CARS. The evaluation of the various available schemes in the context of imaging resulted in a differentiated picture: the time resolved acquisition of spectra proved impractical because of the number of measurements needed to identify a compound properly; spectrally resolved schemes as well as spectral focusing allowed the distinction of tumor from healthy brain tissue. This success was obtained on the basis of Raman levels next to the limit accessible with the laser proving simultaneously the importance of the CH stretching region for biological imaging and the precision of shaping. The solution to the identified limitations and constraints encountered in sensitive samples remain challenging and could be the basis of exciting future developments of each SB-CARS method.

With spectral focusing, the goal of a single channel imaging implementation has been achieved. In comparison with previously demonstrated setup based on passive chirp generation, the shaper allows a better control of the phase of the pulse. The third-order and higher order dispersion is usually left uncorrected and deteriorates the spectral resolution of the method. In contrast, the shaper reproduces exactly the programmed phase function but is limited in the amount of GDD: much higher values are accessible with passive elements. The delay between the broadband pump and Stokes pulses can be used to rapid adjust the Raman shift. In the single-beam approach, it would necessitate an experimentally more demanding rapid shaping apparatus (for example using a 2D LCOS mask [143, 192] or an acousto-optical modulator). Therefore, a setup taking the advantages of both methods could use a shaper and divide the pulse in two pathways with additional chirp. To improve the performances of the setup in the single-beam configuration, a transition from parabolic to optimized phase functions seems promising. The concept would remain the same: to divide the pulse into a “pump” and a “Stokes” regions separated by the selected Raman shift to which the same phase is applied. The constant phase relationship is then ensured and $A(\Omega)$ remains the same

as for the FTL pulse, independently of the chosen phase function. Evolutionary strategies, for example, could then be used to search the phase-functions space for alternatives to simple GDD functions. In addition, an important extension of spectral focusing would be the simultaneous excitation of several Raman levels, for which the scheme with three parabolic functions is a starting point.

A more precise distinction between the tumorous and the healthy tissue was expected from the acquisition of spectra compared to spectral focusing. Here, constraints on pulse energy imposed by the sample resulted in distortions and the inability to identify precisely the bands responsible for contrast. Nonetheless, the identification was possible without previous knowledge of the precise position of the main Raman bands. These promising results could be improved after careful analysis of the phase distortions in the spectrally resolved techniques. In particular, the phase and intensity variations of the broadband signal should be understood and quantified. Modified DQSI equations correcting the influence of the phase of the probe on the broadband signal will allow a better identification of the involved Raman levels [193].

As compared with state of the art CARS or SRS microscopes, the SB-CARS methods based on shaped ultrashort pulses have not yet reached the maturity of simpler systems. The work presented here represents an important extension of SB-CARS capabilities to even shorter pulses and hence even broader spectral ranges. Due to the bandwidth of the laser and its Gaussian spectrum, the signal level for the $3000cm^{-1}$ region remained suboptimal in this first demonstration. An experimental realization with an even broader spectrum is therefore desirable before comparing the performances of the SB-CARS and of state of the art systems for imaging.

A major advantage of the SB-CARS approach, its flexibility, could then be fully exploited. As demonstrated in this chapter, the acquisition of precise and broad CARS spectra and rapid single-channel imaging are available in the setup. Switching between the different modalities simply relies on a change in the applied phase functions. SB-CARS will open new possibilities for the imaging of unknown samples. For example, imaging of a large area by concentrating of a single Raman band to acquire structural information could be combined with precise spectral measurements at selected locations in the sample. If a known compound has to be identified in a biological context, rapid scanning is necessary for its localization while precise spectral information is needed for accurate identification. A setup combining both modalities is desirable in this case.

A simpler way to increase the contrast in the imaging with 10fs pulses is the simultaneous recording of other nonlinear signals. Because they appear at well separated wavelengths highlight other structures and do not suffer from the same issues related to nonresonant signal as CARS, multimodal imaging is indeed very promising with the SB-CARS setup and will be discussed in the next chapter.

5 Multimodal non-linear microscopy with shaped ultra-broadband pulses

The idea behind multimodal non-linear microscopy is to take advantage of the similar requirements for all non-linear effects to increase the acquired information at a low experimental cost. The complementary information and spectral separation of signals makes it easy to obtain well contrasted images while short-pulse lasers are favorable for all effects. However, as seen in the case of CARS, the ideal pulse configuration can differ depending on the exact mechanism involved in nonlinear signal generation: CARS setups usually use two picoseconds pulses with tuned frequency difference while 100fs pulses and shorter are recommended for TPEF and SHG microscopy.

In the previous chapters, the main experimental challenges necessary to explore multimodal imaging with shaped 10fs pulses have been mastered. On one hand the ability to compress pulses down to 10fs in focus and to control their phase exactly has been demonstrated. On the other hand, the developed broadband CARS schemes for biological imaging provide the supplementary dimension of chemical imaging, even if the acquisition of precise spectra is time consuming.

The following investigation examines the benefits of shaping in the context of multimodal microscopy. Based on theoretical considerations, the optimization of the pulse shape for each nonlinear effect is discussed. Specific of multimodal imaging, the effect of phase distortions on each nonlinear effect is compared.

5.1 Broadband nonlinear microscopy

In this section, a theoretical model for the simulation of multimodal nonlinear spectra is presented. In a similar way to the CARS, a great number of photon combinations contribute to the excitation of other nonlinear effects. Interferences between the different pathways are then adequately described by the integral formulations shown in the following. The spectral extent of CARS, TPEF and SHG evolves differently when the pulse duration is decreased. This effect and its implications when comparing a 10fs excitation pulse to the usual >100fs durations are also examined.

5.1.1 Theoretical expressions

In the case of SHG generation with a broadband pulse, the different wavelengths can interact in a way more correctly designed as “sum-frequency generation” (SFG). In SFG, two photons of different energies interact to produce a photon with the sum of the energies[47]:

$$P^{(2)}(\omega_1 + \omega_2) = 2\varepsilon_0\chi^{(2)}(\omega_1 + \omega_2, \omega_1, \omega_2)E(\omega_1)E(\omega_2) \quad (63)$$

Far enough from resonances $\chi^{(2)}$ is independent of ω and the summation over the different available photon pairs can be written as the integral:

$$S^{(2)}(2\omega) \propto \chi^{(2)} \int E(\omega - \Omega)E(\omega + \Omega)d\Omega \quad (64)$$

In the rest of this document, we will refer to sum-frequency generation and second-harmonic generation indifferently as “SHG” signals.

For TPEF, the signal strength depends on various parameters like the two-photon absorption cross-section and to the fluorescence quantum yield of the fluorophore. The two-photon fluorescence cross section σ_{TPEF} [6, 194] summarizes this dependence and links the detected signal to the laser intensity. For a narrowband excitation:

$$S_{TPEF} = \frac{1}{2}\sigma_{TPEF} I_{\omega}^{2} \,. \tag{65}$$

If we consider the emission spectrum as independent of the excitation, we can use this cross section to calculate the signal generated by a broadband pulse. For the spectrally integrated signal S, we obtain [192]:

$$S_{TPEF} \propto \int \sigma_{TPEF}(\omega) \left| \int E(\omega') E(\omega - \omega') d\omega' \right|^{2} d\omega \,. \tag{66}$$

The broadband generation of CARS signal has already been discussed in detail (chapter 2.1.1). We simply remind here the formula

$$S_{CARS}(\omega) \propto \int \chi^{(3)}(\Omega) E_{probe}(\omega - \Omega) \int E^{*}_{Stokes}(\omega' - \Omega) E_{pump}(\omega') d\omega' \; d\Omega \tag{67}$$

As already described, the third-order susceptibility $\chi^{(3)}$ is a complex quantity in contrast with the formulas for SHG and TPEF which display only real quantities.

5.1.2 Pulse duration

Before we consider the effects of shaping on the different non-linear effects, it is helpful to consider how they evolve when the excitation is changed from a longer (1ps) to a shorter (10fs) pulse. In a first approximation, the evolution towards shorter laser pulses for non-linear microscopy seems to be natural. In analogy to the "two-photon" advantage of TPEF [9], a non-linear signal of the order n scales with $(1/\tau)^{n-1}$, τ being the pulse duration and the pulse energy is kept constant. This relation simply relies on the equation $I_{Signal} \propto I_{laser}^{(n)}$ and a shorter pulse with higher peak intensity gives rise to a higher non-linear generation. For example, a pulse train at 100MHz with pulse durations of 100fs will generate 10^5 more TPEF signal than a CW-laser with the same mean power. However, this increase only holds as long as the pulses do not become shorter than the lifetime of the phenomenon responsible for the non-linear signal generation. The phenomena based on purely electronic contributions happen on the scale on which the electron cloud is deformed by the incident field, typically below one femtosecond: this is the case for the SHG process as well as for $\chi_{NR}^{(3)}$. These phenomena are considered instantaneous in our case. On the other hand, the vibrational levels of molecules in liquids have lifetimes in the picosecond range[195]. Hence, a shorter pulse like the 10fs pulse used here does not excite ideally these transitions as pointed out by Cheng et al. [196].

This evolution can also be easily understood in the spectral domain. The nonlinear response function in the time domain is the Fourier transform of the corresponding nonlinear susceptibility. Similarly, a shorter pulse will also have a wider spectrum. The excitation can then be considered ideal when the spectral width of the pulse matches the spectral width of the nonlinear effect. Since SHG is mediated by a nearly frequency independent $\chi^{(2)}$ the shortest pulse will be best suited, while for a Raman transition the combination of two ps-pulses matches the spectrum.

The nonlinear generation is still more efficient with shorter pulses when the spectral acceptance of the effect is exceeded, but with a much less rapid pace than the $(1/\tau)^{n-1}$ rule. It seems, therefore, that the reduction in pulse duration will be beneficial in this case also. The limiting factors have however to be considered: the maximum power a sample can withstand is determined by a variety of photodamage mechanisms, including linear and nonlinear ones. When a pulse becomes short enough phenomena like optical breakdown, plasma formation or two- and three-photon absorption take place [41]. These scale highly nonlinearly with the laser intensity, setting a lower limit to the pulse duration producing the maximum signal. A too short pulse also reduces the specificity of the CARS signal: the non-resonant contribution increases much more rapidly than the resonant one for pulses shorter than the lifetime of the resonance. The non-resonant contribution itself also gives rise to a contrast, but this in turn prevents from identifing if the signal variation is due to a resonant contribution on top of a non-resonant background or to a variation of this background.

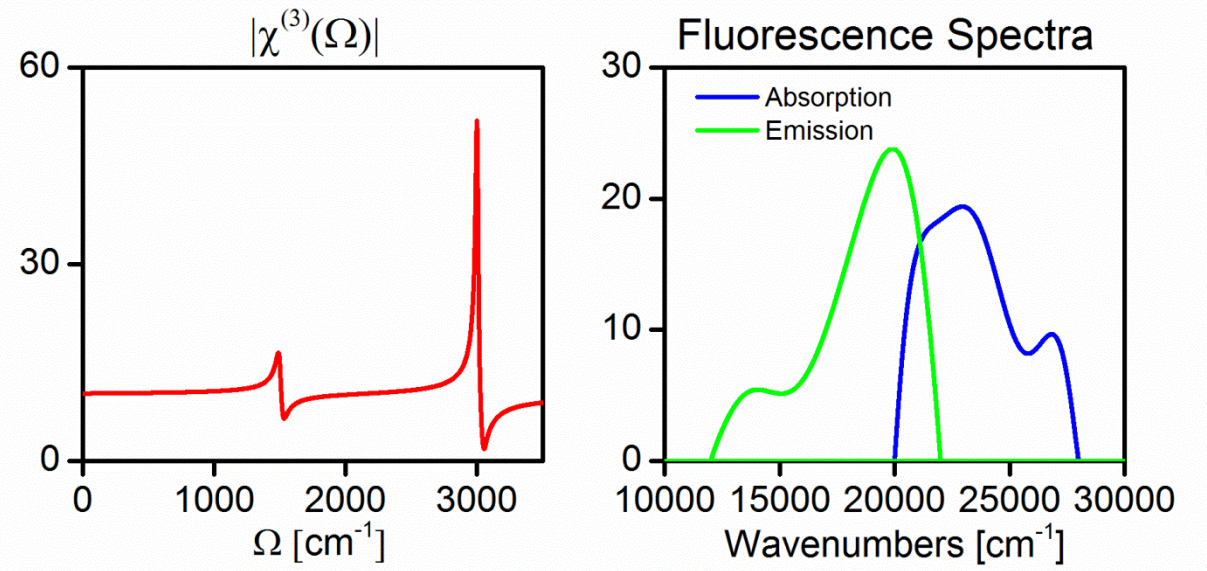

Figure 5.1 Molecular parameters used for the simulation of multimodal nonlinear spectra (resulting spectra in **Figure 5.2**). For CARS, a molecule with bands at 1500cm^{-1} and at 3000cm^{-1} has been chosen. For TPEF, the arbitrary absorption spectrum is chosen to have a broad overlap with the two-photon spectrum of our pulse.

How does the pulse duration affect the spectra of the produced nonlinear signals? We first assume that the pulse used is Fourier-transform limited (FTL). In this configuration the pulse duration is inversely proportional to the spectral width. Let us consider three pulses with the same energy and durations of 1 ps, 100 fs and 10 fs. The pulses are represented in the time domain as well as in the spectral domain in Figure 5.2. The generated nonlinear signals are calculated using the integral formulas presented above (equations (64), (66) and (67)). The parameters for the sample material have been simulated as follows: $\chi^{(2)}$ is chosen to be a constant, $\sigma_{TPEF}(\omega)$is a smoothly varying function ranging from 20000 cm^{-1} to 28000 cm^{-1} (357 nm to 500 nm). The TPEF emission spectrum is also a smoothly varying function shifted to the red in comparison with the absorption (455 nm to 833 nm). For CARS, $\chi^{(3)}$ is simulated with two resonances at 1500 cm^{-1} and 3000 cm^{-1} with respective amplitudes A_i of 100 and 500 and linewidth Γ_i=20 cm^{-1} and 10 cm^{-1}. A constant non-resonant background $\chi_{NR}^{(3)} = 10$ is added. The TPEF absorption and emission spectra as well as

$\chi^{(3)}(\omega)$are shown in Figure 5.1. For clarity, the factors $\chi^{(2)}, \sigma_{TPEF}$ and $\chi^{(3)}$ are adjusted to display signals of comparable spectral intensity with the 10 fs pulse. The simulation intends to compare the influence of pulse duration on the different nonlinear effects.

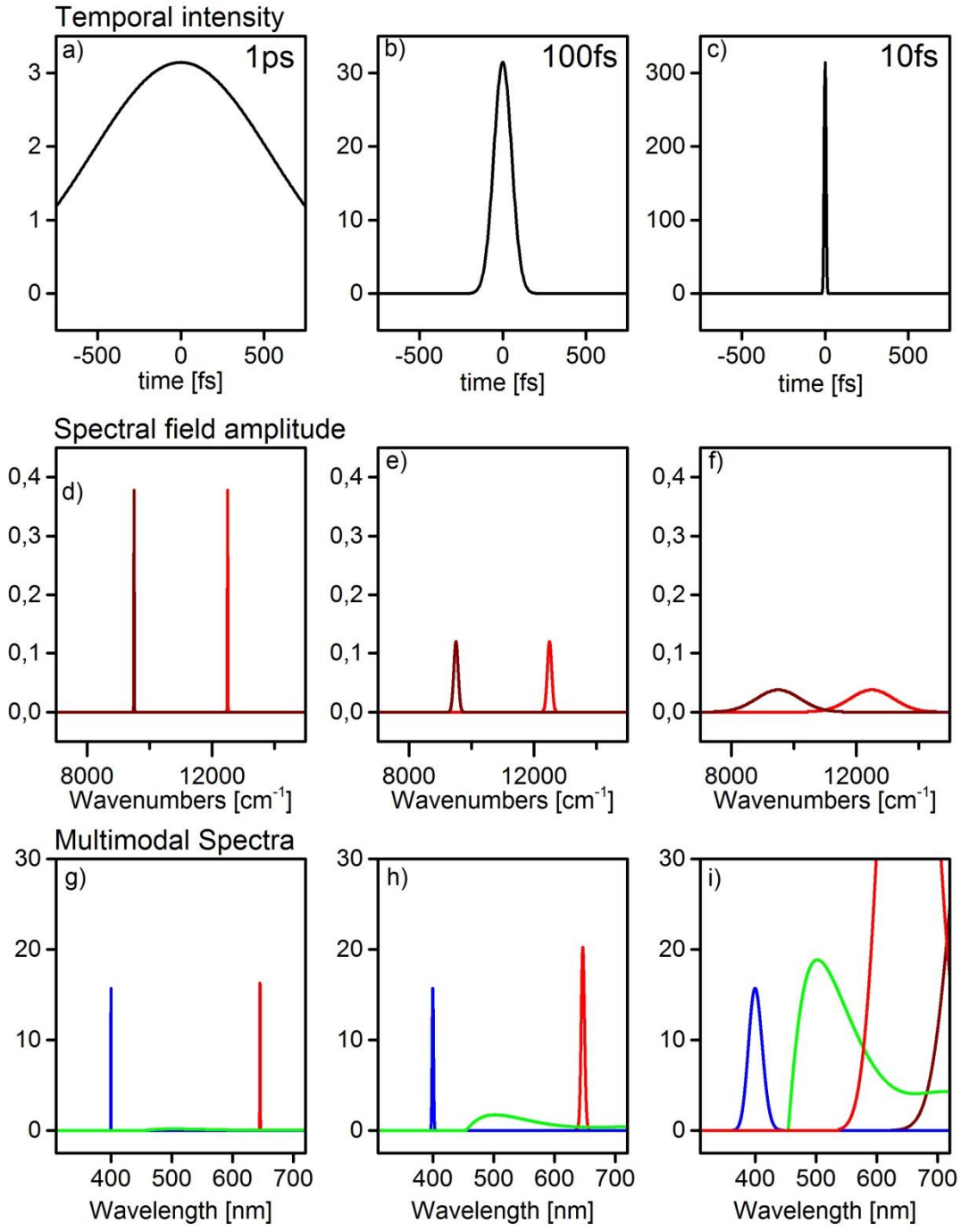

Figure 5.2 Effect of pulse duration on the different nonlinear effects. Three pulses duration are simulated: 1ps (a,d), 100fs (b,e) and 10fs (c,f). The spectra shown in red in (d,e,f) are used to calculate the SHG and TPEF signals. An additional pulse matching the 3000cm^{-1} resonance is shown in brown and used to calculate the CARS signal. The spectra for SHG, TPEF and CARS are represented in (g,h,i) in blue, green and red color respectively. In the 10fs-case (i), the brown curve indicates the CARS signal resulting from the red excitation pulse in f) alone.

The resulting multimodal nonlinear spectra are represented in Figure 5.2 (g), (h) and (i). The simulated data clearly show the expected increase in nonlinear generation and highlights some

interesting differences. For SHG the increase in signal is due to a spectral broadening of the two-photon spectrum. The central spectral intensity in the signal (here at 400 nm) remains unchanged, although the spectral intensity at the central wavelength of the incident laser decreases in favor of neighboring wavelengths. In the case of the TPEF signal, the emission spectrum was assumed to be unchanged and equation (64) results in integrating the larger two-photon spectrum (equivalent to the SHG spectrum).

The CARS signal is enhanced by a combination of these two phenomena: a broadening in the spectral domain and an increase of the intensity. The combined increase results in an integrated signal about 10 times stronger with a 100fs pulse than with a 1ps pulse and a further increase of about 500 times with a 10fs pulse. As mentioned earlier however, it is worth considering how much of this increase is due to vibrationally resonant signal and to nonresonant background. Figure 5.3 compares the CARS signal calculated with the $\chi^{(3)}$ presented above (Figure 5.1) and when the amplitude of the resonances is set to $A_i = 0$. This would for example correspond to the contrast between two regions of the sample with similar $\chi_{NR}^{(3)}$ and only one of them displaying resonances. For each pulse duration, the simulation assumes two pulses separated by 3000 cm^{-1}, different from the SB-CARS setup. The best contrast is obtained with the 1ps pulse where the background represents about 1/15 of the signal from the resonant molecule. In the case of a 100fs pulse this ratio drops to ½: a compromise has to be found between signal intensity and contrast. When a 10fs pulse is used there is almost no difference between the signals from the region without resonances and from the region displaying them. Due to the coherent character of the CARS process the intensity even decreases in the blue wing of the signal when resonances are present. In this spectral region the resonant contribution interferes destructively with the nonresonant background.

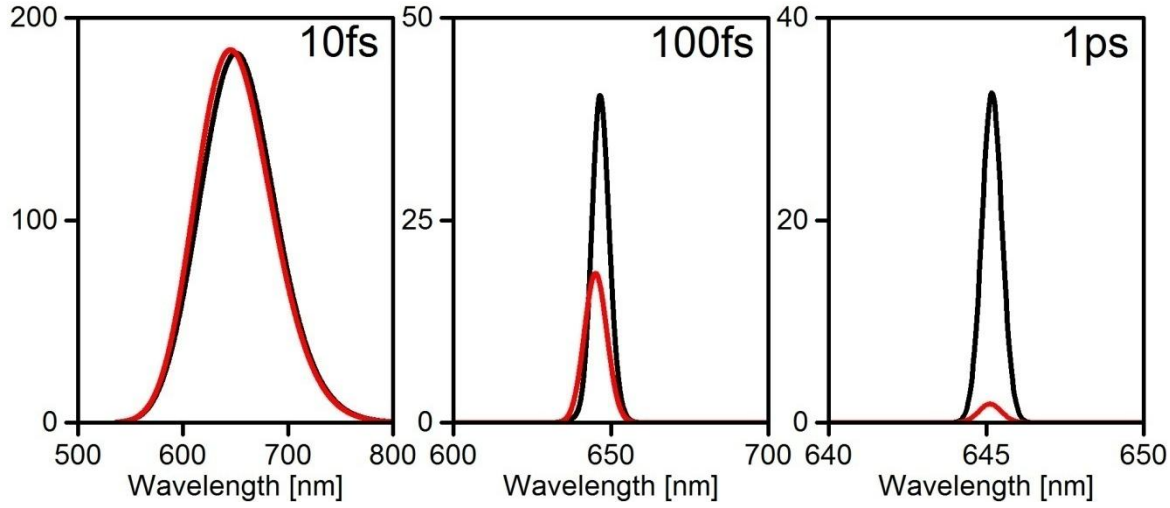

Figure 5.3 Comparison of the CARS signal from a sample with a resonance at 3000cm^{-1} (black curves) and purely non-resonant (red curve). The signal is generated by two pulses separated by 3000cm^{-1} and with durations of 10fs (left), 100fs (center) and 1ps (right).

Based on these considerations a lack of contrast is expected with FTL pulses. Compared to a pair of ps pulses properly tuned to the resonance the excitation by a single 10fs pulse lacks efficiency, in particular for high wavenumbers. A large part of the spectrum cannot contribute to resonant signal when the modes have larger wavenumbers than the bandwidth of the pulse.

Considering the broadening of nonlinear spectra generated by shorter pulses, the stronger signals can come at the cost of an increased overlap between nonlinear signals of different molecules, or produced by different mechanisms. CARS and SHG spectra remain well separated but their broadening favors overlap with the TPEF signals. In fact this problem is not specific of an implementation with ultrashort 10fs pulses since the width of TPEF spectra is independent of pulse duration. Surprisingly, the overlap between signals of different nature is often neglected in literature about multimodal nonlinear microscopy, even when sub-10fs pulses are used [197]. In contrast the TPEF literature is rich of examples of overlapping spectra [198]. Although known emission spectra of fluorescent dyes allow selecting spectral regions without overlap, this can strongly reduce the detected signal. Varying the excitation wavelength gives an additional way to differentiate between the contributions complementary to spectrally resolved detection [13]. Using excitation by broadband pulses, fluorophores can be excited simultaneously. If the emission spectra are not well separated, shaping can then be used to obtain selective excitation and disambiguate the signal origin.

5.2 Influence of shaping

In the following considerations on the influence of shaping in a multimodal nonlinear imaging system, equations (64), (66) and (67) are assumed to describe accurately the physics on the molecular side and the excitation is limited to one shaped broadband pulse. Such a configuration has been extensively studied for microscopy and spectroscopy using Two-photon absorption, CARS or TPEF [92]. Besides the acquisition of CARS spectra with help of the shaper presented earlier, shaping has been used to excite selectively fluorophores [70, 199] or Raman modes [148]. The specificity of this work is to consider the interplay of nonlinear effects of different natures. Besides optimizing nonlinear generation of individual effects, shaped pulses are also used here to tackle the issue of overlapping nonlinear signals. We also take into account the limitation of the peak power imposed by nonlinear photodamage mechanisms to find the ideal pulse configuration.

In continuity with the previous considerations on pulse duration and efficiency of the nonlinear signal generation, the effect of simple phase distortions is first considered. An evolutionary optimization is then performed to selectively generate CARS or TPEF signals.

5.2.1 Influence of chirp

Starting from a FTL pulse obtained by pulse compression *in situ*, it is possible to test distortions that correspond to a constant GVD or to a constant TOD. The central wavelength and steepness of the parabolic function (or of the 3rd order polynomial for TOD) can be easily chosen with the shaper.

Following the previous discussion on pulse duration, we expect the different nonlinear effects to display different responses to pulse distortions. Namely, chirp (GDD) and second order chirp (TOD) should reduce the signal generation efficiency for all effects and affect more strongly CARS, as a 3-photon process, than TPEF or SHG. We first concentrate on CARS and SHG only, TPEF being derived from the two-photon spectrum represented by SHG.

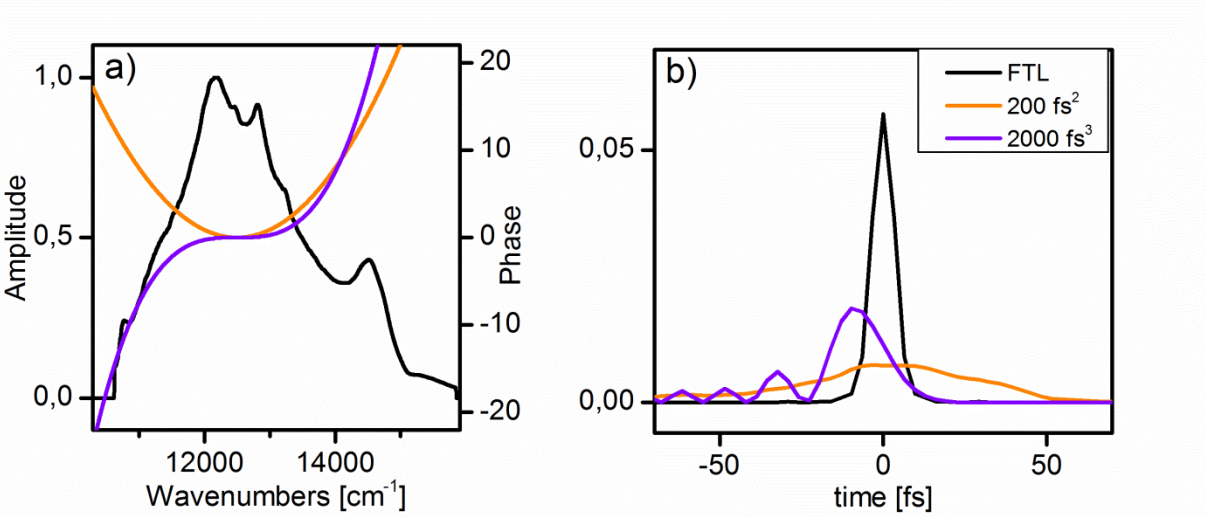

Figure 5.4 Chirped pulses. a) represents the spectral intensity (same for all pulses, left scale) and spectral phase (right scale) for a FTL pulse (phase constant not shown), a pulse with a phase function corresponding to a constant GDD of 200 fs^2 (orange) and a pulse with a constant TOD of 2000 fs^3 (violet). Both phase functions are centered at 12500 cm^{-1} b) Temporal intensity of the FTL, 10fs pulse (black), the 200fs^2 pulse (orange) and the 2000fs^3 pulse (violet).

A measured spectrum from our laser is displayed in Figure 5.4 as well as a GDD and a TOD phase functions. The GDD phase (orange line) is simply a parabolic function; mimicking a pure group delay dispersion of 200fs^2 (no global group delay and no higher order dispersion. The cubic function (violet line) represents a pure TOD phase of 2000fs^3. As can be seen from Figure 5.4 a) this represents moderately steep phase functions considering the resolution of the shaper. However, the distortion of the pulse is quite significant (Figure 5.4 b). The pulse is uniformly stretched by the constant GDD resulting in pulse duration of about 60fs (FWHM).

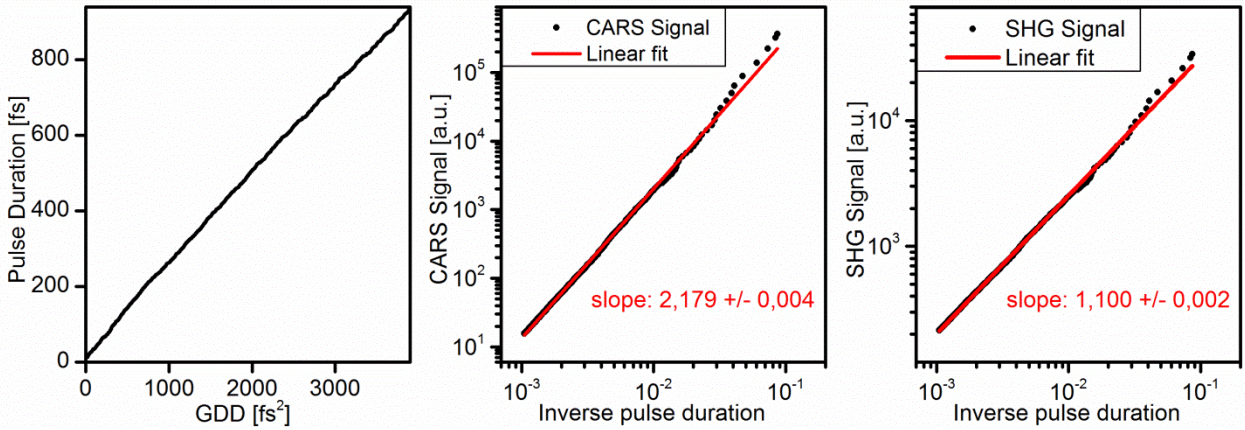

Figure 5.5 GDD and pulse duration. Left: GDD uniformly distorts the pulse in time, the resulting pulse duration is proportional to the amount of GDD (when its value exceed the squared FTL pulse duration). Center: The integrated CARS intensity for a chirped pulse depends quadratically on the inverse pulse duration. Right: The integrated SHG signal is proportional to the inverse pulse duration of the chirped pulse.

This directly impacts on the nonlinear signal generation efficiency of the chirped pulse. The CARS and SHG signals resulting from pulses affected by an increasing amount of GDD or TOD were calculated using the formulas given above. For GDD distortions, the envelope of the pulse in the time domain was also calculated and its full width at half maximum used as a measure of the pulse duration. For GDD values exceeding the square of the FTL pulse duration, the duration of the chirped pulse is proportional to the amount of GDD, as seen in

the left panel of Figure 5.5. The SHG signal is inversely proportional to the pulse duration τ and the CARS signal is proportional to $\frac{1}{\tau^2}$ as confirmed by the log/log plots in Figure 5.5 center and right panels. For TOD distortions, the time dependence is similar to the violet curve in Figure 5.4 b) and the determination of pulse duration is not straightforward. Nevertheless, the SHG/CARS ratio varies in a similar way. The dependence of the integrated signals is summarized in Figure 5.6. Both for GDD and for TOD phases, signal generation rapidly decays, while the SHG/CARS ratio rapidly increases as seen in Figure 5.6 c). The figure suggests that the ratio can only be increased at the cost of signal intensity, and there is little difference between the choice of a GDD or of a TOD phase function to do so, as the integrated signal depends mainly on the peak intensity.

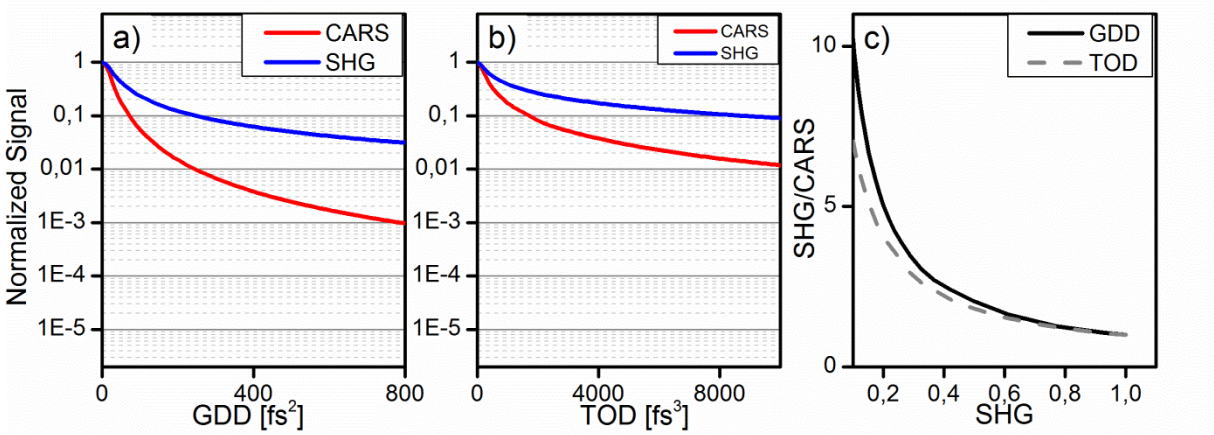

Figure 5.6 Evolution of non-linear signals with increasing chirp. a,b) Integrated CARS (red) and SHG (blue) signals as a function of GDD (a) and TOD (b). The signals are normalized by their respective value for a FTL pulse and displayed on a logarithmic scale. c) Evolution of the ratio SHG signal vs CARS signal as a function of the normalized SHG signal, when applying GDD (black) and TOD (gray, dashed line).

If we look at the generated CARS and SHG spectra, however, the picture is slightly different. Figure 5.7 and Figure 5.8 present the spectra for the phases presented in Figure 5.4 : respectively GDD=200 fs^2 and TOD=2000 fs^2. SHG signals are shown over their whole spectral range, while only the blue wing of the CARS spectra is shown. This corresponds to the experimental requirements of a Single-Beam CARS setup, where the signal can only be detected outside of the range of the exciting laser. Since the nonlinear spectra are not necessarily uniformly affected by phase distortions, quite a different picture appears.

The GDD function slightly narrows the spectra for both contributions and simultaneously decreases the intensity of the whole spectrum. The SHG spectrum will appear quite similar to the SHG generated by a FTL pulse, simply with a smaller intensity (Figure 5.7 b). In a multimodal experiment using a single 10fs-pulse the CARS signal cannot be completely integrated as can the SHG spectrum. Only the blue wing of the spectrum is detected in order to lose as less excitation spectrum as possible. The simulation in Figure 5.7 a) shows that the blue side of the CARS signal is drastically reduced by the 200fs^2 phase. A factor more than 5000 between the chirped pulse and the original one comes out of the calculation. This value has to be compared to the evolution of the integrated signal seen in Figure 5.6 a) : based on this graph, a reduction of about 2 orders of magnitude only is expected.

What happens in the case of a TOD phase function? With a TOD=2000 fs^3 function the reduction of nonlinear generation efficiency is much less than with the GDD=200 fs^2. As

shown in Figure 5.4 these two phase functions have similar steepness on the sides of the excitation spectrum and are therefore comparable in terms of shaper capacity. The TOD phase function has a point of symmetry, namely at 12500 cm^{-1} in this case. It has been shown that such phase functions conserve the corresponding wavelength in the two-photon spectrum [70]. Figure 5.8 shows the typical result of such a phase: the SHG spectrum is strongly narrowed and the two-photon intensity at 25000 cm^{-1} is the same as for a FTL pulse. The effect of the cubic phase distortion on the experimentally detectable part of the CARS signal is also stronger than on the integrated signal but the discrepancy is not as large as for GDD. According to Figure 5.6 a factor 10 is expected with 2000 fs^3 in comparison with the CARS signal from a FTL pulse, instead a factor 100 observed for the blue part of the signal (Figure 5.8 a).

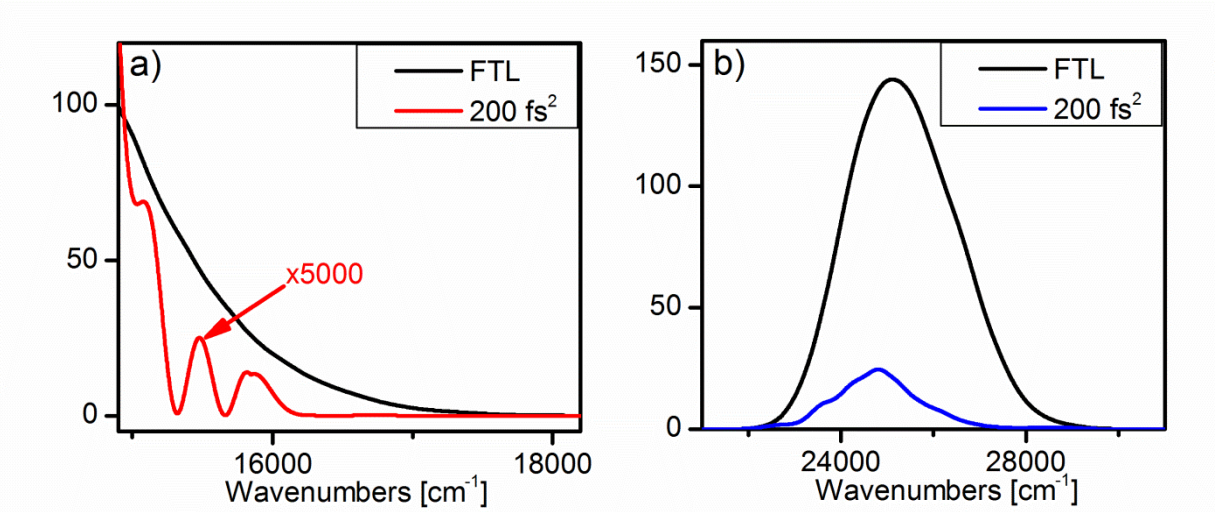

Figure 5.7 Effect of GDD. a) CARS signal generated by a pulse chirped by GDD=200fs^2 (red) compared to the CARS signal of the FTL pulse (black). The signal is shown only on the blue side of the excitation pulse, emulating the experimental conditions for signal detection. Red signal is magnified by a factor 5000 for visibility. b) CARS signal generated by a pulse chirped by GDD=200fs^2 (blue) compared to the CARS signal of the FTL pulse (black).

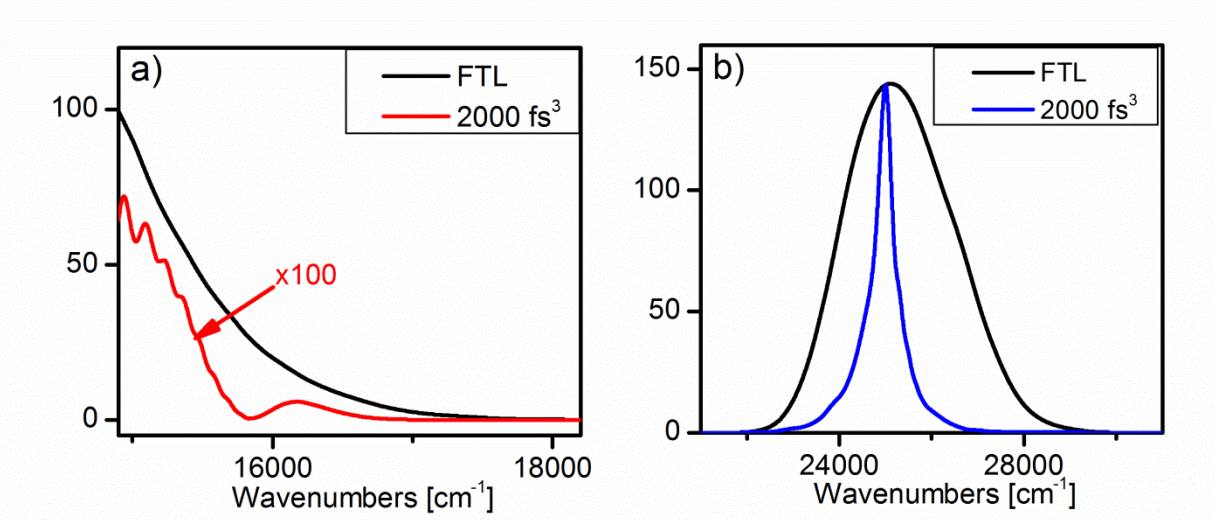

Figure 5.8 Effect of TOD. CARS signal generated by a pulse chirped by TOD=2000fs^2 (red) compared to the CARS signal of the FTL pulse (black). The signal is shown only on the blue side of the excitation pulse, emulating the experimental conditions for signal detection. Red signal is magnified by a factor 100 for visibility. b) CARS signal generated by a pulse chirped by TOD=2000fs^3 (blue) compared to the CARS signal of the FTL pulse (black).

The results of calculations based on the integration of the blue part of the CARS signal (>15000cm^{-1}) are summarized in Figure 5.9, which has to be compared with the totally integrated signal case of Figure 5.6. Two features are particularly interesting for the purpose of distinguishing between overlapping contributions. The first conclusion is that, when considering the part of the CARS spectrum susceptible to overlap with TPEF, the effect of simple GDD and TOD phase distortions is much stronger than what is expected from the simple broadening of the pulse in the time domain. A suppression of the CARS signal by 3 to 5 orders of magnitude is possible by only reducing the SHG signal by a factor of about 10. The same holds then for TPEF, as being proportional to the integrated two-photon spectrum (modulated by the absorption function of the fluorophore). The second interesting finding is that the effects of GDD and TOD phase functions are no longer as similar in Figure 5.9 c) as they were in Figure 5.6 c) providing an additional control of the relative intensities with the choice of the phase distortion. Also important in this context is the effect on the spectral shape of the SHG signal. On the one hand, GDD phase functions almost uniformly attenuate the spectral components of the two-photon spectrum, therefore providing a more predictable effect on the detected signal. On the other hand, a narrower spectrum as provided by TOD could diminish the overlap of SHG and TPEF signals, produce sharper and more recognizable SHG signals and allow exploitation of the absorption curve for the control of the TPEF process.

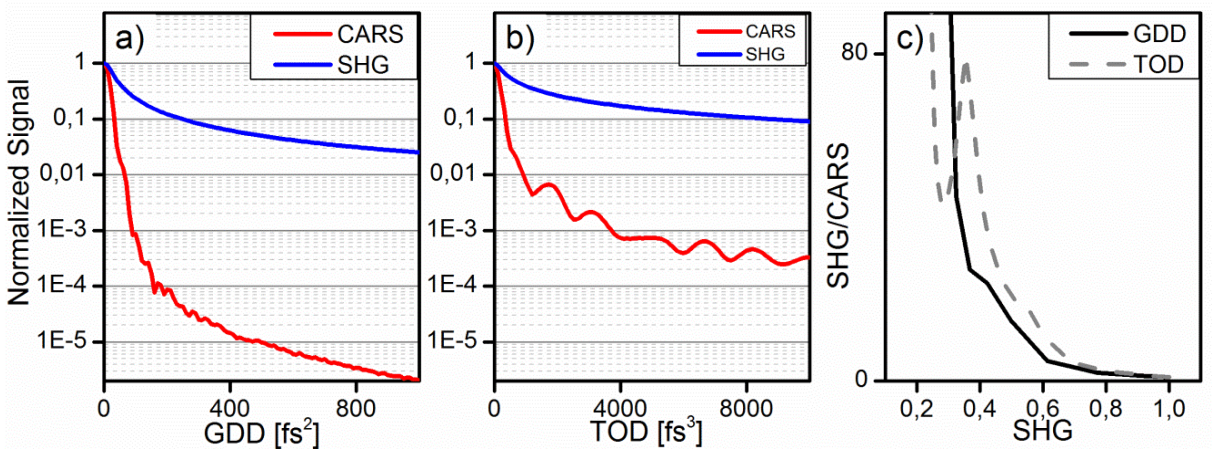

Figure 5.9 Evolution of non-linear signals with increasing chirp. a,b) Integrated CARS (red) and SHG (blue) signals as a function of GDD (a) and TOD (b). The integration limits for CARS are set to the blue side of the excitation spectrum: >15000cm^{-1} , contrary to **Figure 5.6**.The signals are normalized by their respective value for a FTL pulse and displayed on a logarithmic scale. c) Evolution of the ratio SHG signal vs CARS signal as a function of the normalized SHG signal, when applying GDD (black) and TOD (gray, dashed line).

5.2.2 Selective excitation

Worth mentioning at this point is the capacity of shaping to improve the specificity of nonlinear signals obtained with a broadband pulse. Schemes based on simple phase functions or on amplitude shaping will be presented in this part. Rather than optimizing the ratio between different nonlinear signals, we focus here on phases known from former investigations of single effects and their outcome for the other effects as an important parameter in a multimodal setup.

Selective TPEF excitation

As a first example, the aforementioned cubic phase functions for selective TPEF excitation. The very large emission spectra of different fluorophores increase the probability of overlap between them. If the fluorescent molecules are used as dyes for their ability to stain specifically a part of the cell or a molecule of interest, crosstalk between channels assigned to each of them may impair the interpretation of acquired images. Spectrally resolved detection might help to separate the contributions [200-201] but this assumes knowledge a priori of the spectra of each fluorophore separately. Such a condition cannot be fulfilled for endogenous fluorescent molecules.

Figure 5.10 shows an example based on two common fluorophores, DAPI and eGFP. DAPI (4',6-diamidino-2-phenylindole) is an extensively used fluorescent dye. It highlights DNA both in live and in fixed cells [202]. DAPI strongly binds to DNA, mainly in regions rich in T-A base pairs, and the bound form exhibits a much stronger (x20) fluorescence than the free dye. eGFP is an improved form of the green fluorescent protein, widely used in biology [203-204]. The gene coding the fluorescent protein can be recombined with the gene of a protein of interest allowing monitoring its expression in vivo. Alternatively it can be used in fusion proteins, directly tagging the protein of interest. The fluorescence spectra of DAPI and eGFP are shown in Figure 5.10 a) and b) respectively. One-photon absorption and emission spectra are well known and are displayed as a blue and a green line. Two-photon absorption data is more difficult to acquire because its measurement requires pulsed lasers. Available data points from literature (retrieved from www.drbio.cornell.edu) are displayed as red circles. For the purpose of the simulation, a spectrum covering a larger spectral range is simulated by interpolating the known two-photon absorption (TPA) in the covered range and appending arbitrary values outside on the basis of the one-photon absorption spectrum. These values have little impact on the outcome of the simulation, because the region of interest for our laser (350-450 nm) is largely covered by measured data. The excitation spectra have maxima in the wings of the laser approaching a minimum at its center wavelength. Two-photon emission is assumed to be identical to the one-photon excited case.

With a broadband pulse centered at 800 nm both molecules are excited with a similar efficiency. The simulated Gaussian excitation spectrum is shown in Figure 5.10 c) (black line) and results in a broad two-photon spectrum, overlapping in a similar way with the DAPI spectrum on the blue side and with the eGFP on the red side. When TOD phases are applied, the overlap can be tuned to one side while strongly reducing the other. In this simulation both function correspond to TOD=4000 fs^3, in one case centered at 11500 cm^{-1} (red curve in Figure 5.10 c) and in the other case at 13500 cm^{-1}(blue curve). Resulting two-photon spectra are shown in Figure 5.10 d) in red and blue respectively.

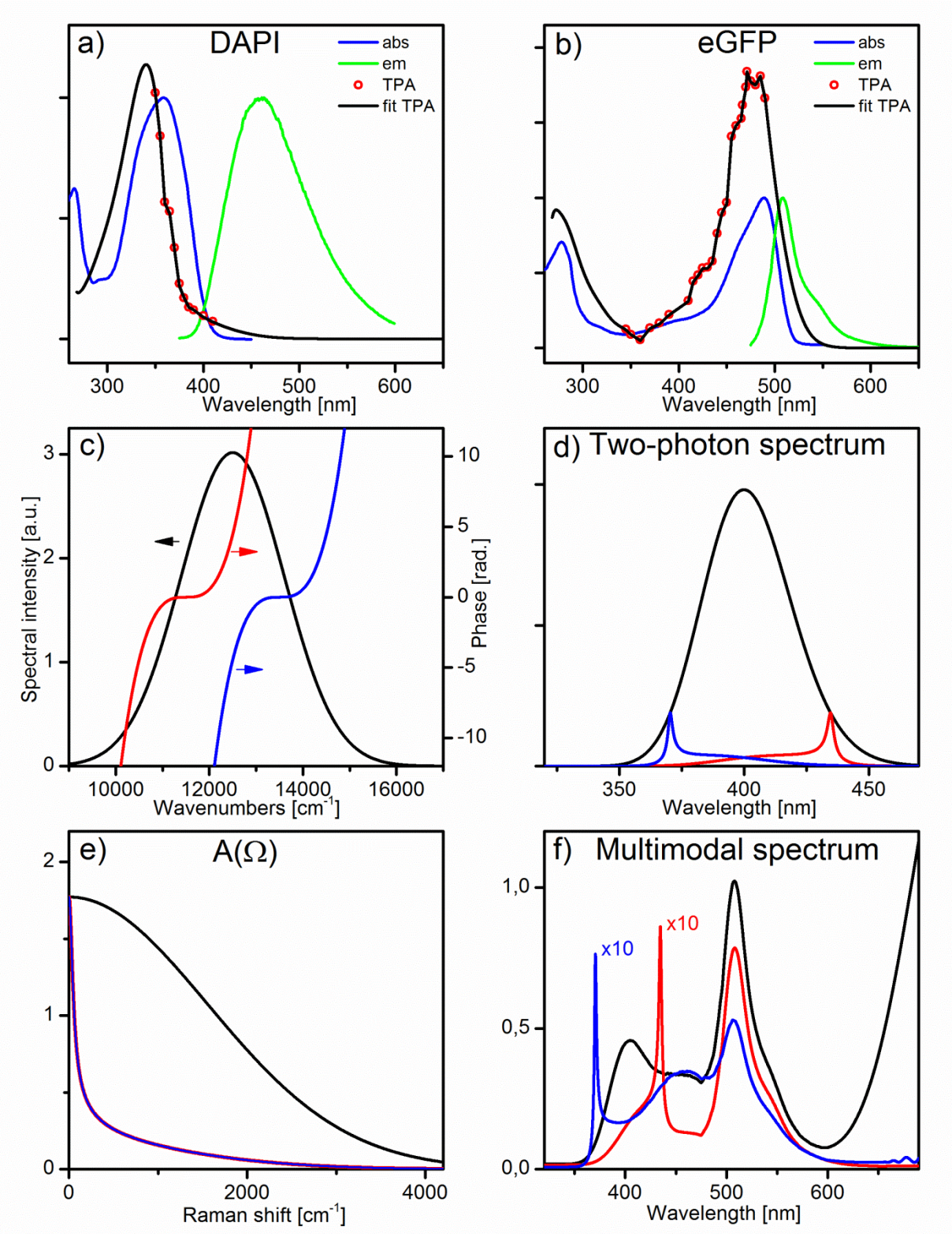

Figure 5.10 Selective two-photon excitation of fluorophores with TOD phase functions. a),b) Fluorescence spectra of DAPI and eGFP respectively. One-photon absorption is displayed in blue, one-photon emission in green. Two-photon absorption from the literature is shown with red circles. For the purpose of the simulation, the two-photon absorption function is interpolated in the region where data is available and arbitrarily set outside. The resulting absorption is shown in black. c) Gaussian spectrum and two TOD phase functions used in this simulation. d) Two-photon spectrum obtained with an FTL pulse (black) and with each of the phase functions (of corresponding color). e) Raman excitation probability obtained with an FTL pulse (black) and with each of the phase functions (of corresponding color). f) Multimodal spectra: addition of CARS,TPEF and SHG spectra. For visibility, the spectra obtained with TOD phase function are multiplied by 10 (red, blue curves) while the FTL case (black) is left unchanged.

The way these phase function affect the multimodal spectrum is shown in Figure 5.10 f). The black curve is the sum of the CARS, of both TPEF and of the SHG contributions when the phase is constantly zero over the spectrum. Fluorescence from DAPI is quite far in the blue and overlaps substantially with the SHG. It also overlaps with eGFP fluorescence over its whole range. In such a case a disentanglement of the contributions with spectral filters is not possible. Pulses with TOD phases produce weaker signals (about one order of magnitude) but the contributions are easier to separate. DAPI fluorescence is about three times stronger when a blue-shifted excitation is used in comparison to the red phase and inversely for eGFP. The SHG signal is at the same time peaked away from the selected fluorescence. With the blue phase a spectral window between 400nm and 470nm is opened to detect almost only DAPI fluorescence, the peak at 370nm is only due to the SHG signal. For a more precise differentiation of signals, spectral detection and comparison of signals obtained with the blue and the red phase can be used.

How does this phase scheme affect the CARS signal? As apparent from Figure 5.10 f) the CARS signal almost vanishes upon application of a TOD=4000 fs^3 phase, as expected from previous considerations on pulse distortions. The effect of both phase functions on the Raman excitation probability is exactly identical: in Figure 5.10 e) the overlap of the blue and of the red curve is almost perfect[2]. Compared to the FTL pulse (black curve), both phase functions have more impact on the large wavenumbers with a rapidly decaying $A(\Omega)$. The exact same $A(\Omega)$ does not however produce the same CARS signal. The CARS signal calculated for the blue TOD function is a factor 2.5 stronger than the CARS signal obtained with the red function. This can be easily understood considering the phase function also determines the efficiency of the probing. The blue phase presents a flat region near to the blue wing of the spectrum were CARS is detected, enhancing the signal generation in this region.

Spectral focusing

A selective excitation scheme for CARS was presented in chapter 4: spectral focusing. This strategy is also based on chirp, but this time on two GDD phase functions. It allows concentrating the energy of the pulse in one Raman transition and is well suited for imaging. The effect of such a phase function on TPEF is presented in Figure 5.11. For CARS, two parameters play a role. Firstly the difference between the central wavenumbers of each parabola, noted $\Delta\omega$, determines the selected Raman transition. Secondly, the amount of GDD of each parabola is responsible for the spectral width of the excitation and accounts for the spectral resolution of the method.

Figure 5.11 (a) presents the dependence of the integrated TPEF signal and of the integrated blue wing (>15000 cm^{-1}) of the CARS signal on GDD. In the simulated example, the same $\chi^{(3)}(\omega)$ was used as in chapter 4.3, mimicking the spectrum of acetonitrile. $\Delta\omega$ was left fixed, tuned at the 2942 cm^{-1} resonance. Both nonlinear signals were chosen to have the same integral with an FTL pulse and their evolution is shown on a log scale to compare their decay

[2] Two TOD=4000 fs^3 functions do not necessarily produce exactly the same $A(\Omega)$: in the particular case of this simulation, the excitation spectrum is symmetric, centered at 12500 cm^{-1} while the blue phase function is centered at 13500 cm^{-1} and the red at 11500 cm^{-1}.

rates. Within the range 0 to 500 fs^2, the evolution is similar to a pure GDD function, because the phase function mainly affects the strong non-resonant contribution of CARS. For bigger GDDs, A(Ω) becomes narrower around the selected region selecting a mainly resonant contribution and the evolution will differ from the pure GDD case. However, the TPEF signal still decreases slower than the CARS signal. In case of overlap between the two signals, this means spectal focusing will provide a more specific CARS signal on the one side, but also a less favorable ratio CARS/TPEF. The best compromise will depend on the initial ratio between the signals, on the ratio between resonant and non-resonant signal for the selected Raman transition and on its bandwidth. The two last factors determine how fast the CARS signal decays with GDD.

Figure 5.11 (b) shows that the TPEF signal also depends on the parameter Δω. This simulation assumes GDD=5000fs^2 and still the same $\chi^{(3)}(\omega)$. The CARS signal is integrated for wavenumbers >15000 cm^{-1} and reproduces the spectrum of the molecule as Δω is scanned (see chapter 4.3.4). At the same time the integrated TPEF signal also varies with Δω and will appear as a background in a measurement of the CARS spectrum with spectral focusing. In our case the maximum of the TPEF signal appears before 1500 cm^{-1}, where no CARS signal is expected, providing an indication on the intensity of this background. The exact form of the background however depends not only on the chosen GDD but also on the absorption spectrum of the fluorophore.

Lastly, a rather intuitive but effective way to obtain selective excitation is to use amplitude shaping. Like in SAM-CARS (chapter 3), the shaper can be used as a filter with an arbitrary transmission curve. Complex filter patterns with high switching rates are achievable: some 10ms with liquid crystal masks but even shorter with acousto-optical devices, or using 2D liquid-crystal masks[143]. This is particularly efficient when used in combination with a PCF-generated supercontinuum[205], which provides large enough bandwidths.

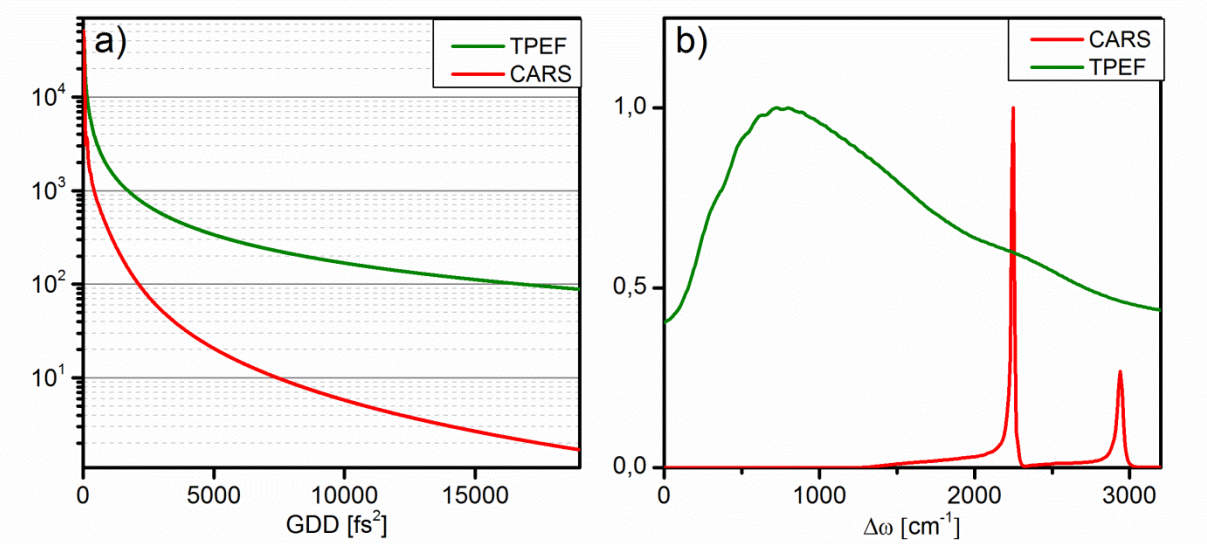

Figure 5.11 Effect of spectral focusing on the TPEF signal. a) Dependence of the integrated TPEF(green) and CARS (>15000 cm^{-1}, red) signal while the amount of GDD of the two parabolas in spectral focusing is increased. b) Normalized CARS spectrum (red) acquired using spectral focusing and dependence of the normalized TPEF signal (green) on the distance between the parabolas.

5.2.3 Closed-loop optimization of CARS/TPEF ratio

After having studied the deterministic effect of usual phase distortions, the benefits of a targeted optimization are tested. In this chapter, a solution of the laser dye DCM in acetonitrile is studied. In the presented excitation scheme, DCM gives rise to large two-photon fluorescence with a broad overlap with the CARS signal. With the right choice of DCM concentration, TPEF and FWM signals can be brought to similar levels. This concentration is determined experimentally, and depends on the setup in various ways: the NA of the collection objective, the distance to the detector, the spectral phase and pulse duration are expected to play a role. The chosen ratio is of about one order of magnitude for a FTL pulse, as seen in Figure 5.12 b) with the red curve. From this starting situation, a closed-loop optimization is performed to increase the ratio between TPEF and CARS signals. The FTL pulse is used as initial guess and processed by the evolutionary algorithm as described in chapter 4.2.2. The chosen parameterization is cubic spline, realizing a smooth function based on 24 points equally distributed in the spectral range, and with phase values varying in -40 to 40 radian boundaries. As shown earlier, an arbitrary high ratio TPEF/CARS can be achieved with sufficiently high GDD or TOD functions at the cost of signal intensity. To avoid a solution where both signals are strongly reduced, the feedback signal is calculated with TPEF/(CARS+TPEF). In the experiment, the signals are assigned based on spectral regions: CARS is most prominent in the red region close to the filter wavelength, whereas for wavelengths further to the blue CARS vanishes and TPEF reaches a maximum. This strategy proves to be very efficient in minimizing the CARS contribution while preserving the TPEF signal.

The obtained spectrum after optimization is shown by the green curve in Figure 5.12 b): the CARS signal vanishes to almost within the noise limit, while the TPEF signal is reduced by a factor 3 only. A closer look at the obtained phase function (red line in Figure 5.12 a)) shows that it is quite similar to a third order dispersion function. A cubic fit (dotted black line in Figure 5.12 a)) reveals that it consists of the sum of GDD=218fs^2 and TOD=-6820fs^3. If we consider CARS to be responsible for the small peak at 740nm, the CARS signal level can be estimated to 0,05 from 300 with a FTL pulse. From previously presented simulations, a 4 orders of magnitude decrease for the CARS signal is consistent for similar values of GDD and TOD, while a factor 10 reduction of the SHG signal is expected. The absorption curve of DCM, and a peaked 2-photon spectrum could explain the observed factor 3.

The closed-loop optimization performs slightly better to suppress the CARS signal while preserving TPEF. The chosen parameterization keeps the phase smoothly varying, preventing artifacts due to shaper resolution. For imaging however, such an optimization could be impracticable.

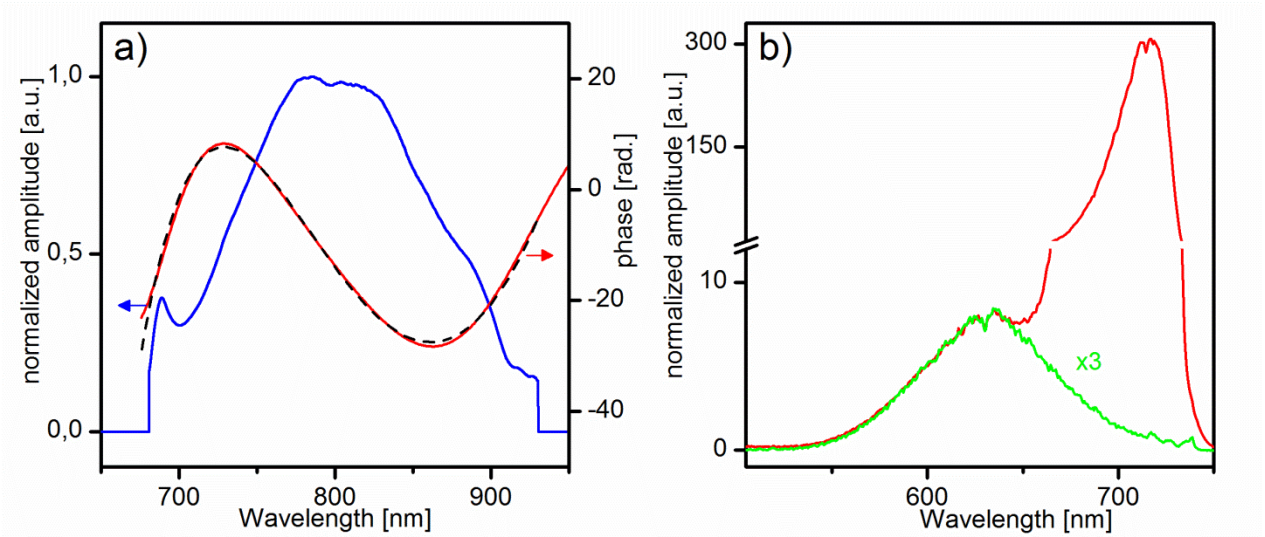

Figure 5.12 Optimization of the ratio TPEF/CARS with an evolutionary algorithm. a) measured laser spectrum (blue) and phase (red) obtained after evolutionary optimization of the ratio between TPEF and CARS signals from a solution of DCM in acetonitrile. Dotted black line: Cubic fit of the phase. b) Multimodal spectrum measured with FTL pulses (red) and after optimization (green). The TPEF signal decreases by a factor of 3 while the CARS signal disappears almost completely.

5.3 Multimodal imaging with shaped pulses

In this section, we will apply the presented shaping schemes for multimodal imaging of various biological samples. Moss leaves, human skin biopsies and rat tail tendon are examined, illustrating various application fields for nonlinear imaging with shaped pulses.

5.3.1 Experimental setup

Throughout the chapter, the setup remains similar to the single-beam setup presented in section 4.2. The excitation pulses originate from the high-power oscillator Fusion (Femtolasers) and are sent through the 4f-shaper. On the detection side, high-content spectrally resolved detection is used alternatively with one-channel detectors for rapid imaging and the advantages of both approaches are discussed.

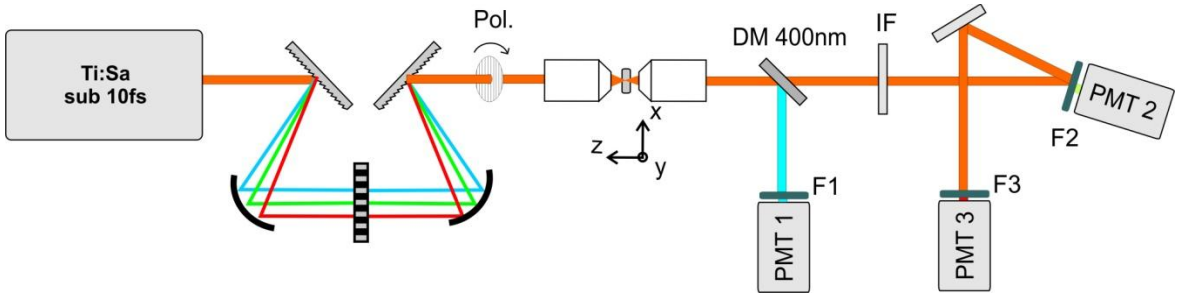

Figure 5.13 Experimental setup for rapid acquisition of multimodal images. DM 400nm: dichroic mirror, IF: Interference filter short-pass (λ<670nm), F1: bandpass filter λ=400nm+/-20nm, F2: bandpass filter λ=550nm+/-20nm, F3: bandpass filter λ =640nm+/-5nm.

A modification of the setup is also used in this part. The excitation and imaging optics remain unchanged, but the detection is realized with three photomultipliers (PMTs). The new setup is represented in Figure 5.13. Spectral separation now relies on a combination of filters. Since the short pass filter used until now for SB-CARS experiments also blocks light for λ<430nm,

a large part of the SHG signal would be lost. To avoid this, a dichroic mirror is used to separate the light around 400 nm from the rest of the beam. The reflected light might still contain reflected laser light, so that an additional bandpass filter around 400nm (Andover 400FS40-25, bandwidth $\Delta\lambda$=40nm) is placed in front of PMT1. Transmitted light is filtered the same way as in previous SB-CARS experiments. It is then separated into the TPEF and CARS channels, using a bandpass filter around 550nm ($\Delta\lambda$=40nm, Andover 550FS40-25). This filter is mounted directly in front of PMT2. The ensemble PMT2/F2 is slightly turned to reflect the remaining light into PMT3. To compensate the absence of a monochromator and avoid background, a last bandpass filter around 640nm ($\Delta\lambda$=10nm, Andover 640FS10-25) is placed in front of PMT3. Spectrally resolved detection is still available for comparison, a flip mirror is used to switch between the setups. Imaging with single-channel detectors can be made at much higher speeds than with the camera: the limiting factor is now the piezo stage. Instead of the step by step approach, the sample is raster scanned with a 500µm/s speed. Analog sample position output channels and PMTs signals are read simultaneously and the image is reconstructed by interpolation after the measurement. The image area is still limited to 100µmx100µm but image acquisition time is reduced from 40min to 30s with a better sampling rate (0.2 µm).

5.3.2 Moss leaves

Imaging of plant cells with nonlinear optical microscopy is a far less developed field than the investigation of animal or human tissues. Nevertheless, the advantages of nonlinear imaging have a great potential for deciphering metabolism mechanisms and uptake of nutrients or pollutants by plant leaves and roots. TPEF, for example, has recently found application in environmental research, overcoming limitations of previously used analytical techniques. The uptake of semivolatile organic compounds by different plants was studied by Wild et al. [206-207] contributing to the understanding of the fate of these chemicals in vegetation. The capacity to image living leaves in 3D allowed localization of the chemicals on a cellular level. Nondestructive, label-free imaging permits monitoring the evolution of compounds concentration over several weeks showing how they migrate, are stored and processed depending on the species. The authors took advantage of the separation between the emission peaks of the autofluorescence of plant cell walls and chloroplasts and of the studied chemical. The same method was applied to study the action of plant protection products (like fungicides), although they do not always display fluorescence unlike e.g. polycyclic aromatic hydrocarbon pollutants [208].

With the additional information provided by the CARS signal, such a limitation could be overcome. Previous studies in our group applied multiplex CARS imaging to leaves of the moss *Plagiomnium rostratum* [95, 209]. Identification of cell walls, chloroplasts and vacuoles based only on the spectrally resolved CARS signal was possible by using principal component analysis. TPEF appeared as an unwanted background in the MCARS spectra and has been removed after analysis with the Maximal Entropy Method (MEM).

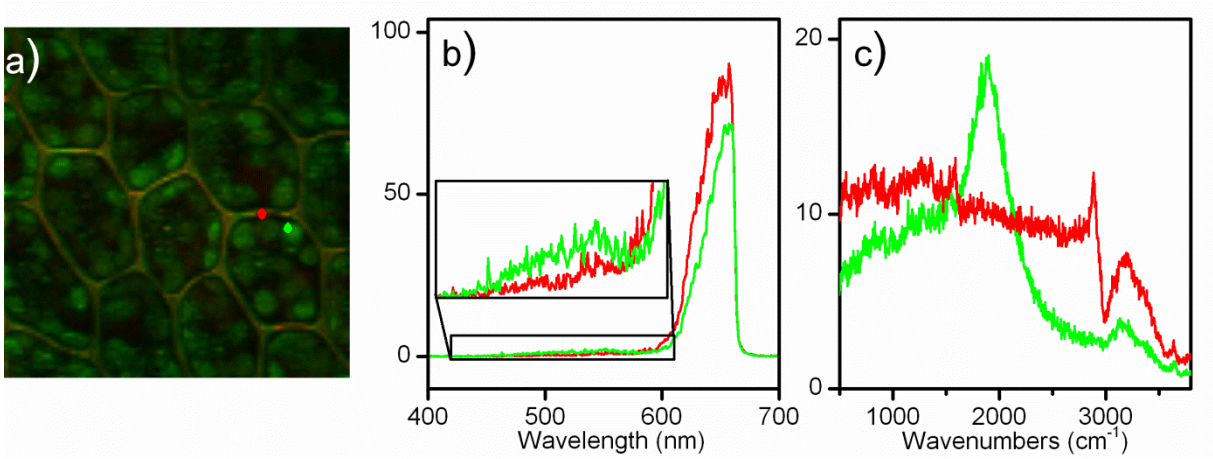

Figure 5.14 CARS and TPEF signals in a Moss leave. a) RGB multimodal image obtained with a 10fs FTL pulse. Green channel: TPEF (integrated from 400nm to 580nm). Red channel: CARS (integrated from 600nm to 680nm). Corresponding multimodal spectra are shown in b): in red, in a cell wall at the position of the red dot in a). In green, in a chloroplast marked by a green dot in a). c) Multiplex CARS spectra of a cell wall (red) and chloroplast (green).

In our single-beam setup we now want to make use of the autofluorescence as an additional contrast mechanism in combination with CARS. A typical multimodal image obtained with FTL 10 fs pulses is shown in Figure 5.14 a). The contrast is provided by CARS for the cell walls and TPEF for chloroplasts. In order to analyze the generated signals, a multimodal spectrum was acquired at each pixel of the imaged 100µmx100µm region. As FTL pulses are used, a very strong CARS signal is obtained in a spectral region from slightly under 600nm to the filter cut at about 670nm. Much less intense TPEF signals appear in the broad region starting at 450nm and up to at least 600nm. Above this wavelength, the potential TPEF signal is overlapped by the much stronger CARS signal. With this configuration, moss leaves are well suited to study overlapping signals: the strength of individual signals can be assessed from the blue region, where only TPEF appears, or from the red region, where CARS dominates strongly, with respect to the region around 600nm where overlap occurs. Integrated CARS signal is then used as the red channel of the RBG image Figure 5.14 a) while TPEF is assigned to the green channel.

Two structures of the cells are well resolved in the obtained image: the cell walls, with a strong CARS signal and the chloroplasts producing TPEF signal. From Figure 5.14 a) it appears that cell walls are not purely red and also give rise to fluorescence. This is expected from literature, but could also be due to the much stronger CARS signal leaking in the TPEF spectral channel (due to a residual overlap, or to insufficient filtering). Thank to spectrally resolved detection, we can observe the emitted spectra to exclude a leakage. A comparison of the multimodal spectra obtained from cell walls and chloroplasts are shown in Figure 5.14 b). The green and red lines correspond respectively to the positions marked by the red dot (cell wall) and by the green dot (chloroplast) in Figure 5.14 a). For better visibility, the weaker TPEF spectra are highlighted in the caption in Figure 5.14 b). The multimodal spectra can be compared with the MCARS spectra obtained from a leaf of the same plant. Unlike SBCARS, the multiplex spectra directly provide the position of the Raman resonances. While membranes of animal cells are constituted of bilayers of phospholipids, plant cell walls are

complex mixtures of cellulose, other polysaccharides and lignin (not always present, dependent on the species). Plant cell walls are denser and more rigid than animal cell membranes, and therefore give rise to a strong (nonresonant) SBCARS signal. In the MCARS spectra, a contribution of the C-H groups of cellulose can be identified in the cell walls around 2900 cm^{-1}. This large band is constituted of the overlap of CH_2 symmetric stretching, various C-H stretching and CH_2 antisymmetric stretching bands [210]. In chloroplasts, a chlorophyll-related band around 1500 cm^{-1} is observed in addition to TPEF, which appears as a broad peak at 678nm (corresponding to a 2000 cm^{-1} shift with respect to the pump wavelength).

The 3D imaging capabilities of multimodal imaging are illustrated in Figure 5.15. Here, the green channel is attributed to the integrated CARS signal, the blue channel to TPEF and the red channel represents the variations of transmitted laser light. To obtain this additional channel, the spectrum of the laser is slightly mismatched with respect to the short-pass filter used in front of the camera. The blocking element in the shaper is moved so that a narrow transmitted laser line appears. However, the contrast obtained with the transmitted light is poor as can be seen in particular in the left panel of Figure 5.15. Each panel represents a 100µmx100µm section in the XY plane, centered at the same position but taken at different depths, with a 5µm step.

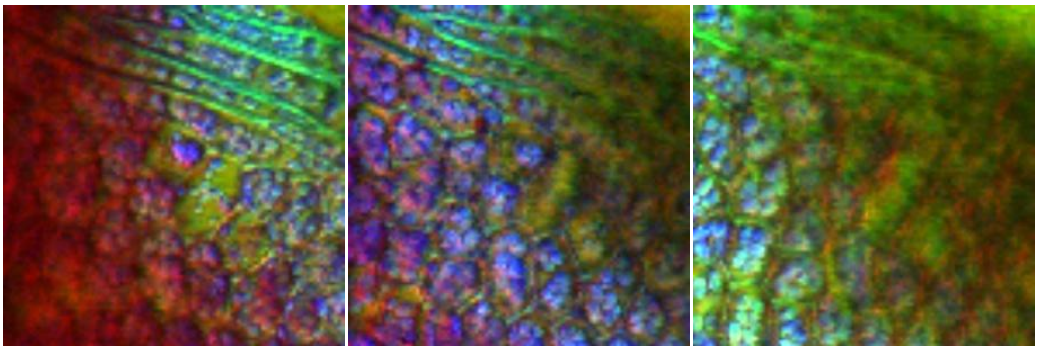

Figure 5.15 3-D multimodal imaging of a moss leaf. Multimodal images (blue: TPEF, Green: CARS, red: transmitted laser) of a 100µmx100µm region are taken at different depths (left: Z=-5µm, center: Z=0µm, right: Z=+5µm).

We now consider the effect of two shaping strategies on the multimodal spectra of *Plagiomnium rostratum:* the use of GDD to control the ratio between CARS and TPEF signals, and Spectral Focusing (SpFoc) to improve the chemical specificity of the CARS signal. The phase functions used are presented in Figure 5.16 and will be used for imaging. For each pulse, the spectral intensity and phase are shown in a first row and the obtained spectra in a second row. The spectra traced in red and green are taken respectively at the reference positions in the cell wall and in the chloroplast marked in Figure 5.14 a).

As discussed earlier on the basis of a simulation, phase distortions affect more strongly the CARS signal than SHG and TPEF signals. Even more so for the SBCARS signal, that is detected on the blue side of the broadband spectrum exclusively. For this imaging example, we have chosen a moderate GDD function of 200fs^2. A simple GDD shaping has some advantages in our case: it reduces very efficiently CARS signal generation in a controlled way, and reduces the two-photon spectrum uniformly. Therefore it is independent of the unknown absorption spectra of the fluorophores present in the sample. Considering the

spectra obtained after applying this phase function in Figure 5.16 e), we see that CARS is reduced to a similar intensity to the TPEF signal, to compare with the two-orders of magnitude ratio observed with a FTL pulse (Figure 5.16 d). In the chloroplast, the CARS signal seems to have disappeared completely, revealing the part of the TPEF spectrum that was previously covered. The spectra also confirm the presence of fluorescence in cell walls.

Multimodal imaging with FTL pulses provided a good contrast for cell walls due to their higher density and hence higher $\chi_{NR}^{(3)}$ than the rest of the cell. To retrieve the chemical specificity of a vibrationally resonant CARS image, Spectral Focusing is used in addition to amplitude shaping. The spectral region of interest is known from literature values for Raman spectra of cell walls and in particular of cellulose, as well as from MCARS spectra of *Plagiomnium rostratum*: a large band around 2900 cm^{-1}. We use a rather weak focusing with a GDD of 2500fs^2 for both parabolas, providing the excitation of a rather large spectral region of about 50cm^{-1} width, centered at 2885cm^{-1} (red curve in Figure 5.16 c). To further avoid photodamage, the central part of the spectrum is removed (blue curve) because it cannot contribute to the excitation of the chosen band. The resulting spectra are shown in Figure 5.16 f): a peak appears in the spectrum around 580nm, due to the chosen Raman band at 2885cm^{-1}. Similarly to the case of a vibration addressed with two ps laser pulses, the narrowband excitation also contains a nonresonant contribution, responsible for the peak in the spectrum corresponding to the chloroplast (in green in Figure 5.16 f). Around the peak, the intensity is due partly to fluorescence and partly to residual nonresonant CARS signal.

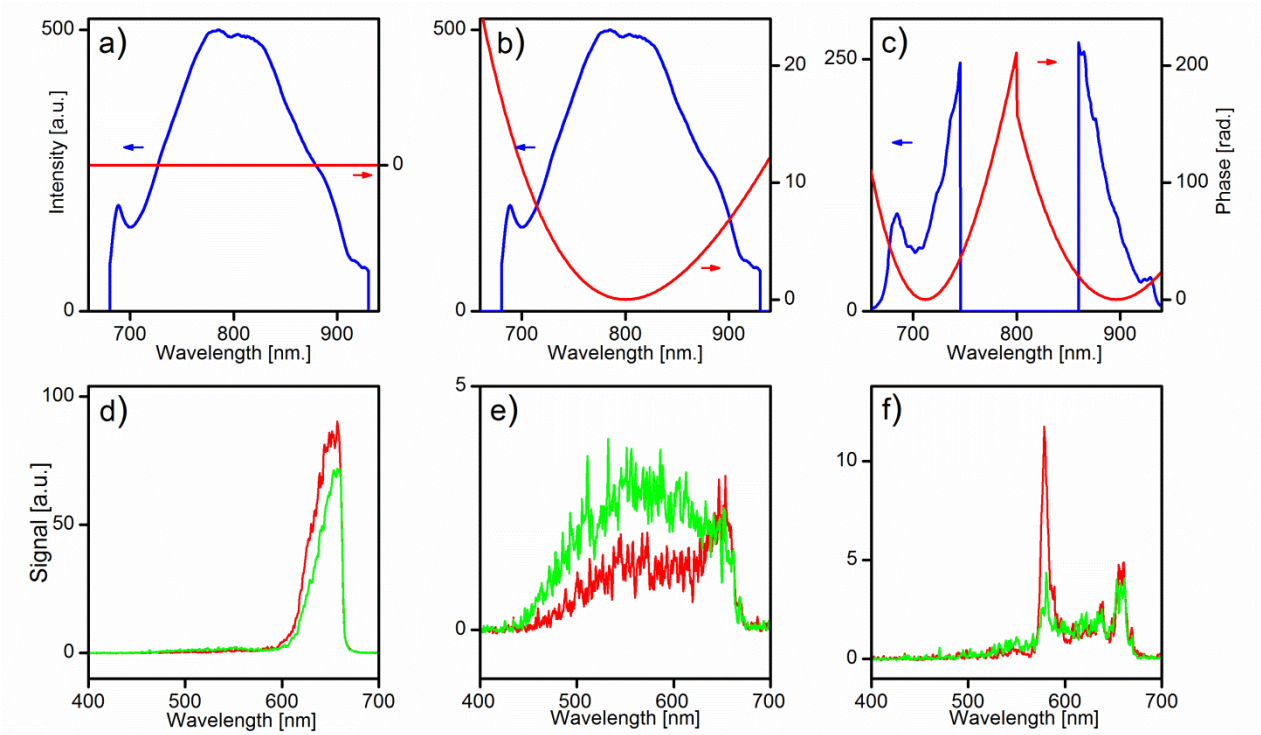

Figure 5.16 Effect of shaping on spectra. a,b,c) spectra (blue) and spectral phases (red) of the pulses referred as FTL, chirped (200 fs^2) and "spectral focusing" pulses in the text. d,e,f) corresponding spectra obtained in the cell wall (red point in **Figure 5.14** a) and chloroplast (green point).

The results for imaging using the phase functions presented above are summarized in Figure 5.17. The images for the red and green channel of the multimodal image presented in Figure

5.14 a) are displayed separately in Figure 5.17 a) and b), respectively. With the GDD phase function, TPEF is now dominant on the whole spectrum. Figure 5.17 d) is obtained by integrating the red part of the spectrum, from 610nm to 670nm, where the CARS signal appears in Figure 5.16 e). The image now contains not only the cell walls but also some chloroplasts, due to the overlap with a stronger TPEF signal. The CARS signal just slightly increases the intensity in the cell walls, as can be seen comparing Figure 5.17 d) with the image obtained integrating the TPEF spectral region, Figure 5.17 e). When the whole spectral range is integrated, simulating an acquisition with a single channel detector directly after the short-pass filter, the CARS signal has almost no influence on the image: Figure 5.17 f) is indistinguishable from Figure 5.17 e). The same is true for CARS in the case of a FTL pulse: the image obtained integrating the whole spectral range (Figure 5.17 c) is identical to the image obtained from the "CARS" spectral region (Figure 5.17 b). Hence, the simple GDD shaping allows switching between the CARS and the TPEF image in a configuration using a single channel detector, and without a priori knowledge of the exact spectral regions of each effect. The images obtained with the pulse tailored to excite only the CH stretching modes are presented in the last row of Figure 5.17. In this case, the image using the integrated signal (Figure 5.17 i) is not satisfactory: features from both the fluorescence image and the CARS image are represented, the chloroplasts are clearly visible and cell walls have a higher signal than with TPEF alone. The shaped pulse is stretched in the time domain resulting in a smaller CARS/TPEF ratio for the integrated signal. The role of TPEF is evident from an analysis of the spectral data. As shown in the discussion over the spectra seen in Figure 5.16 f), the peak concentrating resonant CARS signal is surrounded with a broad TPEF and an additional CARS contributions. As in the case of the FTL pulse, the bluer part of the multimodal spectrum contains exclusively TPEF. Although the signal is quite weak in this region (450nm to 580nm), Figure 5.17 h) shows it is colocalized with the previously identified stronger TPEF signals. In turn, restricting the integration to the CARS peak, an image quite similar to the previous CARS images is obtained (Figure 5.17 g). This is not surprising, given cellulose is expected to be present mainly in the cell walls. Despite the much weaker signals obtained with spectral focusing, the level of contrast is similar to the FTL case.

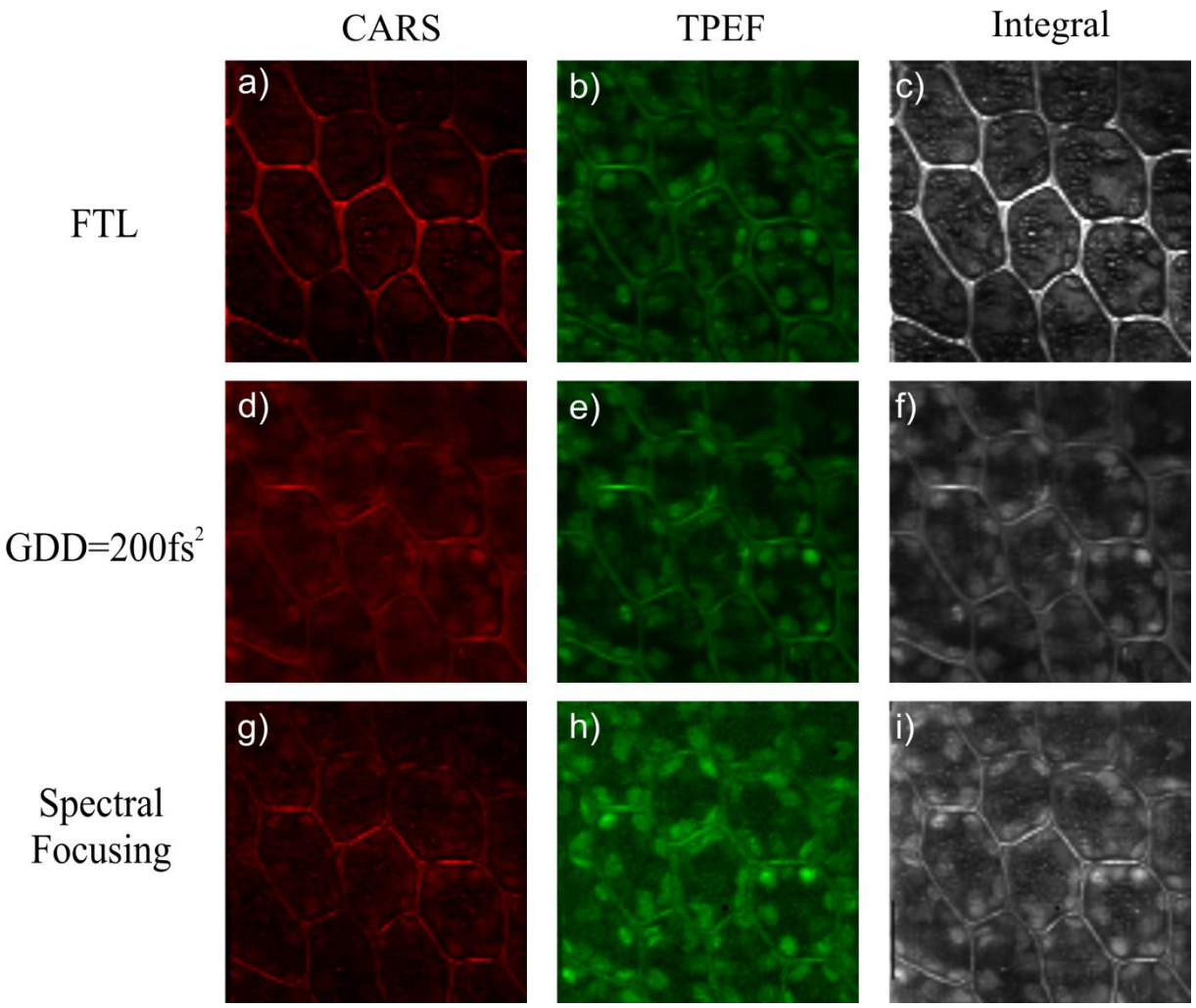

Figure 5.17 **Multimodal imaging with shaped pulses**: a,b,c) images obtained with FTL signals d,e,f) images obtained with the chirped pulses g)h)i) images obtained with the spectral focusing pulse configuration. In a)d)g) the spectral region corresponding to CARS was integrated (600-670nm, 610-670nm and 580-590nm respectively). b)e)h) were obtained by integrating a spectral region containing TPEF (400-570nm, 450-600nm and 400-580nm respectively). When the whole spectrum is integrated, image c)f)i) are obtained.

The observed very strong contrast obtained already with FTL pulses is a specificity of plant cells: in animal tissue the density differences are far less pronounced. Also, a great variety appears among different cell walls of different plants or even of different cells within a plant. In vascular plants, for example, lignin plays a major role for stability, and thicker, chemically more complex cell walls than the case presented in this study are observed. Given the importance of plants, and particularly their cell walls as raw material and for storage in the CO_2 cycle, the presented results could be the preliminary to more thorough investigations of the capabilities of CARS and multimodal imaging for monitoring plant cell growth.

5.3.3 Skin

As a first example of multimodal imaging of animal tissue, this paragraph is devoted to imaging of human skin. Skin is the largest organ of the human body and is responsible for numerous exchanges with the environment, as well as the protection against various pathogens. The structure of the skin is represented in Figure 5.18. It can be divided into three main layers: the epidermis, the dermis and the hypodermis. The epidermis is the protection layer of the skin. It consists mainly of keartinocytes, distributed over 5 under-layers: stratum

basale, stratum spinosum, stratum granulosum, stratum lucidum and stratum corneum, from the deepest to the external one. Each stratum correspond to a step in maturation of keratinocytes: the column-shaped stem keratinocytes in stratum basale produce differentiated daughter cells with increasing keratin content and flatter shape. This way the outer layer is constantly renewed. The epidermis also contains melanozytes, responsible for the production of melanin. The epidermis is separated from the dermis by a membrane called the basement membrane.

The dermis is a thicker layer containing numerous structures: various sensory receptors, hair follicles, sebaceous glands, sweat glands, as well as a network of capillaries. These structures are embedded in a dense extracellular matrix. Collagen fibers are responsible for the strength and elastin fibers for the elasticity of skin. The hypodermis makes the transition to the inner part of the body. It consists of fatty connective tissue.

An important parameter for optical imaging *in vivo* is the thickness of skin. The order of magnitude is of few hundreds of microns with variations across the body: the epidermis thickness is comprised between 50µm and 1.5mm whereas the dermis can be as thin as 300µm and as thick as 3mm [211]. In some cases, the thickness of the layers of the epidermis also plays a role. Stratum corneum, containing mainly dead cells is only about 10µm thick, giving quite easily access to deeper layers where some parameters, are much more comparable to the inner body [212].

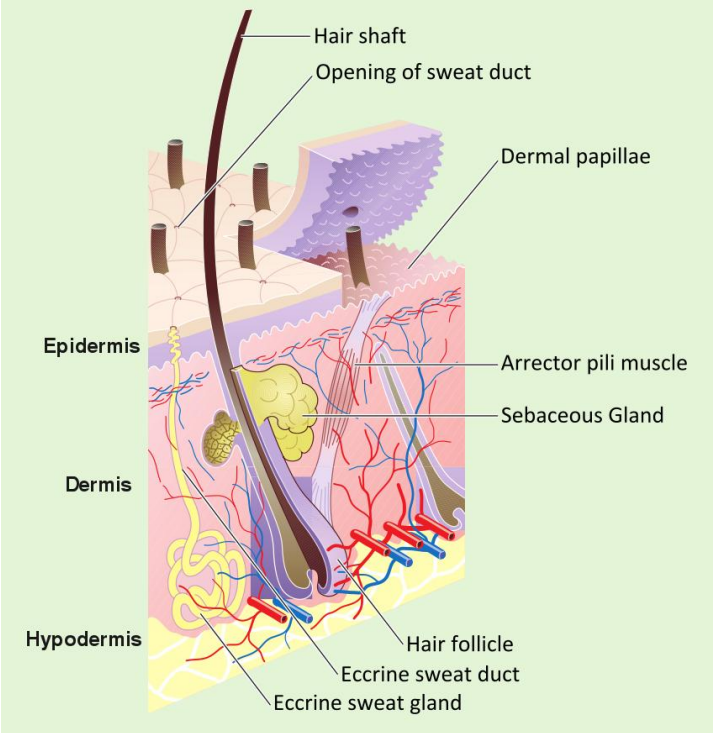

Figure 5.18 Representation of the structure of human hairy thin skin. The total thickness of the skin varies across the body from few 100 µm to few mm. The thinner epidermis is mainly a protection layer. The dermis contains most of the structures interesting for multimodal imaging.
(Madhero88 and M.Komorniczak (Lizenz: Creative Commons by-sa 3.0))

This accessibility of blood vessels to optical diagnostics opens the door to non invasive determination of key pathological parameters, given the ratio between dermal concentration

and blood concentration is known. For diabetic patients, for example, glucose concentration can already be estimated based on dermal interstitial fluid [213].

Multimodal nonlinear microscopy is particularly relevant for the imaging of skin. The typical penetration depths in tissues are of several 100µm with NIR lasers. The high concentration of fluorophores, collagen and locally of fat glands produce highly contrasted images with TPEF [214], SHG [1, 215] and CARS [216] respectively. The complementary structural, chemical and histological (due to cell resolution) information is ideal for diagnosis of diseased skin [217] and monitoring drug delivery[218].

An increased incidence of skin cancer [219] calls for a rapid and precise method of diagnostic, early detection being crucial to a successful cure. Depending on the affected cell group, three main types of skin cancer can be distinguished: malignant melanoma, squamous cell carcinoma and basal cell carcinoma. Malignant melanoma and squamous cell carcinoma affect cells in the epidermis and are easily accessible for *in vivo* imaging. Clinical studies have already been conducted to demonstrate the use of TPEF tomography for diagnosis of malignant melanoma [220]. The most common skin cancer, basal cell carcinoma, affects cells in the dermis. Recent studies based on multimodal imaging identified several features of basal cell carcinoma at different stages, including the presence of lipid reservoirs and deformation of the collagen network around the tumor [221].

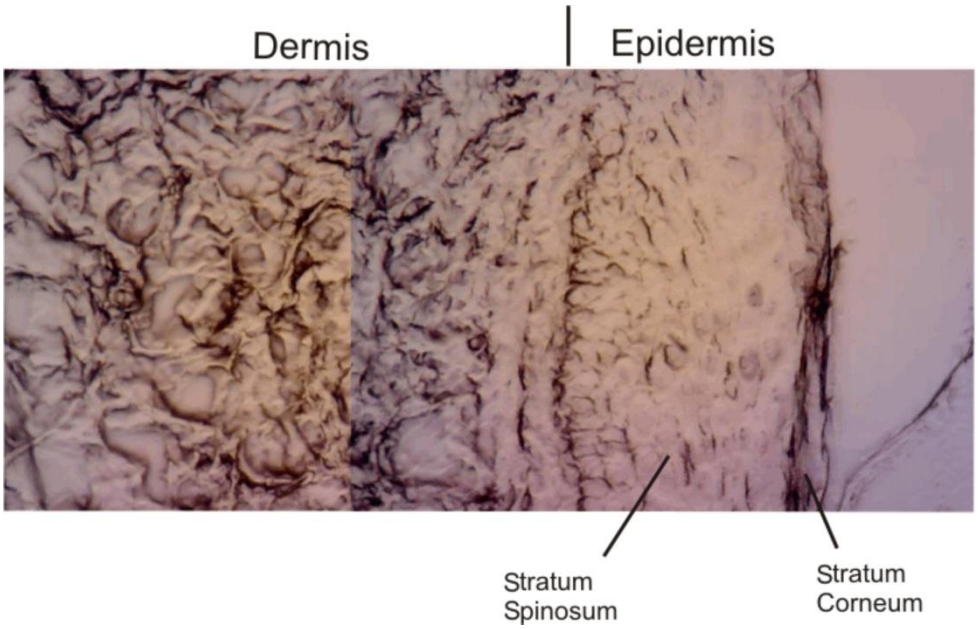

Figure 5.19 Bright field microscope image of the skin sample. The biopsy is mainly transparent and the structures are difficult to identify in the bright field image. The limit between the dermis and the epidermis can be guessed at the indicated position: a change in structure is observed. In the epidermis, the ordered structures appear to be basale cells.

The samples we examine in our setup are longitudinal sections of human skin obtained by cryosection (kindly provided by Prof. Schäkel from the Department of Dermatology of the university Heidelberg). The sections are used as received, without staining or further preparation. A bright-field image of the sample is presented in Figure 5.19. Starting from the skin surface (on the right), some of the skin layers can readily be identified based on the apparent structure: the first thin layer is recognized as the stratum corneum, followed by the

rest of the epidermis appearing as a quite homogenous region. At the bottom of the epidermis, stratum basale can be guessed as a layer of column-like cells. The dermis appears as a much more structured region. This rough identification is used to choose areas of interest that are imaged with the multimodal setup.

Multimodal images of skin surface and of the boundary between dermis and epidermis are shown in Figure 5.20. The pulses used are compressed to the FTL. Images a),b) and c) correspond to the CARS, TPEF and SHG signals (respectively) obtained at the interface between skin and air. The signals detected in the TPEF and SHG channels are near the background level. Although strong fluorescence of the stratum corneum has been reported *in vivo* [222], the emission peak is too far in the blue for detection in the TPEF channel [223]. It could, however explain the small signals detected in the SHG channel. NAD(P)H has an emission length nearer to the selected TPEF region, as well as elastin and collagen. NAD(P)H is absent of the dead cells constituting stratum corneum, but are present already in the dense and thin layer stratum granulosum and could explain the thin bright lines separating stratum corneum and stratum spinosum in the CARS and the TPEF images. In the CARS channel, individual cell contours and nuclei can be guessed in stratum spinosum, but on the basis of a nonresonant and hence unspecific signal. Deeper in the tissue, at the interface with the dermis, the CARS signal shows little difference between the two regions Figure 5.20 d). Some structures appear but they are not easily assigned and look similar to the structures seen in Figure 5.19. In the SHG image (f) and the TPEF image (e), the boundary between dermis and epidermis is easily recognizable. The high concentration of collagen fibers, in particular, clearly delimitates the two layers. The limit is less clear in the TPEF image despite collagen fluorescence and high concentration of elastin, maybe because of the presence in the stratum basale of melanin, which emission maximum better matches the filter used in our setup.

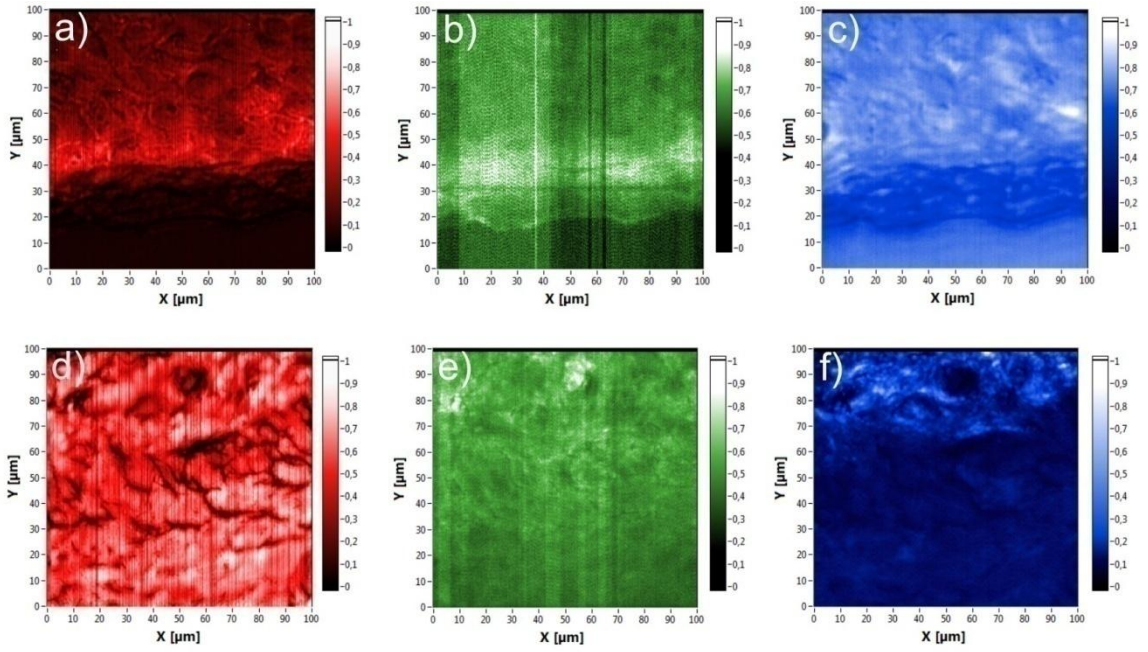

Figure 5.20 Multimodal imaging of the skin surface and of the interface dermis/epidermis. CARS (red, a and d), TPEF (green, b and e) and SHG (blue, d and f) images of the surface of the skin (upper row of images, a,b and c) and of the limit between dermis and epidermis (respectively upper and lower part of d, e and f).

Inside the dermis, multimodal microscopy is ideal to image the interconnected collagen and elastin network with SHG and TPEF, as seen from Figure 5.21 (left panel). The complementary information is completed by the CARS signal. Though the map obtained with CARS largely overlaps with the two other images, it also highlights dense regions with poor fluorophore or collagen content. In the imaged region with all three signals having strong intensities (in comparison with the regions presented in Figure 5.20), the effect of GDD can be tested. As each channel in the RGB image is normalized, the big differences in intensity between the CARS and the TPEF signal are not evident from Figure 5.21. Given the detection geometry, a weak leakage of the CARS signal could account for a parasitic signal in the final image. With as little as $50fs^2$, the CARS signal is drastically reduced while the two other effects are only slightly affected as can be seen in Figure 5.21 in the right panel. In this image, each channel was normalized with the values obtained with FTL pulses. The intensity in the red channel vanishes, the green and blue channel fade moderately but show the same information as previously.

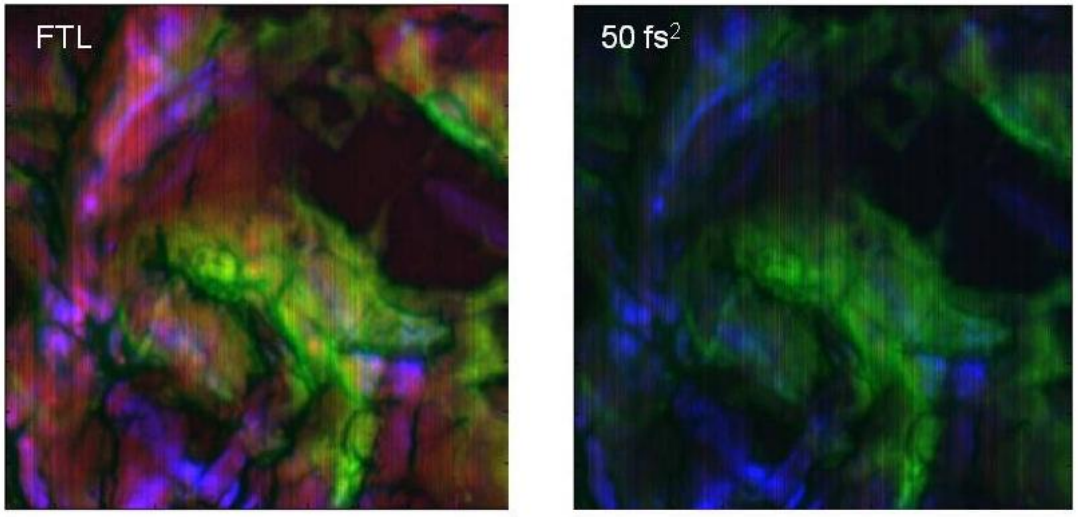

Figure 5.21 Effect of chirp on multimodal imaging. Multimodal images of a 100µmx100µm region in the dermis acquired with FTL (left) and chirped (GDD=50 fs^2, right) pulses. For each channel (red: CARS, Green: TPEF, Blue:SHG), the intensity is normalized with the maximum intensity in the FTL case.

To obtain vibrational contrast with the SB-CARS channel in multimodal images, the use of shaping strategies is necessary. This is illustrated with the imaging of a structure in the dermis. An oval structure of about 200µm over 100µm was identified roughly 500µm from the surface of the skin (see brightfield image in Figure 5.22 a). Because of its foam-like structure, size and position inside the dermis, we identify this structure as a sebaceous gland (see for example images of stained sections in [224]) . Sebaceous glands are present in the dermis of almost all the body. They produce sebum, an oily liquid that protects and lubricates hair and skin surface. The secretion mode is holocrine, which means the cells are disrupted upon release of the synthesized product. During maturation, the sebocytes hence accumulate sebum inside their cytoplasms. The glands are organized in a concentric fashion [225].In a somewhat crude model, pluripotent cells can be located on the outer border of the gland. They divide and produce differentiated cells in the middle. The secreted liquid is then ejected in the hair follicle and reaches the surface of the skin. In reality, a more complex mechanism takes

place and the size of a cell is a better indicator of differentiation stage than the position in the center or the periphery of a lobe of the gland.

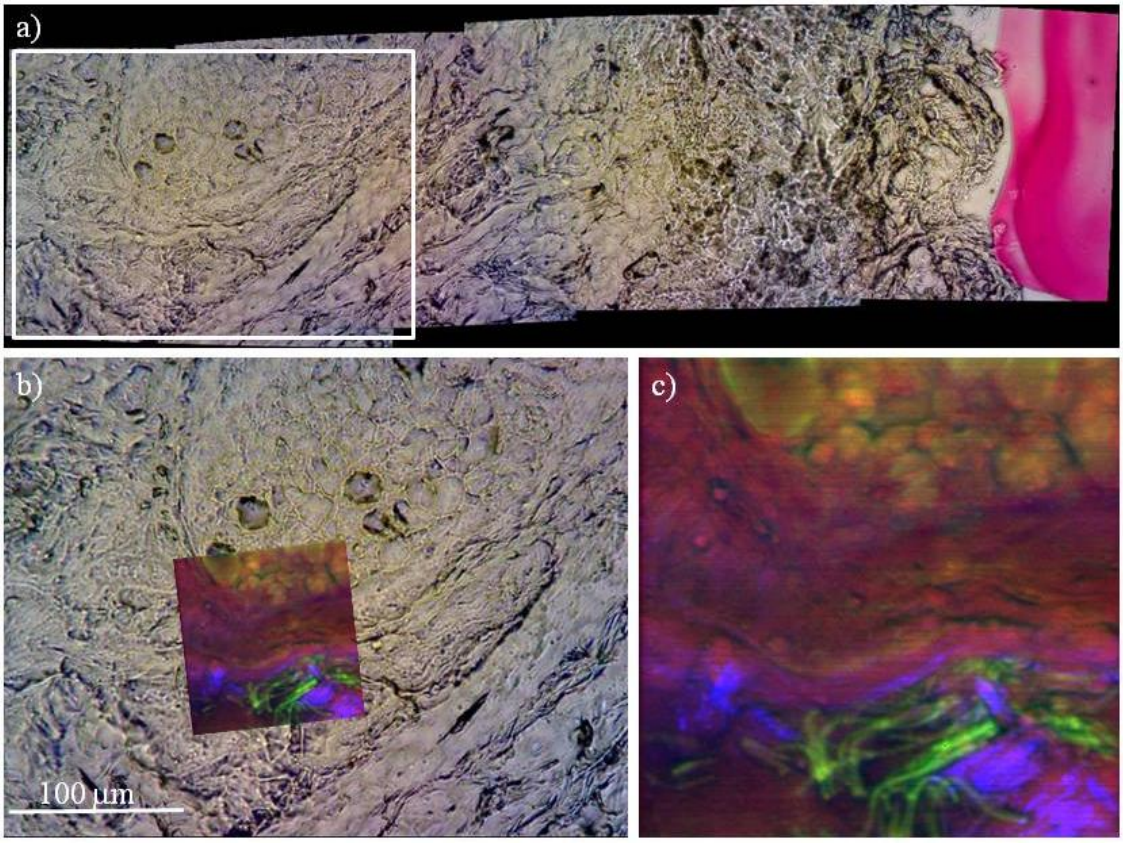

Figure 5.22 Multimodal imaging of a sebaceous gland. a) Panoramic image representing the skin in depth from the surface to the area of interest, obtained by stitching several brightfield microscope images. b) close up on the area marked by a white rectangle in a), and containing the oval structure identified as a sebaceous gland. c) Multimodal image of a 100µmx100µm area in b).

Sebum contains mainly triglycerides, free fatty acids and in a smaller proportion wax esters (as well as a small amount of cholesterol)[226]. Therefore, it is easily detected with vibrationaly resonant techniques like CARS and SRS [37, 227]. A multimodal image of the border of the structure identified as a sebaceous gland is shown in Figure 5.22 c). This image was acquired using rapid acquisition with PMTs and covers a 100µmx100µm area. The imaged section can easily be indentified in bright field images: the region marked by a white rectangle in Figure 5.22 a) is shown in b) with the overlaid multimodal image. Nonlinear effects reveals a wealth of information about the structures appearing in the unstained section. The collagen matrix surrounds the sebaceous gland, but with a 20 to 30µm gap. Interlaced with collagen, the structures appearing in green are identified as elastin fibers [11]. In the upper part, the cells inside the sebaceous gland display fluorescence. A possible explanaition is the higher concentration of NAD(P)H in the living cells of the gland than in the surrounding matrix. However, it more likely is due to fluorescence of oxidized lipids [228]. Again, the CARS channel obtained with FTL pulses provides a limited contrast, without chemical specificity.

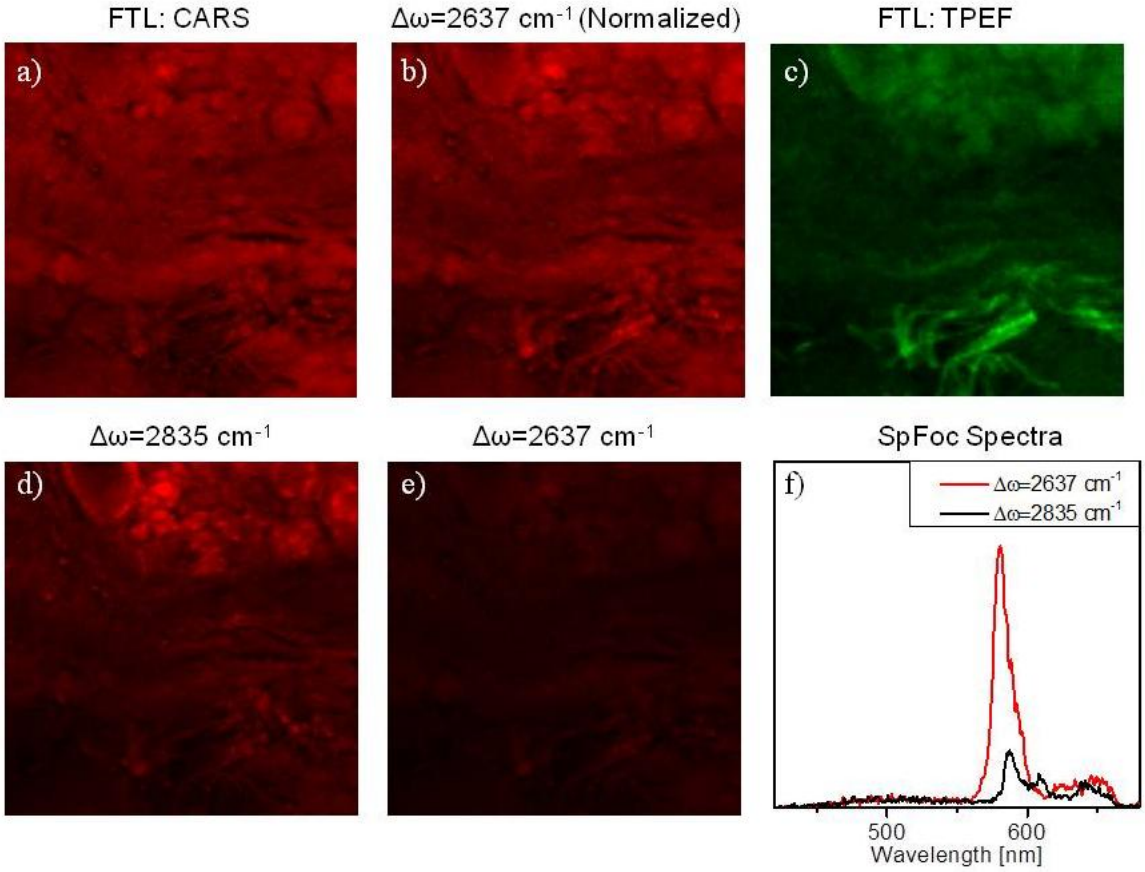

Figure 5.23 Vibrational contrast with spectral focusing. a) Image obtained with FTL pulses. CARS signal integrated from spectrally resolved data. b) Spectral focusing on $\Delta\omega=2637cm^{-1}$, off resonance.c)FTL pulses, TPEF signal integrated from 530nm to 560nm. d) Spectral focusing on $\Delta\omega=2835cm^{-1}$, on resonance. e) same data as (b), normalized with the maximum of (d). f) Spectral focusing spectra obtained in the bright spot in the sebaceous gland. red line: $2835cm^{-1}$, black line: $\Delta\omega=2637cm^{-1}$.

To obtain a chemical map of the lipids in the selected region, we apply spectral focusing. Skin lipids are recognizable by the well known CH_2 stretching band[229]: we apply two GDD= $5000fs^2$ functions centered respectively at 703nm and 878nm, resulting in the selective excitation of a narrow spectral region around $\Delta\omega=2835cm^{-1}$.Multimodal spectra are measured with the monochromator and the ICCD camera for each pixel of the region previously imaged with PMTs (pixel size for the spectrally resolved detection: 1µmx1µm). As previously, a vibrationally resonant peak appears in the acquired spectra, the integration of the corresponding spectral region results in the image shown in Figure 5.23 d). For comparison, images obtained by integrating the CARS and the TPEF signals generated by FTL pulses are shown in Figure 5.23 a) and c), respectively. The spectral focusing image displays a clear increase in contrast in comparison to the FTL image, confirming that the structure identified as a sebaceous gland contains a high concentration of lipids. A comparison with the TPEF image shows a better specificity of the vibrational contrast. In the gland, both signals are colocalized pleading for the attribution of fluorescence in the gland to lipids. To confirm the resonant nature of the signal observed in Figure 5.23 a), the region is imaged with parabolas tuned off-resonance. The parabola centered at 703nm remains unchanged while the second function is now centered at 863nm and $\Delta\omega=2637cm^{-1}$. The signal is strongly reduced, as illustrated by Figure 5.23 e), where the integrated signal was normalized by the maximum of

the resonant signal. The spectra recorded in the bright spot inside the sebaceous gland are also shown in Figure 5.23 f) for the resonant (red line) and the nonresonant case (black line). The spatial contrast obtained with spectral focusing tuned off resonance in shown in Figure 5.23 b). The image is the same as in e) but normalized by its own maximal value. A comparison with a) shows that, as expected, nonresonant and FTL excitation provide the same information.

5.3.4 Polarization shaping: Rat tail

The images shown in this part already proved the use of complementary chemical information. In this paragraph, the tensorial nature of the non linear susceptibility will be exploited. In particular, $\chi^{(2)}$ is sensitive to the orientation of imaged structures. This dependency is known from crystals but has also been studied extensively in biological samples, e.g. on collagen fibers [5] or in myosin structures [7]. The tensor $\chi^{(3)}$ also exhibits a polarization dependency in ordered structures like wood fibers [95]. However the observed extinction factors are weaker than for $\chi^{(2)}$: myosin filaments imaged with THG present a factor 2 in signal between polarizations parallel and perpendicular to the filaments while the extinction is almost complete with SHG [230].

Imaging of orientation of structures in tissues is relevant for diagnostics and for functional biology. For example, collagen plays a role in stability of skin, tendons and other tissues and the orientation of the fibrils determines its response to stress. In this respect, optical nonlinear microscopy is an attractive noninvasive alternative to methods otherwise used for orientation studies. Measuring polarization profiles with SHG has been applied to diseased tissue in a murine model affected by *Osteogenesis imperfect* [231], and showed the ability to differenciate between the *rigor* and the *relaxed* states of motor proteins in muscles[7]. Moreover, since the intensity of nonlinear signals is affected by polarization, this parameter has to be taken into account for quantitative analysis.

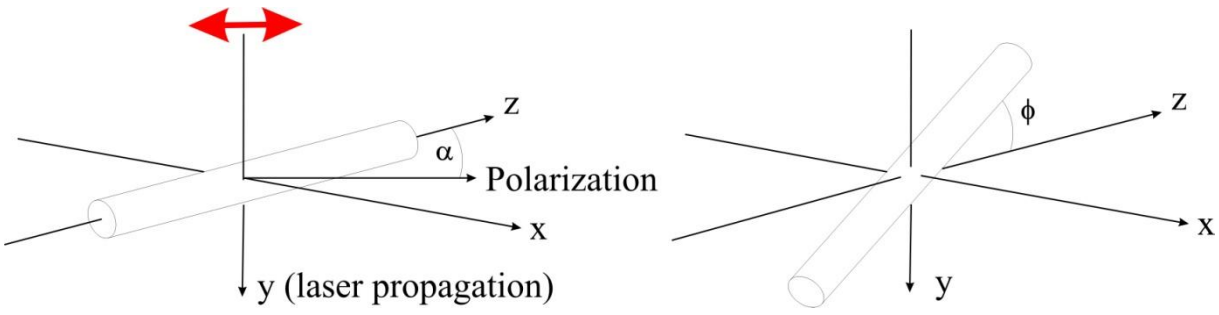

Figure 5.24 Orientation of the collagen fibers. Left(our case): fiber in the (x,z)-plane. Laser propagating along y axis, linearly polarized with an angle α to the direction of the fiber. Right: additional parameter φ for fibers pointing out of the plane.

Here we present a method for simultaneous measurement of SHG signals produced by two perpendicular polarizations. To this end, tendon from a rat tail was chosen as a model system. In the skin, the collagen fibris form an entangled network [232] while tendon collagen presents a well defined, uniaxial orientation of collagen fibrils and is well suited for polarization studies [233].

Rat tails were kindly provided by Vincent Popoff from the Heidelberg University Biochemistry Center. Sprague-Dawley rats were asphyxiated with CO_2 prior to sacrifice[234]. Tails were cut and conserved in methanol or formaldehyde. Shortly before examination under the microscope, a portion of about 1 cm length was removed from the conserved tail and a tendon fiber mechanically extracted. The fiber was then mounted with water on a microscope slide to prevent drying and pressed with a cover slip.

Previous studies of polarization dependence of SHG of collagen in tendons have shown that under right experimental conditions the detected signal depends only on two parameters: the angle α between the polarization of the laser and a parameter ρ, characteristic of the sample [5, 235-236]. The starting point of theoretical considerations is equation (2):

$$\boldsymbol{P_i^{(2)}} = \sum_{jk} \chi_{ijk}^{(2)} E_j E_k \; ; \; i,j,k \in \{x,y,z\}$$

The 27 $\chi_{ijk}^{(2)}$ parameters are not independent: relationships can be derived from symmetry considerations in general and particular cases. Firstly, invariance after permutation of E_j and E_k binds 9 components and holds in any material. When no energy is deposited in the system, the stronger Kleinman symmetry can be applied: any permutation of indices leaves $\chi_{ijk}^{(2)}$ unchanged [237]. This leaves only 10 independent parameters. In our sample, supplementary symmetry is available because the fiber is cylindrical and in a plane perpendicular to the incident light. The illumination scheme is represented in Figure 5.24 (left panel).The laser propagation direction is arbitrary chosen to be along the y-axis, the collagen fiber being along the z-axis. The cylindrical symmetry and the chosen propagation direction finally reduce the theoretical problem to two equations:

$$P_x^{(2)} \propto 2\chi_{xxz}^{(2)} E_x E_z \tag{68}$$

$$P_z^{(2)} \propto \chi_{xxz}^{(2)} E_x^2 + \chi_{zzz}^{(2)} E_z^2 \tag{69}$$

Then, defining $\rho = \chi_{zzz}^{(2)}/\chi_{xxz}^{(2)}$, the resulting far-field intensity along the x and the z polarization directions is given by:

$$I_x \propto [\sin(2\alpha)]^2 \tag{70}$$

$$I_z \propto [\rho \cos^2(\alpha) + \sin^2(\alpha)]^2 \tag{71}$$

The parameter ρ can then be retrieved from polarization resolved measurements. As an intrinsic value of the fibrils, it may be used as a marker for diseases. However, the measurement will not be reliable if the fibrils are not in the plane perpendicular to laser propagation, like in the right panel of Figure 5.24. Experimentally, in freshly prepared tendons values of $\rho = 2{,}6 \pm 0{,}2$ were measured [5]. This corresponds to extinction values of about 7:1. In out setup, we oriented the sample under the microscope so that the incoming polarization was parallel to the fibers. The polarizer after the shaper was removed and the amplitude set to 0. This resulted in a linear polarization turned by 90°. The recorded images are shown in Figure 5.25. As expected, the image obtained with the laser polarized parallel to the fibers gave much more intensity than with laser polarized perpendicular to the fibers. The same experiment was realized with fibers left to dry during several weeks. A much weaker contrast was observed between the two polarizations, demonstrating that ρ is a factor sensitive to aging of the collagen fibers. No analyzer was used between the microscope and the detector. The microscope objectives have numerical apertures of 0,7 or less and did not show

any modification of the polarization. Gratings in the monochromator have a difference of few percent in transmission between both polarizations, which did not affect the proof of principle measurements presented here.

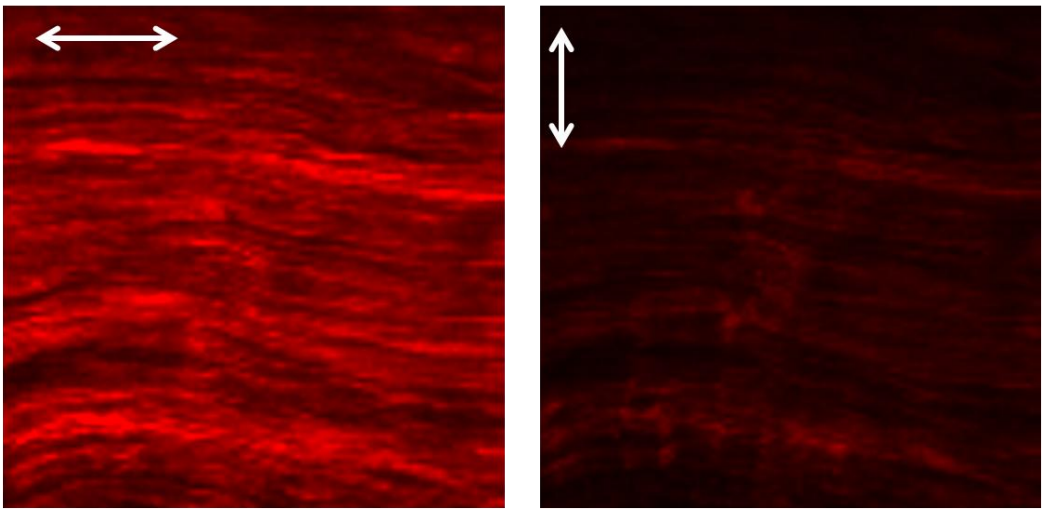

Figure 5.25 Imaging of collagen fibers from a rat tail. With laser light polarized parallel (left) and perpendicular (right) the the fibrils. The images where normalized with the maximum of both measurements.

Polarization dependency measurements are usually realized with waveplates and acquiring one image for each angle α. The idea in this paragraph is to make use of the shaper to realize a polarization measurement in one shot. In a sequential measurement, the image to image reproducibility can be a difficult requirement due, for example, to movement of the sample. The fluctuations of the laser also increase the uncertainty of the experiment. The use of the shaper offers an elegant solution to the challenge of producing simultaneously and detecting two SHG signals with perpendicular polarized light (see section 2.4.4).

For our application, we use the two available linear output polarization states, parallel (//) and perpendicular (⊥) to the incoming laser polarization. To measure the SHG generated by the two polarizations independently we simply divide the pulse into two spectral regions by blocking mechanically the central part of the spectrum in the Fourier plane of our shaper. As a control measurement, the rat tail sample is first scanned with the red and the blue part of the spectrum both in the // configuration. The resulting spectrum is shown in Figure 5.26 b) (blue line). A peak feature is observed in the area situated at half-wavelength of the blocked area, which is absent of the SHG spectrum obtained with the original spectrum (Figure 5.26 a). This peak is the result of sum-frequency generation between the two parts of the excitation spectrum. The feature is reproduced in a simulation using equation (64) (black line in Figure 5.26 b).

Spectra obtained with polarization pulse shaping are shown in Figure 5.26 c). As expected the red and the blue part of the SHG spectrum follow the orientation of the fiber: the signal is maximized for polarization parallel to the fiber and minimized in the perpendicular direction. Interestingly, the SFG peak remains, although with lesser intensity. This peak provides new information additionally to the one-shot comparison of // and ⊥ intensities: it is linked directly to cross terms of $\chi^{(2)}$, inaccessible to usual polarization measurements with only one polarization state of the laser.

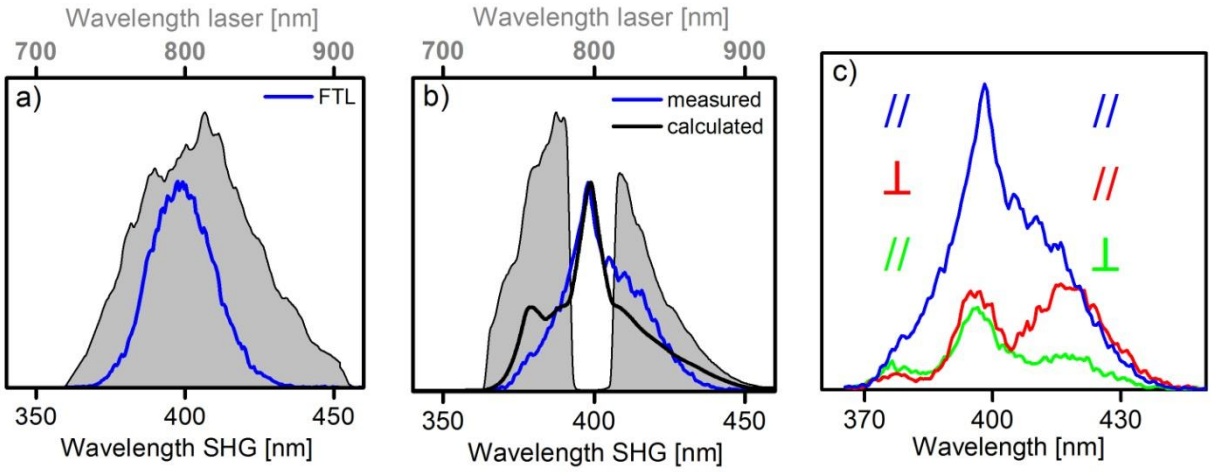

Figure 5.26 Simultaneous measurement of SHG signals produced by perpendicular polarizations inside a broadband pulse. a) Complete laser spectrum (gray area, upper x) and resulting SHG signal (blue line, lower x) obtained with FTL pulses. b) Laser spectrum divided by a blocker in the Fourier plane of the shaper (gray area, upper x). Measured (blue line, lower x) and simulated SHG signals c) SHG spectra obtained by polarization shaping. Blue: red and blue part of the excitation spectrum with parallel polarization. Green: red part with parallel, blue part with perpendicular polarization. Red: red part with perpendicular, blue part with parallel polarization.

5.4 Discussion and Outlook

Multimodal nonlinear microscopy with broadband pulses presents the double advantage of increased nonlinear signal generation and simultaneous excitation of several fluorophores for TPEF and large number of Raman levels. In this work, the use of shaped pulses was explored in theory and experiment. Broadband excitation was compared to excitation with the longer pulse durations commonly used and the increased spectral bandwidth of SHG and CARS signals has been identified as a potential cause of increased overlap. The effect of simple phase distortions has been investigated and dramatic differences have been identified among the studied nonlinear effects.

Multimodal imaging with broadband pulses was demonstrated on plant leaves as well as skin tissue. The results obtained with FTL and shaped pulses have been compared: the FTL case provides the strongest signals while shaping increases specificity. In particular, since the effect of chirp could be predicted, shaping gives access to a method for identification of overlapping contributions of different nonlinear effects. In the case of CARS, the strong nonresonant signal produced by FTL pulses was used to image the structure of the sample while shaping allowed chemical imaging based on the spectral focusing technique developed in the SB-CARS chapter.

In a comparison of spectrally resolved and single-channel implementations, the benefits of a precise determination of the spectral region allowed for each nonlinear signal should not be underestimated. However, in most applications for imaging, only single channel detectors and a set of filters with fixed separation wavelengths are available. In this case, the shaper could be a valuable tool to ensure the correct assignment of the nature of the signal recorded. In addition to the spectral position, the influence of simple phase distortions gives a further indication on whether CARS, TPEF or SHG signals are involved.

As an outlook, two directions seem particularly promising:

- Exploitation of other nonlinear effects
- Polarization shaping.

With the success of the multimodal approach demonstrated in this work, the extension of the number of nonlinear effects considered seems both of practical and of theoretical interest. With additional contrast mechanisms the specificity of imaging will be improved and effects with phase dependencies different from CARS and SHG open the way to new shaping strategies. Two most promising nonlinear effects for our setup are self-phase modulation (SPM) and Third Harmonic Generation (THG). For the detection of SPM, a narrowband region at the center of the spectrum of the 10fs pulse is cut out in the shaper. Nonlinear interaction with the sample fills this spectral hole. Like CARS, SPM depends on $\chi^{(3)}$ but other terms have to be taken into account. Therefore complementary information on the sample can be gained from this measurement. SPM has been used to image neural activity [238-239], demonstrating the high potential of a combination between this contrast mechanism and broadband CARS for brain tissue imaging. Future investigations should compare CARS and SPM for imaging of different samples and the influence of shaping on SPM should be characterized.

THG is also a $\chi^{(3)}$ process and has been extensively used in the multimodal imaging litterature. Phase matching conditions make it particularly sensitive to small objects and interfaces. An application of our setup to THG imaging is however facing a strong limitation due to the absorption by glass of the third harmonic of the central wavelength of the laser (266nm). If fused silica optics are used, THG imaging is possible with a Ti:Sa source [240] with the advantage of a better spatial resolution than with the longer wavelengths mostly used.

Polarization shaping opens a new dimension for multimodal nonlinear imaging. The demonstration presented in this work with only two linear polarizations is only a first step, which proved to be very promising. Further investigations in this direction could concentrate on a better control of the polarization and on the demonstration of the technique for histological samples. Polarization control unravels the tensorial nature of $\chi^{(2)}$ and $\chi^{(3)}$. In the case of CARS, polarization effects can be used to eliminate the nonresonant background [25, 138]. Control of the polarization of the exciting light is necessary to observe nonlinear effects based on induced birefringence, like the Optical Kerr Effect. A contrast mechanism sensitive to the chirality of the molecules could then be accessed in the SB-CARS setup.

6 Conclusion

This work has brought non-linear microscopy with broadband pulses a step further towards rapid imaging of sensitive samples. The use of pulse shaping solves the drawbacks of ultrashort excitation by correcting phase distortions introduced by the microscope objectives, suppressing non-linear photodamage, reducing the nonresonant background in CARS. At the same time, the advantages of broadband excitation are preserved giving access to improved non-linear generation efficiency, large spectral coverage and hence increased specificity. The combination of broadband sources with pulse shaping has been demonstrated to provide setups with high flexibility for efficient excitation tailored to the application.

With **SAM-CARS**, a robust and simple shaping scheme for direct control of the excitation and addressing of the Raman levels of interest. This setup combines the advantages of existing MCARS and ps-CARS setups in an elegant way. SAM-CARS makes available, in the same setup, the acquisition of MCARS spectra and the rapid acquisition of single-band images. The shaping precision allowed identification of polymers with close lying lines and intertwined spatial distribution in a polymer blend. Potential for biological applications has been illustrated with background suppression for the microscopy of *C.elegans*. The contrast improvement in single-channel implementation was also demonstrated.

Current power limitations for the broadband Stokes pulse and restriction to amplitude shaping can readily be circumvented by the **SB-CARS** setup. In this simple implementation, only one broadband pulse provides all the frequencies needed to excite coherently a large number of Raman levels. After demonstrating the challenging coverage of spectral ranges reaching over $3000cm^{-1}$ with different phase control schemes, the merit of each strategy for imaging was discussed. Coherent control schemes based on time-resolved CARS techniques proved impractical due to the necessity to scan a significant number of delays to obtain background free spectra. Spectrally resolved schemes and spectral focusing were then applied to the imaging of the border between healthy murine brain tissue and a tumor, thus demonstrating for the first time relevant medical information on a sensitive sample using a single-beam CARS approach.

In the context of imaging of biological samples, the **multimodal approach** was demonstrated as a powerful complement to the contrast produced by SB-CARS. SHG and TPEF benefit greatly of shorter pulse durations due to the large spectral spectral width of $\chi^{(2)}$ and two-photon absorption respectively. Imaging of plant cells and skin biopsies demonstrated that the large nonresonant CARS signal is useful to retrieve precious structural information. The flexibility of the shaped broadband pulse for multimodal imaging was demonstrated in various ways not accessible in picoseconds implementations: first with the control of the relative intensity of different signals. Second, chemical specific signal was achieved using spectral focusing. Finally, basic polarization shaping capabilities of the shaper opened new perspective for sample characterization with nonlinear microscopy.

Overall, shaped broadband pulses were demonstrated as versatile microscopy tools for microscopy. Many ways to go beyond limitations imposed by nonlinear microscopy with the longer pulses usually used were explored. In this respect, microscopy with broadband pulses

has reached, with this work, the maturity necessary for the study of dynamic processes. To provide a basis for comparison of commercially available narrowband nonlinear microscopes, state-of-the-art scanning and detectors have to be implemented in combination with the schemes presented here. Although SAM-CARS represents the conceptually simpler and relies on the more robust amplitude shaping, the increase of the Stokes pulse energy remains the main hindrance for applications. The SB-CARS setup, in turn, readily provides pulse energies and signal levels compatible with rapid scanning. A characterization of photodamage thresholds would be highly relevant in the perspective of a medical use of SB-CARS and would be best experimented on living cells. Nonlinear photodamage, allowing precise cutting of tissues, could even be used in combination with the shaper to switch between the shaped pulse as an imaging tool and the compressed pulse as a light-scalpel. The promising results on skin imaging with multimodal microscopy further pave the way for *in vivo* observations. The penetration depth for imaging with each nonlinear effect and the evolution of the phase of the pulse in tissues are main questions to be investigated.

On a conceptual level, several problems identified in the course of this thesis offer interesting perspective for further investigations. In SBCARS, a way has to be found to obtain reliable spectral information from sensitive samples. Simulation work could enable better understanding of the phase evolution of the broad signal when amplitude shaping is used. Alternative broadband signal reduction methods for better visibility of the interference features could be achieved using cleverly chosen phase distortion. Relying on spectral focusing as a starting point, new ways for specific single-channel SBCARS are tantalizing. Instead of working exclusively with deterministic phases, future work could use evolutionary optimization for specific phase functions. Spectral focusing performances in terms of signal and resonant to nonresonant ratio provide a figure of merit for the new phases. Alternatively, the concept of two identical phases separated by a given $\Delta\omega$ could be the starting point of the optimization. Schemes combining phase shaping with spectrally resolved detection could help increase the specificity with algorithmic optimization.

Finally, the analysis of further nonlinear effect could complete the contrast achievable with multimodal microscopy. Two most promising extensions are self-phase modulation (SPM) and Third Harmonic Generation (THG). For SPM, a narrowband region at the center of the 10fs pulse is cut out. Nonlinear interaction with the sample fills this spectral hole. SPM depends on $\chi^{(3)}$, however other terms have to be taken into account. Therefore complementary information on the sample can be gained from this measurement. SPM has been used to image neural activity [238-239], demonstrating the high potential of its combination with the brain tissue imaging with broadband CARS. The comparison of both contrast mechanisms for imaging as well as the effect of phase shaping to manipulate their relative contribution has to be investigated. THG is also a $\chi^{(3)}$ process and has been extensively used in multimodal imaging. Phase matching conditions make is particularly sensitive to small objects and interfaces. An application of our setup to THG imaging is however facing a strong limitation due to the absorption of the third harmonic of the central wavelength of the laser (266nm). If fused silica optics are used, THG imaging is possible with a Ti:Sa source [240] with the advantage of a better spatial resolution than with the longer wavelengths usually used.

References

1. Schürmann, S., *Second Harmonic Generation Mikroskopie in biomedizinischen Anwendungen*, in *Institut für Physiologie und Pathophysiologie*. 2010, Dissertation, Ruprecht-Karls-Universität Heidelberg.
2. Brown, E. and T. McKee, *Dynamic imaging of collagen and its modulation in tumors in vivo using second-harmonic generation.* Nature medicine, 2003. **9**(6): p. 796-800.
3. Campagnola, P.J. and L.M. Loew, *Second-harmonic imaging microscopy for visualizing biomolecular arrays in cells, tissues and organisms.* Nature biotechnology, 2003. **21**(11): p. 1356-1360.
4. Sun, C.K., *Higher harmonic generation microscopy.* Microscopy Techniques, 2005: p. 1283-1287.
5. Williams, R.M., W.R. Zipfel, and W.W. Webb, *Interpreting second-harmonic generation images of collagen I fibrils.* Biophysical journal, 2005. **88**(2): p. 1377-1386.
6. Moreaux, L., O. Sandre, and J. Mertz, *Membrane imaging by second-harmonic generation microscopy.* JOSA B, 2000. **17**(10): p. 1685-1694.
7. Schürmann, S., et al., *Second Harmonic Generation Microscopy Probes Different States of Motor Protein Interaction in Myofibrils.* Biophysical journal, 2010. **99**(6): p. 1842-1851.
8. Denk, W., J. Strickler, and W. Webb, *Two-photon laser scanning fluorescence microscopy.* Science, 1990. **248**(4951): p. 73-76.
9. Helmchen, F. and W. Denk, *Deep tissue two-photon microscopy.* Nat Meth, 2005. **2**(12): p. 932-940.
10. Drobizhev, M., et al., *Two-photon absorption properties of fluorescent proteins.* Nat Meth, 2011. **8**(5): p. 393-399.
11. Zipfel, W.R., et al., *Live tissue intrinsic emission microscopy using multiphoton-excited native fluorescence and second harmonic generation.* Proceedings of the national academy of sciences of the United States of America, 2003. **100**(12): p. 7075.
12. Rocheleau, J.V., W.S. Head, and D.W. Piston, *Quantitative NAD(P)H/Flavoprotein Autofluorescence Imaging Reveals Metabolic Mechanisms of Pancreatic Islet Pyruvate Response.* Journal of Biological Chemistry, 2004. **279**(30): p. 31780-31787.
13. Orzekowsky-Schroeder, R., et al., *In vivo spectral imaging of different cell types in the small intestine by two-photon excited autofluorescence.* Journal of Biomedical Optics, 2011. **16**(11): p. 6025.
14. Erikson, A., et al., *Quantification of the second-order nonlinear susceptibility of collagen I using a laser scanning microscope.* Journal of Biomedical Optics, 2007. **12**(4): p. 044002-044002.
15. Debarre, D., et al., *Imaging lipid bodies in cells and tissues using third-harmonic generation microscopy.* Nat Meth, 2006. **3**(1): p. 47-53.
16. Levenson, M.D. and S. Kano, *Introduction to nonlinear laser spectroscopy*. Vol. 140. 1982: Academic Press New York.
17. Kneipp, K., et al., *Single Molecule Detection Using Surface-Enhanced Raman Scattering (SERS).* Physical Review Letters, 1997. **78**(9): p. 1667-1670.
18. Shirley, J.A., R.J. Hall, and A.C. Eckbreth, *Folded BOXCARS for rotational Raman studies.* Opt. Lett., 1980. **5**(9): p. 380-382.
19. Greenhalgh, D.A., *Comments on the use of BOXCARS for gas-phase CARS spectroscopy.* Journal of Raman Spectroscopy, 1983. **14**(3): p. 150-153.
20. Evans, C.L. and X.S. Xie, *Coherent anti-Stokes Raman scattering microscopy: chemical imaging for biology and medicine.* Annu. Rev. Anal. Chem., 2008. **1**: p. 883-909.

21. Zheltikov, A.M., *Coherent anti-Stokes Raman scattering: from proof-of-the-principle experiments to femtosecond CARS and higher order wave-mixing generalizations.* Journal of Raman Spectroscopy, 2000. **31**(8-9): p. 653-667.
22. Maker, P.D. and R.W. Terhune, *Study of Optical Effects Due to an Induced Polarization Third Order in the Electric Field Strength.* Physical Review, 1965. **137**(3A): p. A801-A818.
23. Lotem, H., R.T. Lynch, Jr., and N. Bloembergen, *Interference between Raman resonances in four-wave difference mixing.* Physical Review A, 1976. **14**(5): p. 1748-1755.
24. Oudar, J.-L., R.W. Smith, and Y.R. Shen, *Polarization-sensitive coherent anti-Stokes Raman spectroscopy.* APPLIED PHYSICS LETTERS, 1979. **34**(11): p. 758-760.
25. Cheng, J.-X., L.D. Book, and X.S. Xie, *Polarization coherent anti-Stokes Raman scattering microscopy.* Opt. Lett., 2001. **26**(17): p. 1341-1343.
26. Potma, E.O., C.L. Evans, and X.S. Xie, *Heterodyne coherent anti-Stokes Raman scattering (CARS) imaging.* Opt. Lett., 2006. **31**(2): p. 241-243.
27. Mukamel, S., *Principles of nonlinear optical spectroscopy* 1995: Oxford University Press.
28. Rinia, H.A., et al., *Quantitative CARS Spectroscopy Using the Maximum Entropy Method: The Main Lipid Phase Transition.* ChemPhysChem, 2007. **8**(2): p. 279-287.
29. Duncan, M.D., J. Reintjes, and T.J. Manuccia, *Scanning coherent anti-Stokes Raman microscope.* Opt. Lett., 1982. **7**(8): p. 350-352.
30. Zumbusch, A., G.R. Holtom, and X.S. Xie, *Three-Dimensional Vibrational Imaging by Coherent Anti-Stokes Raman Scattering.* Physical Review Letters, 1999. **82**(20): p. 4142-4145.
31. Ganikhanov, F., et al., *Broadly tunable dual-wavelength light source for coherent anti-Stokes Raman scattering microscopy.* Opt. Lett., 2006. **31**(9): p. 1292-1294.
32. Cheng, J.-x., et al., *An Epi-Detected Coherent Anti-Stokes Raman Scattering (E-CARS) Microscope with High Spectral Resolution and High Sensitivity.* The Journal of Physical Chemistry B, 2001. **105**(7): p. 1277-1280.
33. Potma, E.O. and X.S. Xie, *Detection of single lipid bilayers with coherent anti-Stokes Raman scattering (CARS) microscopy.* Journal of Raman Spectroscopy, 2003. **34**(9): p. 642-650.
34. Cheng, J.-X., et al., *Laser-Scanning Coherent Anti-Stokes Raman Scattering Microscopy and Applications to Cell Biology.* Biophysical journal, 2002. **83**(1): p. 502-509.
35. Evans, C.L., et al., *Chemical imaging of tissue in vivo with video-rate coherent anti-Stokes Raman scattering microscopy.* Proceedings of the national academy of sciences of the United States of America, 2005. **102**(46): p. 16807-16812.
36. Ploetz, E., et al., *Femtosecond stimulated Raman microscopy.* Applied Physics B, 2007. **87**(3): p. 389-393.
37. Freudiger, C.W., et al., *Label-Free Biomedical Imaging with High Sensitivity by Stimulated Raman Scattering Microscopy.* Science, 2008. **322**(5909): p. 1857-1861.
38. Nandakumar, P., A. Kovalev, and A. Volkmer, *Vibrational imaging based on stimulated Raman scattering microscopy.* New Journal of Physics, 2009. **11**(3): p. 033026.
39. Diels, J.C. and W. Rudolph, *Ultrashort laser pulse phenomena*. 2006, San Diego: Academic press.
40. König, K., et al., *Pulse-length dependence of cellular response to intense near-infrared laser pulses in multiphoton microscopes.* Opt. Lett., 1999. **24**(2): p. 113-115.
41. Hopt, A. and E. Neher, *Highly Nonlinear Photodamage in Two-Photon Fluorescence Microscopy.* Biophysical journal, 2001. **80**(4): p. 2029-2036.
42. Fu, Y., et al., *Characterization of photodamage in coherent anti-Stokes Raman scattering microscopy.* Opt. Express, 2006. **14**(9): p. 3942-3951.
43. Müller, M. and J.M. Schins, *Imaging the Thermodynamic State of Lipid Membranes with Multiplex CARS Microscopy.* The Journal of Physical Chemistry B, 2002. **106**(14): p. 3715-3723.
44. Postma, S., et al., *Application of spectral phase shaping to high resolution CARS spectroscopy.* Opt. Express, 2008. **16**(11): p. 7985-7996.

45. Dudovich, N., D. Oron, and Y. Silberberg, *Single-pulse coherently controlled nonlinear Raman spectroscopy and microscopy.* Nature, 2002. **418**(6897): p. 512-514.
46. Leonhardt, R., et al., *Terahertz quantum beats in molecular liquids.* Chemical Physics Letters, 1987. **133**(5): p. 373-377.
47. Boyd, R.W., *Nonlinear optics*. 2003, New York: Academic Press.
48. Volkmer, A., L.D. Book, and X.S. Xie, *Time-resolved coherent anti-Stokes Raman scattering microscopy: Imaging based on Raman free induction decay.* APPLIED PHYSICS LETTERS, 2002. **80**(9): p. 1505-1507.
49. Isobe, K., et al., *Fourier-transform spectroscopy combined with a 5-fs broadband pulse for multispectral nonlinear microscopy.* Physical Review A, 2008. **77**(6): p. 063832.
50. von Vacano, B. and M. Motzkus, *Time-resolving molecular vibration for microanalytics: single laser beam nonlinear Raman spectroscopy in simulation and experiment.* Phys. Chem. Chem. Phys., 2007. **10**(5): p. 681-691.
51. Ogilvie, J.P., et al., *Fourier-transform coherent anti-Stokes Raman scattering microscopy.* Opt. Lett., 2006. **31**(4): p. 480-482.
52. Cui, M., J. Skodack, and J.P. Ogilvie, *Chemical imaging with Fourier transform coherent anti-Stokes Raman scattering microscopy.* Appl. Opt., 2008. **47**(31): p. 5790-5798.
53. Keller, U., *Recent developments in compact ultrafast lasers.* Nature, 2003. **424**(6950): p. 831-838.
54. Krausz, F. and M. Ivanov, *Attosecond physics.* Reviews of Modern Physics, 2009. **81**(1): p. 163.
55. Moulton, P.F., *Spectroscopic and laser characteristics of Ti:Al2O3.* J. Opt. Soc. Am. B, 1986. **3**(1): p. 125-133.
56. Brabec, T. and F. Krausz, *Intense few-cycle laser fields: Frontiers of nonlinear optics.* Reviews of Modern Physics, 2000. **72**(2): p. 545.
57. Curley, P.F., et al., *Operation of a femtosecond Ti:sapphire solitary laser in the vicinity of zero group-delay dispersion.* Opt. Lett., 1993. **18**(1): p. 54-56.
58. Sutter, D.H., et al., *Semiconductor saturable-absorber mirror assisted Kerr-lens mode-locked Ti:sapphire laser producing pulses in the two-cycle regime.* Opt. Lett., 1999. **24**(9): p. 631-633.
59. Zheltikov, A.M., *Let there be white light: supercontinuum generation by ultrashort laser pulses.* Physics-Uspekhi, 2006. **49**(6): p. 605.
60. Russell, P., *Photonic Crystal Fibers.* Science, 2003. **299**(5605): p. 358-362.
61. Wadsworth, W.J., et al., *Supercontinuum generation in photonic crystal fibers and optical fiber tapers: a novel light source.* J. Opt. Soc. Am. B, 2002. **19**(9): p. 2148-2155.
62. Dudley, J.M., G. Genty, and S. Coen, *Supercontinuum generation in photonic crystal fiber.* Reviews of Modern Physics, 2006. **78**(4): p. 1135-1184.
63. Guild, J.B., C. Xu, and W.W. Webb, *Measurement of group delay dispersion of high numerical aperture objective lenses using two-photon excited fluorescence.* Appl. Opt., 1997. **36**(1): p. 397-401.
64. Müller, et al., *Dispersion pre-compensation of 15 femtosecond optical pulses for high-numerical-aperture objectives.* Journal of Microscopy, 1998. **191**(2): p. 141-150.
65. Weiner, A.M., *Ultrafast optical pulse shaping: A tutorial review.* Optics Communications, 2011. **284**(15): p. 3669-3692.
66. Rabitz, H., et al., *Whither the Future of Controlling Quantum Phenomena?* Science, 2000. **288**(5467): p. 824-828.
67. Brumer, P. and M. Shapiro, *Control of unimolecular reactions using coherent light.* Chemical Physics Letters, 1986. **126**(6): p. 541-546.
68. Warren, W.S., H. Rabitz, and M. Dahleh, *Coherent Control of Quantum Dynamics: The Dream Is Alive.* Science, 1993. **259**(5101): p. 1581-1589.
69. Broers, B., H.B. van Linden van den Heuvell, and L.D. Noordam, *Efficient population transfer in a three-level ladder system by frequency-swept ultrashort laser pulses.* Physical Review Letters, 1992. **69**(14): p. 2062-2065.

70. Meshulach, D. and Y. Silberberg, *Coherent quantum control of two-photon transitions by a femtosecond laser pulse.* Nature, 1998. **396**(6708): p. 239-242.
71. Meshulach, D. and Y. Silberberg, *Coherent quantum control of multiphoton transitions by shaped ultrashort optical pulses.* Physical Review A, 1999. **60**(2): p. 1287-1292.
72. Herek, J.L., et al., *Quantum control of energy flow in light harvesting.* Nature, 2002. **417**(6888): p. 533-535.
73. Paschotta, R. and R.P.P. Consulting, *Encyclopedia of laser physics and technology*. Vol. 1. 2008: Wiley Online Library.
74. Cui, M., et al., *Interferometric Fourier transform Coherent anti-Stokes Raman Scattering.* Opt. Express, 2006. **14**(18): p. 8448-8458.
75. Verluise, F., et al., *Amplitude and phase control of ultrashort pulses by use of an acousto-optic programmable dispersive filter: pulse compression and shaping.* Opt. Lett., 2000. **25**(8): p. 575-577.
76. Weiner, A.M., *Femtosecond pulse shaping using spatial light modulators.* Review of Scientific Instruments, 2000. **71**(5): p. 1929-1960.
77. Weiner, A.M., J.P. Heritage, and E.M. Kirschner, *High-resolution femtosecond pulse shaping.* J. Opt. Soc. Am. B, 1988. **5**(8): p. 1563-1572.
78. Hillegas, C.W., et al., *Femtosecond laser pulse shaping by use of microsecond radio-frequency pulses.* Opt. Lett., 1994. **19**(10): p. 737-739.
79. Zeek, E., et al., *Pulse compression by use of deformable mirrors.* Opt. Lett., 1999. **24**(7): p. 493-495.
80. Wefers, M.M. and K.A. Nelson, *Generation of high-fidelity programmable ultrafast optical waveforms.* Opt. Lett., 1995. **20**(9): p. 1047-1049.
81. Brixner, T. and G. Gerber, *Femtosecond polarization pulse shaping.* Opt. Lett., 2001. **26**(8): p. 557-559.
82. Weise, F. and A. Lindinger, *Full control over the electric field using four liquid crystal arrays.* Opt. Lett., 2009. **34**(8): p. 1258-1260.
83. Middleton, C.T., D.B. Strasfeld, and M.T. Zanni, *Polarization shaping in the mid-IR and polarization-based balanced heterodyne detection with application to 2D IR spectroscopy.* Opt. Express, 2009. **17**(17): p. 14526-14533.
84. Plewicki, M., et al., *Independent control over the amplitude, phase, and polarization of femtosecond pulses.* Applied Physics B, 2007. **86**(2): p. 259-263.
85. Plewicki, M., et al., *Phase, amplitude, and polarization shaping with a pulse shaper in a Mach-Zehnder interferometer.* Appl. Opt., 2006. **45**(32): p. 8354-8359.
86. Polachek, L., D. Oron, and Y. Silberberg, *Full control of the spectral polarization of ultrashort pulses.* Opt. Lett., 2006. **31**(5): p. 631-633.
87. Dorrer, C. and F. Salin, *Phase amplitude coupling in spectral phase modulation.* Selected Topics in Quantum Electronics, IEEE Journal of, 1998. **4**(2): p. 342-345.
88. Tanabe, T., et al., *Spatiotemporal measurements based on spatial spectral interferometry for ultrashort optical pulses shaped by a Fourier pulse shaper.* J. Opt. Soc. Am. B, 2002. **19**(11): p. 2795-2802.
89. Stobrawa, G., et al., *A new high-resolution femtosecond pulse shaper.* Applied Physics B, 2001. **72**(5): p. 627-630.
90. Köhler, J., et al., *Zeptosecond precision pulse shaping.* Opt. Express, 2011. **19**(12): p. 11638-11653.
91. Monmayrant, A., S. Weber, and B. Chatel, *A newcomer's guide to ultrashort pulse shaping and characterization.* Journal of Physics B: Atomic, Molecular and Optical Physics, 2010. **43**(10): p. 103001.
92. Silberberg, Y., *Quantum Coherent Control for Nonlinear Spectroscopy and Microscopy.* Annual Review of Physical Chemistry, 2009. **60**(1): p. 277-292.
93. van Rhijn, A.C.W., et al., *Coherent control of vibrational transitions: Discriminating molecules in mixtures.* Faraday Discussions, 2011. **153**(0): p. 227-235.

94. Vacano, B.v., *Chemically selective microspectroscopy with broadband shaped femtosecond laser pulses*. 2008, Dissertation, Philipps-Universität Marburg.
95. Pohling, C., *Multiplex-CARS-Mikroskopie zur schnellen und Raman-äquivalenten Charakterisierung biologischer Proben*. 2012, Dissertation, Universität Heidelberg.
96. Weber, W.H. and R. Merlin, *Raman scattering in materials science*. Vol. 42. 2000, Berlin: Springer-Verlag.
97. Gremiich, H.-U. and B. Yan, *Infrared and Raman Spectroscopy of Biological Materials*. 2000, M. Dekker, New York.
98. Taleb, A., et al., *Raman Microscopy for the Chemometric Analysis of Tumor Cells.* The Journal of Physical Chemistry B, 2006. **110**(39): p. 19625-19631.
99. Krafft, C., et al., *Disease recognition by infrared and Raman spectroscopy.* Journal of Biophotonics, 2009. **2**(1-2): p. 13-28.
100. Krafft, C., et al., *A comparative Raman and CARS imaging study of colon tissue.* Journal of Biophotonics, 2009. **2**(5): p. 303-312.
101. Roh, W.B., P.W. Schreiber, and J.P.E. Taran, *Single-pulse coherent anti-Stokes Raman scattering.* APPLIED PHYSICS LETTERS, 1976. **29**(3): p. 174-176.
102. Otto, C., et al., *Vibrational bands of luminescent zinc(II)-octaethylporphyrin using a polarization-sensitive 'microscopic' multiplex CARS technique.* Journal of Raman Spectroscopy, 2001. **32**(6-7): p. 495-501.
103. Cheng, J.-x., et al., *Multiplex Coherent Anti-Stokes Raman Scattering Microspectroscopy and Study of Lipid Vesicles.* The Journal of Physical Chemistry B, 2002. **106**(34): p. 8493-8498.
104. von Vacano, B., L. Meyer, and M. Motzkus, *Rapid polymer blend imaging with quantitative broadband multiplex CARS microscopy.* Journal of Raman Spectroscopy, 2007. **38**(7): p. 916-926.
105. Kano, H. and H.-o. Hamaguchi, *Ultrabroadband (> 2500 cm[sup -1]) multiplex coherent anti-Stokes Raman scattering microspectroscopy using a supercontinuum generated from a photonic crystal fiber.* APPLIED PHYSICS LETTERS, 2005. **86**(12): p. 121113-3.
106. Kee, T.W. and M.T. Cicerone, *Simple approach to one-laser, broadband coherent anti-Stokes Ramanscattering microscopy.* Opt. Lett., 2004. **29**(23): p. 2701-2703.
107. Meyer, L., *Entwicklung und Aufbau eines femtosekunden-Multiplex-CARS-Mikroskops*, in *Chemistry*. 2006, Diplomarbeit, Philipps-Universität Marburg.
108. Kano, H. and H.-o. Hamaguchi, *Dispersion-compensated supercontinuum generation for ultrabroadband multiplex coherent anti-Stokes Raman scattering spectroscopy.* Journal of Raman Spectroscopy, 2006. **37**(1-3): p. 411-415.
109. Bellini, M. and T.W. Hänsch, *Phase-locked white-light continuum pulses: toward a universal optical frequency-comb synthesizer.* Opt. Lett., 2000. **25**(14): p. 1049-1051.
110. Dudley, J.M. and S. Coen, *Coherence properties of supercontinuum spectra generated in photonic crystal and tapered optical fibers.* Opt. Lett., 2002. **27**(13): p. 1180-1182.
111. Selm, R., et al., *Ultrabroadband background-free coherent anti-Stokes Raman scattering microscopy based on a compact Er:fiber laser system.* Opt. Lett., 2010. **35**(19): p. 3282-3284.
112. Jurna, M., et al., *Background free CARS imaging by phase sensitive heterodyne CARS.* Opt. Express, 2008. **16**(20): p. 15863-15869.
113. Wipfler, A., T. Buckup, and M. Motzkus, *Multiplexing single-beam coherent anti-stokes Raman spectroscopy with heterodyne detection.* Applied Physics Letters, 2012. **100**: p. 071102.
114. Lee, Y.J., Y. Liu, and M.T. Cicerone, *Characterization of three-color CARS in a two-pulse broadband CARS spectrum.* Opt. Lett., 2007. **32**(22): p. 3370-3372.
115. Pestov, D., et al., *Optimizing the Laser-Pulse Configuration for Coherent Raman Spectroscopy.* Science, 2007. **316**(5822): p. 265-268.
116. Lee, Y.J., et al., *Optimized continuum from a photonic crystal fiber for broadband time-resolved coherent anti-Stokes Raman scattering.* Opt. Express, 2010. **18**(5): p. 4371-4379.

117. Wurpel, G.W.H., J.M. Schins, and M. Müller, *Direct Measurement of Chain Order in Single Phospholipid Mono- and Bilayers with Multiplex CARS.* The Journal of Physical Chemistry B, 2004. **108**(11): p. 3400-3403.
118. Rinia, H.A., M. Bonn, and M. Müller, *Quantitative Multiplex CARS Spectroscopy in Congested Spectral Regions.* The Journal of Physical Chemistry B, 2006. **110**(9): p. 4472-4479.
119. Wipfler, A., et al., *Full characterization of the third-order nonlinear susceptibility using a single-beam coherent anti-Stokes Raman scattering setup.* Opt. Lett., 2012. **37**(20): p. 4239-4241.
120. Liu, Y., Y.J. Lee, and M.T. Cicerone, *Broadband CARS spectral phase retrieval using a time-domain Kramers?Kronig transform.* Opt. Lett., 2009. **34**(9): p. 1363-1365.
121. Vartiainen, E.M., *Phase retrieval approach for coherent anti-Stokes Raman scattering spectrum analysis.* J. Opt. Soc. Am. B, 1992. **9**(8): p. 1209-1214.
122. Smith, D.Y., *Dispersion relations for complex reflectivities.* J. Opt. Soc. Am., 1977. **67**(4): p. 570-571.
123. Vartiainen, E.M., K.-E. Peiponen, and T. Asakura, *Phase retrieval in optical spectroscopy: Resolving optical constants from power spectra.* Applied spectroscopy, 1996. **50**(10): p. 1283-1289.
124. Day, J.P.R., et al., *Quantitative Coherent Anti-Stokes Raman Scattering (CARS) Microscopy.* The Journal of Physical Chemistry B, 2011. **115**(24): p. 7713-7725.
125. Cicerone, M.T., et al., *Maximum entropy and time-domain Kramers–Kronig phase retrieval approaches are functionally equivalent for CARS microspectroscopy.* Journal of Raman Spectroscopy, 2012. **43**(5): p. 637-643.
126. Rinia, H.A., et al., *Quantitative Label-Free Imaging of Lipid Composition and Packing of Individual Cellular Lipid Droplets Using Multiplex CARS Microscopy.* Biophysical journal, 2008. **95**(10): p. 4908-4914.
127. Hellerer, T., et al., *Monitoring of lipid storage in Caenorhabditis elegans using coherent anti-Stokes Raman scattering (CARS) microscopy.* Proceedings of the National Academy of Sciences, 2007. **104**(37): p. 14658-14663.
128. Burkacky, O., et al., *Dual-pump coherent anti-Stokes-Raman scattering microscopy.* Opt. Lett., 2006. **31**(24): p. 3656-3658.
129. Saar, B.G., et al., *Video-Rate Molecular Imaging in Vivo with Stimulated Raman Scattering.* Science, 2010. **330**(6009): p. 1368-1370.
130. Freudiger, C.W., et al., *Highly specific label-free molecular imaging with spectrally tailored excitation-stimulated Raman scattering (STE-SRS) microscopy.* Nat Photon, 2011. **5**(2): p. 103-109.
131. Rehbinder, J., et al., *Multiplex coherent anti-Stokes Raman microspectroscopy with tailored Stokes spectrum.* Opt. Lett., 2010. **35**(22): p. 3721-3723.
132. Fu, D., et al., *Quantitative Chemical Imaging with Multiplex Stimulated Raman Scattering Microscopy.* Journal of the American Chemical Society, 2012. **134**(8): p. 3623-3626.
133. Fu, D., et al., *Hyperspectral Imaging with Stimulated Raman Scattering by Chirped Femtosecond Lasers.* The Journal of Physical Chemistry B, 2012. **117**(16): p. 4634-4640.
134. Ozeki, Y., et al., *High-speed molecular spectral imaging of tissue with stimulated Raman scattering.* Nat Photon, 2012. **6**(12): p. 845-851.
135. Oron, D., et al., *Quantum control of coherent anti-Stokes Raman processes.* Physical Review A, 2002. **65**(4): p. 043408.
136. Oron, D., N. Dudovich, and Y. Silberberg, *Single-Pulse Phase-Contrast Nonlinear Raman Spectroscopy.* Physical Review Letters, 2002. **89**(27): p. 273001.
137. Dudovich, N., D. Oron, and Y. Silberberg, *Single-pulse coherent anti-Stokes Raman spectroscopy in the fingerprint spectral region.* The Journal of Chemical Physics, 2003. **118**(20): p. 9208-9215.

138. Oron, D., N. Dudovich, and Y. Silberberg, *Femtosecond Phase-and-Polarization Control for Background-Free Coherent Anti-Stokes Raman Spectroscopy.* Physical Review Letters, 2003. **90**(21): p. 213902.
139. Oron, D., N. Dudovich, and Y. Silberberg, *All-optical processing in coherent nonlinear spectroscopy.* Physical Review A, 2004. **70**(2): p. 023415.
140. Katz, O., et al., *Single-beam coherent Raman spectroscopy and microscopy via spectral notch shaping.* Opt. Express, 2010. **18**(22): p. 22693-22701.
141. Katz, O., et al., *Standoff detection of trace amounts of solids by nonlinear Raman spectroscopy using shaped femtosecond pulses.* APPLIED PHYSICS LETTERS, 2008. **92**(17): p. 171116-3.
142. Natan, A., et al., *Standoff detection via single-beam spectral notch filtered pulses.* APPLIED PHYSICS LETTERS, 2012. **100**(5): p. 051111-3.
143. Frumker, E. and Y. Silberberg, *Femtosecond pulse shaping using a two-dimensional liquid-crystal spatial light modulator.* Opt. Lett., 2007. **32**(11): p. 1384-1386.
144. Frostig, H., et al., *Single-pulse stimulated Raman scattering spectroscopy.* Opt. Lett., 2011. **36**(7): p. 1248-1250.
145. von Vacano, B., W. Wohlleben, and M. Motzkus, *Actively shaped supercontinuum from a photonic crystal fiber for nonlinear coherent microspectroscopy.* Opt. Lett., 2006. **31**(3): p. 413-415.
146. von Vacano, B. and M. Motzkus, *Time-resolved two color single-beam CARS employing supercontinuum and femtosecond pulse shaping.* Optics Communications, 2006. **264**(2): p. 488-493.
147. von Vacano, B., W. Wohlleben, and M. Motzkus, *Single-beam CARS spectroscopy applied to low-wavenumber vibrational modes.* Journal of Raman Spectroscopy, 2006. **37**(1-3): p. 404-410.
148. Vacano, B.v. and M. Motzkus, *Molecular discrimination of a mixture with single-beam Raman control.* The Journal of Chemical Physics, 2007. **127**(14): p. 144514.
149. von Vacano, B., T. Buckup, and M. Motzkus, *Highly sensitive single-beam heterodyne coherent anti-Stokes Raman scattering.* Opt. Lett., 2006. **31**(16): p. 2495-2497.
150. von Vacano, B., et al., *Microanalytical nonlinear single-beam spectroscopy combining an unamplified femtosecond fibre laser, pulse shaping and interferometry.* Applied Physics B, 2008. **91**(2): p. 213-217.
151. Müller, C., et al., *Heterodyne single-beam CARS microscopy.* Journal of Raman Spectroscopy, 2009. **40**(7): p. 809-816.
152. Lim, S.-H., A.G. Caster, and S.R. Leone, *Single-pulse phase-control interferometric coherent anti-Stokes Raman scattering spectroscopy.* Physical Review A, 2005. **72**(4): p. 041803.
153. Lim, S.-H., et al., *Chemical Imaging by Single Pulse Interferometric Coherent Anti-Stokes Raman Scattering Microscopy.* The Journal of Physical Chemistry B, 2006. **110**(11): p. 5196-5204.
154. Lim, S.-H., A.G. Caster, and S.R. Leone, *Fourier transform spectral interferometric coherent anti-Stokes Raman scattering (FTSI-CARS) spectroscopy.* Opt. Lett., 2007. **32**(10): p. 1332-1334.
155. Chen, B.-C. and S.-H. Lim, *Optimal Laser Pulse Shaping for Interferometric Multiplex Coherent Anti-Stokes Raman Scattering Microscopy.* The Journal of Physical Chemistry B, 2008. **112**(12): p. 3653-3661.
156. Sung, J., B.-C. Chen, and S.-H. Lim, *Fast three-dimensional chemical imaging by interferometric multiplex coherent anti-Stokes Raman scattering microscopy.* Journal of Raman Spectroscopy, 2011. **42**(2): p. 130-136.
157. Chen, B.-C., J. Sung, and S.-H. Lim, *Chemical Imaging with Frequency Modulation Coherent Anti-Stokes Raman Scattering Microscopy at the Vibrational Fingerprint Region.* The Journal of Physical Chemistry B, 2010. **114**(50): p. 16871-16880.

158. Chen, B.-C., et al., *Chemical imaging and microspectroscopy with spectral focusing coherent anti-Stokes Raman scattering.* Journal of Biomedical Optics, 2011. **16**(2): p. 021112-021112.
159. Li, H., et al., *Coherent mode-selective Raman excitation towards standoff detection.* Opt. Express, 2008. **16**(8): p. 5499-5504.
160. Li, H., et al., *Standoff and arms-length detection of chemicals with single-beam coherent anti-Stokes Raman scattering.* Appl. Opt., 2009. **48**(4): p. B17-B22.
161. Bremer, M.T., et al., *Highly selective standoff detection and imaging of trace chemicals in a complex background using single-beam coherent anti-Stokes Raman scattering.* APPLIED PHYSICS LETTERS, 2011. **99**(10): p. 101109-3.
162. Roy, S., et al., *Single-beam coherent anti-Stokes Raman scattering (CARS) spectroscopy of gas-phase CO2 via phase and polarization shaping of a broadband continuum.* Journal of Raman Spectroscopy, 2010. **41**(10): p. 1194-1199.
163. Wrzesinski, P.J., et al., *Binary phase shaping for selective single-beam CARS spectroscopy and imaging of gas-phase molecules.* Journal of Raman Spectroscopy, 2011. **42**(3): p. 393-398.
164. Diels, J.-C.M., et al., *Control and measurement of ultrashort pulse shapes (in amplitude and phase) with femtosecond accuracy.* Appl. Opt., 1985. **24**(9): p. 1270-1282.
165. Spielmann, C., L. Xu, and F. Krausz, *Measurement of interferometric autocorrelations: comment.* Appl. Opt., 1997. **36**(12): p. 2523-2525.
166. Yamane, K., et al., *Experimental and theoretical demonstration of validity and limitations in fringe-resolved autocorrelation measurements for pulses of few optical cycles.* Opt. Express, 2004. **12**(12): p. 2762-2773.
167. Ozeki, Y., G. Omura, and K. Itoh, *Broadband group delay dispersion compensation for a microscope objective lens with a specially-designed mechanical deformable mirror.* Opt. Express, 2008. **16**(4): p. 2778-2783.
168. Fittinghoff, D.N., et al., *Collinear type II second-harmonic-generation frequency-resolved optical gating for use with high-numerical-aperture objectives.* Opt. Lett., 1998. **23**(13): p. 1046-1048.
169. von Vacano, B., T. Buckup, and M. Motzkus, *In situ broadband pulse compression for multiphoton microscopy using a shaper-assisted collinear SPIDER.* Opt. Lett., 2006. **31**(8): p. 1154-1156.
170. Kane, D.J. and R. Trebino, *Characterization of arbitrary femtosecond pulses using frequency-resolved optical gating.* Quantum Electronics, IEEE Journal of, 1993. **29**(2): p. 571-579.
171. Iaconis, C. and I.A. Walmsley, *Spectral phase interferometry for direct electric-field reconstruction of ultrashort optical pulses.* Opt. Lett., 1998. **23**(10): p. 792-794.
172. Galler, A. and T. Feurer, *Pulse shaper assisted short laser pulse characterization.* Applied Physics B, 2008. **90**(3-4): p. 427-430.
173. Sung, J., B.-C. Chen, and S.-H. Lim, *Single-beam homodyne SPIDER for multiphoton microscopy.* Opt. Lett., 2008. **33**(13): p. 1404-1406.
174. Lozovoy, V.V., I. Pastirk, and M. Dantus, *Multiphoton intrapulse interference.IV.Ultrashort laserpulse spectral phase characterization and compensation.* Opt. Lett., 2004. **29**(7): p. 775-777.
175. Baumert, T., et al., *Femtosecond pulse shaping by an evolutionary algorithm with feedback.* Applied Physics B, 1997. **65**(6): p. 779-782.
176. Zeidler, D., et al., *Evolutionary algorithms and their application to optimal control studies.* Physical Review A, 2001. **64**(2): p. 023420.
177. Yelin, D., D. Meshulach, and Y. Silberberg, *Adaptive femtosecond pulse compression.* Opt. Lett., 1997. **22**(23): p. 1793-1795.
178. Meshulach, D., Y. Barad, and Y. Silberberg, *Measurement of ultrashort optical pulses by third-harmonic generation.* J. Opt. Soc. Am. B, 1997. **14**(8): p. 2122-2125.
179. Hache, F., et al., *Measurement of ultrashort pulsedurations by interferometricautocorrelation: influence of various parameters.* Appl. Opt., 1996. **35**(18): p. 3230-3236.

180. Evans, C.L. and X.S. Xie, *Coherent Anti-Stokes Raman Scattering Microscopy: Chemical Imaging for Biology and Medicine.* Annual Review of Analytical Chemistry, 2008. **1**(1): p. 883-909.
181. Freudiger, C.W., et al., *Multicolored stain-free histopathology with coherent Raman imaging.* Lab Invest, 2012. **92**(10): p. 1492-1502.
182. Heinrich, C., et al., *Selective imaging of saturated andunsaturated lipids by wide-fieldCARS-microscopy.* Opt. Express, 2008. **16**(4): p. 2699-2708.
183. Polack, T., D. Oron, and Y. Silberberg, *Control and measurement of a non-resonant Raman wavepacket using a single ultrashort pulse.* Chemical Physics, 2005. **318**(1–2): p. 163-169.
184. Roy, S., et al., *Single-beam coherent anti-Stokes Raman scattering spectroscopy of N_2 using a shaped 7 fs laser pulse.* APPLIED PHYSICS LETTERS, 2009. **95**(7): p. 074102-3.
185. Lepetit, L., G. Chériaux, and M. Joffre, *Linear techniques of phase measurement by femtosecond spectral interferometry for applications in spectroscopy.* J. Opt. Soc. Am. B, 1995. **12**(12): p. 2467-2474.
186. Hellerer, T., A.M.K. Enejder, and A. Zumbusch, *Spectral focusing: High spectral resolution spectroscopy with broad-bandwidth laser pulses.* APPLIED PHYSICS LETTERS, 2004. **85**(1): p. 25-27.
187. Naumov, A.N. and A.M. Zheltikov, *Frequency–time and time–space mappings for single-shot coherent four-wave mixing with chirped pulses and broad beams.* Journal of Raman Spectroscopy, 2001. **32**(11): p. 960-970.
188. Langbein, W., I. Rocha-Mendoza, and P. Borri, *Single source coherent anti-Stokes Raman microspectroscopy using spectral focusing.* APPLIED PHYSICS LETTERS, 2009. **95**(8): p. 081109-3.
189. Rocha-Mendoza, I., W. Langbein, and P. Borri, *Coherent anti-Stokes Raman microspectroscopy using spectral focusing with glass dispersion.* APPLIED PHYSICS LETTERS, 2008. **93**(20): p. 201103-3.
190. Pegoraro, A.F., et al., *Optimally chirped multimodal CARS microscopy based on a single Ti:sapphireoscillator.* Opt. Express, 2009. **17**(4): p. 2984-2996.
191. Langbein, W., I. Rocha-Mendoza, and P. Borri, *Coherent anti-Stokes Raman micro-spectroscopy using spectral focusing: theory and experiment.* Journal of Raman Spectroscopy, 2009. **40**(7): p. 800-808.
192. Pillai, R.S., et al., *Multiplexed two-photon microscopy of dynamic biological samples with shaped broadband pulses.* Optics express, 2009. **17**(15): p. 12741-12752.
193. Wipfler, A., *Personal Communication*. 2013.
194. Xu, C. and W.W. Webb, *Measurement of two-photon excitation cross sections of molecular fluorophores with data from 690 to 1050 nm.* J. Opt. Soc. Am. B, 1996. **13**(3): p. 481-491.
195. Laubereau, A., D. von der Linde, and W. Kaiser, *Direct Measurement of the Vibrational Lifetimes of Molecules in Liquids.* Physical Review Letters, 1972. **28**(18): p. 1162-1165.
196. Cheng, J.-X. and X.S. Xie, *Coherent Anti-Stokes Raman Scattering Microscopy: Instrumentation, Theory, and Applications.* The Journal of Physical Chemistry B, 2003. **108**(3): p. 827-840.
197. Selm, R., et al., *Simultaneous second-harmonic generation, third-harmonic generation, and four-wave mixing microscopy with single sub-8 fs laser pulses.* APPLIED PHYSICS LETTERS, 2011. **99**(18): p. 181124-3.
198. Xu, C., et al., *Multiphoton fluorescence excitation: new spectral windows for biological nonlinear microscopy.* Proceedings of the National Academy of Sciences, 1996. **93**(20): p. 10763-10768.
199. Ogilvie, J.P., et al., *Use of coherent control for selective two-photon fluorescence microscopy in live organisms.* Opt. Express, 2006. **14**(2): p. 759-766.
200. Lansford, R., G. Bearman, and S.E. Fraser, *Resolution of multiple green fluorescent protein color variants and dyes using two-photon microscopy and imaging spectroscopy.* Journal of Biomedical Optics, 2001. **6**(3): p. 311-318.

201. Dickinson, M., et al., *Multi-spectral imaging and linear unmixing add a whole new dimension to laser scanning fluorescence microscopy.* Biotechniques, 2001. **31**(6): p. 1272-1279.
202. Kapuscinski, J., *DAPI: a DMA-Specific Fluorescent Probe.* Biotechnic & Histochemistry, 1995. **70**(5): p. 220-233.
203. Heim, R., A.B. Cubitt, and R.Y. Tsien, *Improved green fluorescence.* Nature, 1995. **373**(6516): p. 663-664.
204. Shaner, N.C., P.A. Steinbach, and R.Y. Tsien, *A guide to choosing fluorescent proteins.* Nat Meth, 2005. **2**(12): p. 905-909.
205. Yuan, L., et al., *Multimodal Nonlinear Microscopy by Shaping a Fiber Supercontinuum From 900 to 1160nm.* Selected Topics in Quantum Electronics, IEEE Journal of, 2012. **18**(3): p. 1209-1214.
206. Wild, E., et al., *Use of two-photon excitation microscopy and autofluorescence for visualizing the fate and behavior of semivolatile organic chemicals within living vegetation.* Environmental Toxicology and Chemistry, 2007. **26**(12): p. 2486-2493.
207. Keyte, I., et al., *Investigating the foliar uptake and within-leaf migration of phenanthrene by moss (Hypnum cupressiforme) using two-photon excitation microscopy with autofluorescence.* Environmental science & technology, 2009. **43**(15): p. 5755-5761.
208. Jones, E.W. and C. Kevin, *Seeing Chemicals in Environmental Samples.* Environmental science & technology, 2007. **41**(17): p. 5934-5938.
209. Pohling, C., T. Buckup, and M. Motzkus, *Hyperspectral data processing for chemoselective multiplex coherent anti-Stokes Raman scattering microscopy of unknown samples.* Journal of Biomedical Optics, 2011. **16**(2): p. 021105.
210. Blackwell, J., P.D. Vasko, and J.L. Koenig, *Infrared and Raman Spectra of the Cellulose from the Cell Wall of Valonia ventricosa.* Journal of Applied Physics, 1970. **41**(11): p. 4375-4379.
211. Wilhelm, K.P., et al., *Bioengineering of the Skin: Skin Imaging & Analysis*. Vol. 31. 2006, New York: Informa Healthcare.
212. von Lilienfeld-Toal, H., et al., *A novel approach to non-invasive glucose measurement by mid-infrared spectroscopy: The combination of quantum cascade lasers (QCL) and photoacoustic detection.* Vibrational Spectroscopy, 2005. **38**(1−2): p. 209-215.
213. Stout, P.J., et al., *Comparison of glucose levels in dermal interstitial fluid and finger capillary blood.* Diabetes technology & therapeutics, 2001. **3**(1): p. 81-90.
214. Laiho, L.H., et al., *Two-photon 3-D mapping of ex vivo human skin endogenous fluorescence species based on fluorescence emission spectra.* Journal of Biomedical Optics, 2005. **10**(2): p. 024016-024016.
215. Tai, S.-P., et al., *Optical biopsy of fixed human skin with backward-collected optical harmonics signals.* Opt. Express, 2005. **13**(20): p. 8231-8242.
216. Benalcazar, W. and S. Boppart, *Nonlinear interferometric vibrational imaging for fast label-free visualization of molecular domains in skin.* Analytical and Bioanalytical Chemistry, 2011. **400**(9): p. 2817-2825.
217. Breunig, H.G., et al., *Combined in vivo multiphoton and CARS imaging of healthy and disease-affected human skin.* Microscopy Research and Technique, 2012. **75**(4): p. 492-498.
218. König, K., et al., *Applications of multiphoton tomographs and femtosecond laser nanoprocessing microscopes in drug delivery research.* Advanced Drug Delivery Reviews, 2011. **63**(4−5): p. 388-404.
219. Rogers Hw, W.M.A.H.A.R. and et al., *INcidence estimate of nonmelanoma skin cancer in the united states, 2006.* Archives of Dermatology, 2010. **146**(3): p. 283-287.
220. Dimitrow, E., et al., *Sensitivity and Specificity of Multiphoton Laser Tomography for In Vivo and Ex Vivo Diagnosis of Malignant Melanoma.* J Invest Dermatol, 2009. **129**(7): p. 1752-1758.
221. Vogler, N., et al., *Multimodal imaging to study the morphochemistry of basal cell carcinoma.* Journal of Biophotonics, 2010. **3**(10-11): p. 728-736.

222. Koenig, K. and I. Riemann, *High-resolution multiphoton tomography of human skin with subcellular spatial resolution and picosecond time resolution.* Journal of Biomedical Optics, 2003. **8**(3): p. 432-439.
223. Na, R., et al., *Autofluorescence spectrum of skin: component bands and body site variations.* Skin Research and Technology, 2000. **6**(3): p. 112-117.
224. Gareau, D.S., et al., *Confocal mosaicing microscopy in Mohs skin excisions: feasibility of rapid surgical pathology.* Journal of Biomedical Optics, 2008. **13**(5): p. 054001-054001.
225. Tosti, A., *A COMPARISON OF THE HISTODYNAMICS OF SEBACEOUS GLANDS AND EPIDERMIS IN MAN: A MICROANATOMIC AND MORPHOMETRIC STUDY.* J Investig Dermatol, 1974. **62**(3): p. 147-152.
226. Webster, G.F. and A.V. Rawlings, *Acne and its therapy*. Vol. 40. 2007: Informa HealthCare.
227. Saar, B.G., et al., *Coherent Raman scanning fiber endoscopy.* Opt. Lett., 2011. **36**(13): p. 2396-2398.
228. Chunqiang, L., et al., *Multiphoton Microscopy of Live Tissues With Ultraviolet Autofluorescence.* Selected Topics in Quantum Electronics, IEEE Journal of, 2010. **16**(3): p. 516-523.
229. Saar, B.G., et al., *Imaging Drug Delivery to Skin with Stimulated Raman Scattering Microscopy.* Molecular Pharmaceutics, 2011. **8**(3): p. 969-975.
230. Chu, S.-W., et al., *Studies of $\chi(2)/\chi(3)$ Tensors in Submicron-Scaled Bio-Tissues by Polarization Harmonics Optical Microscopy.* Biophysical journal, 2004. **86**(6): p. 3914-3922.
231. LaComb, R., O. Nadiarnykh, and P.J. Campagnola, *Quantitative Second Harmonic Generation Imaging of the Diseased State Osteogenesis Imperfecta: Experiment and Simulation.* Biophysical journal, 2008. **94**(11): p. 4504-4514.
232. Sun, Y., et al., *Multiphoton polarization imaging of the stratum corneum and the dermis in ex-vivo human skin.* Opt. Express, 2003. **11**(25): p. 3377-3384.
233. Yasui, T., Y. Tohno, and T. Araki, *Determination of Collagen Fiber Orientation in Human Tissue by Use of Polarization Measurement of Molecular Second-Harmonic-Generation Light.* Appl. Opt., 2004. **43**(14): p. 2861-2867.
234. Celis, J.E., et al., *Cell Biology, Four-Volume Set: A Laboratory Handbook*. Vol. 1. 2005: Academic Press.
235. Freund, I., M. Deutsch, and A. Sprecher, *Connective tissue polarity. Optical second-harmonic microscopy, crossed-beam summation, and small-angle scattering in rat-tail tendon.* Biophysical journal, 1986. **50**(4): p. 693-712.
236. Stoller, P., et al., *Polarization-Modulated Second Harmonic Generation in Collagen.* Biophysical journal, 2002. **82**(6): p. 3330-3342.
237. Kleinman, D.A., *Nonlinear Dielectric Polarization in Optical Media.* Physical Review, 1962. **126**(6): p. 1977-1979.
238. Fischer, M.C., et al., *Two-photon absorption and self-phase modulation measurements with shaped femtosecond laser pulses.* Opt. Lett., 2005. **30**(12): p. 1551-1553.
239. Fischer, M.C., et al., *Self-phase modulation signatures of neuronal activity.* Opt. Lett., 2008. **33**(3): p. 219-221.
240. Yelin, D., et al., *Third-harmonic microscopy with a titanium–sapphire laser.* Applied Physics B, 2002. **74**(1): p. s97-s101.

Danksagung

An erster Stelle gilt mein Dank Herrn Professor Dr. Marcus Motzkus für die Möglichkeit, in seiner Arbeitsgruppe zu promovieren. Dass ich diese Zeit als eine Herausforderung sehen durfte, ist ihm zu verdanken. Besonders zu schätzen wusste ich seine Bemühungen, uns die besten Bedingungen zu schaffen. Seine intensive Vernetzung in der Community eröffnete mir die Möglichkeit an der aktuellen medizinischen Forschung teilzuhaben.

Herrn PD Dr. Dirk-Peter Herten danke ich für die freundliche Übernahme des Zweitgutachtens.

An zweiter Stelle möchte ich mich bei Herrn Dr. Tiago Buckup für seine effiziente Betreuung bedanken. Seine Anregungen und konstruktive Kritik haben zur Bereicherung dieser Arbeit beigetragen. Auch war seine Tür für Diskussionen stets offen.

Die Hilfsbereitschaft von Herrn Professor Dr. Hans-Robert Volpp, unter anderem bei der Vorbereitung zur Kenntnisstandprüfung, werde ich nicht vergessen.

An dieser Stelle möchte ich meinen CARS-Brüdern Dr.Christoph Pohling und Alexander Wipfler für die gemeinsame Zeit danken. Der Platz und die Worte fehlen, um euren Beitrag hier zusammen zu fassen. Für seine einleuchtenden Einsichten, zahlreichen Ideen und beindruckenden Labview Kenntnisse danke ich Dr. Jens Möhring. Ein herzliches Dankeschön geht an Marie Marek und Julia Herz für die Versüßung des Uni-Alltags und ihre Unterstützung, besonders während des Zusammenschreibens. Meinen Bürogenossen Jan-Philip Kraack und Dzmitry Starukhin danke ich für die angenehme Atmosphäre. Takeshi Miki und Jiang Man möchte ich für unterhaltsame Diskussionen und den gemeinsamen Kampf gegen die deutsche Sprache danken.

Des weiteren bedanke ich mich bei Dr. Bernhard von Vacano, der mich mit der Begeisterung für nichtlineare Mikroskopie angesteckt hat, sowie Lukas Brückner, in dem ich einen würdigen Nachfolger fand. Die angenehme Zusammenarbeit an dem multimodalen Aufbau hat direkt zu dieser Arbeit beigetragen.

Ohne die Unterstützung meiner Familie und Freunde, sei es in Paris, Frankfurt oder Köln, hätte diese Arbeit nicht zustande kommen können. Nicht zuletzt möchte ich Elena für ihre Geduld, ihr Mitgefühl und ihren unerschöpflichen Optimismus danken.